UNIVERSITÀ DEGLI STUDI DI PADOVA

UNIVERSITÁ DEGLI STUDI DI PADOVA

DIPARTIMENTO DI SCIENZE CHIMICHE

Scuola di Dottorato di Ricerca in Scienza ed Ingegneria
dei Materiali e delle Nanostrutture

Ciclo XXVII

PLASMONIC AND MAGNETIC NANOSTRUCTURES FOR MULTIPLEXING DETECTION AND MULTIPLE IMAGING TECHNIQUES IN BIONANOMED

Direttore della Scuola: Ch.mo Prof. Gaetano Granozzi

Supervisore: Ch.mo Prof. Moreno Meneghetti

Dottorando: Dr. Lucio Litti

Anni 2012-2014

Table of Contents

Abstract

In the last years nanotechnology is strongly influencing the progresses of medicine, in particular against cancer, both for diagnostic and therapeutic purposes.
Nanostructures can be planned with properties useful for a specific application. However, the same nanostructure can be synthesized also for more diagnostic techniques. In addiction, one can also plan these nanostructures for what is called multiplexing, namely the presence in the same diagnostic signal of information related to many analytes at the same time. The nanostructures can be synthesized for obtaining targeting, which increases the ability of discriminating different type of tumour associated antigens or, in the case of therapeutic purposes, for the ability of being directed to a specific site.
In the present thesis, nanostructures have been synthesized for their applications in particular with two techniques like surface enhanced Raman spectroscopy (SERS) and magnetic resonance imaging (MRI), which are complementary techniques for imaging. The nanostructures have been functionalized also with antibodies for targeting antigens.
SERS exploits the huge enhancement of electromagnetic fields of plamonic nanostructures. It is shown that this technique can be used for quantitative measurements of clinically interesting anticancer drugs, with a linear range response in the order of nanomole per millimetre square of SERS active area, which is appropriate also for clinical purposes. It is also demonstrated how molecules with a poor Raman cross section could be revealed with the help of a protocol, called *Reactive-SERS*, which considers a simple photoactivated reaction.
Nanoparticles are obtained with laser ablation and they are found easy to functionalize due to their unique naked surface. It is shown that their properties are useful in laser desorption ionization mass spectrometry. Used as a matrix, they are compared with chemically produced particles and with a widely used organic matrix and they always show the lowest background especially in the low mass region under 500 Da, which is important for the identification of small molecules.
Multiplexing analysis are carried out with gold nanoparticles (AuNP) functionalized with different dyes, as SERS reporters, associated to different antibodies. The library of optimized thiolated reporters is increased and makes possible to investigate more complex biological samples. This application is also translated to the cultural heritage research field for the characterization of paint stratigraphic samples.
Multimodal contrast agents are developed, coupling the SERS activity, typical of dye functionalized gold nanoparticles, with magnetic sensitive moieties, like iron atoms in alloy nanoparticles or with Gd^{3+} ions linked to gold nanoparticles. A new polymer, called *SuperDOTA*, is synthetized for achieving high Gd^{3+} loadings on the surface of nanoparticles. Preliminary results show that AuNPs, functionalized with both a SERS reporter dye and *SuperDOTA*-Gd, have useful properties for *in vivo* MRI tumour analysis and *ex-vivo* SERS imaging.

Riassunto

Negli ultimi anni le nanotecnologie stanno fortemente influenzando i progressi della medicina, in particolare contro il cancro, sia per quanto riguarda la diagnostica che la terapia.

Le nanostrutture possono essere pianificate con proprietà utili per specifiche applicazioni. Ad ogni modo, la stessa nanostruttura può essere sintetizzata anche per più tecniche diagnostiche. In aggiunta, si possono ottenere nanostrutture per quel che viene chiamato multiplexing, ovvero la presenza nello stesso segnale diagnostico di informazioni relative a più analiti simultaneamente. Le nanostrutture possono essere sintetizzate per ottenere targeting, che aumenta l'abilità di discriminare differenti tipi di antigeni associati a tumori o, nel caso di obiettivi terapeutici, per l'abilità di raggiungere un sito specifico.

Nella presente tesi, le nanostrutture sono state sintetizzate per applicazioni con due particolari tecniche come la spettroscopia Raman amplificata da superfici (SERS) e l'imaging per risonanza magnetica (MRI), che sono tecniche di imaging complementari. Le nanostrutture sono state altresì funzionalizzate con anticorpi per il riconoscimento di antigeni.

Il SERS sfrutta l'enorme amplificazione dei campi elettromagnetici di una nanostruttura plasmonica. Viene mostrato che questa tecnica può essere usata per misure quantitative di farmaci antitumorali di interesse clinico, con un range di risposta lineare nell'ordine delle nanomoli per millimetro quadrato di superficie SERS attiva, che risulta appropriato anche per applicazioni cliniche. Viene in oltre dimostrato come molecole con una bassa sezione d'urto Raman possano essere rivelate con l'aiuto di un protocollo, chiamato *Reactive-SERS*, che sfrutta una semplice reazione fotoattivata.

Le nanoparticelle sono ottenute per ablazione laser e risultano quindi facili da funzionalizzare a causa della loro peculiare purezza superficiale. Viene mostrato che le loro proprietà sono utili per la spettrometria di massa a ionizzazione per desorbimento laser. Usate come matrice, sono state confrontate con particelle prodotte chimicamente e con una matrice organica largamente utilizzata e hanno sempre mostrato un rumore di fondo inferiore, specialmente nella zona dei bassi pesi molecolari, sotto i 500 Da, che è una zona importante per l'identificazione di piccole molecole.

L'analisi in multiplexing viene fatta con nanoparticelle di oro (AuNP) funzionalizzate con differenti coloranti, come SERS reporters, associati a differenti anticorpi. La libreria di coloranti tiolati ottimizzati è stata incrementata e rende possibile investigare campioni biologici più complessi. Questa applicazione è stata anche traslata alla ricerca applicata ai beni culturali per la caratterizzazione di campioni pittorici stratigrafici.

Sono stati sviluppati agenti di contrasto multimodali, accoppiando l'attività SERS, tipica delle particelle di oro funzionalizzate con coloranti, e agenti sensibili a campi magnetici, come atomi di ferro in nanoparticelle di lega o ioni Gd^{3+} legati alle nanoparticelle di oro. Un nuovo polimero, chiamato *SuperDOTA*, è stato sintetizzato per raggiungere alte concentrazioni di Gd^{3+} sulla superficie delle nanoparticelle. Risultati preliminari mostrano che queste AuNP, funzionalizzate sia con coloranti SERS reporter che con *SuperDOTA*-Gd, hanno proprietà utili per analisi *in vivo* di tumori con MRI ed imaging *ex vivo* con SERS.

1. Introduction

"I want to build a billion tiny factories, models of each other, which are manufacturing simultaneously… The principles of physics, as far as I can see, do not speak against the possibility of manoeuvring things atom by atom. It is not an attempt to violate any laws; it is something, in principle, that can be done; but in practice, it has not been done because we are too big."
Richard P. Feynman (1918-1988), Noble Prize in Physics in 1965

During "There's Plenty of Room at the Bottom", a lecture at the American Physical Society meeting at Caltech in 1959, Richard P. Feynman inspired the concepts of nanotechnology. He concluded his talk with two challenges: the fist was the construction of a nanomotor, the second was the writing of the content of a book page at the scale of 1/25000. Both the challenges were won in 1960 and 1985, respectively. At present time, reaching the nanometre scale is no more a challenge. Nanotechnology is becoming important in many fields and is finding new applications every day in energetics, informatics and health care.

Noble Metal Nanoparticles as Plasmonic Substrates

Especially for metals, scaling from the bulk materials to nanometre size particles, strongly influences their electronic configuration and, as a consequence, their physico-chemical properties.
The metallic behaviour of long ordered materials breaks down into size-dependent or quantum confinement effects, when the particles size falls to nanometre range.[1]
Techniques based on X rays are very helpful in understanding this evidences, like *X-ray diffraction* (XRD).
Starting from clusters of few hundreds to few thousands of Au atoms, in the range particles of 1-2 nm, Cleveland et al. performed computational analysis to understand which geometrical arrangement could be favoured.[2] They report that there are three preferential stable gold nanocrystallites that could be practically synthetized in this range. These nanoparticles were synthesized and they were characterized with mass spectrometry. Their core masses were found to be 14k, 22k and 28k (k = 1000au or 5.08 Au atoms, so the three populations are made of about 70, 110 and 140 Au atoms).[2] They also registered XRD spectra of these AuNPs clusters and compared them with those calculated for the predicted structures. The favourite geometrical arrangements, from the energetic point of view, are the Marks Decahedra (m-Dh), as show in Figure 1.1.

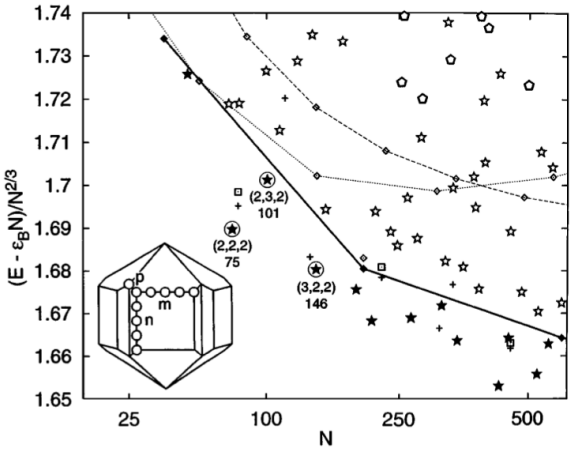

Figure 1.1: Energies of structurally optimized Au_N ($N \leq 520$). N represent the number of gold atoms in each cluster. ε_B =3.93eV represents the cohesive energy of atoms in bulk gold. The stable m-Dh clusters, compared with experimental data, are denoted with filled stars with the indices (m,n,p) as in the inset figure. From Ref. 2.

The comparisons between the experimental XRD pattern and the predicted ones for different geometrical arrangements are shown in Figure 1.2.
We can see that only the m-Dh motif has a reasonable similarity with the experimental data for all the nanoparticles studied. The signals observed at large *s* (the *x* coordinate in Figure 1.2), giving information on the internal atomic structure, recall the *fcc* structure of bulk gold.[2] Especially for the Au_{14k} nanoparticles (the first-top graph in Figure 1.2), the Marks Decahedral configuration in which the apical atoms were removed, overlaps perfectly with the experimental data.

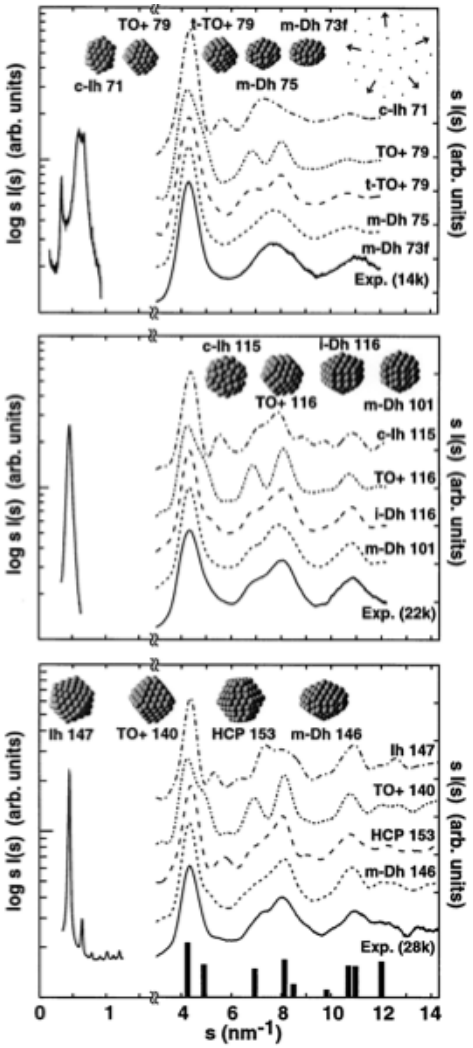

Figure 1.2: The comparison of the experimental ("Exp.") XRD pattern with the calculated ones for different geometrical arrangement of Au atoms. $s = 2\sin\theta/\lambda$, *where* θ *is the scattering angle and* $\lambda = 1.5405\,\text{Å}$. *The bottom bars represent the predicted scattering pattern for bulk gold. On the top, the experimental XRD for* Au_{14k}, *at the centre for* Au_{22k} *and at the bottom for* Au_{28k}. *Form Ref.* 2.

Increasing the nanoparticles size, the diffraction pattern of *fcc* bulk gold become clear.[3] Petkov at al. synthetized three populations of particles of 3, 15 and 30 nm.[3]
The XRD patterns of these samples show essentially the same Bragg feature of bulk gold, but the signals become more broadened decreasing the size. As expected, reducing the lattice dimension, the peculiar long order of bulk crystals is lost and a large number of defects grow up.
In fact, comparing XRD data of Figure 1.2 and Figure 1.3, we found a progressively broadening of the diffraction signals decreasing the size of nanoparticles. This indicates that the lattice is no more regular as in the bulk material.

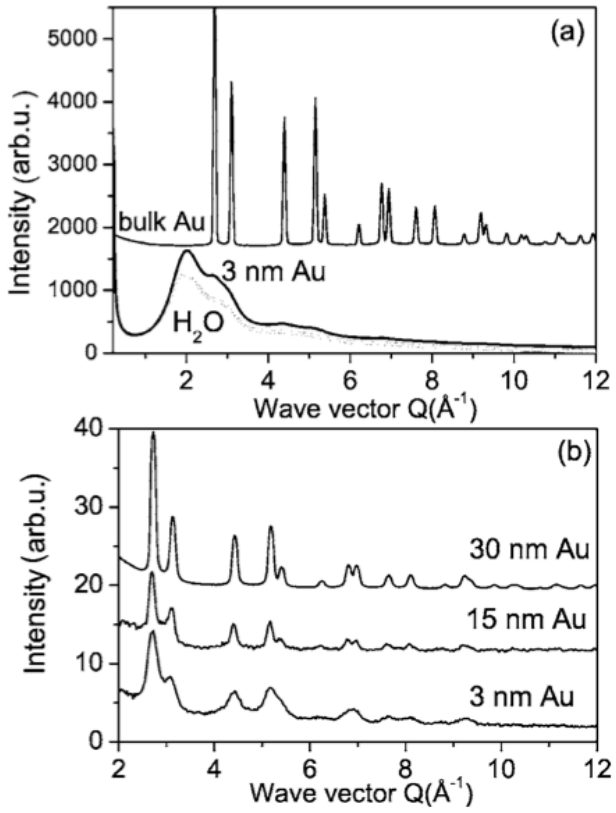

Figure 1.3: XRD pattern for bulk gold and 3 nm particles in water (a) and for the three population of nanoparticles studied by Petkov et al. (b). From Ref. 3.

The authors used the atomic Pare Distribution Function (PDF) to compute some interesting data regarding the defects of the crystal lattices in nanoparticles.
PDF is another way to represent diffraction data. It is a Fourier transform of the experimentally observable structure function, that explains the coherent part of the total scattering intensity.[3] In a first approximation, peaks represent the interaction with the nearest neighbour atoms.
The first important consideration, coming from Figure 1.4, is that the bulk gold expresses well defined structural features extending at long distance, but, for all nanoparticles, it vanishes at distance smaller than the nanoparticles size.

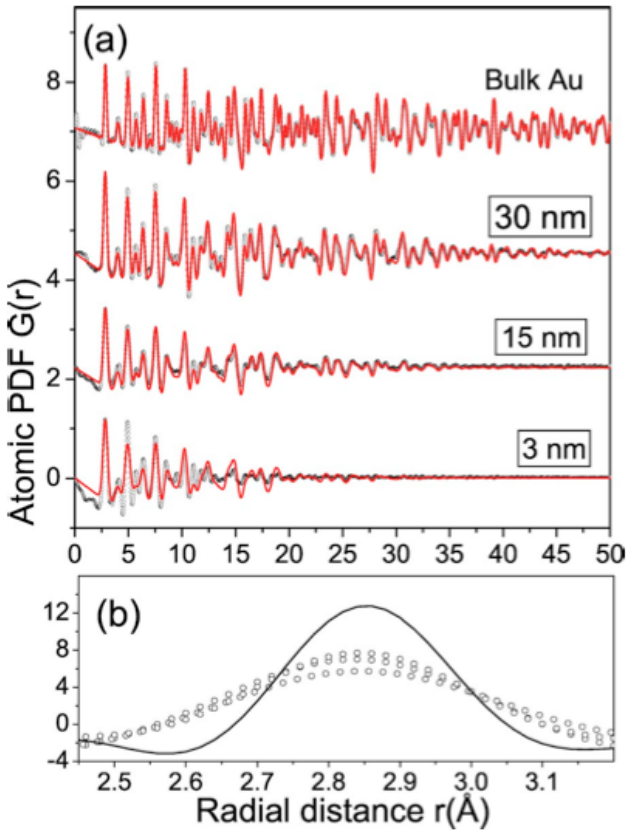

Figure 1.4: Experimental atomic PDFs for bulk gold and the three populations of AuNPs studied by Petkov et al. (a). At bottom (b), the first peak for the bulk gold (continuous line) is sharper than for the nanoparticles (symbols). From Ref. 3.

For all the studied nanoparticles, the first peak is always approximately at 2.85Å, that is the average interatomic distance in gold, but the bands are broader than for bulk gold (Figure 1.4b). This fact reflects a sort of distribution in the first neighbour atomic distances in nanoparticles, and remains almost constant changing the nanoparticles dimension. The authors concluded that the structural disorder, and not the nanoparticles size, is responsible for the limitation of coherence in the studied gold nanostructures.[3]

In nanoparticles, the numbers of total atoms to surface atoms ratio decreases in smaller particles, explaining why the X-ray diffraction pattern becomes broader decreasing the nanoparticles size. The cores of nanoparticles maintain the *fcc* structure of bulk gold, but the lattice become less regular approaching the surface, affecting the distribution in interatomic distances.

Considering the electronic configuration of a bulk metal, we find an extended delocalization of orbitals over the entire crystal lattice. This gives the peculiar high electron mobility of metals, reflected in physical properties like electrical and thermal conductivity.

In particles approaching the nanometre size, this orbital delocalization is limited by the particle dimension, falling into discrete electronic band structures in the case of the smaller particles.[1] In this case the nanoparticle physical properties become strongly influenced by size, shape, environment and surface coverage.

For the compound $[Au_{55}(PPh_3)_{12}Cl_6]$, for example, it was found a discrete band gap of 170 meV, attributed to the Au_{55} core. [1]

In Figure 1.5 the Differential Pulse Voltammetry (DPV) for clusters of Au_{147} and Au_{38}, both capped with hexanethiols, are shown. 15 oxidation states were found for the Au_{147} cluster. Different states and also a well defined HOMO-LUMO band gap is

present for the Au_{38}. This example shows how the delocalization in a metal crystal lattice vanishes when the particle size decreases to nanometre scale.

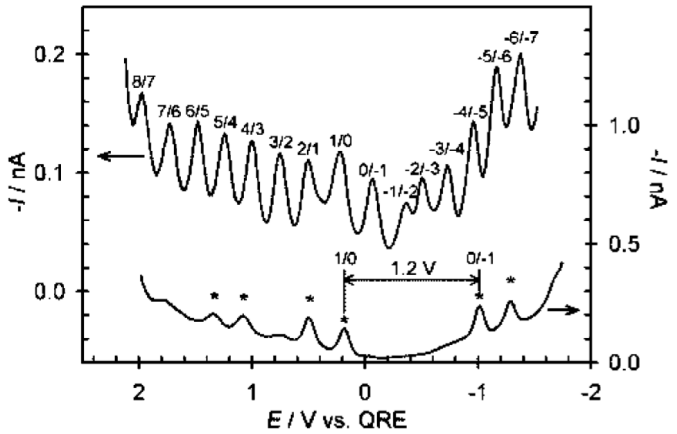

Figure 1.5: Differential Pulse Voltammetry (DPV) for Au_{147} (upper) and Au_{38} (down) capped with hexanethiol. The electronic level spacing increases while decreasing the particle size. From Ref. 1.

Compared to bulk metal, physical and optical properties of nanoparticles have consistent variations only when the energy level spacing exceed k_BT. Therefore, in metal nanostructures bigger than 0.5-1.0 nm still remains a consistent electronic mobility. The interaction with electromagnetic fields, in this situation, could be explained with a classical approach, taking into account a mechanical collective oscillation of the electron gas. [1, 4, 5] This excitation is called plasmon.
These oscillations take place when exited near the electron plasma frequency, that is related to the electron density of material. At the surface of bulk metals, plasmons take the form of surface plasmon polaritons, also simply called surface plasmon (SP).[4] The SP, optically exited, propagate on the material surface, but, when the surface plasmon is confined into a particle with dimension comparable to the incident wavelength, all the particle's free electron participate to the collective oscillation. The surface plasmons located in nanoparticles, or other confined structures, are called localized surface plasmons (LSPs). [4]

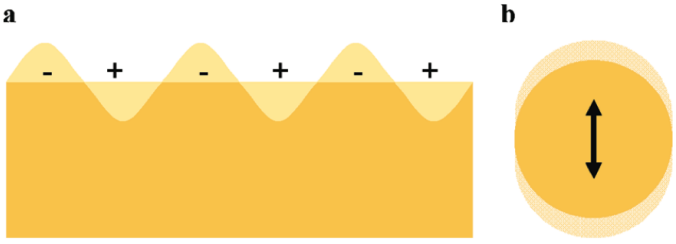

Figure 1.6: A cartoon representing the surface plasmon polaritons in bulk metals (a) and the localized surface plasmon in nanoparticles (b). From Ref. 4.

Gustav Mie was a physician that solved analytically the Maxwell equation for the scattering and absorption of light by spherical particles. At the beginning of the 20th century, he proposed an exhaustive explanation for the localized surface plasmon effect based on the principles of classical electromagnetic theory.

The expressions, calculated by the Mie theory, of the total scattering (σ_{sca}), extinction (σ_{ext}) and absorption (σ_{abs}) cross section are the follow: [4]

$$\sigma_{sca} = \frac{2\pi}{|k|^2}\sum_{L=1}^{\infty}(2L+1)(|a_L|^2 + |b_L|^2)$$

...Equation 1.1

$$\sigma_{ext} = \frac{2\pi}{|k|^2}\sum_{L=1}^{\infty}(2L+1)\left[Re\left({a_L}^2 + {b_L}^2\right)\right]$$

...Equation 1.2

$$\sigma_{abs} = \sigma_{ext} - \sigma_{sca}$$

...Equation 1.3

Where k is the incoming field wave vector, L are integers representing the dipole and higher multipoles of the scattering. a_L and b_L are parameters given by the Riccati-Bessel functions, representing the particle and environment refractive indexes. [4]
When the particle size is much smaller than the incident wavelength, the electron oscillation acts principally as a simple dipole and the Mie equations 1.1 and 1.2 could be approximated to: [4]

$$\sigma_{sca} = \frac{32\pi^4\varepsilon_m^2 V^2}{\lambda^4}\frac{(\varepsilon_1 - \varepsilon_m)^2 + (\varepsilon_2)^2}{(\varepsilon_1 + 2\varepsilon_m)^2 + (\varepsilon_2)^2}$$

...Equation 1.4

$$\sigma_{ext} = \frac{18\pi\varepsilon_m^{3/2}V}{\lambda}\frac{\varepsilon_2(\lambda)}{[\varepsilon_1(\lambda) + 2\varepsilon_m]^2 + \varepsilon_2(\lambda)^2}$$

...Equation 1.5

Where:

$$\varepsilon_m = {n_m}^2$$

...Equation 1.6

$$\varepsilon_1 = {n_R}^2 - {n_I}^2$$

...Equation 1.7

$$\varepsilon_2 = 2n_R n_I$$

...Equation 1.8

n_m is the environment refractive index, n_R and n_I are the real and imaginary part of the particle refractive index, so ε represent the dielectric function of the medium (ε_m) and of the particle ($\varepsilon_{1\ and\ 2}$).
This approximation takes into account particles smaller than 10 nm, but the predictions was found reasonably correct also for bigger particles [4], up to 100nm.
When $\varepsilon_1(\lambda_{LSPR}) = -2\varepsilon_m$ the extinction cross section is maximized, reaching the resonant condition with the localized plasmon of the particle.

This explains two important evidences. The first is that only the materials with negative values of dielectric function ε_1 can reach the resonance conditions. For noble metals this is verified into the visible region. For gold nanoparticles in water, the predicted localized surface plasmon resonance is located at 520 nm, well in agreement with experimental results.
The second fact is the dependence of the localized surface plasmon from the environment, like the solvent or molecules bound to the surface of the nanoparticle. This dependence is also expressed by the slope of the real part of the dielectric function in Figure 1.7.

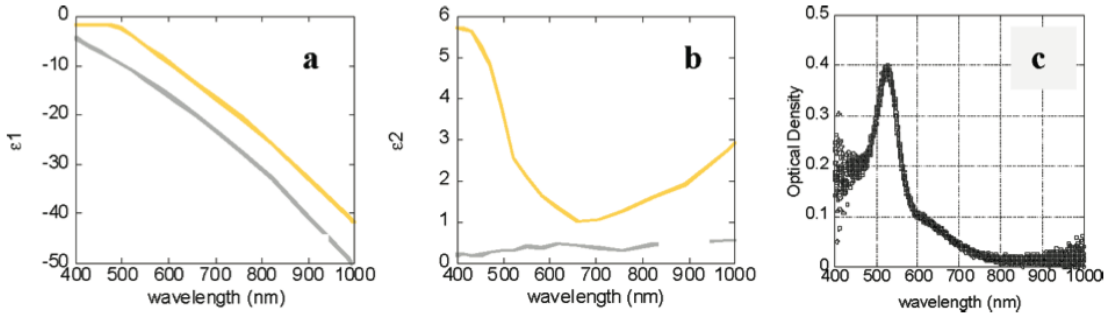

Figure 1.7: The real (a) and imaginary (b) part of dielectric function for gold (yellow line) and silver (grey line). In (c) are reported an absorption spectra of colloidal gold nanoparticle. From Ref. 4.

The Mie theory, complemented by the Gans theory, which takes into account also spheroidal particles, can be used to fit experimental absorption spectra of gold nanoparticles.[6] Instead of expensive and more demanding techniques, like transmission electron microscopy, this fitting allows the routine evaluation of colloidal gold nanoparticles, giving information on size, shape, aspect ratio and total absorption cross section of the nanoparticles.[6]
LSPs have also some other important properties. First of all, the electromagnetic field near to the nanostructure surface is greatly enhanced, with a strong distance dependence from the surface.[4] Second, the nanostructure extinction coefficient has a maximum at the plasmon resonance frequency. For example, a single silver nanoparticle of 80 nm scatters light with a cross section a million times greater then the fluorescence cross section of fluorescein molecule, or thousands times greater than a fluorescein loaded nanoparticles of the same dimension.[5]
Taking into account the sensitivity to the dielectric environment and the field enhancement due to the localized surface plasmons, it does not surprise the great interest that can be found for the functionalization of such a nanomaterials for sensing tools development.[5]
Relativistic effects help to understand the chemistry of gold atoms, both in the case they are linked to other gold atoms or on the surface of nanostructures.
The relativistic effect induces the contraction of most penetrating atomic orbitals, e.g. the *s* and *p* shells, affecting the consequent expansion of *d* and *f* shells.[7] The relativistic contraction of *6s* has its maximum effect at Z=79, corresponding to gold.[7]
It reflects in three main aspects. First, the atomic radius of neutral gold is similar to silver, and the ionic radius for the first oxidized cation Au(I) is smaller than that for Ag(I). Second, the relativistic contraction of *6s* influence also the *5d* orbital, enabling the easy hybridization to *sd* orbitals and, therefore, their linking to neighbour atoms.

Third, the so called *aurophilic* effect, that is the weak *5d – 5d* interaction that becomes important for the formation of complexes with Au(I)-Au(I) bonds.[7]
The ubiquitous ligand used for the functionalization of the gold surface is the thiol group, even though the nature of the thiol-gold interaction has been systematically investigated only in recent yeas.[7-9]
Jadzinsky at al. prepared in 2007 gold nanoparticles covered with p-mercaptobenzoic acid (p-MBA). [8] One of the most interesting highlight of their research is the extremely narrow size distribution of the particles [$Au_{102}MBA_{44}$], allowing them to obtain nanoparticle crystals and to perform X-ray crystal structure analysis.
Their results show that the gold atoms effectively assume a Marks decahedron geometry, consistent with the *fcc* crystal structure. In addiction they observed that gold atoms up to 5.5Å from the centre of the particle do not bound any sulphur. Atoms between 6 and 6.3Å bound one sulphur and gold atoms in the shell between 7.5 and 8Å bound two sulphur atoms.[8] This observation implies the formation of S-Au-S and Au-S-Au bridges, both observed also in other studies.[7-9]
The sulphur atoms appear to be hybridized as sp^3, with two orbital engaged with gold atoms, one with the rest of the molecule and the last as lone pair electrons. The sulphur also acts as a chiral centre and optical activity was found in thiol functionalized gold nanoparticles.[7, 8]
The thiolate-gold bond has a strength close to that for gold-gold bond, so it strongly influences the lattice structure at the particle-environment interface.[7] Surface gold atoms can in fact be *extracted* from the crystal lattice due to the formation of Au-S-Au-S-Au chains.[7-9] This extracted atoms are called adatoms and was found of crucial importance in the formation of self assembled monolayer at the low coverage regime, as shown in Figure 1.8.[7]
The adatom and vacancies migration allows changes between gold-sulphur bond conformations and, moreover, translations of thiolated molecules on the metal surface.[7, 9]

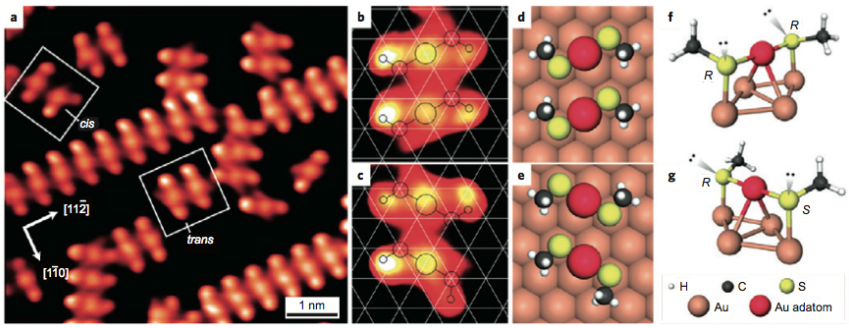

Figure 1.8: (a) The STM image of a self assembled CH_3SH over a pure gold substrate. (b-d) and (c-e) The close-up image of the same sample on the situation of cis-trans and tran-trans assembling and relative atomic models. In (e-f) is shown the peculiar Au-S-Au_{adatom}-S-Au chain with the tetrahedral geometry of sulphur molecular orbitals. From Ref. 7.

Raman Spectroscopy and SERS

In 1930 C. V. Raman received the Noble Prize in Physics on "*his work on the scattering of the light and for discovery the effect named after him*".
The Raman effect is the inelastic scattering of radiation by molecules or crystals in a solid, liquid or gas sample. [10]
Every species has its own electronic configuration which assumes a stable electronic spatial distribution that could be perturbed by an incident electromagnetic field. The response of the electronic system is called polarizability.
An electromagnetic field interacting with a chemical species, in a non-absorptive process, induces an oscillating dipole governed by the polarizability. The scattered light shows three main contributions, one from the scattered field at the same frequency of the incoming one (Rayleigh scattering), and two at slightly smaller (Stokes Raman scattering) or larger (anti-Stoke Raman scattering) frequencies than that of the original field. Reyleigh scattering effect is usually several order of magnitude more intense than Raman scattering. [11]
Raman scattering frequencies are usually related to a variation of the molecular polarizability induced by vibrational normal coordinates. Therefore, Raman spectroscopy is considered a vibrational spectroscopy although other degrees of freedom, like for example those of electron spins, can induce other features in the inelastic scattered light.
One of the main difference between IR and Raman spectroscopy are the different selection rules, that makes these two techniques complementary, especially when the analysed species have an inversion centre. In this case the active modes in IR and in Raman are mutually exclusive.[11] The second main difference is that Raman spectroscopy allows to obtain vibrational spectra exiting the sample at different frequencies.[10] This possibility allows to avoid problems related to the presence of fluorescence in the scattered light.
The advent of lasers made this technique more suitable for routine analysis by using monochromatic and intense radiation sources.
The Raman scattering cross sections are usually very small, but the overall signal can be enhanced by several order of magnitude in particular situations, like when the laser excitation is close to an absorption band (called Resonance Raman Spectroscopy, RRS)[10] or/and when the molecules are close to a plasmonic surface (called Surface Enhanced Raman Scattering, SERS).[12-15]
In RRS, only the vibrations related to the chromophore are usually enhanced. Therefore, the vibrations not involved in the enhancement result to be almost invisible in the spectra.[10] The RRS has the advantage to selectively amplify the spectrum of molecules or chromophores according to their absorption properties, although in these cases it can lack of all the vibrational information given by normal Raman spectra.
In Figure 1.9 are reported two RRS spectra of pyrene obtained by exciting at different frequencies, in resonance with different excited states. As a function of the exited transition, different peaks become dominant because of their different coupling to the excited states.

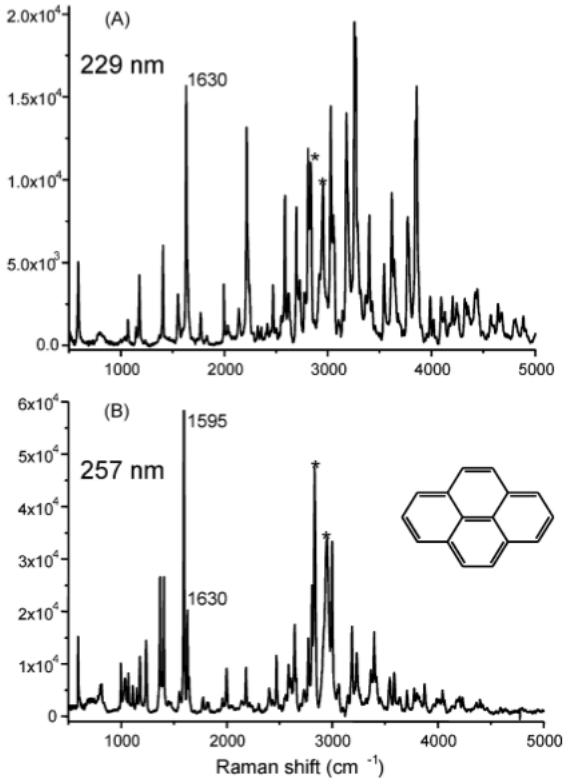

Figure 1.9: Resonance Raman spectra of pyrene at 229 nm excitation (A) and 257 nm excitation (B). The two spectra show many differences in particular as relative intensities of peaks.
From Ref. 10.

Some problems are, however, related to RRS. The first is a technical one, because there are a finite number of laser systems which are commercially available for excitation. The second is the possible photodamaging of samples occurring and at resonance conditions. The third is the fluorescence, which is larger in resonance situations and that is often much more intense than Resonance Raman scattering.[10]
The use of plasmonic nanostructures as substrate for Raman spectroscopy has the advantage of quenching the fluorescence and, much more important, increasing the Raman intensities over several order of magnitude.[10, 13-18]
This amplification effect is called "surface enhanced Raman scattering" (SERS).
The first proposal of enhancements, up to 10^6, can be found in the '80s, measuring rhodamine 6G adsorbed over silver.[15] The SERS cross section was found comparable to that of fluorescence, foreseeing the possibility of single molecule SERS, as it was possible with fluorescence.
The mechanism involved into the surface enhancement is partially understood but it can be still considered an open issue.
However there is a fixed point to take into account, the molecule has to be close to the metallic surface.[13-15, 18]
A first proposed enhancement mechanism is called "chemical enhancement" (CE). By this effect, the molecule has to be physically or chemically absorbed over the metal surface and new resonances take place due to one or more of the following states: metal-ligand complex formations, creation of new charge transfers states (understandable with coordination chemistry) or transient hot electrons or electron-hole pairs formation between metal and adsorbed molecule.[15]
In a recent review, Moskovits, reports some excellent studies on the SERS enhancement factor calculations, comparing computational and experimental results that look at the enhancement mechanisms of SERS.[15] He concludes that only chemical enhancement is not sufficient to understand the huge amplification

(sometimes over 10 order of magnitudes) provided by SERS. For the author, the complex formation could not result in amplifications up to one order of magnitude, unless it acts with the opening of new resonances, as charge transfer states. In this case, most theories evaluated the coupling of the adsorbate vibrations with the plasmon of the metal surface, considering that a metal hot electron, or a hole, or both are present on the adsorbate. Then, these return to the metal with information on the vibrations of the adsorbate.[15]

At present time, it is widely accepted that the chemical enhancement gives a contribution to the SERS enhancement up to the order of 10^2.[14, 15, 18]

The second, much more important, amplification mechanism is the "electromagnetic enhancement" (EE), almost exclusively due to the plasmon resonance. The EE theory states that SERS arises from the concentration of the electromagnetic field due the collective oscillations of a localized surface plasmon.[14, 15] In SERS, the nanostructures behave as receiving and radiating antennae, concentrating light and exciting the molecule in close proximity to them.[15]

Therefore, the SERS effect originates primarily from the metal structures since the enhancement factor is a property of the plasmonic substrate.[15]

Usually observed electromagnetic enhancement factor vary from 10^4 to 10^6.[15, 18]

Obviously, the chemical and the electromagnetic enhancement are present simultaneously, but the contribution of the second one is dominant.

Since the EE mainly derives from the collective oscillation of electrons in plasmons, configurations allowing positive interferences of such enhanced electromagnetic fields creates further near field amplifications. Tips, junctions and roughly surfaces are only some examples of situations which are called "hot spots".

It is reported that in a plasmonic substrate, where less than 100 sites over 10^6 are hot spots, the 24% of the entire signal comes from these few hot sites.[15]

In Figure 1.10 are shown some calculation based on discrete-dipole approximation (DDA) performed by Amendola at al. on the electromagnetic enhancement factor of gold nanoparticles alone and in dimer form.[18] The results show an increase of enhancement between 2 and 3 orders of magnitude in the hot spots with respect to the nanoparticles alone.

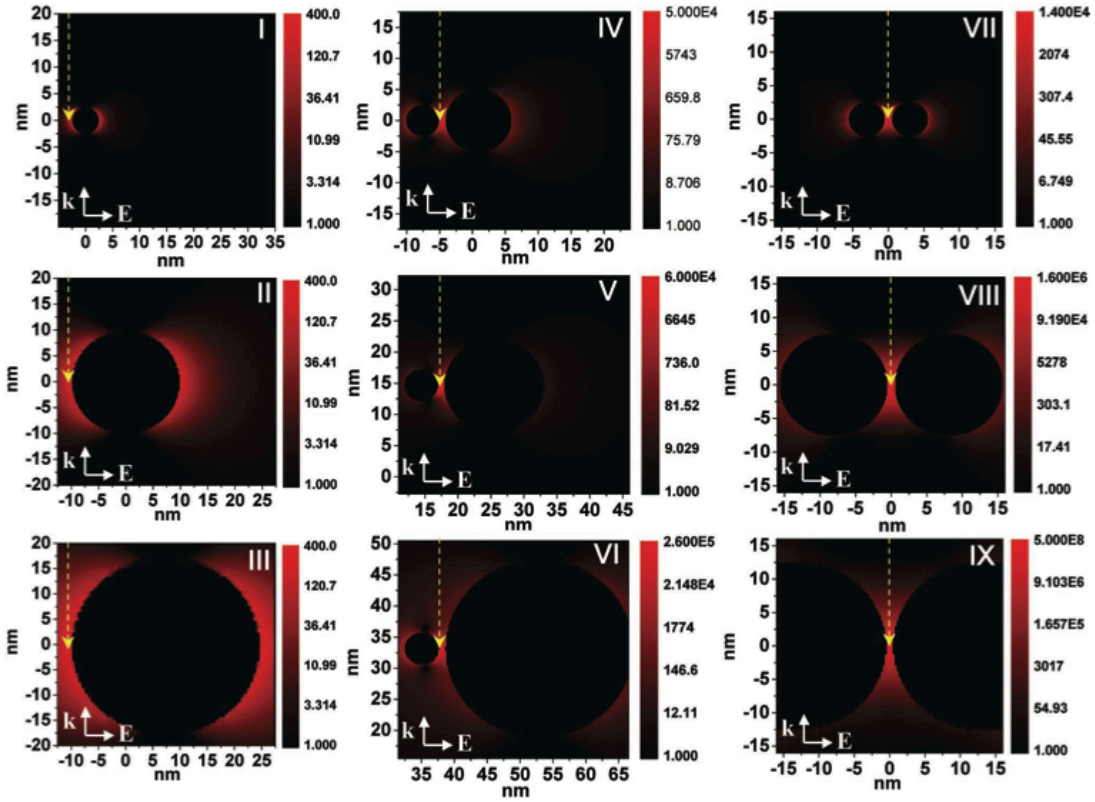

Figure 1.10: Discrete-dipole approximation (DDA) calculation of electromagnetic enhancement factor for gold nanoparticle between about 10 and 30 nm, for isolated particles or for dimers. The results show bigger enhancement within junctions . From Ref. 18.

Nuclear Magnetic Resonance as Imaging Technique

The interaction of matter with an external magnetic field primarily involves the electron and nuclei spins which change their state energies. Different populations on these states produces a magnetization of the sample. An electromagnetic field interacting with the spin states causes a perturbation of the state populations, and the net magnetization changes its orientation. Most techniques based on these interactions look at the spin nuclei and, for practical applications like magnetic resonance imaging (MRI), protons present in water are considered. Since the dynamic of the excited spin states depends on the nuclei environment, different responses can be observed in different tissues. This is the rationale of the MRI investigations in medicine.

The electromagnetic radiation used in MRI is in the radiowave spectral region and is considered a safe radiation. Usually the contrast in the recorded images is poor and contrast agents are needed for its enhancement. Nanosized optimized contrast agents, are very important for these applications.[19-23]

Compared to the optical spectroscopy, where a continuous scanning of the radiation frequency is performed, in magnetic resonance spectroscopy a single pulse, or a sequence of radiofrequency pulses, are applied.[24]

The pulse has the effect to induce a temporary perturbation of the system, that returns to the initial equilibrium state in a time also depending on the environment conditions.

The entire phenomenon is represented in Figure 1.11. The *z* axis is along the direction of the static magnetic field B_0. The nuclear net magnetization is aligned to the field, along the *z* axis. The radiofrequency pulse (RF in the figure) has the effect to change the orientation of the magnetization vector. Frequently used pulses rotate the magnetization on the *xy* plane, so they are called "π/2 pulses". This means that the population of the two spin states becomes equivalent (magnetization projection over *z* axis equal to zero) and that a magnetization appears in the xy plane .
At the end of the pulse, the orientation induced by the electromagnetic field relaxes to the initial state along the *z* axis.

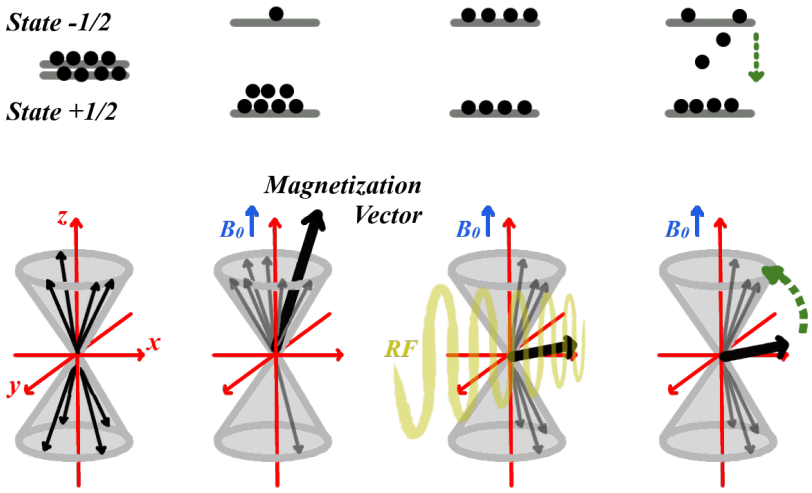

Figure 1.11: Cartoon representing the effect of the external magnetic field B_0 and the effect of the radiofrequency pulse RS in a magnetic resonance experiment.

The signal decreasing in time domain in the *xy* plane, called "Free Induction Decay", is the observable in magnetic resonance spectroscopy experiments.
There are two main mechanisms involved in such relaxation, both expressed in term of time required to re-establish the equilibrium after the radiofrequency pulse.
The first is known as *longitudinal relaxation* and is called T_1, the second is the *transverse relaxation*, called T_2.
As a first approximation, the longitudinal relaxation is related to the restoring of population ratio between the two spin states, so it is mostly related to the recovery of the projection of the magnetization on the *z* axis.
The T_1 relaxation in biological samples is mostly due to the rotational and translational degree of freedom of molecules (especially water). If the tumbling frequency of protons matches the Larmor frequency, spin re-equilibration is favourite and so a short T_1 is shown.[25] For solid and slowly moving structures, the molecular tumbling frequency is too low. For unstructured tissues and fluids it is high. An intermediate situation is found on moderately sized proteins and fatty tissues and, for these situations, T_1 is shorter than for the other one.[25]
The transverse relaxation T_2 is the dephasing of the spin states in the xy plane affecting therefore the magnetization in this plane. After the π/2 pulse, the maximum magnetization in the *xy* plane comes from an initial phase coherence of the individual spin protons. In amorphous structures, mobile molecules are not constrained and they exhibits long T_2, while water molecules in hydration layers or in solid non-moving structures have very short T_2 values.[25]

Since the longitudinal and the transverse relaxation take into account the mobility of protons for the restoring of the equilibrium state, tissues showing long T_1 often show also long T_2 and vice versa.
The Magnetic Resonance Imaging (MRI) is a diagnostic technique in which tissues are subject to a strong magnetic field and are irradiated with electromagnetic waves in the radiofrequencies. The differences in term of relaxation times, T_1 and T_2, due to the different responses exhibited by protons in different environments, are used to map the samples.
The magnetic resonance imaging is a powerful diagnostic technique because it uses high penetrative and save radiation for biological tissues.
Simply changing the pulse programme, different tissues are empathized measuring T_1 or T_2.
The advent of magnetic contrast agents allowed to overcome the not trivial discrimination of tissues that appear similar in MRI, as it will be reported in subsequent paragraphs.

Synthesis of Noble Metal Nanoparticles by Laser Ablation

The Laser Ablation Synthesis in Solution (LASiS) is a *top down* method for colloidal nanoparticle preparation starting directly from bulk materials.[6, 26, 27] This method has extensively been used for this thesis work.
The approaches to the nanoparticle synthesis can be classified according to the methodologies used, namely growing particles from atomic precursors (*bottom up approach*) or "extracting" them from a bulk macroscopic target (*top down approach*).
The first one involves wet chemistry techniques, which often needs also reagents which can be toxic and can produce by-products and wastes.[1] LASiS is simple, produce naked particles [28] and respects the 12 principles of green chemistry.[26, 27]

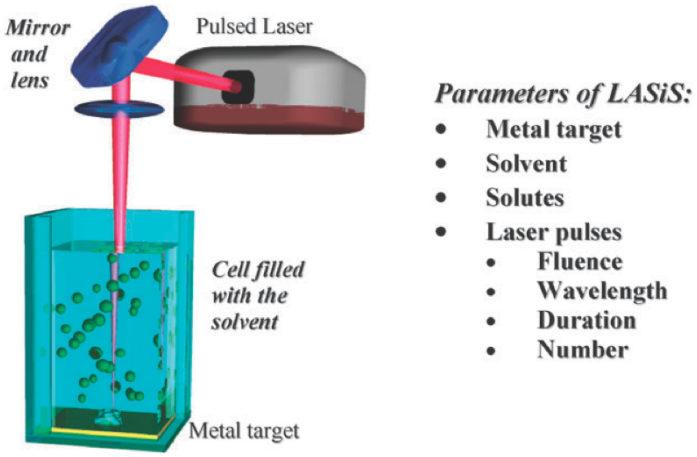

Figure 1.12: The main feature of a laser ablation set-up and the principal parameters to take into account are represented schematically. From Ref. 26.

The ablation set-up consists of a pulsed laser focused on the surface of the target. Usually, the ablation process is performed in a gas atmosphere, [27] but in the present work the target was ablated at the bottom of a flask, filled with a solvent, usually water.

The parameters to take into account in a LASiS synthesis are several, from the laser parameters, to the solution and, certainly, the target composition.
Some general practical remarks have to be made. Since it is important that the largest possible fraction of laser energy reaches the target, the excitation wavelength has to be carefully chosen. In particular, the absorption of the laser by the solvent or by the produced nanoparticles has to be avoided.
The nanoparticle synthesis follows some processes that are well characterized, but several details still remain not yet completely understood.
Amendola and Meneghetti published a recent comprehensive review focused on this topic.[27]
Considering, as starting time, the moment in which the pulse hits the target surface, the first phenomenon to occur is the linear and nonlinear absorption of the laser energy.
The detachment of the ablated material starts at a timescale between 1-100*ps*. The high energy absorbed causes a large temperature gradient between the irradiated spot and the surrounding material. Accepted theories, regarding this detachment process, talk about three main mechanisms: the vaporization, the "coulombic explosion" and the "explosive boiling".[27]
The "explosive boiling" is believed to be the main mechanism involved with *ns* laser pulses.[27] It occurs when the irradiated material is superheated up to the thermodynamic critical temperature, then a spinodal decomposition takes place and nanomaterial homogeneously nucleate.[27]
The ablated material is highly concentrated in space and contains highly ionized species. At this stage, the so called "plasma plume" is observed.
When the pulse duration is between 100 *ps* to 1 *ns*, there is a temporal and spatial overlaps between the pulse and the plasma plume. The laser irradiates the plasma, increasing its lifetime, its energy and its homogeneity. The phenomenon is known as "plasma shielding" and it is particularly important in laser ablation with *ns* pulses, where sharper size distribution of nanoparticles is observed with respect to those observed for *ps* or *fs* pulses.[27]

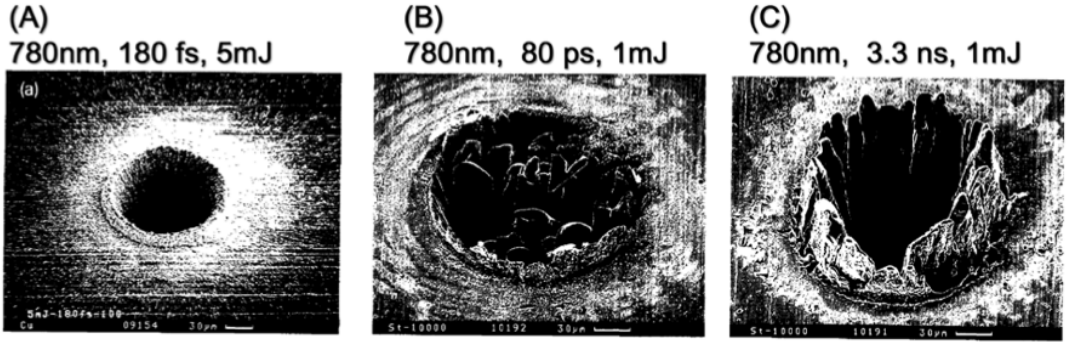

Figure 1.13: The crater on the irradiated target spot area in gas-phase laser ablation. The differences using fs (A), ps (B) or ns pulses (C) are evident, mostly involving the increasing predominance of thermal process while increasing the pulse duration time. From Ref. 27.

The mean lifetime of the plasma plume is between 100*ps* and 100*ns* depending also on the solvent above the bulk material. In LASiS, the plasma is confined close to the crater area by the solvent, where the plasma plume progressively transfer its thermal energy (temperatures about 10^3 K) both to the solution and to the target.

These huge energies were proved to initiate chemical processes involving the solvent and the ablated material. For example, organic solvents, especially toluene, degrade into a carbon graphitic-like shell over the surface of gold nanoparticles.[29]
In laser ablation of gold in NaCl aqueous solution at micromolar concentration, the influence of the solvent and solute was found fundamental for the colloidal stability.
Gold nanoparticles obtained in aqueous solutions show a little percentage of surface atoms (3-7%) with negative charges.[26] Gold oxidation states of (I) and (III) were found through XPS and the presence of Au-O species was also revealed with vibrational spectroscopies.[26] It is believed that the high energy of the plasma plume determines a partial oxidation of the gold nanoparticle surface and that both Cl^- than OH^- help to develop Au-O^- negative charges.[6, 27]
This effect produces a coulombic repulsion between nanoparticles, which gives stability to the aqueous AuNP colloid without any added surface coverage.
Other phenomena related to the laser ablation can be understood as shockwaves and cavitation bubbles determined by the high pressure and temperature present in the ablation process.[6, 27] Figure 1.14 summarizes the main processes occurring in LASiS.

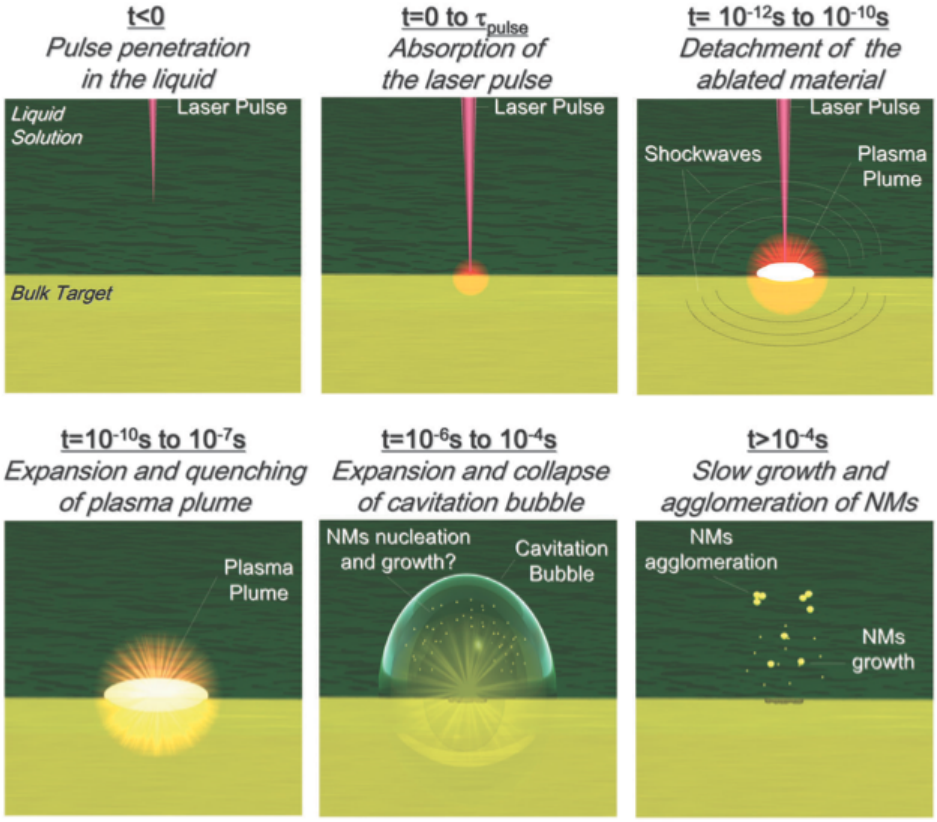

Figure 1.14: Cartoon representing the temporal evolution and the steps involved on the nanomaterial (NMs) formation during the laser ablation in solution.
From Ref. 27.

The main pros of LASiS, compared to wet chemistry nanoparticle synthesis, are the versatility, since different starting materials and different solvents can be used; the easy experimental set up, that remains almost unchanged for the synthesis of different particles, the cheapness of the synthesis, and last but not least, the ablation is waste free, the target unused can be re-used simply by changing the upper solution.

As drawbacks, one should recall that the nanoparticles size distribution is often broader than that obtained with chemical synthetic methods and that it is not trivial to obtain non-spherical particles, due to the nature of ablation process.

Application in Cancer Treatment and Diagnosis

In recent times cancer surpassed heart diseases as leading cause of death in US population for which data are available.[30]
Cancer is the term used for the irregular proliferation of cells, that sometimes can diffuse into other sites through the vascular system. These cells are not foreigner, but come from the same organism. Sometimes, during cell replication, or caused by external agents, the DNA could be damaged. Most often such modifications cause the death of the cell, but there is the possibility that the cell is able to survive, and continue to replicate with its modified DNA. In such a situation, a population of cancer cells grew up. The tissue formed by these cells is called tumour.[11]
Nanomedicine indicates that nanotechnology is involved in the treatment and/or diagnosis of diseases.[30, 31] This implies the knowledge of the properties of materials by changing their size, shape, structure, or by modifying the surface with ligands. Nanoparticles can integrate different functions also for improving cell targeting, which is useful for imaging or for therapy.[31]
From a therapeutic point of view, because of poor pharmacokinetic profiles and broad mechanism of action, small drug molecules have often a poor specificity for the target diseased tissue and other healthy ones.[32] Using nanoparticles, consistent variation in pharmacokinetics are found. Their high potential stays in reducing the off-target toxicity and improving the therapeutic index of carried active moieties.
Looking at the diagnosis, nanotechnology offers the possibility to improve efficient and multiple contrast agents for optical, magnetic, radio and acoustic imaging.[19, 20, 31]
A general strategy for the preparation of multifunctional particles for nanomedicine has to take into account as many as possible points among the following:

- Stealth features have to be improved to evade the immune system and prevent opsonization.[20, 32, 33]
- A protective layer has to be designed to prevent the degradation of sensible loaded drugs, protein, DNA and so on.[32]
- Targeting moiety for assisting the enhanced permeability and retention effect (EPR) on tumour, increasing selectivity and accumulation.[30, 32, 33]
- Considering membrane permeation features and intracellular targeting moieties, or taking into account endosome escape mechanisms, improve the efficacy to specific intracellular targets.[32]
- Designing imaging agents also for obtaining information on the efficiency of delivery and dose/effect responses.[32]
- A planned drug-release behaviour. This could be a target-dependent assembly or disassembly, like pH sensible structures or enzyme cleavable moieties.[11, 32]

Theranostic is a treatment that combines therapy and diagnostic into the same material, a challenge easier to be achieved through nanotechnology.[20]
An excellent example of multifunctional nanomedicine, with unusual *in vivo* targeting approach, was provide by Von Maltzahn et al.[34] They used a two steps targeting mechanism. In the first step, gold nanorods covered by polyethylene glycol accumulate to the tumour thanks to the EPR effect. Then infrared irradiation is used to cause a temperature increase in the tumour tissues, where gold nanorods are accumulated. As a consequence, a biological coagulation cascade occurs and a second

type of nanoparticles, functionalized with targeting peptides for such an enzymatic cascade, reach the tumour. These second targeted nanoparticles are iron oxide nanostructures, providing MRI contrast, or drug loaded liposomes. The authors show a 40 fold drug response increase using both these "communicating" nanoparticles instead of the drug loaded liposomes alone.[34]
Despite the clear advantages provided by sophisticated multifunctional nanoparticles, their longer and more complex synthesis reflects over the costs of the products.[32]
In 2011, any of the therapeutic nanoparticle formulations at advanced clinical trials, or just approved by FDA, present an active targeting moiety.[32]
The enhanced accumulation yield, due only to the enhanced permeability and retention effect, and the higher drugs loading provided by nanosystems are just some of the important improvements that can be obtained.
New functionalities add new variables too. For example, adding targeting features could compromise the stealth properties. In fact, it was shown that the same non-targeting particles have longer circulating lifetime.[32] Furthermore, the dynamic nature of tumour markers affect the efficacy of active targeting. For example it was shown that the Her2/neu receptor density decreases by 40% after the treatment with Trastuzumab conjugated nanoparticles.[32]

Brand name	Composition	Indication	Status
	Liposome-based nanoparticle		
Doxil/Caelyx	PEGylated liposomal doxorubicin	Ovarian cancer, Kaposi's sarcoma	Approved
DaunoXome (Galen)	Liposomal daunorubicin	Kaposi's sarcoma	Approved
Myocet (Sopherion)	Non-PEGylated liposomal doxorubicin	Breast cancer	Approved
	Micelle-based nanoparticle		
Genexol-PM	Paclitaxel-loaded PEG-PLA micelle	Breast cancer, lung cancer	Approved
NK911	Doxorubicin-loaded PEG-pAsp micelle	Various cancers	Phase 2
NK012	SN-38-loaded PEG-PGlu(SN-38) micelle	Breast cancer	Phase 2
NC-6004	Cisplatin-loaded PEG-PGlu micelle	Various cancers	Phase 1
SP1049C	Doxorubicin-loaded pluronic micelle	Gastric cancer	Phase 3
NK105	Paclitaxel-loaded PEG-PAA micelle	Breast cancer	Phase 3
	Polymer-drug conjugates-based nanoparticle		
OPAXIO (Cell Therapeutics)	Paclitaxel combined with a polyglutamate polymer	Ovarian cancer	Phase 3
IT-101	Camptothecin conjugated to cyclodextrin-based polymer	Various cancers	Phase 1/2
HPMA-DOX (PK1)	Doxorubicin bound to HPMA	Lung cancer, breast cancer	Phase 2
HPMA-DOX-galactosamine (PK2)	Doxorubicin linked to HPMA bearing galactosamine	Hepatocellular carcinoma	Phase 1/2
CT-2106	Camptothecin poly-L-glutamate conjugate	Various cancers	Phase 1/2
	Albumin-based nanoparticle		
Abraxane	Albumin-bound paclitaxel nanoparticles	Metastatic breast cancer	Approved

Figure 1.15: List of passive targeted nanoparticle formulations in advanced clinical trials in 2011. The status "approved" is referred to the approval for clinical practice by the American Food and Drug Administration (FDA). From Ref. 32.

Name	Composition	Target	Comments	Status
MCC-465	PEGylated liposomal doxorubicin containing antibody GAH targeting agent	Tumor antigen	Metastatic stomach cancer	Phase 1
MBP-426	Liposomal oxaliplatin containing human transferrin protein targeting agent	Transferrin receptor	Advanced or metastatic solid tumors	Phase 1/2
SGT-53	Liposomal p53 cDNA containing antibody fragment targeting agent	Transferrin receptor	Solid tumors	Phase 1
CALAA-01	siRNA-loaded polymeric nanoparticles containing human transferring protein targeting agent	Transferrin receptor	Solid tumors	Phase 1
BIND-014	Docetaxel-loaded polymeric nanoparticles containing peptide targeting agent	Prostate specific antigen	Advanced or metastatic cancer	Phase 1

Figure 1.16: List of active targeted nanoparticle formulation in advanced clinical trials in 2011. From Ref. 32.

Therapeutic Drug Monitoring

The advantages provided by nanotechnology in developing targeted therapies are important to reduce size effects due to the systemic diffusion of active drugs. However, this is not sufficient when taking into account the individually variability of drug responses concerning efficacy, tolerability and toxicity. Such variables depend on patients factors, such sex, age, genetic background, and also depend on environmental factors like concomitant medications, smoking, diet and the personally belief in treatment and cure.[35]

Statistic studies show that over 2 million of US patients support serious drug side effects per years, with 100 000 patients dying.[35]

The therapeutic drug monitoring (TDM) is based on the idea that the concentration of a drug in the plasma, or in the blood, reflect the concentration of the drug at the target site better than the given dose.[35]

Monitoring the drug concentration in patients allow to adjust the dosage in prolonged therapies and helps in understanding the pharmacokinetic and pharmacodynamics related to individual factors.

A disease where TDM could be particularly useful is cancer. Cytotoxic drugs are characterized by very narrow therapeutic interval, that is the range in which the concentration is higher enough to have clinical effects, but not too high to be toxic.[35, 36]

Nussbaumer at al. published an extensive review on the analytical performances for the quantification of anticancer drugs in biological and environmental samples. [36] The authors reported that the highest sensibility is achieved by mass spectrometry coupled to liquid chromatography, frequently reaching the limit of detection of the order of ng per mL.

In clinical practise, almost every drug is measured using chromatographic techniques.[36]

Perspectives for the therapeutic drug monitoring could not escape the development of new point-of-care (POC) analytical methods.

In principles, a POC device has to be easy to use, portable, cheap and, of course, it must provide robust analytical measurements in term of selectivity and sensitivity.

Using POC for TDM allows patients to monitor the efficacy of their therapy at their own home, or allows doctors to personalize and adjust drug doses in function of individual therapeutic response.

Paper based POC devices found really promising applications. Paper is cheap, light weigh, biocompatible and easy to use, dispose, store, transport and modify. [37]

The most popular application of a POC based on paper sampling tool is for the glycemic index monitoring in blood, but for cancer the issue seems to be more complicated.

Both for treatment and diagnosis, a single marker measurement is not sufficient for cancer. Therapies often involve formulation of multiple drugs [11] and a correct diagnosis have to take into account different biological features as selected proteins concentration level and the presence of particular DNA or RNA sequences or of circulating tumour cells.[38]

The analytical technique used for cancer POC devices has to be capable to distinguish and measure multiple analytes simultaneously.

Mass spectrometry was used as analytical tool by Espy at al.. They defined a new protocol which required only 60 seconds between sampling and the output of results.[39] The protocol uses a drop of blood, adsorbed on a paper, and alum for its coagulation. The paper is than connected to a high voltage field and few tens of

microliter of solvent are added at the edge of the paper. The solvent migrates to the other edge of the paper and, due to the high voltage, is sprayed into the mass spectrometer. Limits of detection and quantification ranges are shown to be compatible with clinical applications for eight different anticancer drugs.[39]

The surface enhanced Raman spectroscopy, due to the fingerprint signature provided by vibrational transitions and the high sensitivity provided by the localized surface plasmon amplifications, can be a valid alternative for the TDM field.

Since the SERS is a surface technique, the interaction and the distribution of the analytes on the plasmonic surface have to be taken into account.

In the case of molecules with reasonable Raman cross sections, and that effectively adsorb on the surface of plasmonic substrates, SERS is a very effective technique because many molecules can be recognized by their own Raman spectra with only one measurement.[13]

Quantitative SERS evaluations have to consider some issues like the reproducibility of signals, principally due to the SERS substrate. The surface enhancement acts only on molecules very close to the plasmonic surface, and even the fluorescence quenching act in the same way. This could be counterintuitive, but lowering the amount of analytes often results in an increase of the signal to noise ratio. [13] Homogeneous and reproducible distribution of hot-spots is needed for reproducibility, since the highest percentage of the collected signals come from these points.[15]

Instrumental parameters, such as excitation wavelength, laser power and time exposure are crucial variables to consider for maximizing the scattering and preventing photo-decomposition, especially in resonance Raman conditions.

Farquharson et al. reported quantitative estimation of 5-fluoruracil anticancer drug by SERS on less than 1mL of saliva and in less than 5 minutes.[40] The SERS substrate used by the authors were silver nanoparticles embedded in a sol-gel matrix. The limit of detection was reached at 150ng/mL.

Song et al. used core-shell Fe_3O_4@AuNP and Fe_3O_4@AgNP as SERS substrate for the quantification of thiram (a fungicide). The authors first mixed the nanoparticles with the analyte solution, then used the magnetic susceptibility of the iron oxide core to concentrate the particles in a spot where the SERS signals were than acquired. A linearity regime is reported up to 0.5 micromolar concentration of thiram.[41]

A different approach was exploited by Hidi at al., using a microfluidic device to transport methotrexate solutions (an antibiotic) over silver nanostructure.[42] SERS quantitative evaluation shows a linearity range between 0.2 and 2 μM of methotrexate, with a detection limit of about 0.17 μM.

Advanced Diagnostic Tools

In most patients, by the time the cancer is detected, metastasis already occurred. In the case of lung cancer, the percentage of metastatic patients at the time of the diagnosis is more than 80%.[33, 43]

The enhanced permeability and retention effect, present in many solid tumours, is effective only when the tissue is larger than about 5mm in diameter.[33]

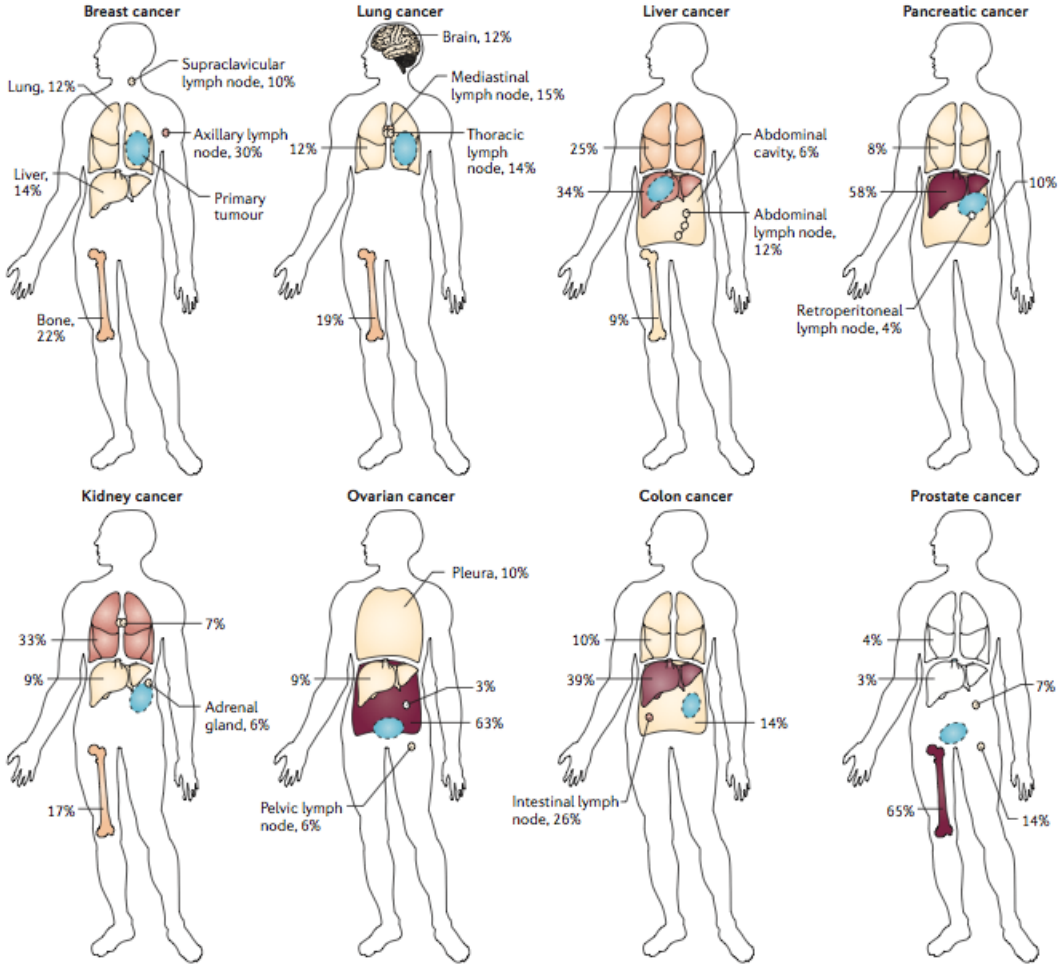

Figure 1.17: An image representing the preferred arrival sites and relative probabilities for some of the most diffuse tumours. The light blue areas are the starting location of tumours. From Ref. 33.

Taking into account these evidences, the development of nanotechnology for high contrast imaging or high theragnostic efficiency, but still with nanoparticles accumulation in tumour only by EPR effects, seems to be suitable only at an advanced stage of the disease.

Contrast agents for *in vivo* imaging of tumour remain of absolute importance, especially approaching its surgical operation.

Magnetic resonance imaging (MRI) is one of the most powerful total-body imaging technique used in medicine. The reason is that MRI combines safe and high penetrative radiation with an huge variety of information given by specific responses of tissues to the magnetic field. Moreover, where the sample appears too much homogeneous, the advent of contrast agents (CAs) overcome such lack in selectivity, as in the case of soft tissues differentiation.[20]

The most used imaging techniques based on MRI are T_1 or T_2 weighted signals.
As just mention in a previous paragraph, T_1 and T_2 are related to the spin relaxation times of the spin populations.
CAs help in shortening these two relaxation times, but the effect, for a single agent, will be stronger for one of the two. Therefore, a CA could be referred preferentially as a T_1 or T_2 contrast agent.
A common property has to be the high magnetic moment of the CA. T_1 contrast agents are generally paramagnetic metallic cations with a high number of unpaired electrons. Gd(III), for example, have a S^8 ground state.[19,21] The longitudinal relaxation is strongly influenced by dipole-dipole interactions or spin couplings, so water molecules coordinated to the paramagnetic metal strongly interact and their protons relaxed at shorter times.[19, 21]
In comparison, the transversal relaxation mechanism is affected by field inhomogeneity. Iron oxide nanoparticles (FeO_xNPs) have a high concentration of paramagnetic centres (iron cations). Their magnetic moment is than very intense, creating important field inhomogeneity that involved a large number of water molecules, also at the outer coordination spheres.[19] FeO_xNPs are most known as T_2 contrast agents.
A significant limitation of MRI CAs is their low sensitivity. At least micromolar concentration of paramagnetic agent have to be present to improve an image contrast.[32] This makes often necessary the validation with other diagnostic techniques.[19]
FeO_xNPs as T_2 CAs are often more sensitive than other T_1 CAs like Gd(III) complexes, but improves only a negative contrast in T_2 weighted images.[19]
The general strategies to improve the efficacy of T_1 CAs involved the increment in coordinated water molecules or the synthesis of macromolecule containing more metallic cations.[19, 21]
However, a really advance is provided by the synthesis of a new class of materials, incorporating the better advantages of MRI and of other complementary imaging techniques, the so called multimodal contrast agents (MCAs).[19]
Magnetic resonance imaging is a total-body technique and shows spatial resolution of the order of tens of micron in the best cases.[19, 21] Optical techniques can be considered complementary techniques because, although they do not have a great body penetration, they can use much more sensitive contrast agents (at nanomolar or less for SERS), and show sub-micron spatial resolution. Furthermore they also show the possibility of multiplexing analysis, in particular in the case of SERS.[13]
Kircher at al. proposed triple multimodality MRI-photoacoustic-SERS nanoparticles for *in vivo* passive targeting and imaging of tumour.[22] They functionalized 60 nm gold nanoparticles with a Raman active dye. Then they covered the AuNP with a sol-gel matrix and functionalized the external surface with a DOTA-Gd(III) complex. The *in vivo* model was a mice with an implanted brain tumour. The authors reported the pre-surgical MRI imaging and photoacoustic and SERS imaging during the surgery for a better removal of tumour margins.

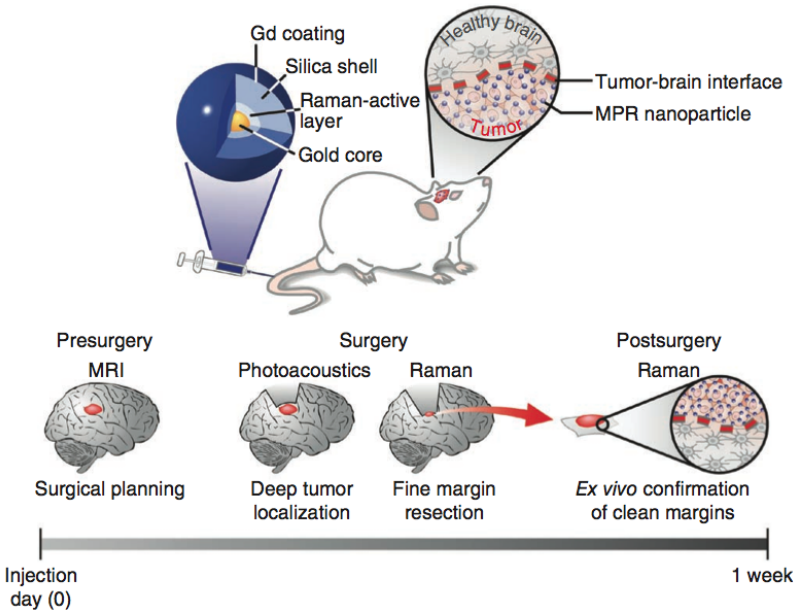

Figure 1.18: Representation of the nanoparticles and protocol used by Kircher at al. for multimodal contrast agents imaging. From Ref. 22.

The early diagnosis of cancer is the second main issue on the prevention of metastasis.

About 60% of patients with ovarian cancer just present metastasis by the time of the diagnosis. Therapies at such advanced state are often not very effective, with a survival at 5 years of about 30-40%. By contrast, the same survival percentage rise to 95% if the cancer is detected when it is still confined to the ovary.[43]

After free DNA was found in the serum of cancer patients, a special attention was focused on circulating biomarkers for the diagnosis and prognosis of cancer. Despite free DNA is released in plasma also by healthy patients, the progressive differentiation of tumour from normal tissues causes discrete clinically relevant peculiar characteristic, as in the case of specific proteins expression.[32, 43]

Tumor biomarker	Expression in cancer tissues (% of tumors that express biomaker)	Expression in normal tissues/cells
	Solid tumors	
Folate receptor	Ovarian cancer (90%), renal cancer (86%), lung cancer (72%), breast cancer (43%), brain cancer (25%), pancreatic cancer (50%)	Kidney, colon, lungs, placenta, bladder
EGFR	Non–small-cell lung cancer (40–80%), colorectal cancer (50–80%), ovarian cancer (35–70%), gastric cancer (41–83%), pancreatic cancer (30–50%), breast cancer (14–91%), bladder cancer (31–72%), head and neck (80–100%), glioma (40–63%)	Cells that originate from all three germ cell layers, particularly those of epithelial origin (e.g., the skin, liver, and gastrointestinal tract
HER2	Non–small-cell lung cancer (18–37%), colorectal (26–90%), ovarian cancer (10–15%), gastric (38–45%), breast cancer (25–30%), bladder cancer (9–36), glioma (20–54%)	Skin, breast, placenta, epithelial cells on gastrointestinal, respiratory, reproductive and urinary tract
PSMA	Prostate cancer (56.7–100%), high-grade prostatic intraepithelial neoplasia (48.6–100%)	Prostate, kidney, small bowel, colon
PCLA	Prostate primary tumor (96.6%), metastatic prostate carcinoma (85.3%)	Brain vasculature, benign prostate tissue
Transferrin receptor	Colon cancer (48%%), breast cancer, kidney cancer, lung cancer, stomach cancer, ovarian cancer*	Skin, pancreas, liver, brain (anterior pituitary), testis
MUC1	Breast cancer (90%), lung cancer, prostate cancer and colorectal cancer*	Mammary gland, respiratory, urinary and reproductive tracts
	Tumor vasculature	
$\alpha_v\beta_3$ integrins	Melanoma, breast cancer, prostate cancer, pancreatic cancer, ovarian cancer, cervical cancer, glioblastoma, and tumor endothelial vessels*	Platelets, very low levels in resting endothelial cells and normal organs
VCAM-1	Leukemia, lung and breast cancer, melanoma, renal cell carcinoma, gastric cancer*	Up-regulated on endothelial cells in response to inflammation
VEGFR	Highly expressed on neovascular endothelial cells**, 73%100% in some non-small cell lung cancers	Monocytes, macrophages
Tem1	Highly expressed on neovascular endothelial cells** including colon, brain and lung cancers	Expressed on normal endothelial cells
APA	Up-regulated on perivascular cells of tumor blood vessels, Stromal cells surrounding prostatic carcinoma cells (73%), nonkeratinizing type cervical squamous cell cancer (90%) renal cancer (clear cell cancer)*	Expressed in the proximal tubules and glomerulus of nephron (kidney), up-regulated in inflamed synovia, granulation tissue, low expression in capillaries and venules of pancreas, lymphoid tissue and intestinal mucosa
	Supporting cells	
TAMs	Breast, prostate, ovary, cervix, stomach, lung, glioma, and bladder cancers*	**
TAFs–FAP	Overexpressed in 90% of stromal fibroblasts in colon, lung, and breast carcinoma	Fibroblasts in healing and inflammation
TEMs	*	Endothelial cells, hematopoietic cells

*Percentages of tumors expressing these receptors is not available. **Not applicable.

Figure 1.19: Common tumor biomarkers that can potentially be used as targets for nanoparticle. PSMA, prostate-specific membrane antigen; PCLA, prostate cancer lipid antigen; MUC1, mucin-1; VCAM-1, vascular cell adhesion molecule 1; VEGFR, vascular endothelial growth factor receptor; Tem1, tumor endothelial marker 1; TAMs, tumor-associated macrophages; TAFs-FAP, tumor-associated fibroblasts–fibroblast activation protein; TEMs, Tie-2–expressing monocytes; APA, aminopeptidase A. From Ref. 32.

Most of actually used tests, approved for disease detection, are protein-based assay.[43, 44] Probably, the most popular one is the enzyme-linked immunosorbent assay (ELISA). In a classical simple protocol, the bottom of a well is functionalized with a specific antibody. The relative antigen, if present on the sample, is than recognized and fixed. A second antibody is finally added for the detection. This second antibody is coupled with a peroxidase, that reacts with a colorimetric reagent developing a colour whose intensity is proportional to present antigen. The ELISA test is robust,

linear and is considered an immunological analytical tool. In this way an effective high number of clinically relevant biomarkers could be quantified in biological fluids, such as serum, urine or saliva.
The real issue for the early diagnosis of cancer is reaching the adequate detection limits.
Surface enhanced laser desorption ionization (SELDI) is a promising ionization source for mass spectrometry, usually coupled with time-of-flight, used in proteomic studies.[43, 44]
This technique has the same immunological selection of ELISA, ea. by an antibody functionalized surface, but the second step consists in the addition of an organic matrix and in the irradiation with a laser for the desorption of the antigen ions to the mass analyser.[43]

Protein	Approximate concentration, pmol/L	Cancer type
Abundant proteins		
Albumin	600 000 000	—
Immunoglobulins	30 000 000	—
C-reactive protein	40 000	—
Putative cancer biomarkers		
Apolipoprotein A1	40 000 000	Ovarian
Transthyretin fragment	6 000 000	Ovarian
Inter-alpha-trypsin inhibitor fragment	4 000 000	Ovarian
Haptoglobin-α subunit	1 000 000	Ovarian
Vitamin D-binding protein	10 000 000	Prostate
Classical tumor markers		
Alpha-fetoprotein	150	Hepatoma, testicular
Prostate-specific antigen	140	Prostate
Carcinoembryonic antigen	30	Colon, lung, breast
Human choriogonadotropin	20	Testicular, choriocarcinoma
Human choriogonadotropin-β subunit	2	Testicular, choriocarcinoma

Figure 1.20: Serum concentration of selected proteins. The cancer type attribution come from SELDI-TOF studies. Form Ref. 44.

Quantitative SELDI-TOF studies found higher prostate specific antigens concentrations in patients with prostate cancer with respect to healthy ones. Data regression analysis resolved discrete patterns of SELDI peaks attributed to prostate cancer instead of benign prostate signatures.[43] Despite such impressive results, some crucial drawbacks related to measurement reproducibility was remarked by Diamandis.[44] This author attributes these effect to non uniformly data acquisition and computational treatments, in addition to case variability in immunological procedures.[44]
The discovery of new clinically relevant biomarkers remains one of the most crucial challenges.
In this field, the analysis of representative tumour tissues is essential, but it could be sometimes difficult to obtain, as for example in the case of patients with non small-cell lung cancer (NSCLC) where the surgery is frequently not a component of the treatment.[45]
Even in cases where primary tissue is available, the tumour sample could not be representative, if long time and therapies passed from the diagnosis to the biopsy. In other cases, like for the prostate, the disease is often indolent for 10-15 years and the metastasis are often located in bones, from where a fresh biopsy is difficult.[45]
Backman at al. reported the characterization of cancer epithelia cells based on the nucleus dimensions.[46] Cancer cells show a nucleus large up to 20 μm, instead of 5-10

μm for non-dysplastic cells. The measurements were provided *in vivo* on endoscopic screening by scattered light carried on with optical fibre.
Even at the early stage of cancer, few metastatic cells could be found in blood. These circulating tumour cells (CTCs) could be collected from blood draws and are considered well representative of the state of the disease.[45]
The American Food and Drug Administration approved the use of CellSearch® as clinical protocol for the extraction and enumeration of CTCs from blood.[45, 47]
It is an immunologic based method in which magnetic nanoparticles are functionalized with an anti epithelial cell adhesion molecule (EpCAM) antibody. This step serves to enrich the sample with EpCAM expressing cells, followed by immunological fixation for the confirmation of presence of cytokeratin and the absence of leukocyte marker CD45.[45]
The extracted cells are epithelial cancer cells, demonstrated to be prognostic for several cancer types.[45]
A second diffuse procedure for CTCs speciation is the CTC-chip technology, based on α-EpCAM antibody functionalized microfluidic channels.
Punnoose at al. published a comparative study between CellSearch® and CTC-chip on their efficacy in capturing CTCs.[45] The authors tested these two methods with spiked samples and with real samples of blood from human patients. They found that both CellSearch® than CTC-chip have over 70% efficiency in capturing cells expressing high EpCAM levels, but the percentage falls down to about 50% on low EpCAM expression. In some cases CTC-chip also showed efficiency over 100%, attributed probably to non-specific interactions and so in false-positive events.
Most remarkably, the author used CTCs of different cancer types and, after the analysis with the two procedures, submitted the isolated CTC to other histological tests. The authors confirmed the clinical relevance of CTCs as tumour biomarkers and evaluated a minimum number of 3 CTCs/mL of blood (ea. 3 cells over millions) as statistical relevant index of tumour presence, for sample homogeneity and minimal assay error. Finally the authors marked the potentially upgrade provided by targeting these CTCs with more than one antibody, both for false-negative recovering and for more complete speciation of the sample.[45]
Gold nanoparticles functionalized with a SERS active dye and a peptide sensible to the epidermal grow factor (EGF) receptor were used by Wang et al. for the detection of 1-720 CTCs/mL of blood.[47] The authors reported clear fingerprint spectra of their SERS labels over the CTCs and successfully used their protocol to monitoring the evolution of the disease. A patient that had 11 CTCs/mL was than threated with usual chemotherapy for 2 month. At the end no more CTCs were detected.
The improvement of SERS labels on this kind of application provides some important advantages due to the vibrational high sensitivity character of the technique. Sharp Raman signals are suitable for multiplexing analysis.

Applications in Cultural Heritage

In the field of Cultural Heritage, the development of non-destructive, or at least micro-destructive techniques have a relevant importance.

By this point of view, Raman spectroscopy provides clear advantages. The technique is non-destructive and can be performed *in-loco* using a series of new generation portable Raman spectrometers.[48]

The high spatial resolution, intrinsic of this optical technique, offers the possibility to obtain chemical maps of the sample. In addition, since it is a vibrational spectroscopy, Raman spectra give chemical speciation both for organic and inorganic components, even if they are present in mixture.[48]

For this kind of applications, near infrared laser excitation is frequently used, due to the low fluorescence generally reported into this spectral range. However, the Raman scattering efficiency decreases with the fourth power of wavenumber, and the usual detector efficiencies also decrease in the near-infrared, so that longer acquisition times, are sometimes needed.[48]

The discrimination of the same anion in different compounds is a clear demonstration of the usefulness of Raman spectroscopy. For example, different carbonate based minerals have informative frequency shifts: $CaCO_3$ has a symmetric C=O stretching at 1086cm^{-1}, whereas $CaMg(CO_3)_2$ has the analogue band at 1094cm^{-1} and $MgCO_3$ at 1117cm^{-1}.[48]

Taking into account biological materials, Edwards at al. analysed the skin of an ancient egyptian mummy from the twelfth dynasty (about 2000 a.C.).[48] They found well defined amide I and associated proteins modes at 1660, 1450 and 1240cm^{-1}, revealing that the skin was well preserved. In addition, other bands at lower frequencies revealed the presence of residual chemicals coming from the mummification process, ea. the sodium sulphate from the natron used as desiccant.[48]

Despite the large number of information provided by Raman spectroscopy, only the species with sufficient Raman cross section could be easily measured, but differentiations among very similar macromolecules, such as different proteins, is not trivial. As the building blocks are essentially the same, in principle they show the same bands.

An important upgrade, overcoming this issue, was provided by Sciutto et al. for the characterization of a paint stratigraphy.[49] They used gold nanoparticles functionalized with an ovalbumin specific antibody and a Raman active dye. Their results showed positive targeting of the ovalbumin present in the artwork allowing also the simultaneous chemical identification of the inorganic materials present in the stratigraphy.

2. Aims of the Project

During my Ph.D. I focused my attention on the development of new nanomaterials and protocols for the characterization of clinical relevant samples, both *in vitro* and *in vivo*.

Gold nanoparticles were always used as the basis of the studied nanosystems. Raman was extensively employed because of its higher analytical potential and, exploiting together the plasmonic nanoparticles and Raman spectroscopy, the surface enhancement effect (SERS) was used to improve the analytical sensitivity of analysis.

The gold nanoparticles, which were obtained by laser ablation synthesis in solution (LASiS), were used also as substrate for laser desorption ionization mass spectrometry. We tested AuNP for different low weight molecules, including interesting cytotoxic and anticancer analytes. Our results show the possibility of upgrading this technique to the low mass region, where the signals from the commonly used organic matrix predominate.

The quantitative determination of four clinically used anticancer drugs was explored with SERS experiments. Reference solutions reveal detection limits up to ng per millimetre square of SERS active area, useful for the actual clinical requirements. Moreover, advanced statistical models were applied for recognizing a drug, Irinotecan, and its active metabolite.

The limitations provided by molecules with intrinsic low Raman cross section was investigated and potentially solved with a new protocol for analyte derivatization and analysis, called *Reactive SERS*.

Nanomaterials were synthetized for multiplexing targeting and analysis of proteic samples. The main applications were developed in nanomedicine, with the identification of cancer cells, but the protocols have been applied also in the cultural heritage field with the characterization of ancient paint stratigraphic samples.

The organic synthesis of new optimized Raman active dyes was pursued to extend the potential complexity of SERS multiplexing analysis.

The development of new software helped in a complete automatization of the SERS measurements protocols. Interactive algorithms were developed for working in synergy with the micro-Raman instrument and provided lowering of the data acquisition and manipulation times.

The new optimized dye library was used for the selection of the most efficient dyes for *in vivo* diagnosis of tumour using innovative multimodal contrast agents. A gold-iron nanoalloy nanoparticles were used for magnetic resonance, computed tomography and SERS imaging.

A new class of polymer was also planned and synthetized, as a potent T_1 MRI contrast agent. This molecule has multiple branches, bonding DOTA-Gd(III) residues, and a thiol for a stable linkage to the gold nanoparticle surface. It is called *SuperDOTA* and it was just characterized and associated to SERS tags as another generation of multimodal contrast agents.

3. Therapeutic Drug Monitoring

Among the new therapeutic strategies against cancer, a special issue is that of the personalization of therapies.
Individual dose/response effects have to be monitored to adjust the treatment at optimum dosage, where the drug has maximum effect, still remaining non toxic.
The best analytical performances for anticancer drugs monitoring are usually obtained with chromatographic techniques coupled with mass spectrometry.[36]
Exploration of solutions for problems related to the therapeutic drug monitoring are part of the present work. First, a possible solution to the limitations of the laser assisted ionization mass spectrometry was analyzed,[28] since this technique has high sensitivities, but shows problems in analysing low molecular weight molecules. Second, another approach, alternative to the use of mass spectrometry, was considered for revealing four widely clinically used anticancer drugs using a high sensitive quantitative evaluation based on surface enhanced Raman scattering.[12] This technique is very sensitive and suitable, in principle, for measurement at single molecule level.[17] Third, new reactions and analyses were developed for detecting molecules with low Raman and SERS cross sections.

Gold Nanoparticle assisted LDI for mass spectrometry at low molecular weight

In mass spectrometry there are two fundamental building blocks regarding the measurement: the *ion source* and the *mass analyser*.
In general, one obtains the mass distribution and the relative abundance of the components extracted by the sample.
The *ion source* provides the the different components of the sample as ions. Then, they are accelerated within the *mass analyser* by high voltage electric field. In *Time-of-Flight* (TOF) *mass analyser* the ions are accelerated through a linear or curved trajectory. Since the external electric field is constant, ions with different mass over charge (*m/z*) ratios acquire different accelerations, arriving at the end of the trajectory at different times. The time of arrival to the detector for every single ion is correlated to its *m/z* ratio and the signal intensities represent their relative abundance. An efficient and effective ionization of samples is, therefore, of crucial importance.
The ionization of the sample can occur at different levels. For example the *inductively coupled plasma* (ICP) decompose every species to atomic level, giving information on elemental composition.
The *laser desorption ionization* (LDI) is considered, on the other hand, a soft ion source, meaning that molecules remain integer, or fragmentations takes place in small amounts.[50] In LDI there is an ablation process on the surface of a solid sample, due to a laser irradiation. The ablated material is than directed into the *mass analyser*.
To optimise the absorption of the laser and the consequent desorption of the sample, highly absorptive organic molecules (referred to as *matrix*) are added in large excess to the sample. The analytes have to be dispersed into the matrix crystals. These crystals absorb the laser radiation and sublime, carrying the sample ions, so the technique is known as *matrix assisted LDI* (MALDI).[50]

An important drawback of this approach is, clearly, the abundance of matrix signals in mass spectra. For this reason, molecules under 500-800 Da are not usually investigated with the MALDI-TOF mass spectrometry.[28, 50]
Nevertheless, MALDI-TOF is the elected technique for peptides and polymers.[28, 50]
Mass spectrometry is a well known high sensitive analytical technique, but before using MALDI for the therapeutic drug monitoring with low mass molecules, we had to overcome the problem of the low mass region.
Due to the localized surface plasmon resonance (LSPR), gold nanoparticles (AuNPs) emerged as suitable inorganic matrixes for LDI.[51, 52] Their high surface area allows a high loading and the LSPR band is usually broad, especially when the nanoparticles aggregate, and covers the visible region.
Therefore, visible pulsed lasers can be used for NPs assisted LDI. This can be important for preventing photoblenching of molecules sensible to UV or near-UV irradiation.[51]
Nanoparticles can also be functionalized for selective reactions with analytes present in a complex solution. A simple centrifugation is than sufficient to separate the nanoparticles and their loading for subsequent MALDI analysis.[51]
Nevertheless, the use of capping agents, needed to stabilize commercial AuNPs, still remains a strong interference for the analysis of the low mass region.
Gold nanoparticles obtained by laser ablation synthesis in solution (LASiS) have, in principle, the sufficient high surface purity to provide mass analysis of lightweight molecules.
The nanoparticle size is another important variable for the desorption yield. In first approximation, smaller NPs have higher specific area (involving great matrix to analyte molar ratio) and, with the same excitation wavelength, the temperature reached by laser irradiation increases in decreasing particles size.[28, 51, 53]
We have studied AuNPs, obtained by LASiS, as matrix for LDI, in comparison with commercial AuNPs and 2′,6′-Dihydroxyacetophenone (DHAP), an organic matrix usually employed in MALDI. Commercial AuNP are synthesised by citrate based wet chemistry.[51]
The gold nanoparticles obtained by LASiS have usually a broader dimensional dispersion than NPs produced by wet chemistry.[26, 27] To account a reliable comparison against the citrate-AuNP, we used a size selected LASiS-AuNP. The size selection was performed by centrifugal gradient, as reported in literature.[54]
In Table 3.1 and Table 3.2 are reported all the matrixes used, and the studied analytes.

Table 3.1: Inorganic and organic matrixes used for MALDI-TOF mass spectrometry experiments. All the nanoparticles solutions were prepared with similar gold atoms concentration. The DHAP solution is saturated in acetonitrile with 0.1% of TFA.

Matrixes				
LASiS-AuNP-I	LASiS-AuNP-II	Citrate-AuNP-I *Sigma Aldrich*	Citrate-AuNP-II *BBI international*	DHAP-TFA *Sigma Aldrich*
10.6nm ±22%	18.6nm ±35%	10.2nm ±12%	19.6nm ±8%	-
$2.1 \cdot 10^{-7}$ M *in [AuNP]*	$3.2 \cdot 10^{-8}$ M *in [AuNP]*	$2.1 \cdot 10^{-7}$ M *in [AuNP]*	$2.6 \cdot 10^{-8}$ M *in [AuNP]*	0.263 M *in [DHAP]*
2.6 mg/mL *in [Au]*	2.6 mg/mL *in [Au]*	2.6 mg/mL *in [Au]*	2.6 mg/mL *in [Au]*	40 mg/mL *in [DHAP]*

Table 3.2 Analytes used for testing the AuNP assisted MALDI .

Analytes				
name / structure	*molecular weight*	*stock solution concentration*	*analysed quantity*	*skills*
L-arginine 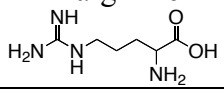	174.20 g/mol	$1.1 \cdot 10^{-3}$ M *in water*	100 ng 574 pmol	polar aminoacid
D(-)fructose 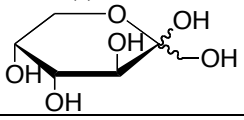	180.16 g/mol	$1.1 \cdot 10^{-3}$ M *in water*	100ng 555 pmol	natural monosaccharide
Atrazine 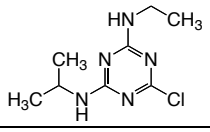	215.68 g/mol	$2.3 \cdot 10^{-4}$ M *in MeOH:water 1:1*	25ng 116 pmol	herbicide
Anthracene 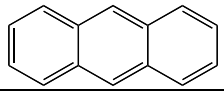	178.23 g/mol	$1.9 \cdot 10^{-3}$ M *in MeOH:water 2:1*	175ng 981 pmol	apolar aromatic molecule
Paclitaxel 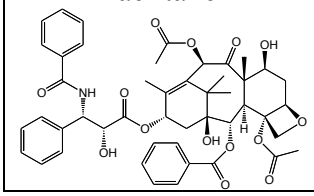	853.91 g/mol	$1.3 \cdot 10^{-4}$ M *in MeOH:water 1:1*	57.5ng 67 pmol	anticancer drug

As a first step, we acquire the mass spectra of the pure matrixes, in Figure 3.1. Especially in the range below 500Da the LASiS-AuNP-I and II show negligible background, with few and low intense signals.

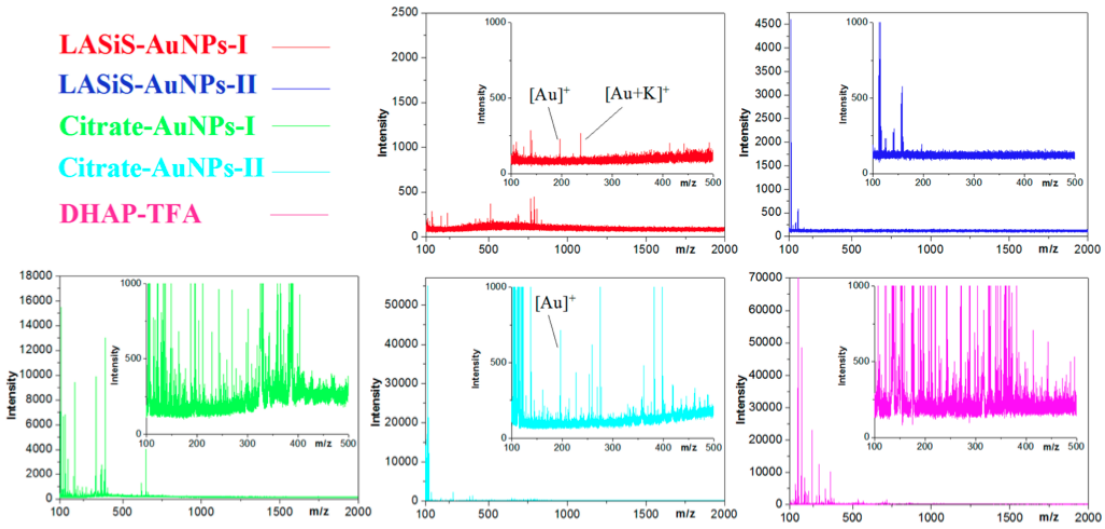

Figure 3.1: LDI-TOF mass spectra of the pure matrixes. From Ref. 28.

All colloidal solutions were pre-concentrated to the same atomic gold concentration. Dialysis membranes were used before depositing the particles, for the purification of the nanoparticle solutions. In this way we removed the largest amount of free citrate and other molecules, like tannic acid or sodium azide, present in the commercial

solution as reported in the specification sheet. However, a consistent amount of capping agents still remain over the Citrate-AuNPs, populating the background into the low mass range of mass spectra.
The supernatant, taken by the dialysis membrane of Citrate-AuNP-I, were mixed with LASiS-AuNP-I and than analysed by MALDI-TOF. As expected, high signals grew up into the low mass range.

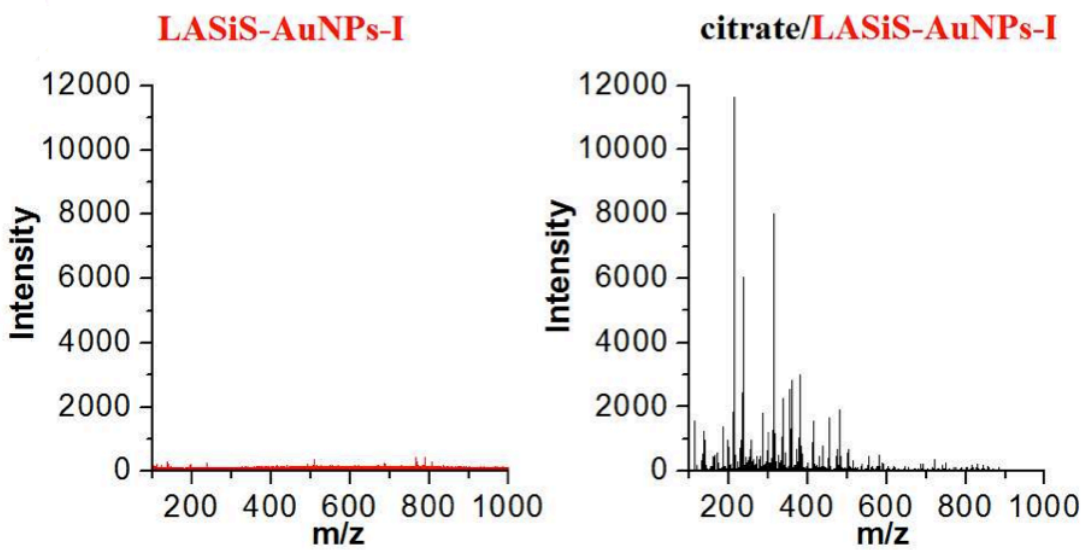

Figure 3.2: Mass spectrum of LASiS-AuNP-I, on the left. It presents negligible signals. On the right, the mass spectrum of LASiS-AuNP-I after the addition of the Citrate-AuNP-I supernatant, obtained by the dialysis membrane. In this case, lots of signals are present under 600 Da. From Ref. 28.

This feature makes LASiS-AuNP interesting for analysis of molecules under 500 Da. Five different analytes with different characteristics were chosen, to analyze the performances one can obtain with the LASiS-AuNP.
Arginine is a polar, basic aminoacid. It has amines and a carboxylate functional group, which show good affinity with the gold nanoparticles surface.
In Figure 3.3, the LASiS-AuNP-II matrix performs better than the Citrate-AuNP-II. The molecular peak, relative to the addition of a proton ($[M+H]^+$=175.29 *m/z*), is the base peak and the sodium and potassium adducts are also clear and intense. The spectra relative to the Citrate-AuNP shows much more peaks. In the case of the organic matrix DHAP, the peak at 175.29 *m/z* is very intense, but the same peak is found also for the matrix alone, making the attribution unsafe.

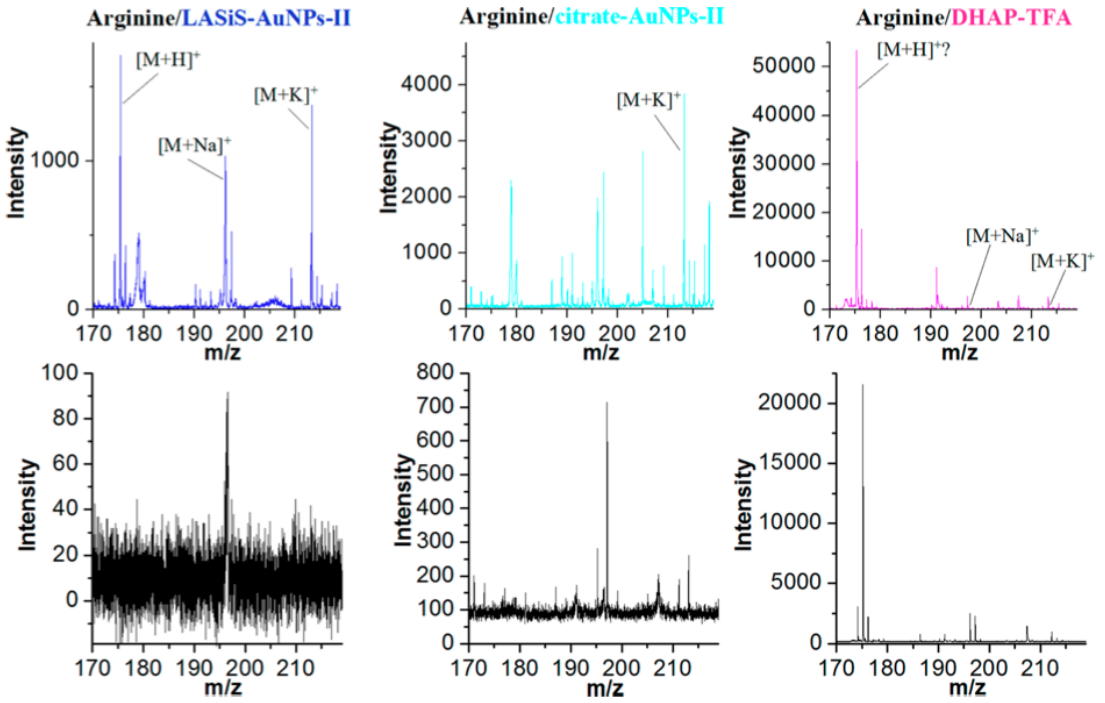

Figure 3.3: LDI-TOF mass spectra of selected AuNPs and DHAP with Arginine. The black spectra at the bottom are those of the matrixes alone. The clearest attribution are provided by LASiS-AuNP. From Ref. 28.

Fructose is a natural monosaccaride. It is water soluble, but it does not present highly polar functional groups. In Figure 3.4 are reported the mass spectra using LASiS-AuNP, Citrate-AuNP and DHAP as matrixes. Also in this case the laser ablated nanoparticles performs better than the Citrate-AuNPs. The $[M+Na]^+$ peak, at 203.24 *m/z* in LASiS-AuNP-II, is also present with Citrate-AuNP-II but its intensity is much lower. The spectra of Fructose with DHAP is again ambiguous since the only signal with a *m/z* corresponding to the analyte is also present as background ($[M+K]^+$ at 219.32 *m/z*).

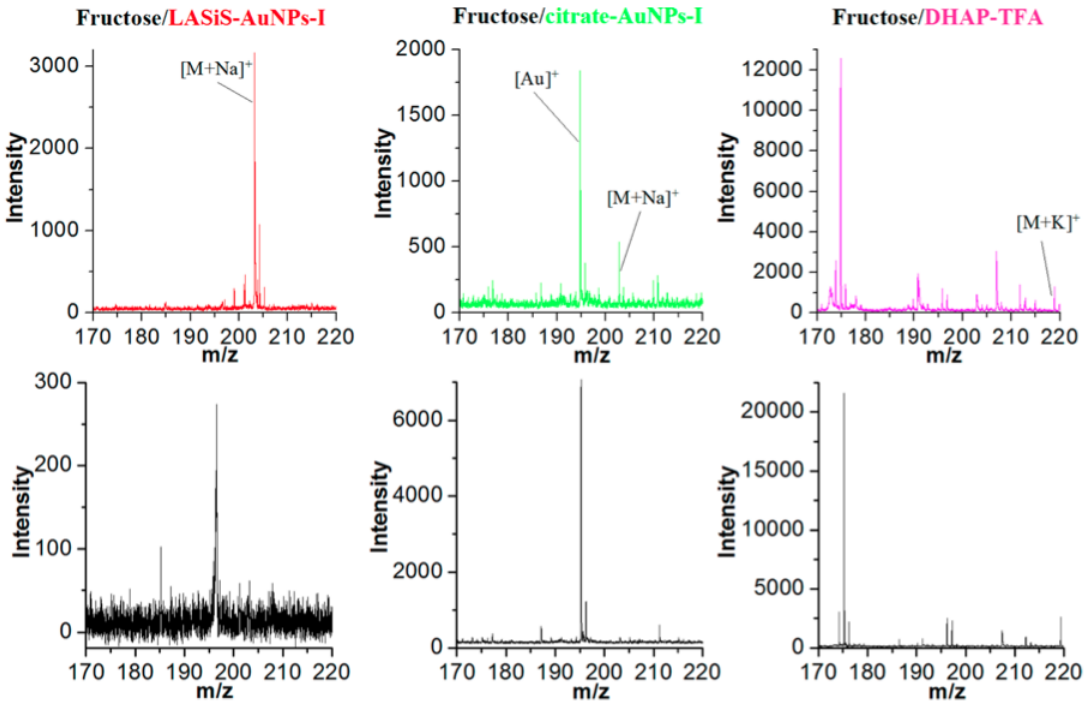

Figure 3.4: LDI-TOF mass spectra of selected AuNPs and DHAP with Fructose. The black spectra at the bottom are those of the matrixes alone. From Ref 28.

Atrazine is an aromatic heterocyclic compound. It is used as fungicide and its secondary amines do not contribute to a consistent polarity. The molecule is slightly water soluble. In Figure 3.5, the mass spectra with the LASiS-AuNP, the $[M+Na]^+$ peak at 239.43 *m/z* is the only signal in the range of interest. The same peak is evident also with the Citrate-AuNP and with DHAP, but the spectra is rich of other signals, partially due to the matrix and partially probably due to Atrazine fragmentations.

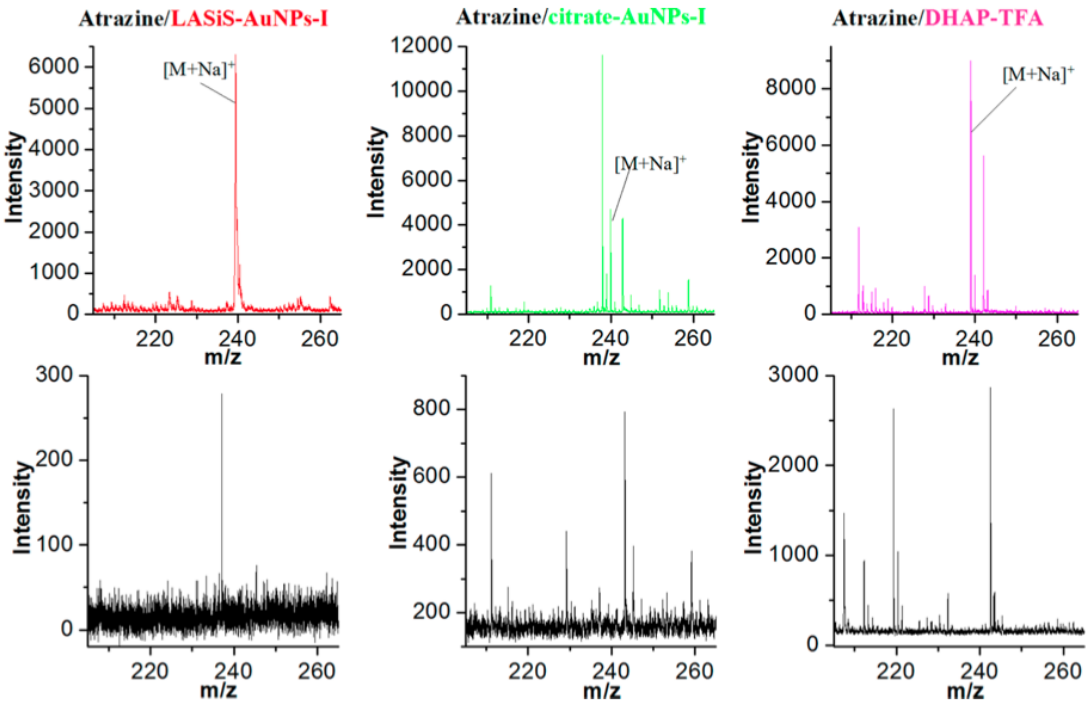

Figure 3.5: LDI-TOF mass spectra of selected AuNPs and DHAP with Atrazine. The black spectra at the bottom are those of the matrixes alone. From Ref. 28.

Anthracene is an apolar aromatic molecule. It is very slightly soluble in water. In this case, all the matrixes are not very efficient for this molecule. The molecular ion signal is present using LASiS-AuNP and the $[M+Na]^+$ is present with Citrate-AuNP at 201.22 *m/z*. Any peak relative to Anthracene can be found using the organic DHAP matrix.

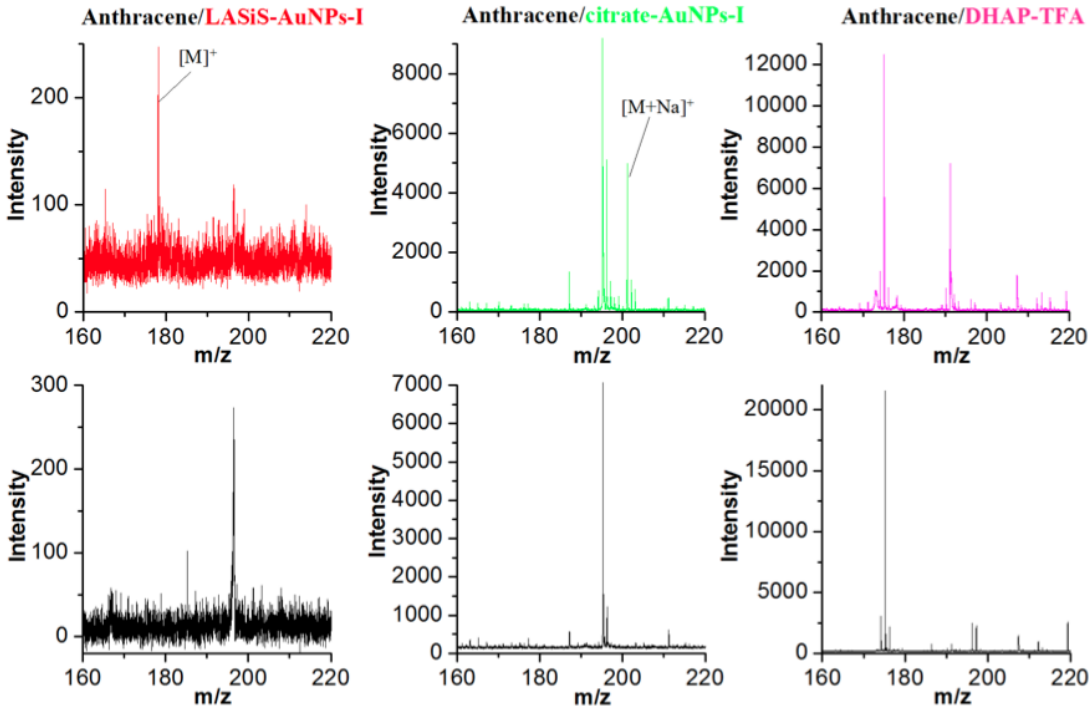

Figure 3.6: LDI-TOF mass spectra of selected AuNPs and DHAP with Anthracene. The black spectra at the bottom are those of the matrixes alone. Any signal from the analyte is recorded with the DHAP matrix. From Ref. 28.

Paclitaxel is a widely used anticancer drug, belonging to the family of Taxanes.[36] It is approved for a broad spectrum of human malignancies and is characterized by a slight solubility in water.[36, 55]

Paclitaxel is a relatively heavy molecule, in comparison to the other molecules. Its sodium adduct ion $[M+Na]^+$, at 876.42 *m/z* for the LASiS-AuNP-I, falls outside the critical range of the low masses. Therefore, it is well defined for all the tested matrixes , with a negligible background in all cases, as could be seen at Figure 3.7.

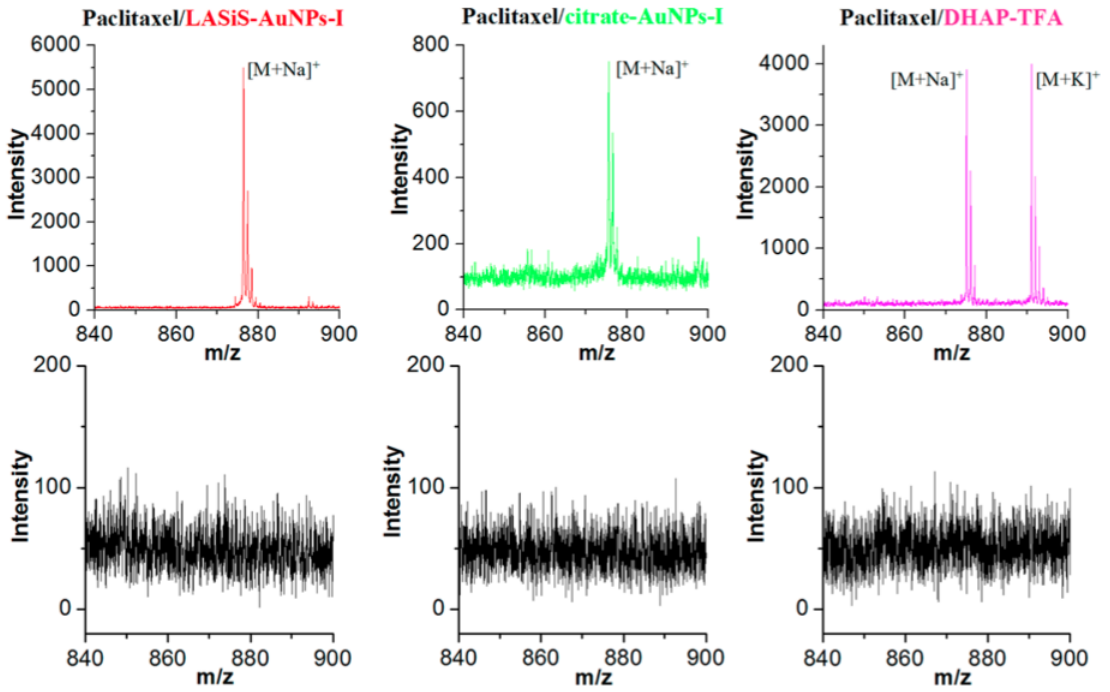

Figure 3.7: LDI-TOF mass spectra of selected AuNPs and DHAP with Paclitaxel. The black spectra at the bottom are those of the matrixes alone. The mass range of interest falls outside the critical low mass region, so negligible backgrounds were found with all matrixes. From Ref. 28.

With this study we concluded, therefore, that gold nanoparticles are suitable to extend the mass range of the LDI-TOF mass spectrometry under 200 Da, but attention has to be made to the surface coverage of such nanoparticles. LASiS-AuNPs give better performances compared to Citrate-AuNPs, mostly due to the fact that LASiS produces naked nanoparticles, since only water and bulk gold, are used for their synthesis.

Citrate-AuNPs were dialysed before their deposition, but also in this case a consistent amount of citrate still remains over the nanoparticle surface. For LASiS-AuNPs the nanoparticles are produced with a surface negative charge which stabilizes the solution by electrostatic repulsion, and no other molecules are needed for their colloidal stability.[26, 27] The clean surface is believed to allow analytes to stay closer to the nanoparticles, resulting in a more efficient laser induced ionization.

We also observed that smaller nanoparticles, ea. LASiS-AuNP-I and Citrate-AuNP-I, often give better signals with respect to the bigger ones, as also reported in the literature.[51-53] The results suggest that the surface chemistry of nanoparticles plays the major role in the ionization yield and therefore for the quality of mass spectra, especially in the low mass region.

Considering the different characteristics of the studied analytes , polar molecules show the clearest signals, while anthracene is the case in which, because of solubility and of low polarity, the recorded peaks are very weak. Our results confirm the general understanding of the importance of the polarity of the molecules and of the matrix.

Figure 3.8 reports the results for Paclitaxel in particular for the signal reproducibility and linearity. Interestingly, LASiS-AuNP-I, performs better in term of correlation coefficient and sensibility.

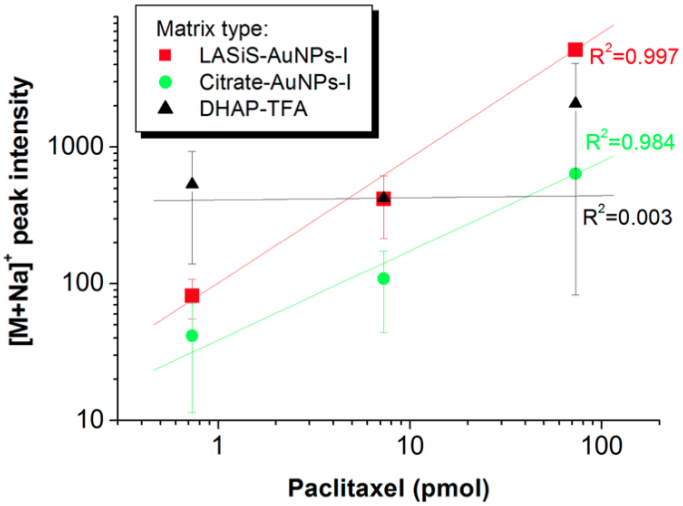

Figure 3.8. Log-log calibration curve of $[M+Na]^+$ signal of Paclitaxel on different matrixes and different sample deposition amounts. The error bars represent the standard deviation over three different acquisitions. From Ref. 28.

Quantitative determination of chemotherapy drugs with Surface Enhancement Raman Scattering

The surface enhanced Raman Scattering was considered for a quantitative determination for three clinically relevant anticancer drugs: Sunitinib, Paclitaxel and Irinotecan. For the last one, also its active metabolite SN-38 was considered.

Sunitinib malate is a small molecule active on several targets as inhibitor for tyrosine kinases such as c-KIT, fms-like tyrosine kinase 3 (FLT3), platelet-derived growth factor receptor (PDGFR) and vascular endothelial growth factor receptor (VEGFR).[56, 57] All these receptors play important roles in tumour grow and angiogenesis, regulating cell proliferation, differentiation, and survival.

The therapeutic practice for the administration of Sunitinib requires dose of 25 mg once daily for 4 weeks every 6 weeks. The steady state concentration is reached after 4 weeks of daily dosing with a plasma concentration of 32 ng/mL (80 nM).[57]

Paclitaxel is the second wide spread anticancer drug used in clinics. It acts against a broad spectrum of tumours, as breast cancer, ovarian carcinoma and lung cancer. Its mechanism of action regards the stabilization of dysfunctional microtubules, that are structural intracellular moieties. Paclitaxel is involved in inhibition of cell replication, and induction of cell death. The minimum plasma concentration of Paclitaxel required for of clinical activity is about 40 ng/mL (50nM).[55]

Irinotecan, also known as CPT-11, is a semisynthetic derivative of the natural alkaloid camptothecin.[58, 59] It is used in cancer therapy against a large variety of solid tumours and for metastatic colorectal cancer.[59, 60] CPT-11 presents a complex metabolism. In fact, its pharmacologic activity is mostly due to its active metabolite SN-38. It is reported to be cytotoxic and a potent selective inhibitor of Topoisomerase I, a nuclear enzyme responsible for relaxation of supercoiled DNA during replication and transcription.[58, 59] The mechanism of action of CPT-11 involves a reversible complex between SN-38 and DNA/topoisomerase I, causing a single strand break in DNA. Irinotecan is usually submitted to patients with a 30-90 minutes infusion every three weeks.[59, 60] Pharmacokinetics studies show a plasma concentration peak of Irinotecan and SN-38 respectively of 35.5 and 7 ng/mL (60.5 and 17.9 nM).[59] While

the steady state plasma concentration during the therapy reach 25 ng/mL (42.7nM) for Irinotecan and 5.8 ng/mL (14.9nM) for SN-38.[59]
We explored the reliability of a SERS based quantitative determination protocol for these three drugs and for the active metabolite SN-38.
Before acquiring calibration curves, we evaluated the best experimental condition for the SERS measurement.

Table 3.3: The analysed drugs

Drug Name (CAS number) Chemical Formula (Molecular Weight) *IUPAC Name*	**Chemical Structure**
Sunitinib (CAS 341031-54-7) $C_{22}H_{27}FN_4O_2 \cdot C_4H_6O_5$ (532.56 g/mol) *N-[2-(Diethylamino)ethyl]-5-[(Z)-(5-fluoro-1,2-dihydro-2-oxo-3H-indol-3-ylidene)methyl]-2,4-dimethyl-1H-pyrrole-3-carboxamide (2S)-2-hydroxybutanedioic acid (1:1) salt*	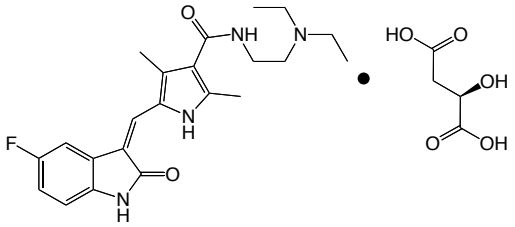
Irinotecan (CAS 100286-90-6) $C_{33}H_{38}N_4O_6 \cdot HCl$ (623.14 g/mol) *(S)-4,11-diethyl-3,4,12,14-tetrahydro-4-hydroxy-3,14-dioxo-1H-pyrano[3',4':6,7]indolizino[1,2-b]quinolin-9-yl ester*	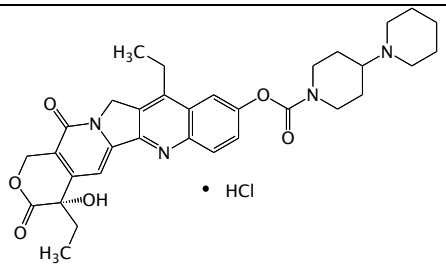
SN-38 (CAS 86639-52-3) $C_{22}H_{20}N_2O_5$ (392.40 g/mol) *(4S)-4,11-Diethyl-4,9-dihydroxy-1H-pyrano[3',4':6,7]indolizino[1,2-b]quinoline-3,14(4H,12H)dione*	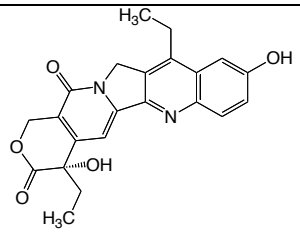
Paclitaxel (CAS 33069-62-4) $C_{47}H_{51}NO_{14}$ (853.91 g/mol) *(1S,2S,3R,4S,7R,9S,10S,12R,15S)-4,12-bis(acetyloxy)-1,9-dihydroxy-15-{[(2R,3S)-2-hydroxy-3-phenyl-3-(phenylformamido)propanoyl]oxy}-10,14,17,17-tetramethyl-11-oxo-6-oxatetracyclo[11.3.1.0^{3,10}.0^{4,7}]heptadec-13-en-2-yl benzoate*	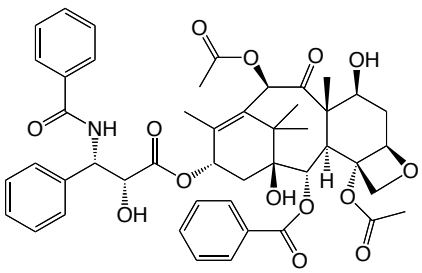

Exploring best measurement conditions

First we determined the best experimental conditions for recording the best SERS signals.

Both the excitation wavelength and the nature of the SERS substrate were investigated. For comparison, we also used Doxorubicin, an anticancer drug active as a DNA intercalating agent,[11] since it is known as efficient SERS analyte.[61, 62]

Table 3.4: Doxorubin used as reference SERS analyte. From Ref 12.

Doxorubicin (CAS 25316-40-9) $C_{27}H_{29}NO_{11} \cdot HCl$ (579.98 g/mol) *(7S,9S)-7-[(2R,4S,5S,6S)-4-amino-5-hydroxy-6-methyloxan-2-yl]oxy-6,9,11-trihydroxy-9-(2-hydroxyacetyl)-4-methoxy-8,10-dihydro-7H-tetracene-5,12-dione*	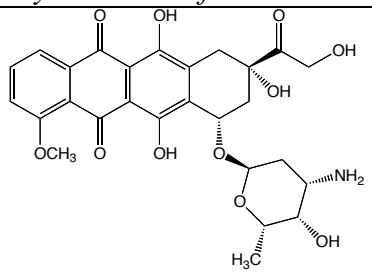

Klarite substrates, a commercial SERS substrate, were used with excitation wavelengths at 488, 633 and 785nm.

Klarite is a silicon slide uniformly covered with gold. The SERS active area is a 4x4 mm^2 surface where ordered gold pyramids are present, as shown in Figure 3.9 and 3.10. Enhanced fields can be found at the edges and at the tops of the pyramids (hot spots).

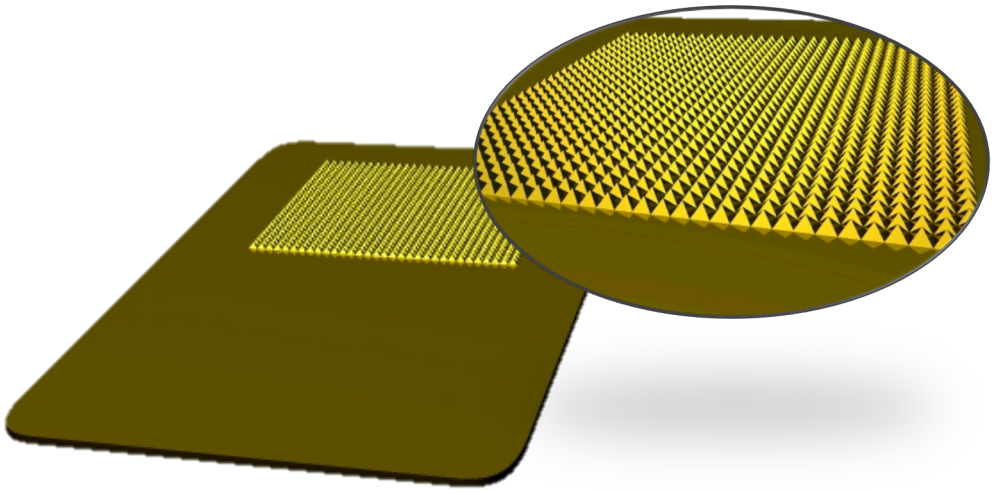

Figure 3.9: A picture representing a Klarite substrate. The SERS active area is the 4x4mm square where the pyramids provide hot-spot features.

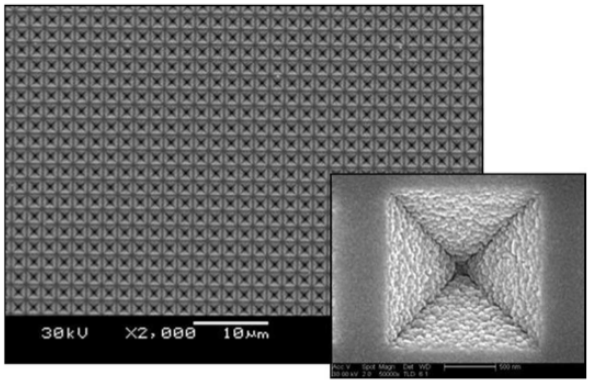

Figure 3.10: SEM image of a Klarite substrate. From Ref. 13.

1μg of each drug was spotted over Klarite substrates simply drying a drop of the relative solution. A home-made Viton mask with a cylindrical hole was used to limit deposition surface to a 1.8 mm^2.
Raman measurements were acquired with the substances deposited over a pure silicon slide to prove that the Raman spectra originated from SERS.
The same results obtained with the non-SERS silicon surface was obtained with the Klarite substrate using the 488 nm excitation, showing that in this configuration there was not a SERS enhancements. The observed intensities, when exciting at 785 nm on Klarite, were too low to be used for a quantitative analysis.
SERS spectra of Doxorubicin, Sunitinib, SN-38 and CPT-11, deposited on Klarite substrates, were obtained exciting at 633 nm. In particular, Doxorubicin spectra showed a maximum at 1230-1250 cm^{-1}, Sunitinib at 1280-1330cm^{-1} and at 1570cm^{-1}, whereas Irinotecan and its metabolite SN-38 have a similar spectra characterized by a series of peaks in the 1350-1600 cm^{-1} range.
Any appreciable signal was detected for Paclitaxel exciting at 633nm, even for long acquisition times.
Doxorubicin, as expected, shows the higher intensities, about two hundred times more than the second better performer, Sunitinib.
The Raman scattering efficiency can be explained in terms of the absorption characteristics of the analytes. In Figure 3.11 one can see the distance between the maximum absorption band of the compounds and the excitation wavelengths used for the experiments. Considering that gold substrates show their activity in the red spectral region,[15] one observes that closer are the drug's maximum absorption to the excitation wavelength, higher are their Raman bands.[12]
The main absorption band of Doxorubicin is the nearest to the 633 nm exciting line, whereas for Paclitaxel it is the farthest. Therefore, Doxorubicin benefits of both the contribution of SERS and of the pre-resonance electronic situation.

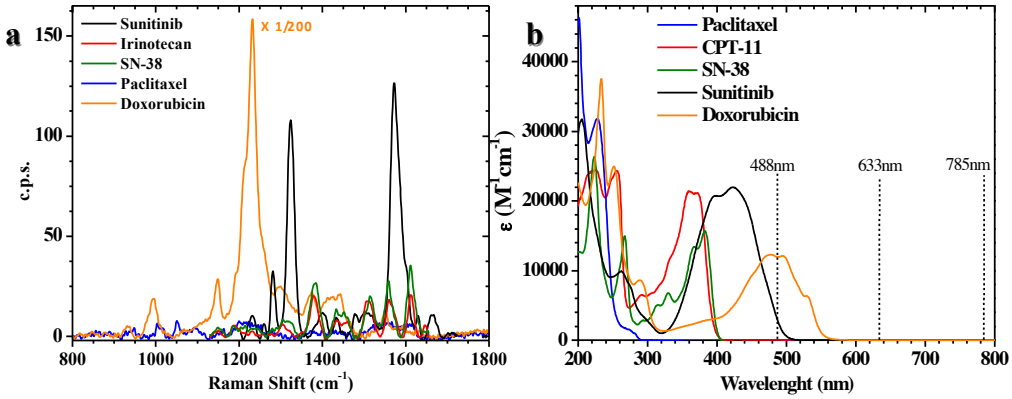

Figure 3.11: The optical extinction cross sections of the molecules studied (b) and their SERS spectra obtained from 1μg of substance at 633nm excitation over a Klarite substrate (a). From Ref. 12.

Table 3.5: A resume of the signals obtained with different excitation wavelengths and SERS substrates.

SERS Substrate / *Laser Wavelength*	Klarite	Si
488nm	No signals	No signals
633nm	Suitable for quantification	No signals
785nm	Too low for quantifications	No signals

The second step was that of identifying the better SERS substrate among the commercial Klarite and other substrates obtained by drying plasmonic nanoparticles in cylindrical aluminium wells. The nanoparticles considered were laser ablated gold and silver nanoparticles (AuNPs-LASiS and AgNPs-LASiS) and commercially available AuNPs and AgNPs. The nanoparticles size was 30 nm for the LASiS particles and 60 nm for the commercial ones.
The performances were compared measuring 1μg of Sunitinib at 633 nm excitation and are reported in Figure 3.12.

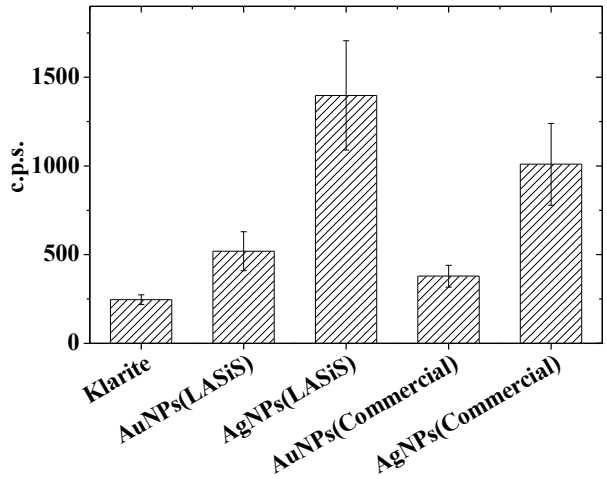

Figure 3.12: signals of the most intense Raman band of Sunitinib (at 1320cm^{-1}) acquired with 633 nm excitation over different SERS substrates. Error bars represent the standard deviation for a set of 10 measurements recorded in random points. From Ref. 12.

Despite the highest intensities obtained with laser ablated silver nanoparticles, the Klarite substrate shows less point-to-point variability.
Nevertheless, laser ablated nanoparticles perform better than the corresponding ones obtained by wet chemistry. This reflects the higher surface purity of the nanoparticles obtained by LASiS.
The above measurements show that the better conditions for SERS measurements are obtained with the Klarite substrate and the 633nm laser excitation.

Calibration curves for chemiodrugs

We measured the intensity (counts per second, c.p.s.) variation of representative Raman bands for each drug, by changing the amount deposited over Klarite substrates.
We used the band at 1322cm^{-1} for Sunitinib and at 1385cm^{-1} for both Irinotecan and SN-38. The mass range explored varied between 10 and 10^3 ng. For this reason we found useful to express the calibration curves in a logarithmic scale.
In a typical measurement procedure (see Appendix A4), we dried 6μL of drug solution over a surface of about 1.8 mm^2 of Klarite active substrate. We recorded the Raman spectra in 133 points within this area. The acquisition time for every spectra varied with the drug concentration in the range of 15-120 seconds. These times correspond to measurement time between 30 minutes to 4 hours for a single sample.
For *limit of quantification* (LQ) we mean the lowest amount of drug at which the logarithm of Raman intensity is linearly correlated to the logarithm of analyte mass. Therefore, LQ is larger than *limit of detection* (LD), which is the lower amount of analyte clearly identified above the noise.
In Figure 3.13, we report the Raman bands intensities as a function of both the total mass of analyte deposited and the mass per unit area.

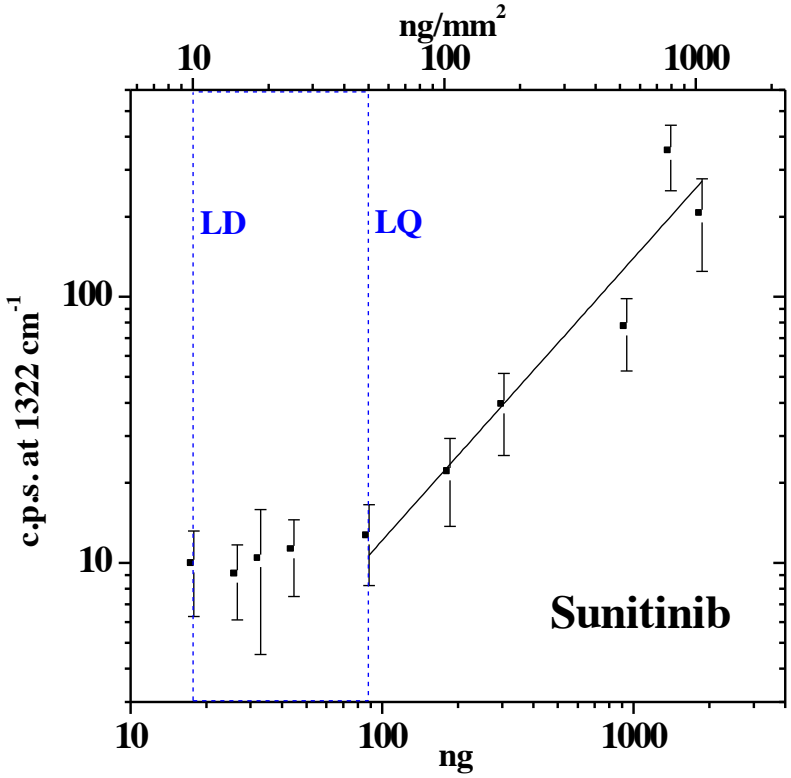

Figure 3.13: Continue…

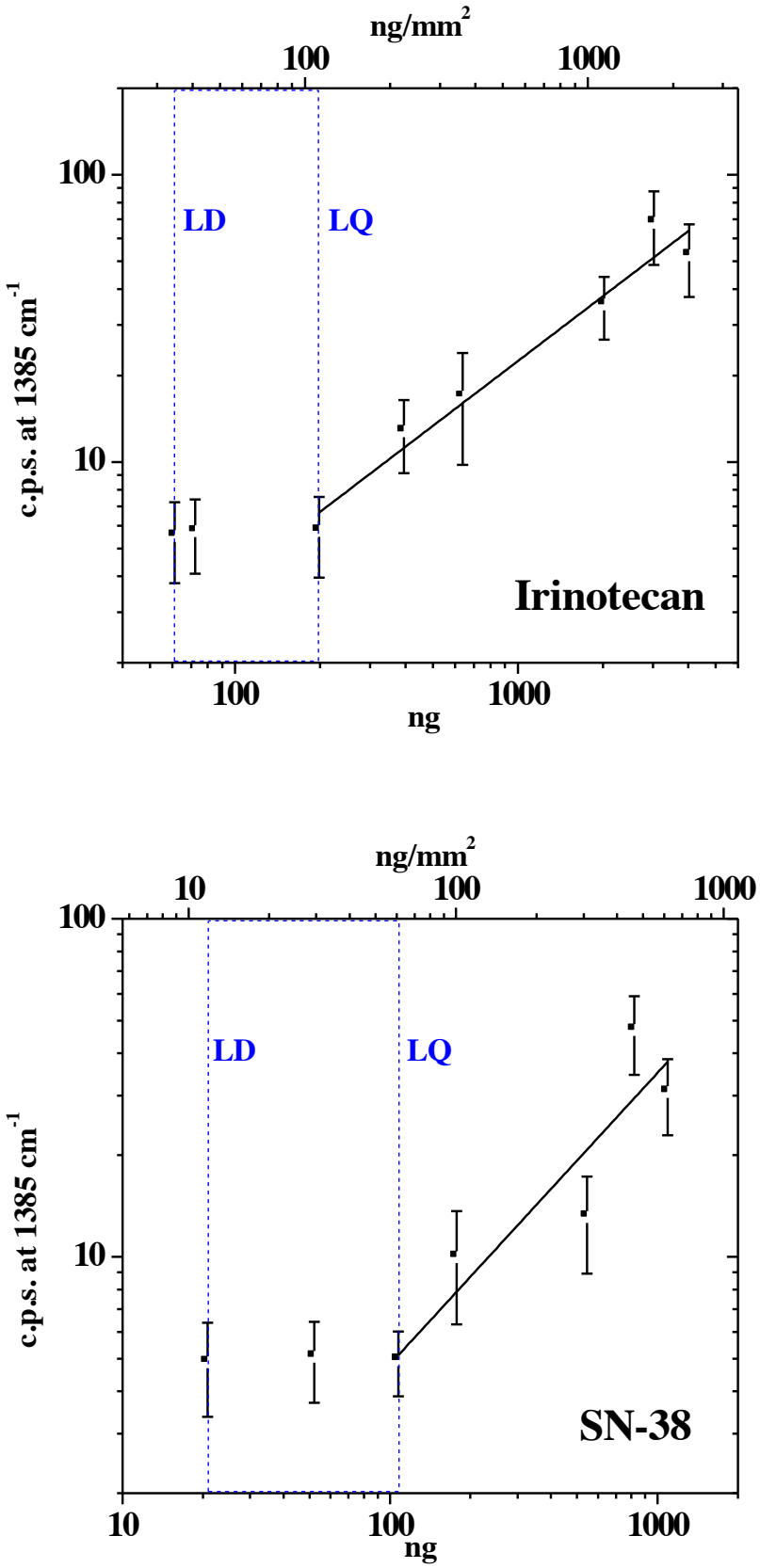

Figure 3.13: Calibration curves of SERS intensity as a function of deposited drug mass or mass to spotted surface ratio. The most characterizing Raman band is taken for each drug: 1322 cm^{-1} for Sunitinib, 1385 cm^{-1} for Irinotecan and SN-38. From Ref. 12.

We choose to express the total spotted mass, or the mass/area ratio, because SERS is a surface techniques and the active surface involved could be a more sensitive parameter than the bulk analyte quantity. This implies that LQ and LD can be improved by reducing the deposition area with the same analyte mass. For example, we used 6μL of solution over a 1.8 mm^2, but if you dry just 100 μL over 0.5 mm^2 one can increase the sensibility by a factor of 60.
In Table 3.6 the main results for Sunitinib, Irinotecan and SN-38 are shown.
The LQ for all the three drugs falls in the order of 10^2 pmol/mm^2. Despite the three analytes are different and have different SERS efficiency (this is reflected on the curve slopes), this effect could be explained by the fact that the largest amount of SERS signal comes from few structural features, called *hot-spots*. [13-15]
In the upper limit of the curves, we observed the saturation of the Raman intensity for 1-4·10^3 pmol/mm^2. This is probably related to the saturation of the hot spots.[13]

Table 3.6: Main results from the calibration curves of Sunitinib, Irinotecan and SN-38. From Ref. 12.

	Slope			Linearity range			Limit of Detection		
	c.p.s /ng	c.p.s. /(ng /mm^2)	c.p.s. /(nmol /mm^2)	ng	ng /mm^2	pmol /mm^2	ng	ng /mm^2	pmol /mm^2
Sunitinib	1.06 ±0.09	1.88 ±0.16	748 ±60	88 - 1872	50 - 1059	125 - 2657	18 - 26	11 - 15	26 - 37
Irinotecan	0.751 ±0.004	1.327 ±0.007	778 ±5	198 - 4032	112 - 2280	191 - 3886	60 - 70	34 - 40	58 - 68
SN-38	0.86 ±0.09	1.52 ±0.15	598 ±60	107 - 1092	60 - 620	153 - 1580	20 - 50	11 - 28	29 - 72

Taking into account the concentration levels required for clinical practice, about 32 ng/mL for Sunitinib, 25 ng/mL for Irinotecan and 6 ng/mL for SN-38, our actual measurement protocol will require the deposition of several millilitre of sample to reach the linearity regime.
Nevertheless, the scope of this study was to verify the feasibility of SERS as an analytical tool for therapeutic drug monitoring (TDM) with the aim of developing a point-of-care (POC) device.
Klarite substrates have the lower signal variability, but laser ablated AgNP showed more than three times higher SERS efficiency (see Figure 3.12). The optimization of AgNP based SERS substrates, mostly in term of structural homogeneity, could result in consistent analytical reproducibility improvement.
In conclusion, quantitative determination of anticancer drugs with SERS is an interesting open issue for the development of TDM-POC devices.

Speciation between Irinotecan and SN38 by PCA

Irinotecan has a complex metabolism that transforms it into the active SN-38, as just recalled above. Therefore, monitoring therapies involving Irinotecan cannot avoid the concomitant quantification of SN-38.
Raman spectroscopy and SERS, due to the fingerprint features provided by vibrational transitions, are usually a powerful qualitative techniques.[13] Nevertheless, Raman spectra of Irinotecan and SN-38 show very small differences, especially in the region between 1350 and 1650cm^{-1}, where the most intense bands are located.

In such a frequency region, vibrational transitions due to molecular structures with extended delocalized electrons occur.[63] In fact, comparing their molecular structure in Table 3.3, Irinotecan differs from SN-38 only in a non conjugate moiety.
We spotted 1μg of each solution, and the same amount of a mixture of Irinotecan and SN-38, over the active area of a Klarite substrate. Than we mapped the entire 4x4 mm^2 surface at a resolution of less than 100 μm between adjacent points (more than 1900 spectra acquired). As for the previous experiments, SERS spectra were collected with the 633 nm excitation.
The white-light photograph of the Klarite is reported in Figure 3.14a. By a macroscopic point of view, SN-38 dry as small crystals while Irinotecan as an amorphous deposit. The mixture solution presented both these characteristics.
The entire surface was mapped, but as a reference spectrum for each deposition, we took only the measurements at the centre of the three spots. The spectra obtained by the average of these points are shown in Figure 3.14c.

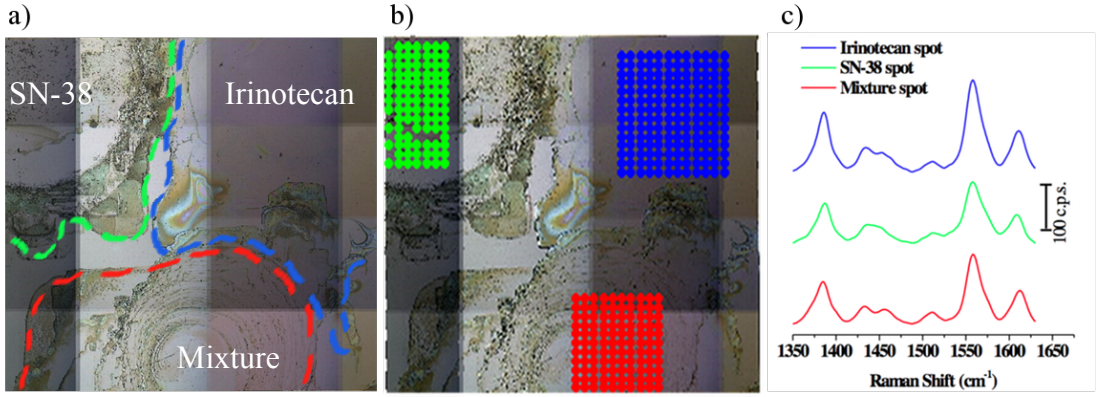

Figure 3.14: The optical microscope image of the drugs dried over the active surface of a Klarite substrate (a). The picture is collected mounting several snapshots with the instrument software. In (b) are shown the acquisition points used to obtain the average spectra of the pure drugs and mixture, in (c).

Distinguishing between Irinotecan, SN-38 and mixture simply by the spectra in Figure 3.14-c is not trivial, since the only slight difference, found with naked eye, is the double peak at 1450 cm^{-1}.
Principal Component Analysis (PCA) is a statistical analysis that takes into account all possible correlations between the variables describing a dataset of samples. In this case every spectra is a sample and every frequency is a variable. PCA computes such correlations, between intensities at every frequency along every spectra, considering them as describing the same kind of information.
In this way, the multivariate analysis is more sensitive to small differences in a dataset by quantitatively accounting for the Raman fingerprint.
PCA results in a set of mutually independent new variables called principal components (PCs). Every PC expresses a particular spectral feature redundant through the dataset in such a way that the firsts PCs represent the most recurring ones. As a result, every spectra has its own peculiar coefficient (called *PC's score*) for every PC.

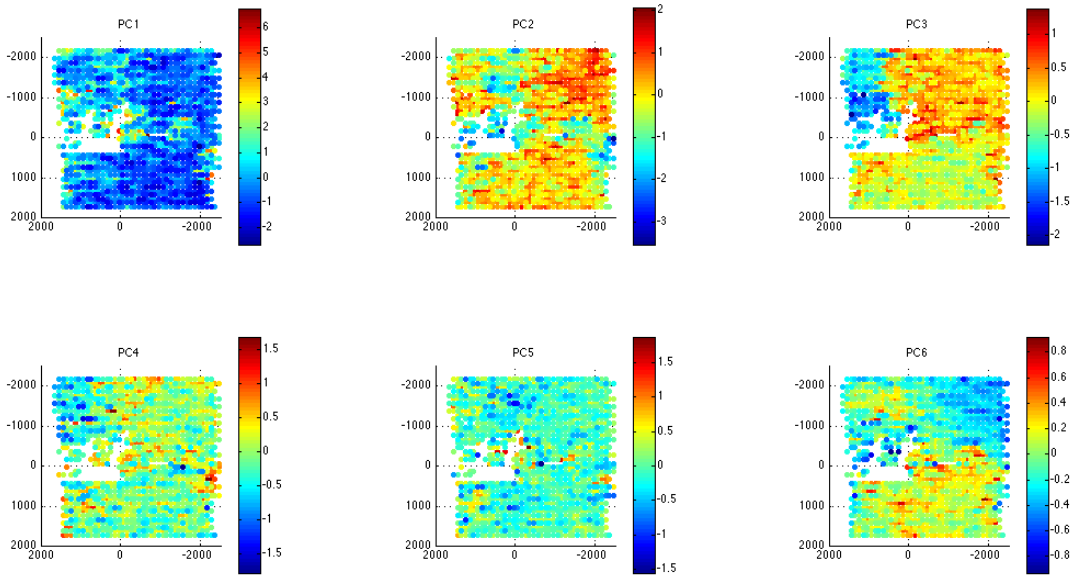

Figure 3.15: false colour maps of PC's scores for the first six principal components. Each point in the maps represents an acquisition point. Spectra with intensity lower than 100 c.p.s. were not considered, giving the empty holes. PC1, 2, 4, 5 and 6 do not provide differences between the three spots, but along PC3 the pure drugs assume opposite values. From Ref. 12.

The scores for PC 1, 2, 4, 5 and 6 of every spectra of the dataset have similar values for both Irinotecan, SN-38 and the mixture. These PCs only provides a good contrast between the deposition area and the free zone of the substrate (see Figure 3.15).
Instead, PC3 is a good distinctive element between the two drugs, as indicated by the opposite average score of 0.29±0.10 for Irinotecan and of -0.95±0.16 for SN-38 (see Table 3.7). In the mixture spot, as expected, the PC3's score assumes an intermediate value, close to zero at -0.10±0.08.

Table 3.7: The average PC's scores are calculated for the areas shown in Figure 3.14-b, giving numerical information for every spotted solution of pure drugs and mixture. From Ref. 12.

Principal Component	Variance Explained (%)	Irinotecan Mean Score (Zone 1)	SN-38 Mean Score (Zone 2)	Mixture Mean Score (Zone 3)
PC1	27.8	-0.50 ± 0.39	0.67 ± 0.66	-0.92 ± 0.25
PC2	10.5	0.67 ± 0.24	0.12 ± 0.27	0.23 ± 0.18
PC3	**4.5**	**0.29 ± 0.10**	**-0.95 ± 0.16**	**-0.10 ± 0.08**
PC4	3.1	0.03 ± 0.12	-0.43 ± 0.22	-0.12 ± 0.14
PC5	2.0	-0.03 ± 0.11	0.12 ± 0.18	-0.01 ± 0.11
PC6	1.2	-0.28 ± 0.06	-0.03 ± 0.09	0.15 ± 0.05

When the score map of PC3 is overlapped to the image of the substrate, there is a good contrast passing through each different spots (Figure 3.16).
Therefore, the PCA of SERS spectra can be used as a systematic and operator-independent approach for the discrimination of Irinotecan and its active metabolite SN-38.

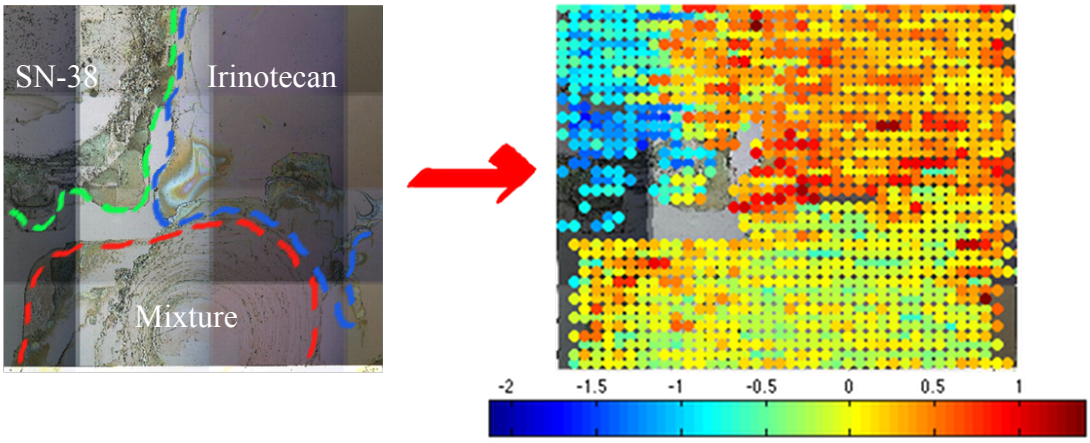

Figure 3.16: The PC3's score map overlapped to optical microscope image of the Klarite. The different score values well follow the boundaries between each spot. SN-38 assumes negative values for PC3, while Irinotecan has positive score and the mixture shows an intermediate value, close to zero.

Reactive SERS

The application of surface enhanced Raman scattering to the quantitative determination of small molecules, like drugs, was found very useful and effective. Portable Raman spectrometers can be purchased from several company and the time required for analysis is consistent with routinely applications.

Despite the potential of SERS based analysis to any substance, because of the vibrational nature of the Raman effect, in practise the range of allowed analytes is strongly limited by molecules with high Raman scattering cross section. This is particularly true approaching the low concentration regime.

For example, Nie and Emory published a study on the single-molecule detection with SERS.[17] They used silver nanoparticles excited at 514 nm. The probe molecule was Rhodamine 6G. Such a result is very impressive, but a crucial remark regards the Raman scattering cross section of Rhodamine 6G. When excited at 514 nm, the cross section of its most intense Raman band at 604 cm^{-1} is about 3 million times grater than the CO stretching vibration at 1020 cm^{-1} of methanol.[15]

To extend the potential of SERS, as a quantitative technique, to molecules with small Raman scattering efficiency, a new protocol was developed.

The idea is that of using gold nanoparticles functionalized with a molecule which can react with a specific functional group present in the target analyte. Therefore, a chemical reaction can occur at the surface of the gold nanoparticles, associated to a measurable variation of the SERS spectra of the original reagent, as schematically shown in Figure 3.17. We called this approach *Reactive-SERS*.

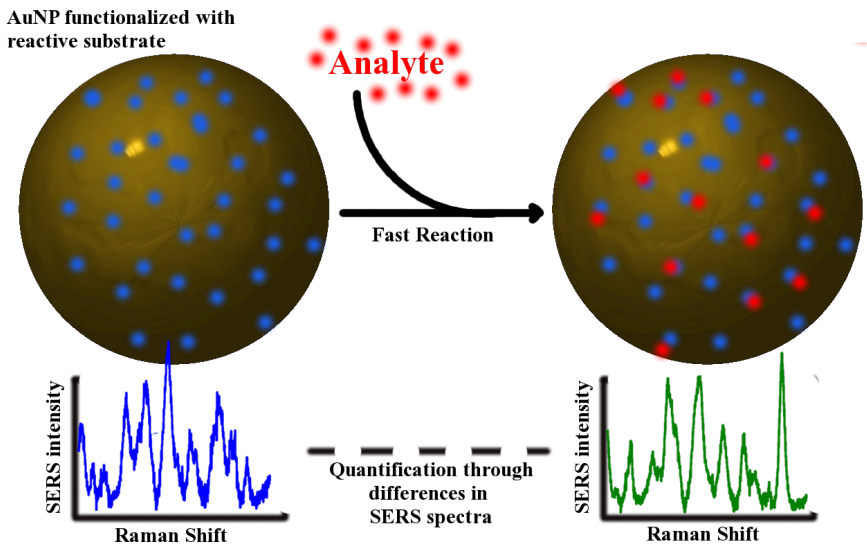

Figure 3.17: The key steps of the Reactive-SERS protocol. Gold nanoparticles are functionalized with a molecule which can react with the target analyte. The chemical reaction occurring between the reactive and the analyte vary the Raman spectra in a quantitative way.

The reactive substrate and the photoreaction involved

Bis[2-(4-azidosalicylamido)ethyl] disulphide (called $ASAES_2$, see Figure 3.18) is a commercially available reactive substrate used especially in biochemistry as cross linker.[64-66]

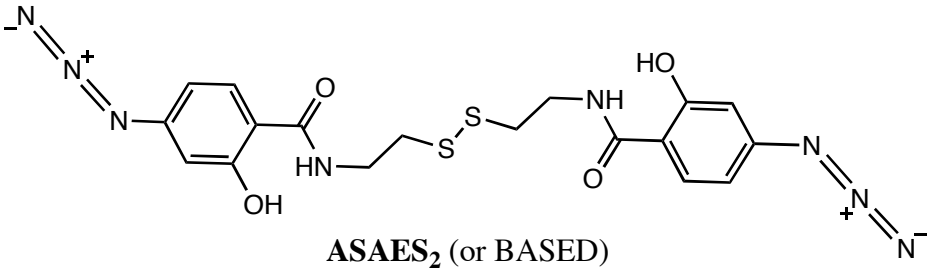

$ASAES_2$ (or BASED)
Bis[2-(4-azidosalicylamido)ethyl] disulfide
CAS: 199804-21-2

Figure 3.18: Molecular structure of Bis[2-(4-azidosalicylamido)ethyl] disulphide

It consists of two identical aromatic azide moieties linked by a sulphur bridge.
Since the synthesis of the first organic azide, phenyl azide, by Peter Grieß in 1864, this functional group found a great attention and several field of applications.[66-68]
Many azide containing compounds are instable because of the possible release of molecular nitrogen, occurring also in explosive reactions.[68]
The resonance structures reported in Figure 3.19 help to understand why the nitrogen release is favoured. These resonances structures also provide information about the chemistry of the azide. In fact electrophiles usually attack the first nitrogen atom, the closest to the *R* group in Figure 3.19, while nucleophiles go to the third nitrogen.[68]

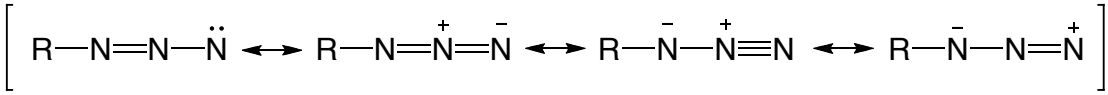

Figure 3.19: Limit resonance structures for the azide group. The release of molecular nitrogen leaves the electron deficient group R-N: .

The most popular reaction involving azides is the Huisgen cycloaddiction, that, in its classical form, takes place with an alkyne. More discussions regarding the Huisgen reaction could be found in Chapter 5.
In *Reactive-SERS* we are interested into the photochemistry of the aromatic azide group.
Upon high temperature or irradiation into the near UV region (typically under 400 nm), the release of molecular nitrogen occurs, leaving a singlet nitrogen atom.[67-70]
In Figure 3.20 are summarized the principal structural pattern that phenyl azide follows after UV irradiation, as currently accepted by the literature.[67, 70]

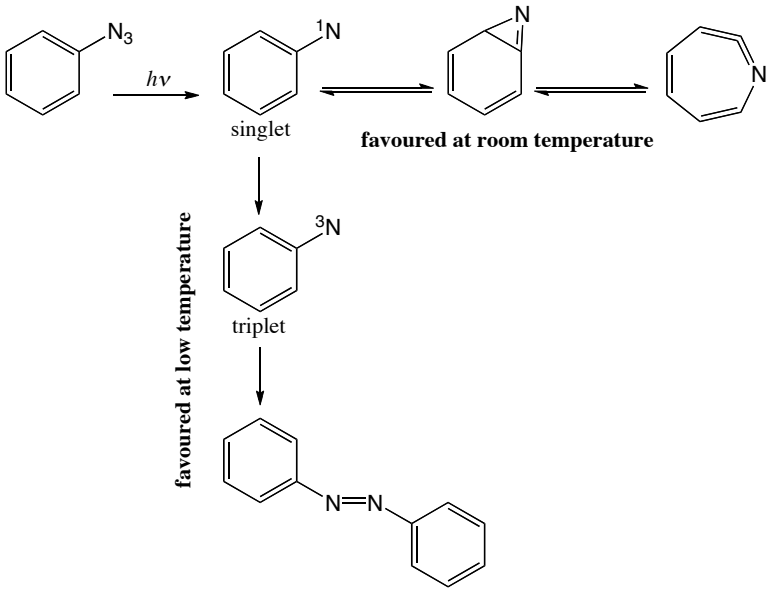

Figure 3.20: The dynamic of phenyl azide after UV irradiation.

It was found that the photochemistry of phenyl azide in solution is temperature dependent. At ambient temperature the singlet phenylnitrene undergoes rearrangement to the cyclic ketenimine. At temperature below 180 K the *inter system crossing* (ISC) drives the molecule to triplet state of phenylnitrene and the coupling with another triplet phenylnitrene, or an unreacted phenyl azide, yield preferentially di-azo compounds.[67]
All of these derivatives of the phenyl nitrene were found reactive toward insertion into multiple bonds, intramolecular cyclization and addition to heteroatom like phosphorous, sulphur and nitrogen.[67, 68, 70]
Polar solvents enhance the reaction rate of orto-azidophenol,[69] while para-azidophenol transforms preferentially to para-aminophenol using acetonitrile instead of water.[71]
In biochemistry, $ASAES_2$ is found useful as photoactivate coupling agent, due to the reactivity of the aromatic azide toward amines. This cross-linkage could eventually be cleaved by the reduction of the sulphur bridge.[64-66]
To test the chemistry of $ASAES_2$ we used diethylamine (DEA) in acetonitrile.[67, 68, 70]

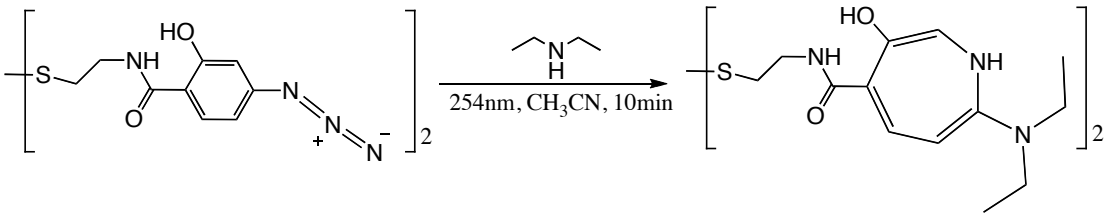

Figure 3.21: The reaction scheme of the photoreaction of $ASAES_2$ with diethylamine.

Three reaction mixtures were prepared according to Table 3.8. The reaction mixture *A* was used as reference whereas the reaction *B* and *C* were in double excess of $ASAES_2$ and in stoichiometric amount, respectively.

Table 3.8: The proportions between $ASAES_2$ and DEA tested in photoreactions with acetonitrile as solvent.

	$ASAES_2$ (mM)	DEA (mM)	Molar ratio (mol_{DEA} / mol_{ASAES2})
A	3.15	-	0
B	3.15	4.32	0.5
C	3.15	8.65	1.1

All the reagents were dissolved in acetonitrile. The photoreaction was activated under irradiation with a common UV lamp for 10 minutes.
The reaction products were than characterized by MALDI-TOF mass spectrometry (see Figure 3.22).

Table 3.9: Molecular structure and mass assignment for the reaction products between $ASAES_2$ and DEA.

	Calculated mass peaks
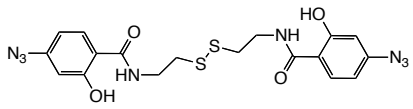	$ASAES_2$ = 474.09 Da $[M+H]^+$ = 475 *m/z* $[M+Na]^+$ = 497 *m/z* $[M+K]^+$ = 513 *m/z*
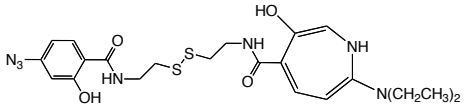	mono-adduct = 519.17 Da $[M+H]^+$ = 520 *m/z* $[M+Na]^+$ = 542 *m/z* $[M+K]^+$ = 558 *m/z*
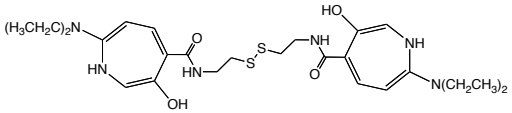	di-adduct = 564.26 Da $[M+H]^+$ = 565 *m/z* $[M+Na]^+$ = 587 *m/z* $[M+K]^+$ = 603 *m/z*

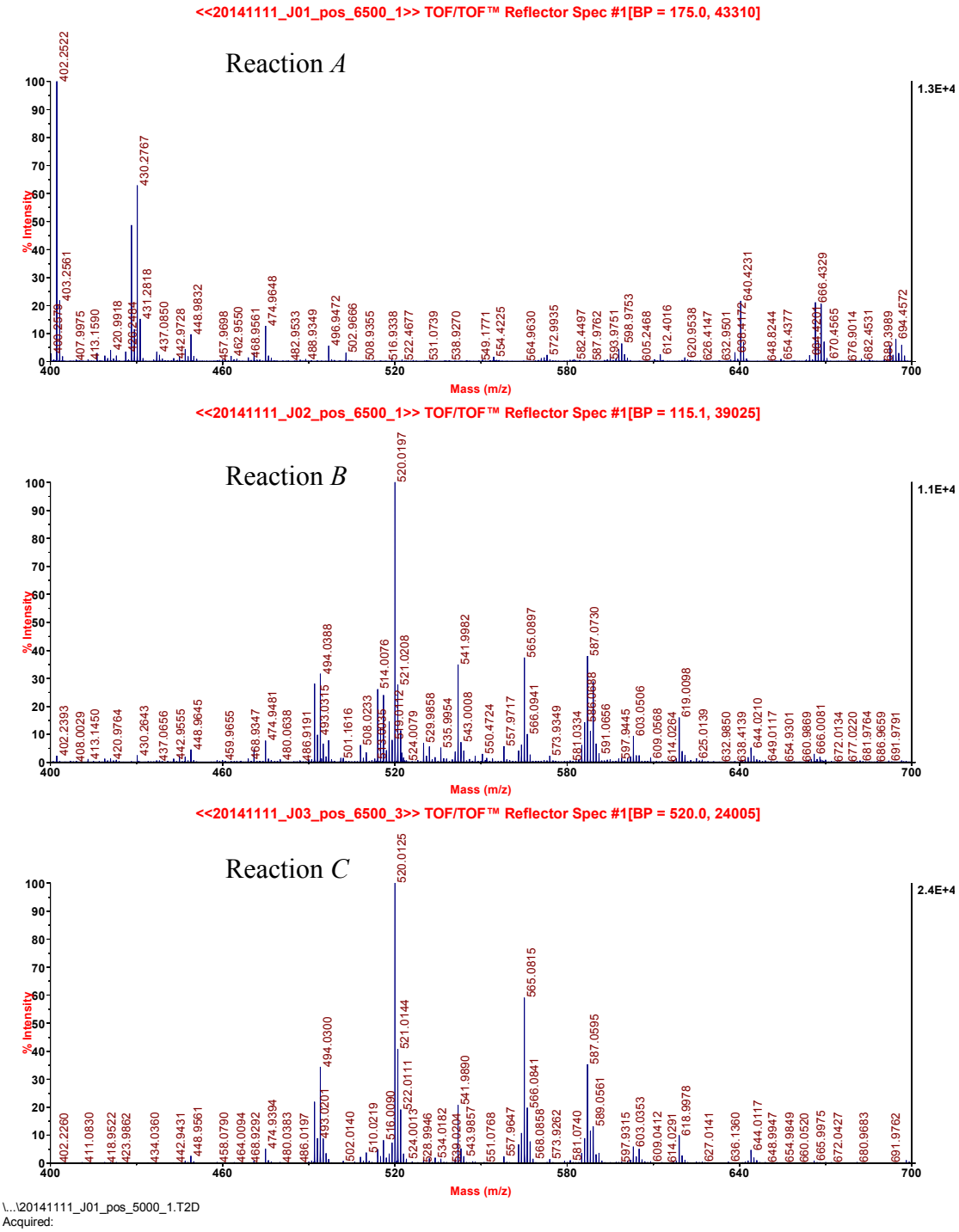

Figure 3.22: MALDI-TOF spectra of the reaction between $ASAES_2$ and DEA. The matrix used was DHAP+TFA 0.1%.

Peaks present for the reaction mixture *A* show the products without the presence of DEA. The mass spectra of reaction *B* and *C* show intense signals related to the mono and the bis-adduct. The mono-adduct $[M+H]^+$ is observed at mass 494.0 *m/z*, whereas $[M+Na]^+$ at 520.0 *m/z* both for reaction *B* and *C*. The bis-adduct has its $[M+H]^+$ and $[M+Na]^+$ peaks at 565.0 and 587.0 *m/z* are also observed both for reaction *B* and *C*.
The mass spectra of reaction *C* still shows a consistent abundance of the mono-adduct The reaction showed, therefore, to be effective within few minutes of irradiation using a common UV lamp.

Stability of $ASAES_2$ toward reduction

The scheme of *Reactive SERS* needs the reactive molecule bound to the nanoparticles surface.

However, using $ASAES_2$ as reactive substrate, it is not possible to reduce the disulphide to obtain a thiol which is highly reactive with AuNP, since almost every reducing agent reduces also the azide group. This was observed with molecular hydrogen, hydrides as $NaBH_4$, other thiols as dithiothreitol (DTT) and phosphine groups. [64, 68, 72]

For this reason, the scheme was adjusted, as reported in Figure 3.23. The first step is the photoreaction, as in the precedent paragraph. The second step is the reduction of both the disulphide bond, and the unreacted azides, with the tris-(2-carboxyethyl) phosphine (TCEP). The final step is the reaction of the thiols with the gold nanoparticles surface.

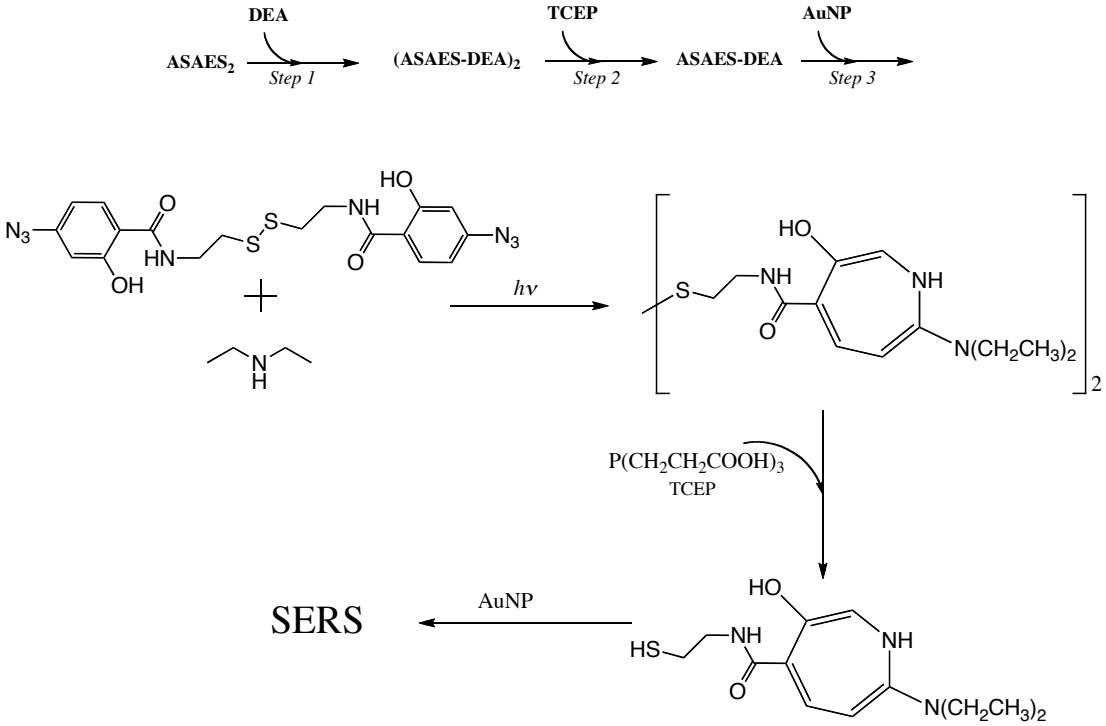

Figure 3.23: The Reactive SERS protocol adapted for $ASAES_2$

The use of TCEP, instead of other soft reducing agents such as DTT for example, allow the entire protocol to be made in a single batch and without any purification. During the synthesis all thiols are added and the gold nanoparticles can be mixed directly with the crude reaction mixture.

TCEP is a well known reducing agent for disulphide bonds[64, 72] and the reaction with an azide group is known as Staudinger reaction.[68]

The mechanism involved in reduction of azides by phosphines starts from the addiction of the azide to the phosphor atom. Than molecular nitrogen is released and the phosphine is oxidized in presence of water.

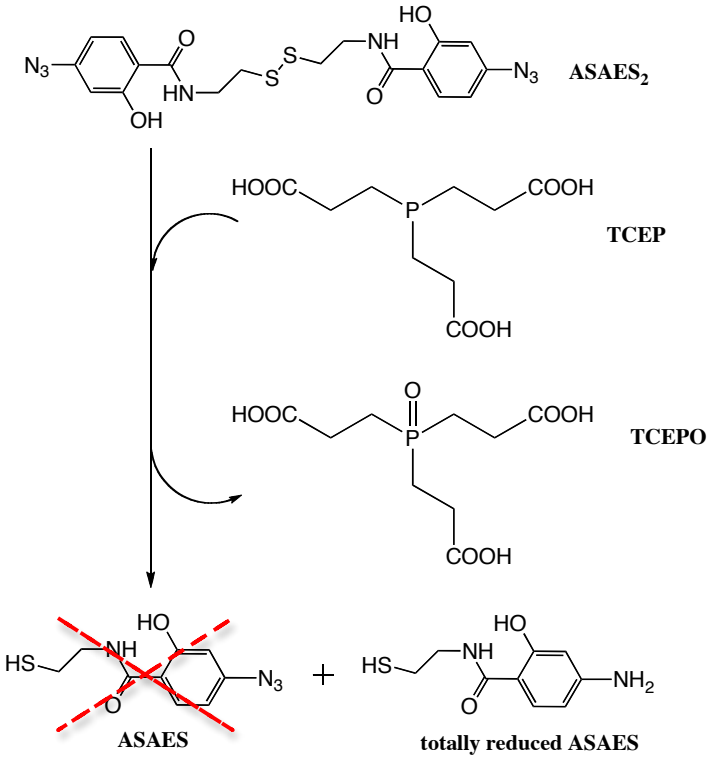

Figure 3.24: The mechanism involved in Staudinger reaction.
Adapted from Ref. 68.

We tested the reduction of $ASAES_2$ with TCEP with different excess of reagents. We used the proportion of TCEP:$ASES_2$ of 1:20, 1:1 and 10:1. The solvent used was acetonitrile. The reaction was carried out at ambient temperature under mechanical agitation for 1 hour. Then, the reaction mixtures were analysed by MALDI-TOF mass spectrometry.

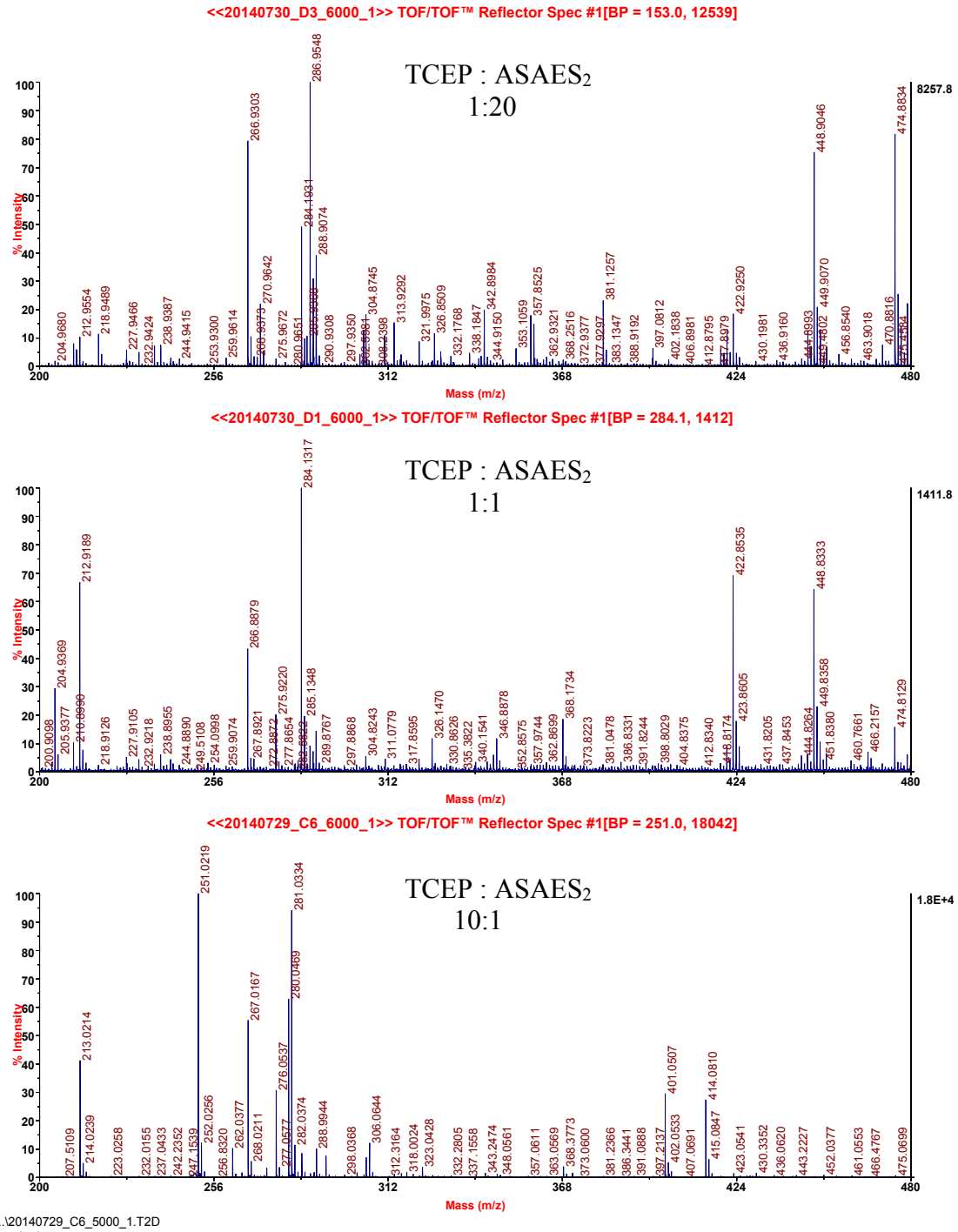

Figure 3.25: MALDI-TOF analysis of the reaction between TCEP and ASAES$_2$. The matrix used was DHAP+TFA 0.1%.

Table 3.10: Molecular structures and attribution of the MALDI-TOF in Figure 3.25.

	Calculated mass peaks
$ASAES_2$	M = 474.09 Da $[M+H]^+$ = 475 *m/z* $[M+Na]^+$ = 497 *m/z* $[M+K]^+$ = 513 *m/z*
TCEP	M = 250.06 Da $[M+H]^+$ = 251 *m/z* $[M+Na]^+$ = 273 *m/z* $[M+K]^+$ = 289 *m/z*
TCEPO	M = 266.06 Da $[M+H]^+$ = 267 *m/z* $[M+Na]^+$ = 289 *m/z* $[M+K]^+$ = 305 *m/z*
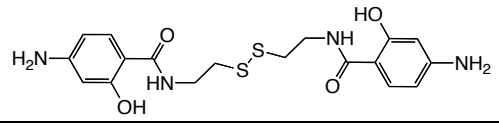	M = 422.11 Da $[M+H]^+$ = 423 *m/z* $[M+Na]^+$ = 445 *m/z* $[M+K]^+$ = 461 *m/z*
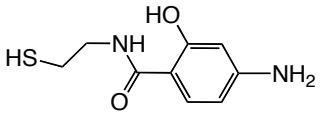	M = 212.06 Da $[M+H]^+$ = 213 *m/z* $[M+Na]^+$ = 236 *m/z* $[M+K]^+$ = 251 *m/z*
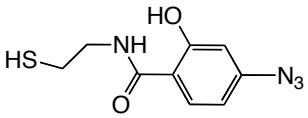	M = 238.05 Da $[M+H]^+$ = 239 *m/z* $[M+Na]^+$ = 261 *m/z* $[M+K]^+$ = 277 *m/z*

At the highest dilution of TCEP (1:20), the reduction occurs slightly, nevertheless the peaks of the reduced azide at 422.9 and 448.9 *m/z* are present, while any signals referred to ASAES were found. For the stoichiometric reaction (1:1) both the feature of the reduced azide in $ASAES_2$ and in ASAES are present. In the mass spectra of the reaction with an excess of TCEP (10:1) only complete reduction occurs and the only peaks found are from the reduced ASAES.
These results also show a preferential reduction of the azide group before that of the disulphide group.

Quantification of DEA with Reactive-SERS as a proof of principle

As a proof of principle, we used the entire protocol reported in Figure 3.23 for the three solutions of Table 3.8, namely for the reaction of diethylamine (DEA) with $ASAES_2$.
After the reduction of the three solution with TCEP, gold nanoparticles were added to the reaction mixtures. The thiolated ASAES and ASAES-DEA are expected to bound preferentially to the nanoparticles surface, due to the strong reaction of thiols with gold.
The functionalized AuNPs were purified by centrifugation and the SERS spectra were acquired with the 633 nm excitation. We normalized the SERS spectra to the band at 1460 cm^{-1} for a quantitative evaluation.
The results reported in Figure 3.26a, show that the band at 1325cm^{-1} is sensible to the amount of DEA and its intensity results to be linearly correlated to the initial concentration of DEA (see Figure 3.26b) and, therefore, although an assignment of all the bands was not obtained, to the concentration of the molecular adduct ASAES-DEA.

These results show the possibility of obtaining the concentration of a molecule like DEA, which does not show a SERS spectrum, by using its reaction with a molecule which change its SERS spectrum after the reaction. The scheme, which is shown here for a molecule with an amine group can be clearly extended to other molecules with other groups provided the identification of a Reactive-SERS molecule which reacts with these groups. The scheme can be therefore useful also for the quantification of paclitaxel when the appropriate Reactive-SERS molecule is found.

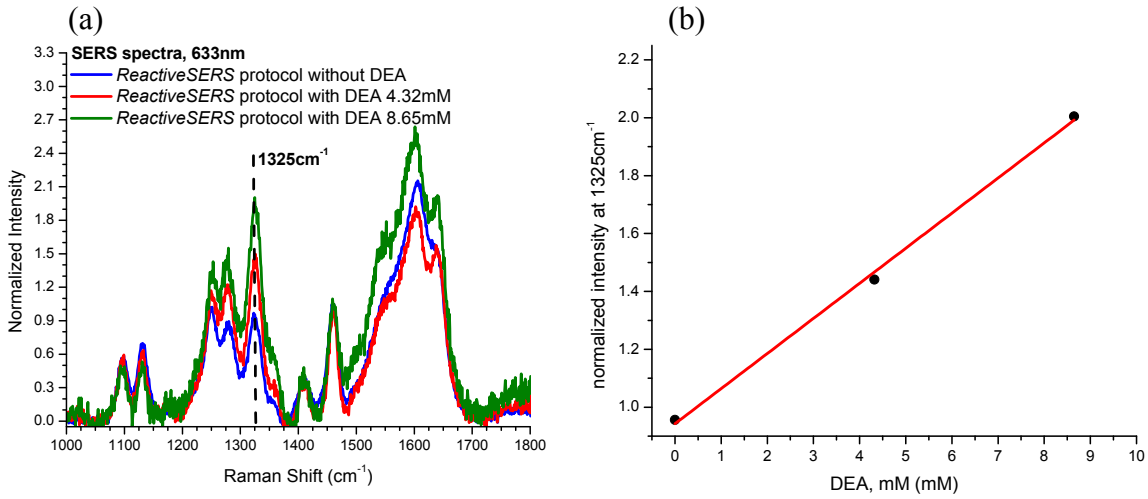

Figure 3.26: On the left, the SERS spectra acquired over AuNP surface for the ReactiveSERS protocol at different amount of DEA, the spectra were normalized at the band at 1460 cm^{-1}. On the right, the normalized intensity of the band at 1325 cm^{-1} well follow the increment of DEA concentration through the three reaction studied.

4. Advanced Diagnostic Tools, part 1

In the introduction chapter the so called *Circulating Tumour Cells* (CTCs) were recalled as emerging powerful cancer diagnostic signals. These cells originate from tumours even at their early growing stages. Their counting and their phenotypization are technological and clinical challenges, because CTCs, at early tumour stages, are present in blood only in very low amount.

Immunological analytical protocols, coupled with surface enhanced Raman scattering as detection technique, were recently shown to give impressive results in this field.[47, 73] Despite various strategies and nanotechnological architectures that could be adopted, the main features of a useful nanostructure, which must be functionalized with a targeting units, like an antibody, are water solubility and presence of strong SERS signals.[47, 73, 74] Such a nanosytems show specific interactions with antigens usually present on the cell membrane.[47, 73, 74] Therefore, recording SERS spectra of each cell, with a conventional micro-Raman instrument, one identifies the presence of an antigen when the SERS spectrum of the reporter, present in the nanostructure, is observed.

A relevant advantage provided by the SERS spectra is *multiplexing,* namely the simultaneously detection of multiple analytes with a limited spectral detection window. For example, the simultaneous detection of two different nanosystems, coupled with each own targeting moiety and Raman reporter, required an optical window of only 92 nm using 633 nm as excitation wavelength.[74] This is because Raman spectroscopy is a vibrational technique, so different molecules could be recognised by their fingerprint signals, that usually stay between zero and 2000 cm^{-1}. It results into an optical window of 52, 92 and 146 nm, exciting respectively at 488, 633 or 785 nm. However, much smaller spectral windows are usually needed because vibrational bands show widths of the order of 1 nm or less. If compared to fluorescence, SERS provides a superior and trustfully chemical attributions into a smaller wavelength range and with comparable signal intensities.[13-15, 17]

AuNP, synthetized by laser ablation in solution, were used as SERS substrate for the synthesis of two different SERS-tags, sensitive to different prostate cancer antigens. [74] Antibodies specific for PSMA (prostate specific membrane antigen) and PSCA (prostate stem cell antigen) were used for the two different nanostructures. We used these two dyes as SERS reporters, TR-SH (Texas-Red functionalized with a thiol function) and MG-SH (Malachite Green functionalized with a thiol function). They were chosen because of their absorption band near the 633 nm excitation wavelength, where also the surface plasmon resonance of AuNPs is present. To guarantee better enhancement performances, AuNP were first aggregated by a centrifugation. This operation has the double effect of generating a localised surface plasmon resonance in the near infrared and to produce a nanostructure, rich in nanoparticles junctions where the incident electromagnetic field is strongly enhanced (*hot spots*). TR-SH was associated to the nanostructure with the anti-PSMA antibody and MG-SH for the nanostructure with the anti-PSCA antibody.

We used these nanostructures in cancer cell antigen detection. Four different cell types were used, two expressing only one of the two selected antigens, PSMA and PSCA, one expressing both and one expressing none of them.

Every cell culture was fixed and treated with a mixture of both SERS-nanostructures,. After incubation, cells were washed with PBS solution and micro-Raman measurements were obtained for each cell.

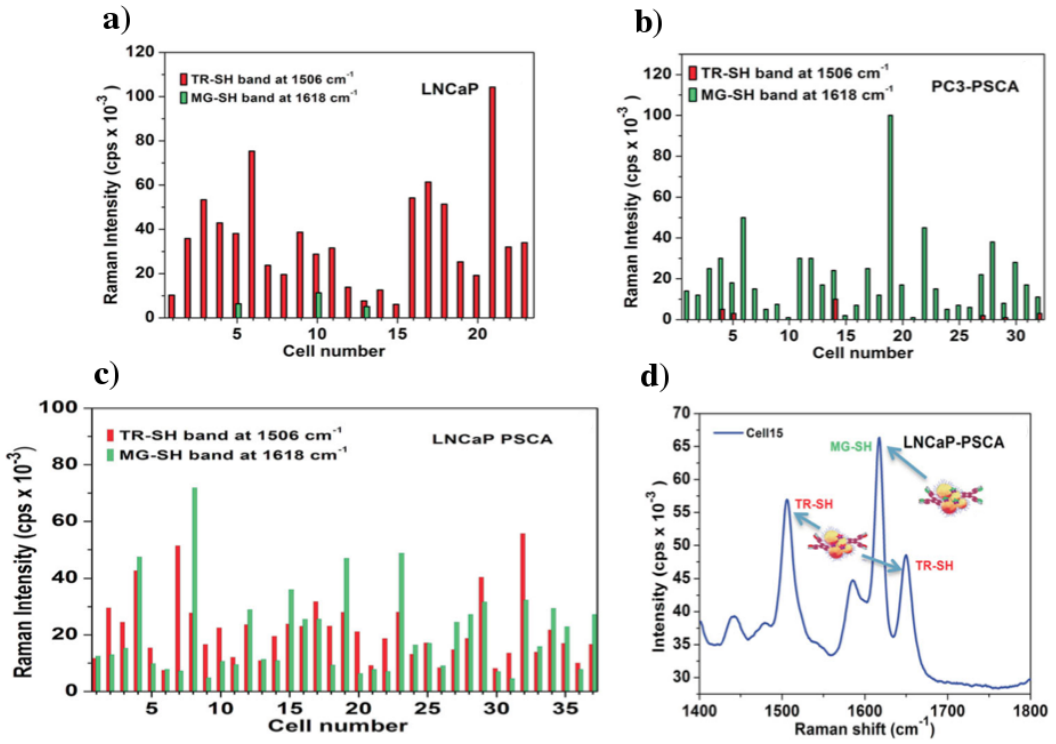

Figure 4.1: a) LNCap cells show preferential interaction with TR-SH SERS-tag, meaning that they express the associated PSMA antigen. In b) PC3-PSCA cells act in the same way, but with the PSCA antigen, reflecting in high MG-SH signals. In c) both the Raman reporters were present, since cells express both the antigens. In d) a representative Raman spectrum, from the cell number 15 in c), shows both the bands associated to TR-SH and MG-SH (multiplexing). From Ref. 74.

Although all the cells were incubated with both nanostructures, the cells expressing PSMA (LNCaP in Figure 4.1a) correctly showed the SERS bands of TR-SH, which was present in the nanostructure functionalized with the anti-PSMA antibody. In the case of PC3-PSCA cells, expressing PSCA (Figure 4.1b), the SERS signals were those of MG-SH, because of the antibody for PSCA and MG-SH were associated together. The almost equivalent abundance of the two SERS signals in LNCaP-PSCA cells showed the presence of both antigens on the cell membrane, as expected. The fourth cell culture (not shown), not expressing any of the two antigens, showed very small signals only in few cases.
The ability to perform multiplexing analysis at cellular level was, therefore, fully verified, but the number of analytes observed in the SERS spectra can be greatly enhanced adding more different SERS-tags.
A library of new SERS tags is therefore important.

Raman active dyes library

In the following, new dyes were selected and modified to become optimized Raman reporters for SERS multiplexing analysis using AuNP. These molecules show the following characteristics:

- at least one thiol moiety is present for a covalent binding to AuNP, which allows to obtain a stable structure also in an aggressive environment like a biological environment;
- the optical absorption has to be in resonance, or preresonance, with the excitation wavelengths used for the registration of the SERS spectra, namely 633 nm or 785 nm;
- the SERS spectrum shows few sharp intense bands, different from those of other SERS-tags for multiplexing analysis;
- soluble in water because this is the solvent of election for biological samples.

The two dyes used for the above recalled work were TR-SH and MG-SH (Figure 4.2), optimized for 633 nm excitation wavelength.

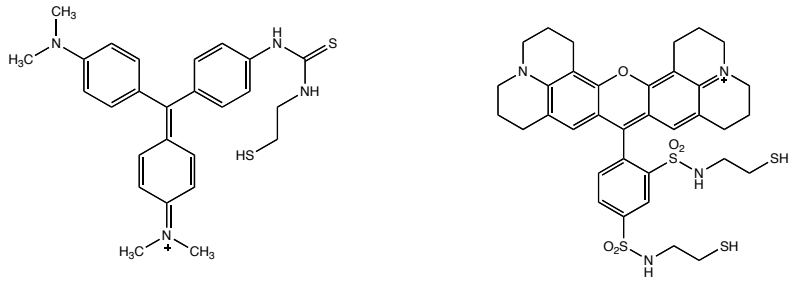

MG-SH
Cysteamine functionalized Malachite Green

TR-SH
Cysteamine functionalized Texas Red

Figure 4.2: molecular structures of the two Raman reporters just present in our dye library.

Part of my work was that of functionalizing three new Raman reporters. While one of them was found good for both 633 and 785 nm excitations, the other two were found to be best performer only at 785 nm.
The experimental procedures are reported in Appendix A7.

Lipoic Nile Blue

Nile Blue A (NB) is an aromatic dye used in photodynamic therapy.[75] It is also a SERS active dye over silver electrode when excited at 488nm.[76]
The molecule was conjugated with a lipoic acid according to the reaction scheme reported by Ho et al.[77], and reported in Figure 4.3.

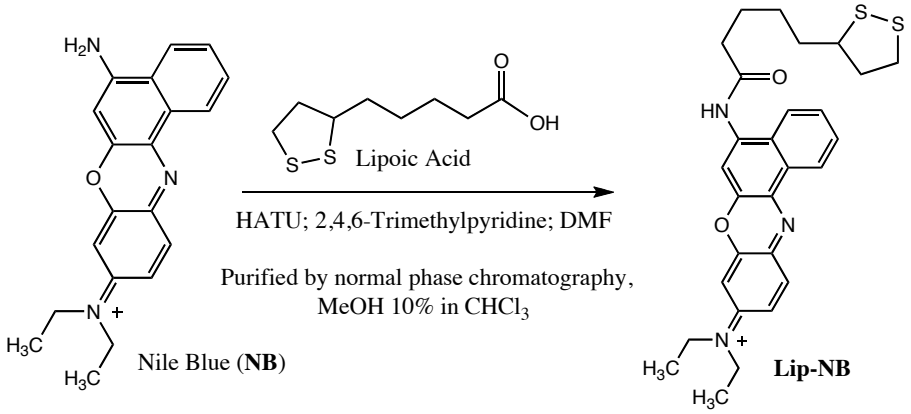

Figure 4.3: the reaction scheme for the conjugation of Nile Blue A with Lipoic Acid.

The mixture was purified by phase chromatography and characterized by ESI-TOF.
The absorption pattern of LipNB, seemingly to NB, is sensitive to environment polarity and acidity.[77, 78] The absorption spectrum of LipNB in acetonitrile is show in Figure 4.4.

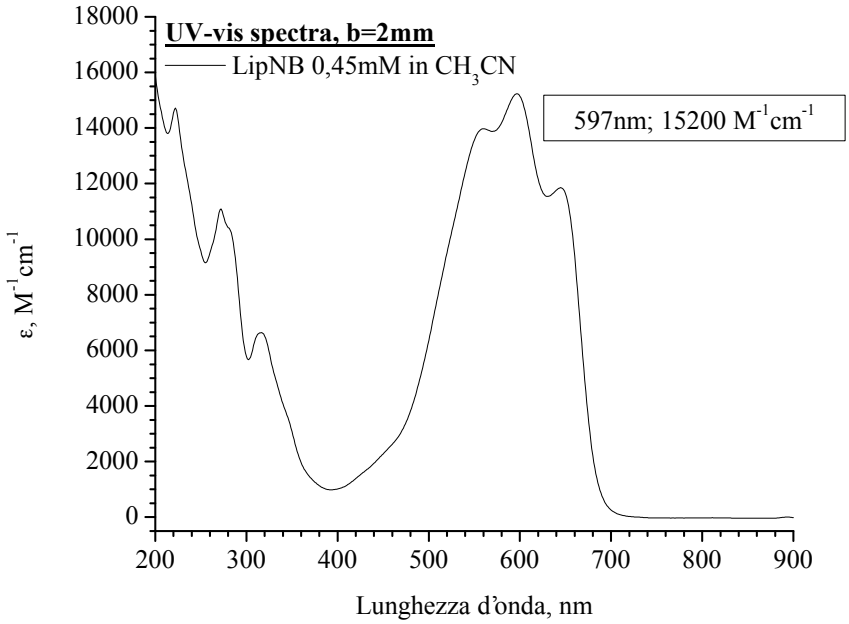

Figure 4.4: UV-vis-NIR molar extinction coefficient for LipNB in acetonitrile.

To test its efficiency for SERS, AuNP were functionalized with LipNB and purified with centrifugation.
In Figure 4.5 the same solution of LipNB 1.12 μM in water was analysed with Raman spectroscopy before and after the addition of AuNPs. The analysis of supernatant, obtained by the nanoparticles purification steps, shows that LipNB was quantitatively

linked to AuNPs. While fluorescence dominates the spectra of free LipNB in solution, intense and sharp Raman peaks rise after the conjugation with plasmonic gold nanoparticles.

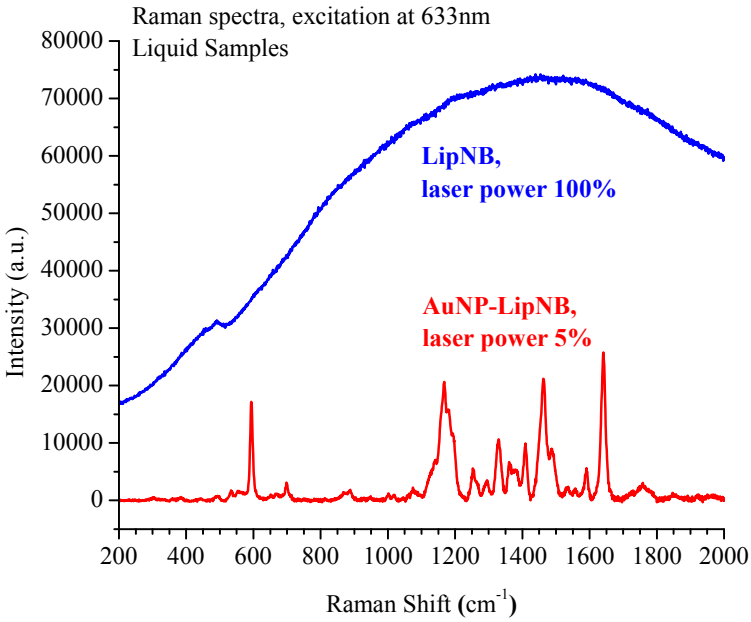

Figure 4.5: A solution of LipNB before and after gold nanoparticles are added. The SERS effect quenches the fluorescence and increases the Raman signals.

The same experiment with AuNP, but carried out with NB, show consistent spectra differences if compared to AuNP-LipNB, especially in the 1100-1600 cm^{-1} region (see Figure 4.6), where bands related to amines and amides are found.[76]

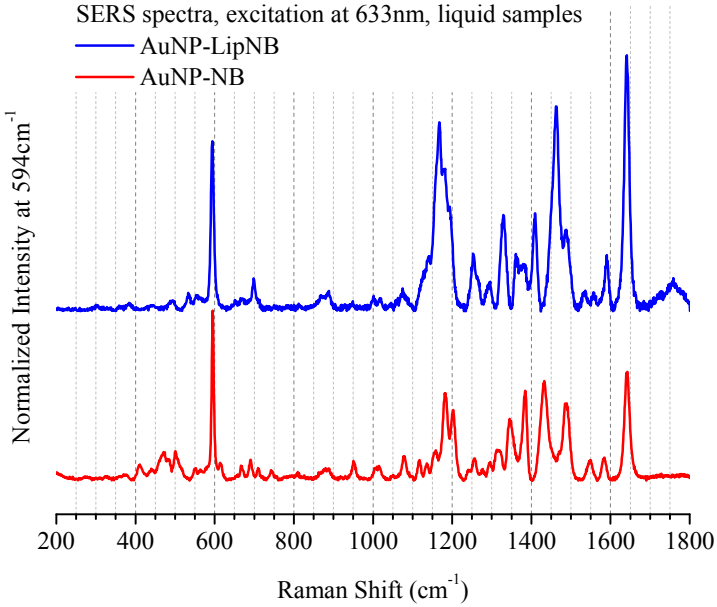

Figure 4.6: SERS spectra of gold nanoparticles functionalized with NB or LipNB. The intensities are normalized to the peak at 594 cm^{-1}. Great differences are evident especially in the 1100-1600cm^{-1} region.

The stability of LipNB vs pH was also studied to exclude the release of the dye at extreme acid or basic conditions. We modified the pH solutions of a LiNB with HCl or NaOH from pH 1 to pH 10. The same overall intensity pattern was found at all pH, showing the stability of the molecule. Some small changes were only observed at pH higher than 7, as shown in Figure 4.7, in particular for the bands at 1184, 1382, 1490 cm^{-1}. The results are in good agreement with those previously reported by Ni et al. for NB on silver electrode excited at 488 nm.[76]

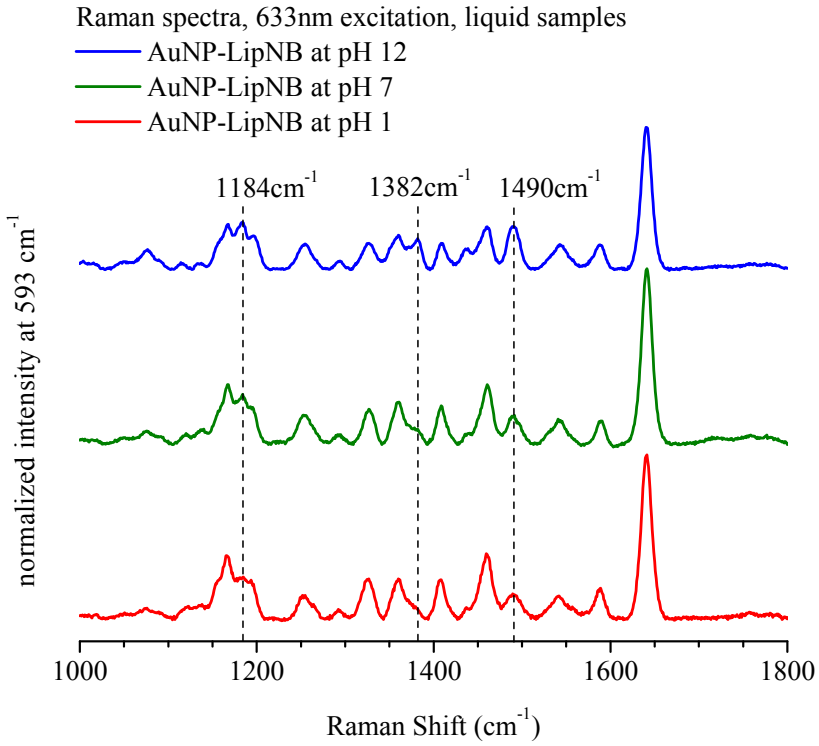

Figure 4.7: Raman spectra of the same solution of AuNP-LipNB at different pH show the sensitivity of this dye to the environment acidity.

Thiolated Cyanine-7

In the field of infrared optical probes, cyanine-7 dyes plays an important role. Moreover, some interesting recent studies show their applications also as SERS-tags for *in vivo*[79, 80] and *in vitro*[81] detection of cancer cells.
The commercially available IR783 was found to react with thiols.[82] According to the reaction scheme of Figure 4.8, the thiol derivative (Cy7SH) was obtained in stoichiometric amount of dithiothreitol (DTT) in dichloromethane (DCM) and in presence of tri-ethylamine (TEA).

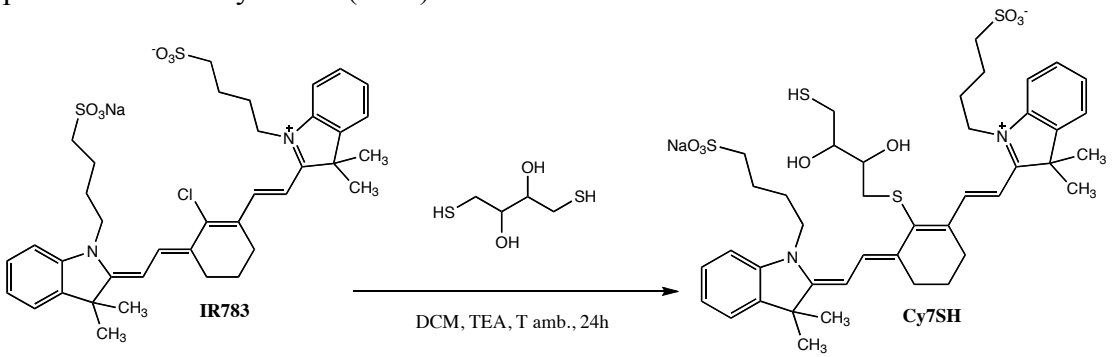

Figure 4.8: The reaction scheme between IR783 and dithiothreitol to produce Cy7SH dye.

The reaction was purified by liquid phase extraction and the product crystallized in saturated NaCl aqueous solution.
A little amount of the dark green solid was dissolved in methanol and characterized by MALDI-TOF mass spectrometry.

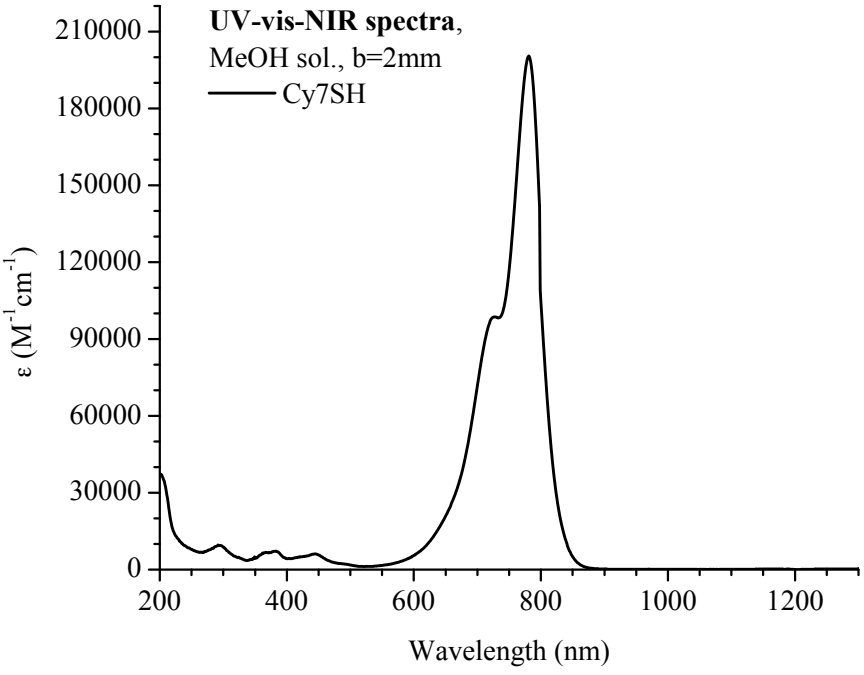

Figure 4.9: UV-vis-NIR molar extinction cross section of Cy7SH in methanol.

The absorption behaviour of Cy7SH shows that a resonance condition occurs with the 785 nm laser line.
The SERS spectra excited at 785nm , is shown in Figure 4.10.

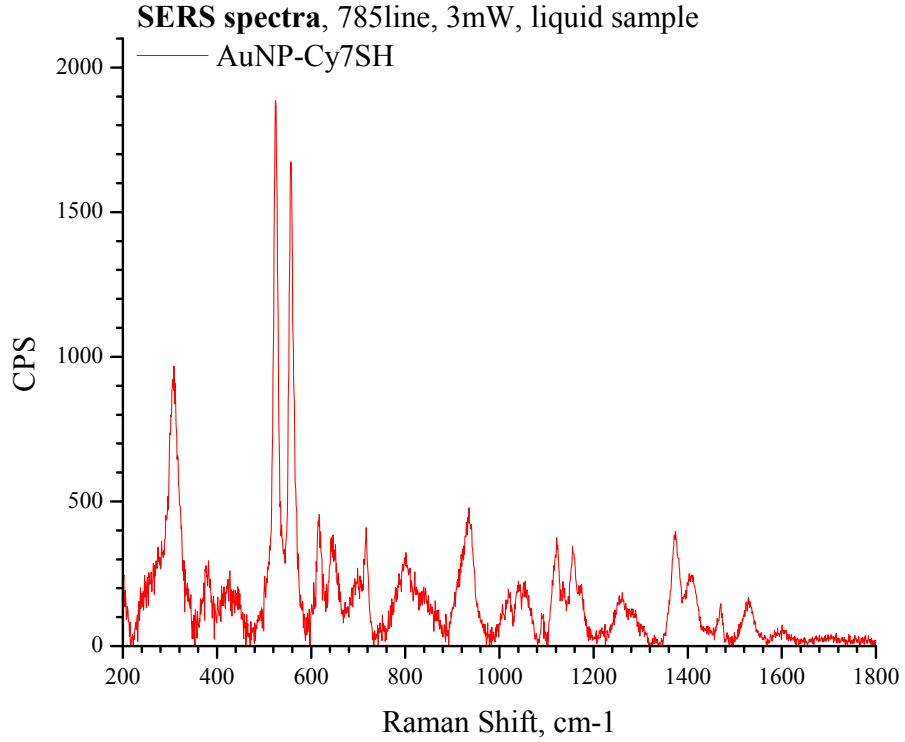

Figure 4.10: SERS spectra at 785nm excitation of AuNP-Cy7SH dispersed in aqueous solution at nanomolar concentration.

The two intense peaks between 500 and 600 cm^{-1} are the characteristic SERS signature of this dye.

Dithiolated Si-Naphthalocyanine

Phthalocyanine and Naphthalocyanine are highly conjugated macrocyclics showing interesting optical properties widely explored in photodynamic therapies and electron or energy transfer.[83, 84]

Li et al. reported that Si-phthalocyanine chloride undergo easily axial substitution with nucleophiles, especially with alkoxide ligands.[85] Moreover, they reported that mercaptoethanol preferentially links to silicon through oxygen instead of sulphur, and that these axial thiol-functionalized phthalocyanines form well-oriented self-assembled monolayers on gold surfaces.[85] Following this suggestions Si-naphthalocyanine di-chloride ($NPCyCl_2$) was used for obtaining the bis-thiol derivative $NPCy(SH)_2$ (briefly reported also as NPCySH) as reported in Figure 4.11.

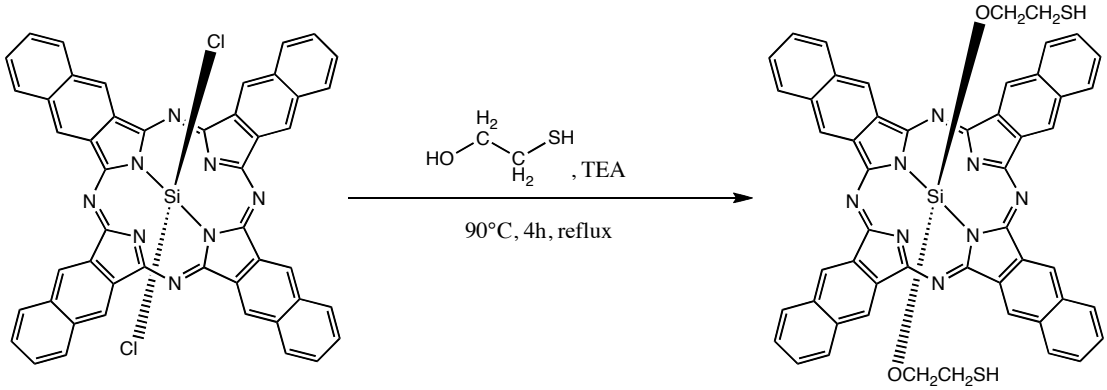

$NPCyCl_2$ **$NPCy(SH)_2$**

Figure 4.11: The synthetic route used to functionalize $NPCyCl_2$.

The product was characterized by MALDI-TOF mass spectrometry. In Figure 4.12 the UV-vis-NIR absorption spectra of $NPCy(SH)_2$ is shown.

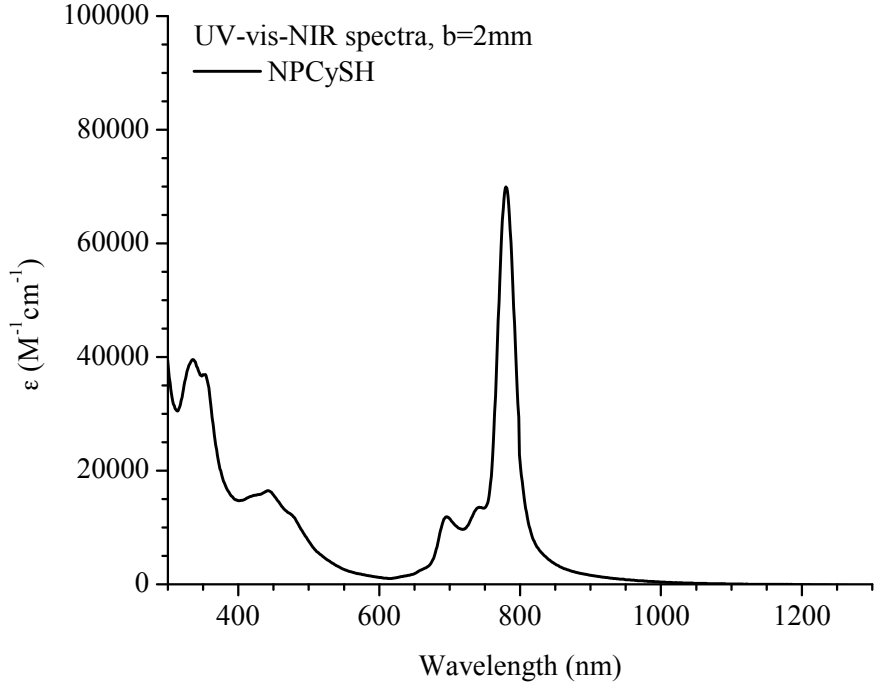

Figure 4.12: The UV-vis-NIR molar extinction cross section of $NPCy(SH)_2$ in methanol.

Also in this case the main absorption band of *NPCy(SH)₂* at 780 nm is in resonance with the 785 nm laser line.
The SERS spectra is reported in Figure 4.13.

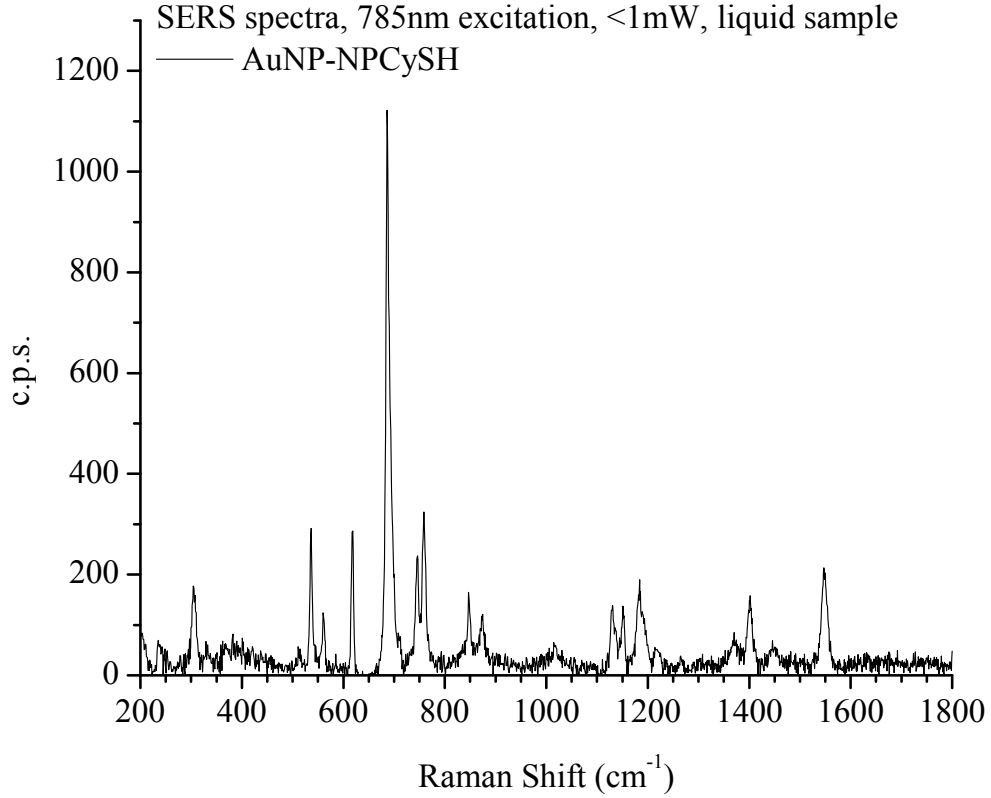

Figure 4.13: SERS spectra of about 3nM AuNP-NPCySH dispersed in aqueous solution at nanomolar concentration.

The Raman signature of $NPCy(SH)_2$ is the sharp intense peak at about 686 cm^{-1}.

Raman reporters library

Five Raman reporters are available for two different near infrared excitation wavelengths. Their optical behaviour clearly explains their high SERS performance with the occurrence of a resonance or a preresonance condition with the excitation wavelengths at 633 nm and 785 nm, as reported in Figure 4.14.

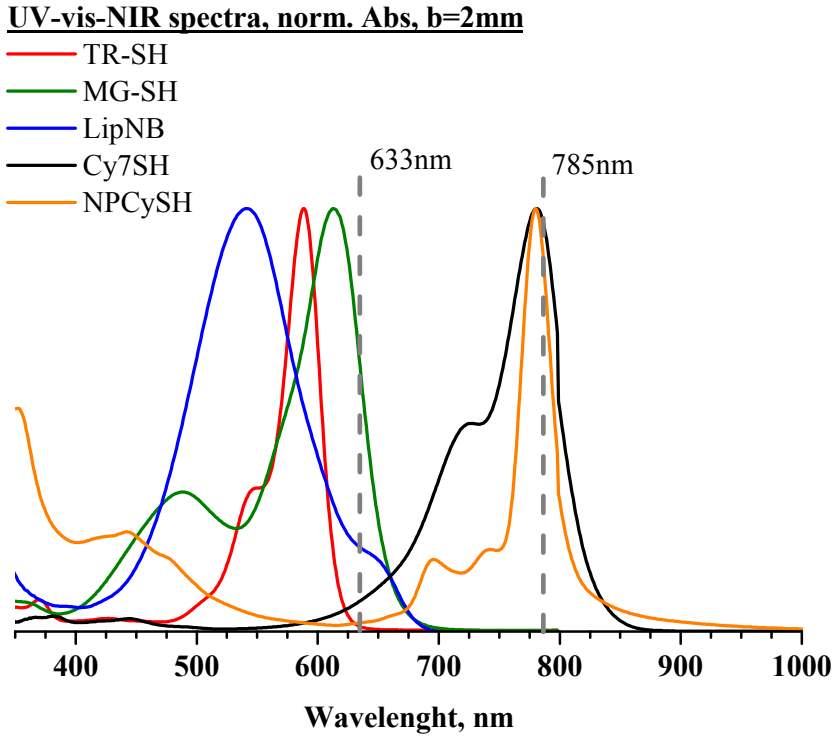

Figure 4.14: Normalized absorption spectra for the five Raman reporters.

Coupling of these molecules with AuNP allows to obtain what is called surface enhanced resonance Raman scattering (SERRS), because the two resonance conditions with the localized plasmon band of the AuNP and the absorption spectrum of the molecules occurs.
The functionalization of the dyes with a thiol, or an equivalent group like a disulfide, guarantees a stronger interaction with AuNP, as just discussed in the introduction chapters.
Moreover, one can observe that these Raman reporters have their own peculiar vibrational signatures which allows their simultaneous use for multiplexing analysis.

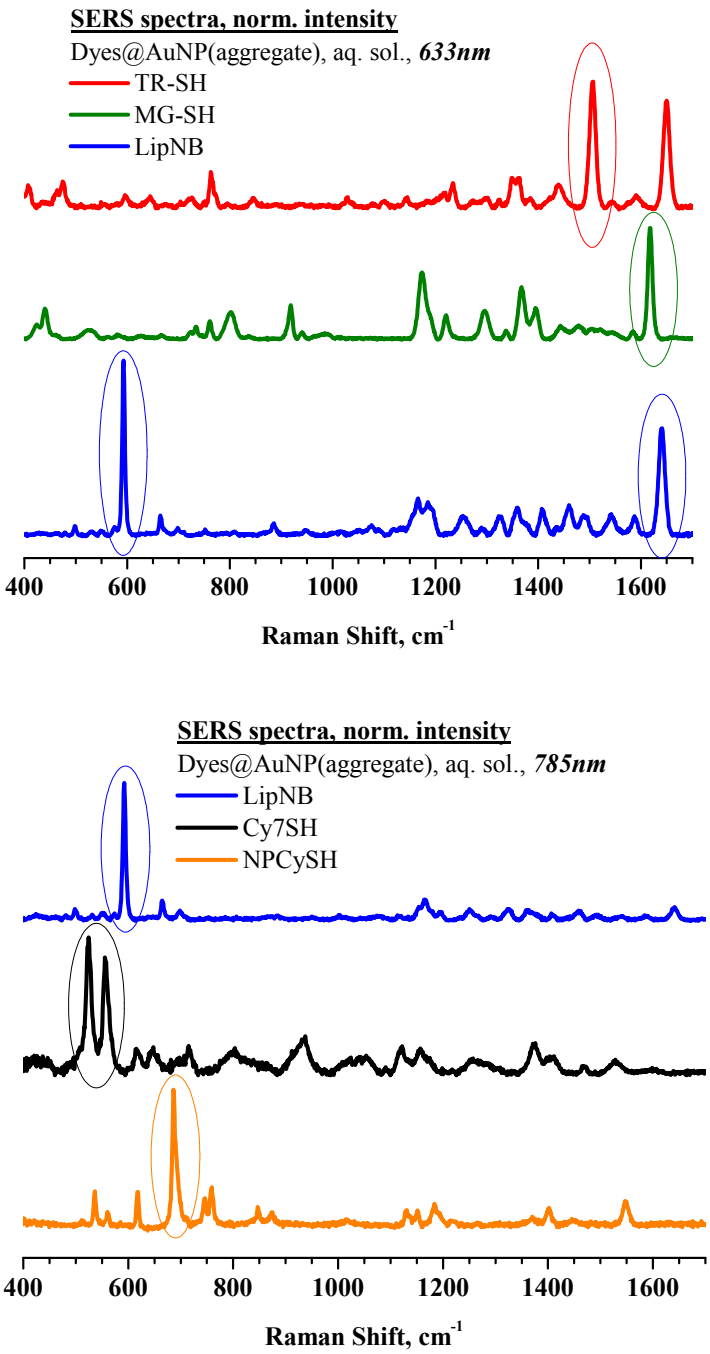

Figure 4.15: SERS spectra of the Raman reporters. Each dye has its own band signature, evidenced by the coloured circles.

Figure 4.15 shows that TR-SH and MG-SH are optimized for the 633nm excitation, whereas Cy7-SH and NpCy-SH for the 785 nm one. LipNB shows high SERS signals with both excitations.

Processing of experimental SERS data

In a typical experiment, a sample containing cells expressing different antigens are incubated with a series of nanostructures, each containing a different SERS reporter associated to a specific antibody. Cells, fixed on a glass slide, are then washed with PBS solution for removing all the nanostructures which have not recognized the cell antigens with their antibodies. SERS spectra are finally recorded for each cell.
Recording all the spectra and their interpretation is usually a challenge task which must be faced with dedicated programs that were written during the period the present work was developed.
To show the developed procedure I used the following nanostructures in a proof-of-principle experiment :

- AuNP + MG-SH + Ab_1
- AuNP + Cy7SH + Ab_2
- AuNP + $NPCy(SH)_2$ + Ab_3

where "Ab_i" are the following antibodies:

- Ab_1 = mixture of antibodies specific for CD44 and NCad antigens
- Ab_2 = mixture of antibodies specific for PSCA and PSMA antigens
- Ab_3 = single antibody specific for EpCam antigen.

These antigens were found to be important for cancer diagnosis. [45, 74, 86]
Two different cell populations were used to verify the targeting efficiency of such nanosystems: "HeLa" cells, which show both CD44 and NCad, and "LNCap/PSCA" cells which show PSCA and EpCam antigens. Some of these cells were also mixed together in the "mixed" sample.
The experiment followed the scheme reported in Figure 4.16.

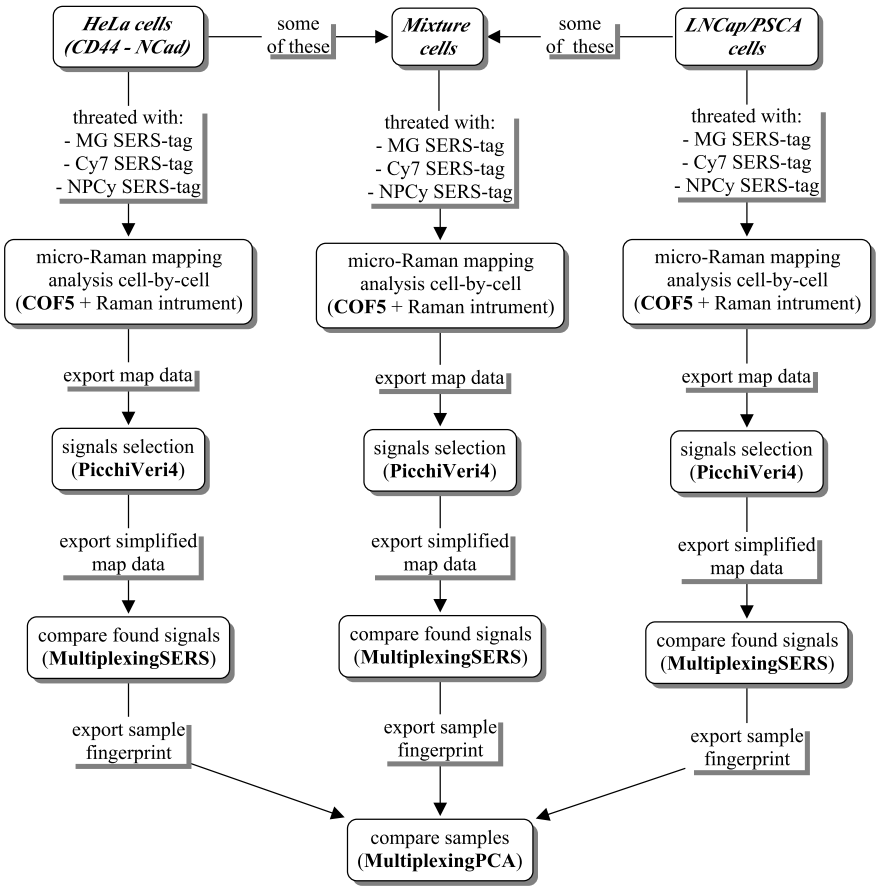

Figure 4.16: Key steps involved in a multiplexing analysis. Many of the analysis are obtained with home made programs.

In the following paragraphs the programs will be introduced for the different tasks.

Identification of cells for recording the SERS spectra

The number of cells of a typical sample can be very large (also several thousand of cells) and for this reason one needs an automated procedure for recording their coordinates on the slide. These coordinates are then given to the Raman instrument for the automatic acquisition of the spectra of all the cells.

A software was developed for the semi-automated localization of cells on a image acquired by the microscope camera of the micro-Raman instrument.

The software, called *Cell On the Floor* is now at its fifth version (COF5).

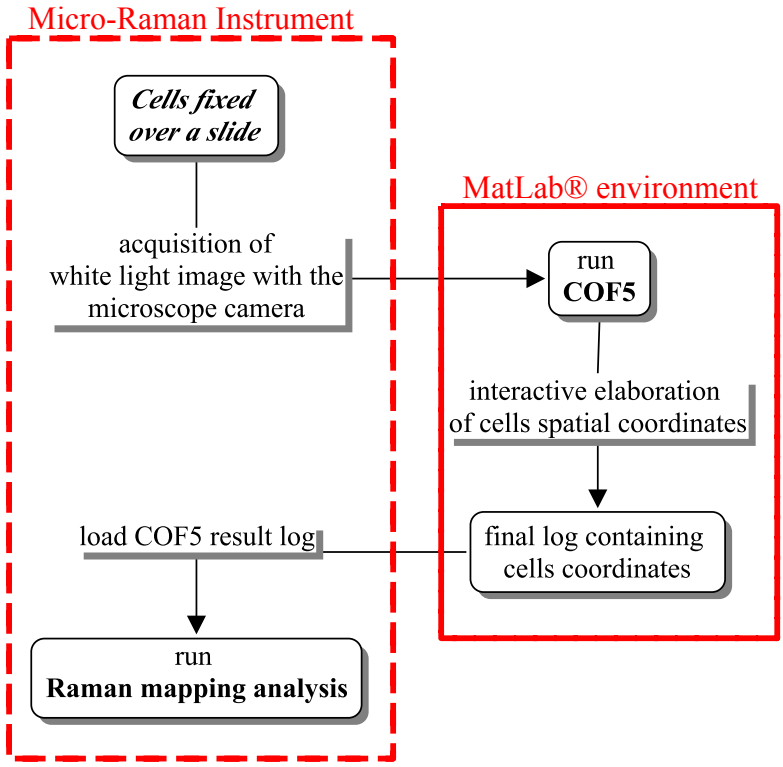

Figure 4.17: COF5 acts in close synergy with the micro-Raman instrument, because it takes the white light image and returns a list of coordinates where the spectra have to be acquired.

This software is written in MatLab® environment and it was developed for the identification, the localization and the counting of cells on a surface.
The program code produces data readable by the *WiRE4*® software, which is the program which governs the inVia instrument of the Renishaw® company.
The identification is based on the contrast difference between cells and the background. Therefore, a sufficiently clean glass surface and a high resolution image are important.

Figure 4.18: At the left, a typical image usable with COF5. On the right, the coordinates and dimension of the sample are introduced. Into this example, the image extends by more than 1mm in length and about 0.8 mm in height.

The image elaboration starts with the binary image into the bottom-right box and the real image at the central-left one (see Figure 4.19).
Every red dots in the *main box* corresponds to a point which will be analysed.

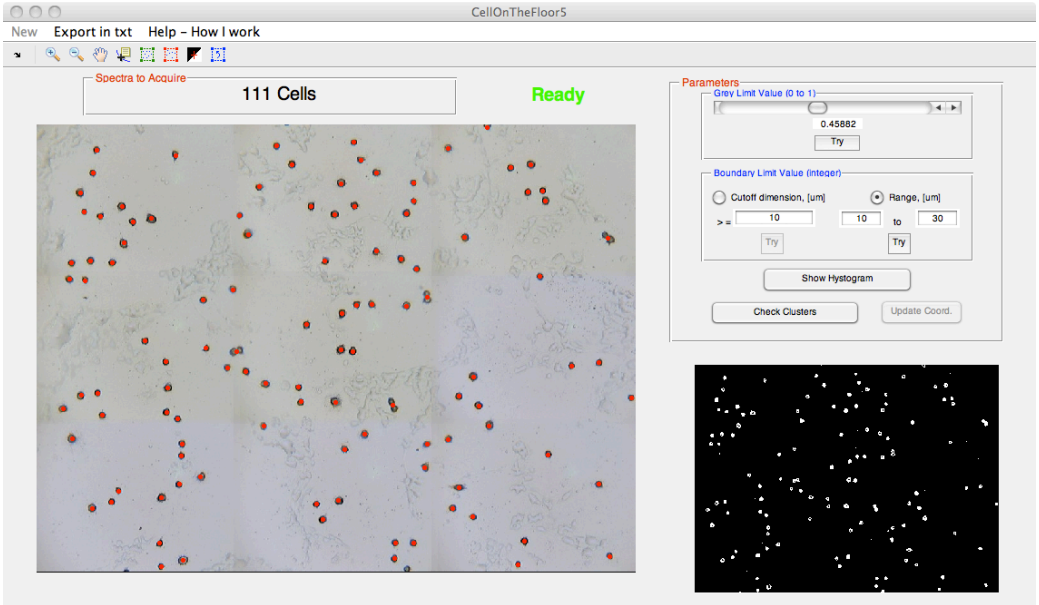

Figure 4.19: The main windows of COF5. The cell searching results are shown into the main box at the centre-left of the window, as red dots.

The code works by fixing a grey contrast value (*Grey Limit Value*) into the pristine image. Pixels brighter than the fixed value appear as white into the binary picture, while the other appear black. A red dot is reported at the centre of isle of nearby points and real coordinates are given to every red dots.
The *Parameters* panel allows the user to change the values for the image elaboration, such as the *Grey Limit Value* or the *Boundary Limit Value*. The last one is extremely useful to avoid the identification of too much bigger or smaller isles, such as dust. For example, setting the *Boundary Limit Value* at *Range* mode within 10 and 30 μm, only the isles (cells) found into this dimension range will be selected, as you can see with the *Show Histogram* function.

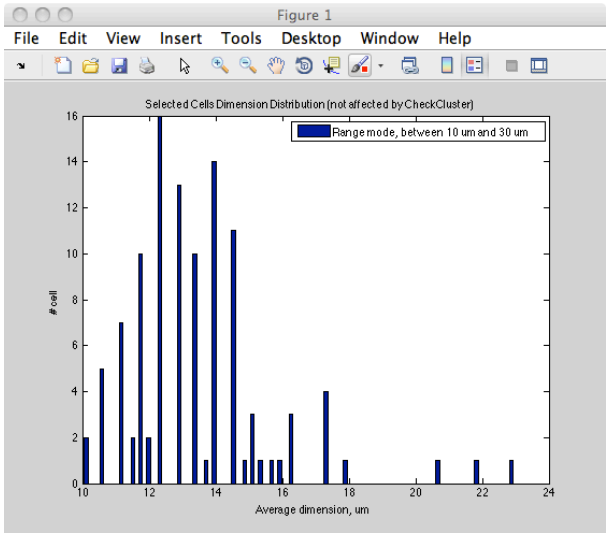

Figure 4.20: The graph shown using the Show Histogram function. A clear dimension distribution is found centered at about 13 μm. The larger elements are due to cell clusters or impurities.

As one can see in Figure 4.20, a distribution centered at about 13 µm identifies the cells. Nevertheless, especially three elements have an unusual large dimension, close to double of the average dimension. These elements can be identified as cell clusters, namely cells which are sticked together. The *Check Clusters* allows to edit manually the point of analysis, as in Figure 4.21.

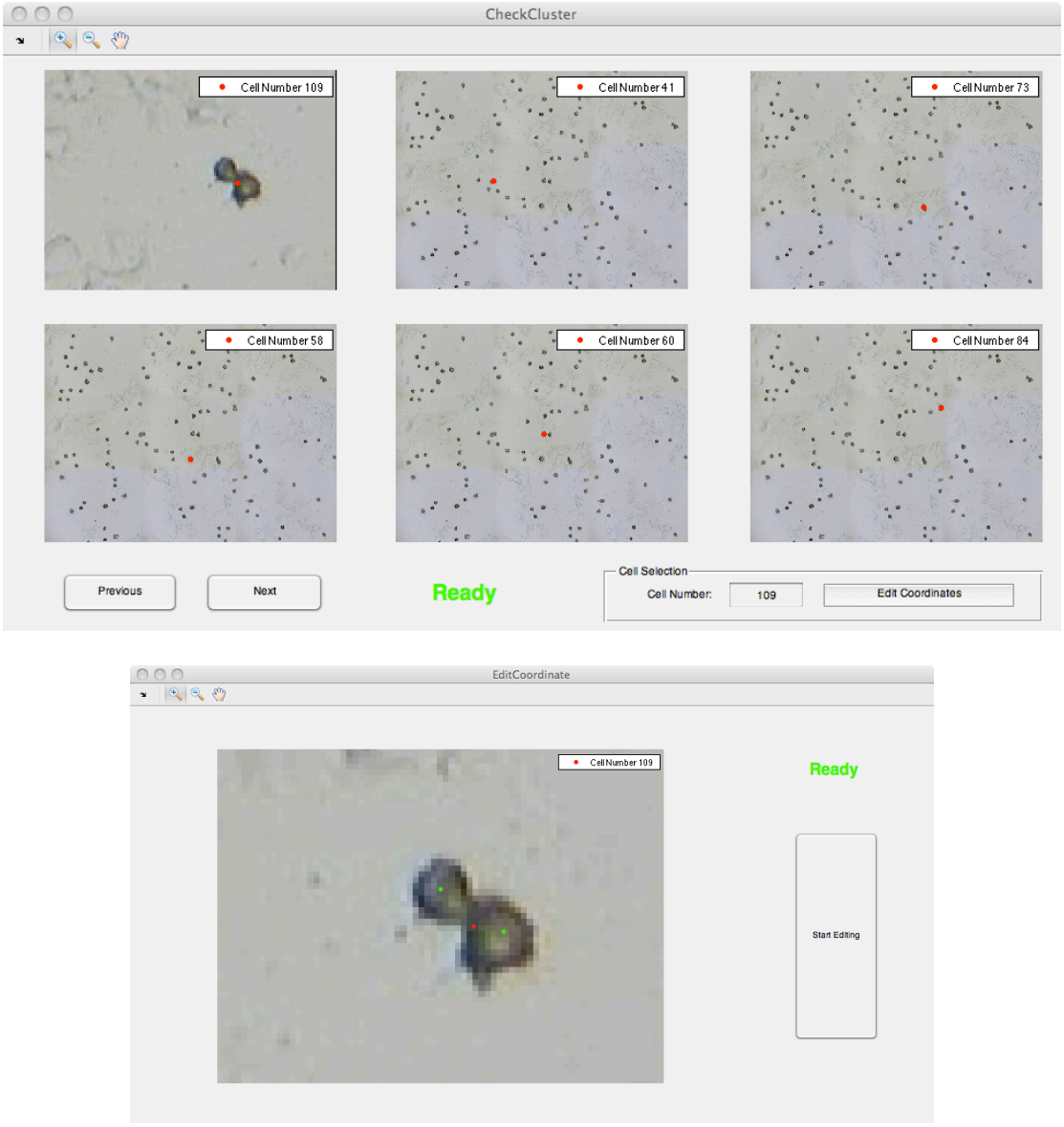

Figure 4.21: Top, the Check Clusters main window clearly shows the presence of a cell cluster recognized as a single bigger element. Below, the Edit Coordinate function allows to change manually the red dot with the green ones. The new coordinates are further uploaded into the main box of COF5.

As a final step, a text log containing a list of coordinates, related to the points of analysis into the *main box* of COF5, is exported for uploading by the *WiRE4*® software.

Softwares for data analysis

After recording the spectra of all the identified cells one has to analyse all the spectra for the presence of one or more SERS reporter.
To make more easy and automatic this task, three different interactive graphical user interfaces were developed with the following aims:

1. evaluation the presence/absence and signal intensity distribution of a particular SERS-tag, that is the presence of specific bands associated to the relative SERS reporter;
2. evaluation the simultaneous occurrence of multiple SERS-tags in the same spectrum;
3. comparison between different samples in order to understand the presence of different type of cells.

The program for point 1 was called *PicchiVeri4*. In Figure 4.22 the main window with a representative dataset of cell is shown. The software works by selecting an user defined Raman Shift into the panel "*Signal Selection*". Than a false colour map shows the cells distribution on the *xy* plane, while the *z*-elevation reflects the intensity found at the selected frequency.
In "*False-Positive Selection*" the user can fix a lower intensity value, below which all signals are considered as noise. It is often a good practice to carefully check this value because of the occurrence of false positive or negative cases. To provide assistance to the user, all spectra can also be manually checked one-by-one, if needed.

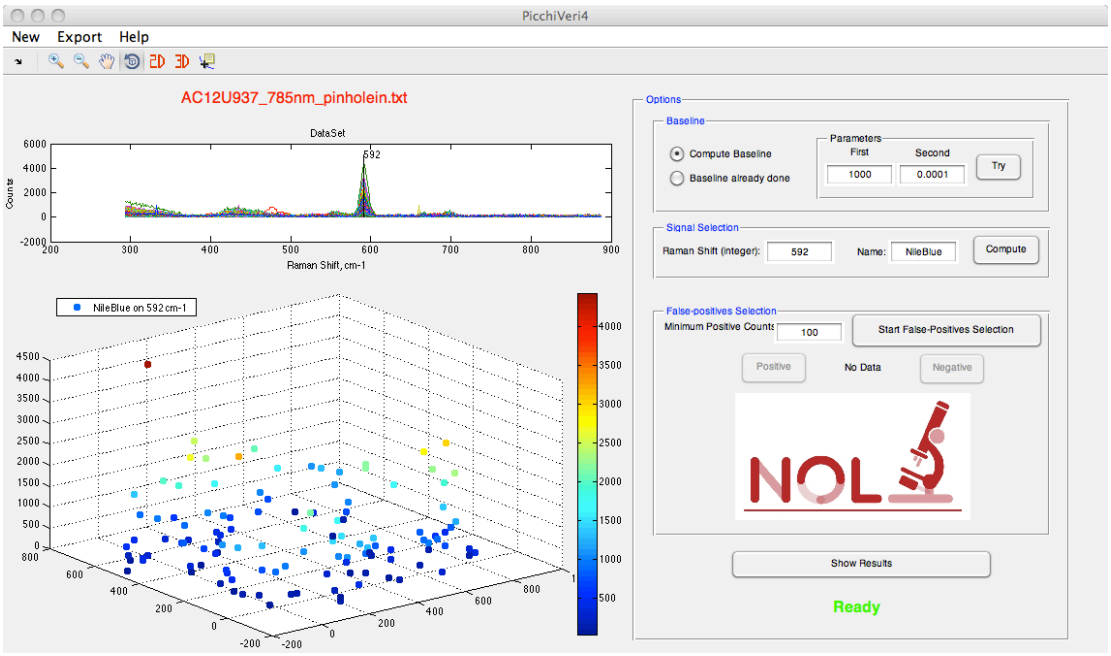

Figure 4.22: The main window of PicchiVeri4, a representative dataset is relative to cells targeted with a SERS-tag carrying LipNB.

PicchiVeri4 also provides a couple of graphics for the analytic results. These are the intensity distribution of positive signals (left in Figure 4.23) and the overall counting of positive and negative elements (right in Figure 4.23).

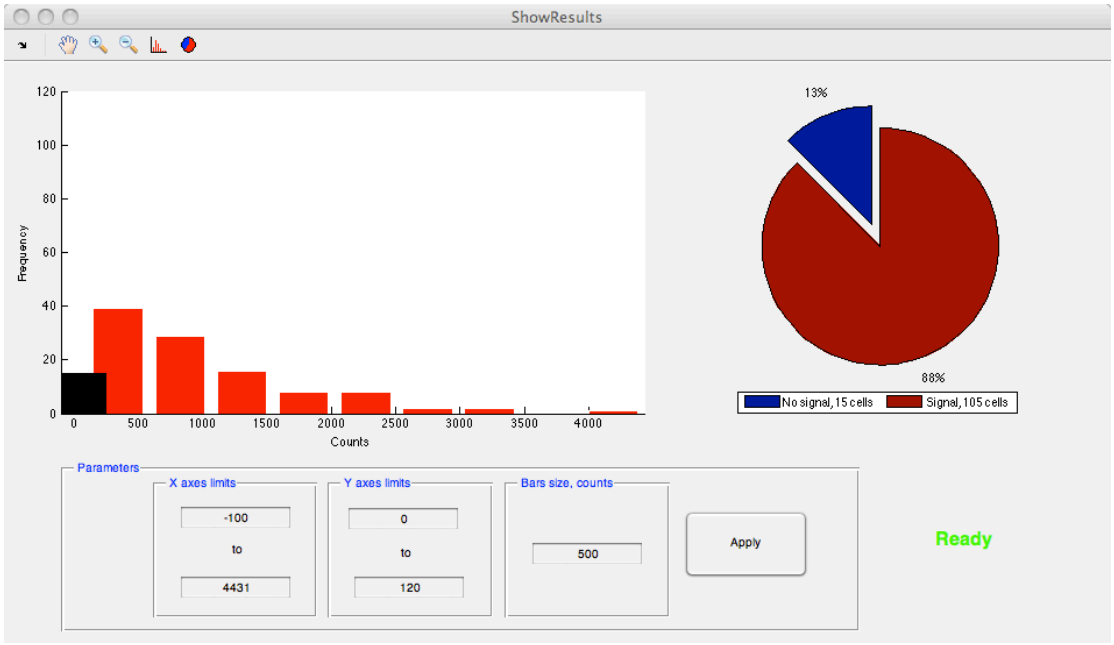

Figure 4.23: Graphs provided by PicchiVeri4. The signal intensity distribution (left) reports how many elements show SERS signals, while the black bar reflect the spectra without signals. A pie graph (right) gives immediate information about the targeting efficiency.

Returning to the proof of principle example reported above, with three types of nanostructures and two type of cells, the collected spectra have to be analysed by *PicchiVeri4* three times for each type of cell, to obtain the results related to each Raman reporter.
Now the simultaneous presence of more than one SERS-reporter is evaluated by another program, *MultiplexingSERS,* which unifies the results of the three runs of *PicchiVeri4* for the three SERS-reporter.

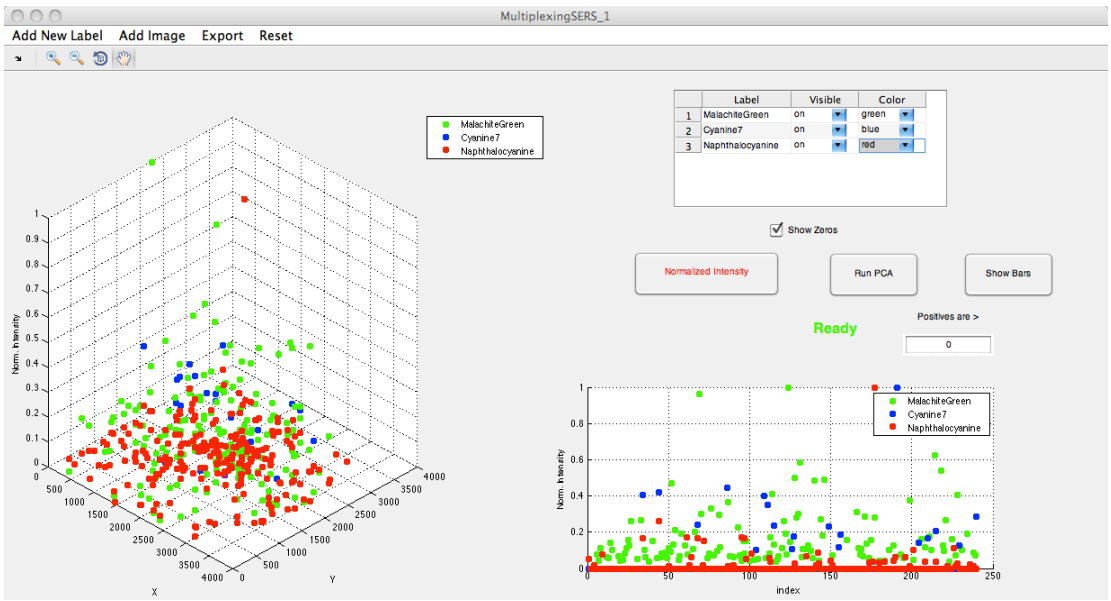

Figure 4.24: Main window of MultiplexingSERS. The signal related to the different SERS-tags are represented in different colours for each cell examined.

The main result provided by this program is the number of cells with the presence of single and multiple SERS-reporters. In Figure 4.25, one can see that 103 cells show only the signal related to MG-SH, 14 only that for Cy7SH and 17 cells that of $NPCy(SH)_2$. Furthermore, 1 cells shows the presence of MG-SH and Cy7SH, 23 MG-SH and $NPCy(SH)_2$, and 5 Cy7SH and $NPCy(SH)_2$. Finally 77 cells do not present any SERS-reporter signal.

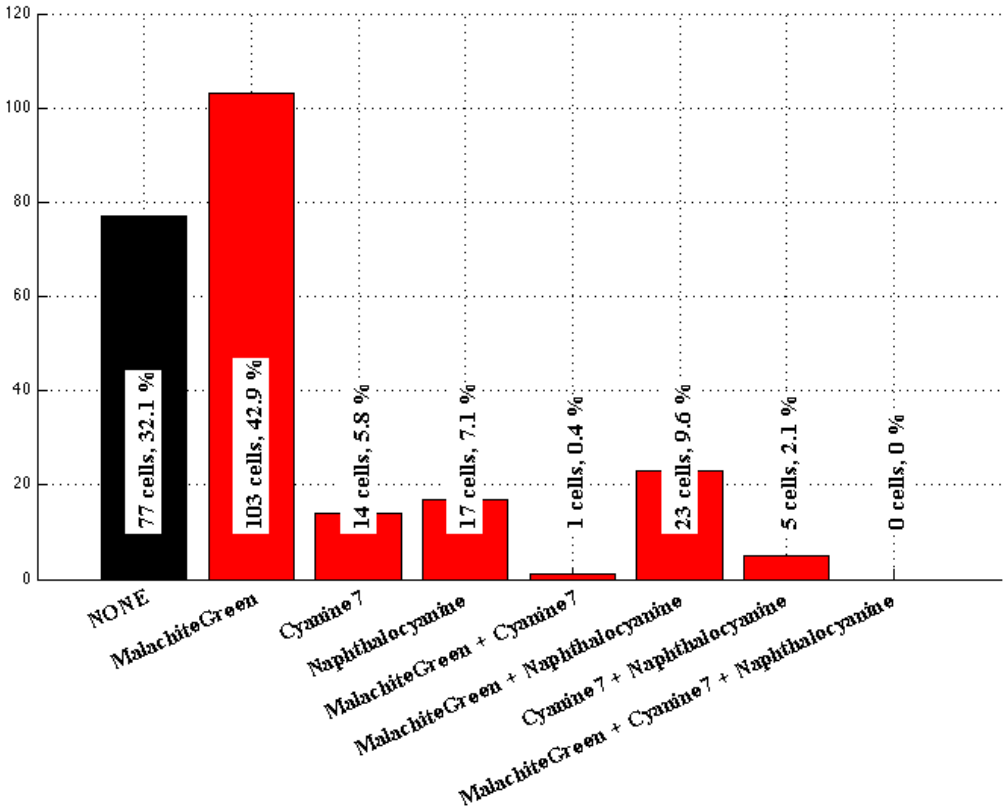

Figure 4.25: A graph representing the SERS-tag occurrence distribution found. Over the 40% of the overall cells express only the antigen for the SERS-tag associated to MG-SH. Nevertheless there are a consistent amount (>30%) of elements not recognized by any of the submitted SERS-tags.

Finally the program *MultiplexingPCA* operates a PCA (Principal Component Analysis) to characterize the different type of cells present in a sample according to point 3 of the above list. In this case the comparison between sample with single type of cells and sample with mixed type of cells allow to identify, in the mixed samples the different cells.

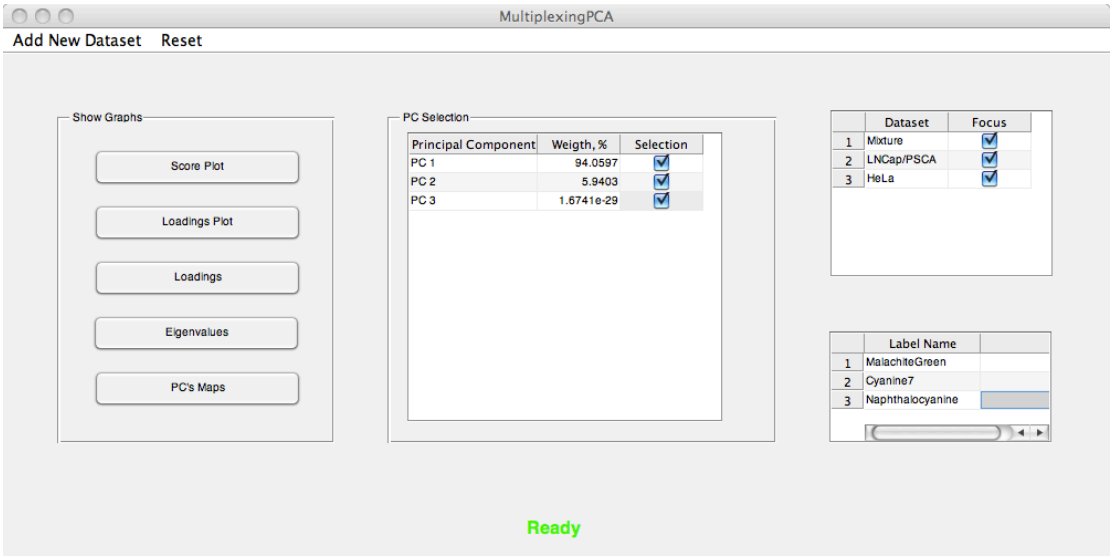

Figure 4.26: The main window of MultiplexingPCA. In this software more cell samples are taken into account together. Under principal component analysis is possible to distinguish between heterogeneous populations.

The principal component analysis (PCA) is a statistical method to find and represent similarities. Here, we applied PCA to the dataset composed by the signals recorded for the HeLa, LNCap/PSCA and mixed samples.
In Figure 4.27 the score plot for the first two principal component is shown. "LNCap/PSCA" cell are represented in blue, "HeLa" in black and the "mixture" in red. The stars rapresent hypothetical samples in which the signal comes from only one Raman reporter.
One observes that "LNCap/PSCA" are present in a cluster located close to the 100% of NPCy$(SH)_2$, with a tail directed toward Cy7SH.
At the other side, "HeLa" cells are close to MG-SH and 50 elements are overlaped exactly at 100% of MG-SH.
Some Mixed cells are close to the region of "LNCap/PSCA" and some others to that of "HeLa" making possible to identify HeLa and LNCap/PSCA cells in the sample.

a)

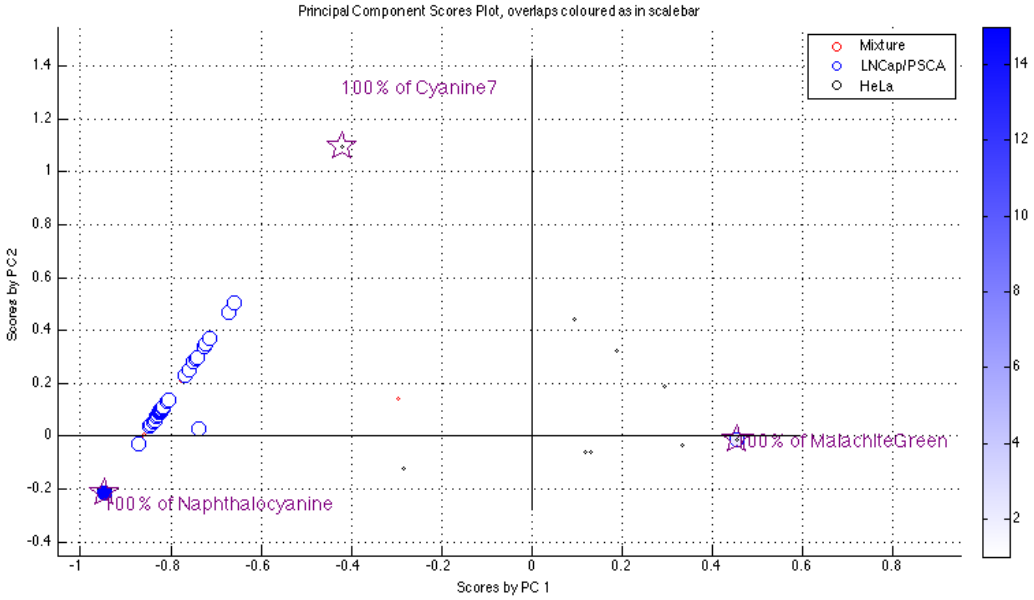

b)

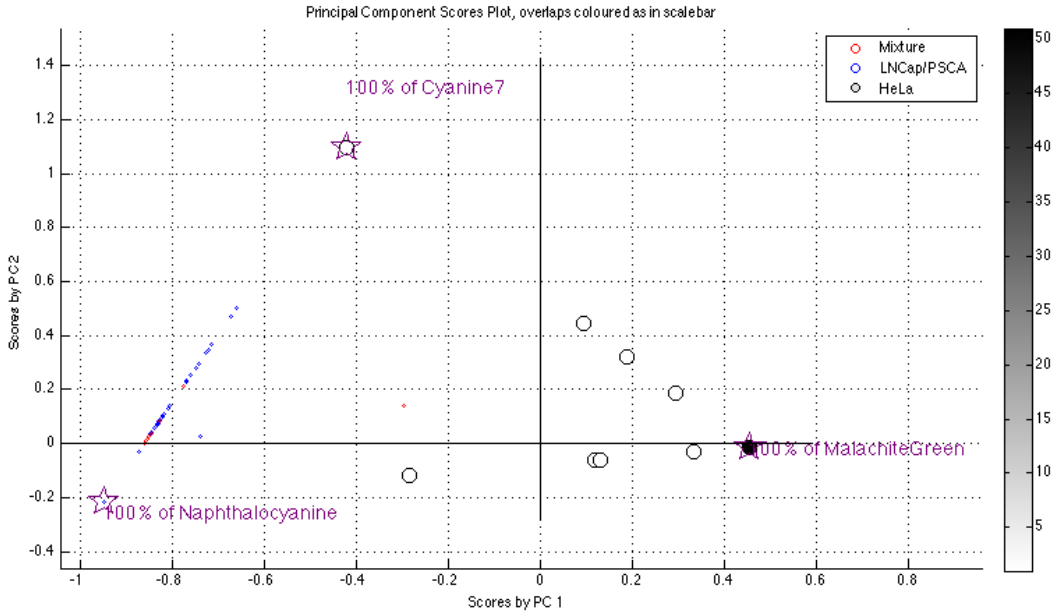

Figure 4.27: Continue…

c)

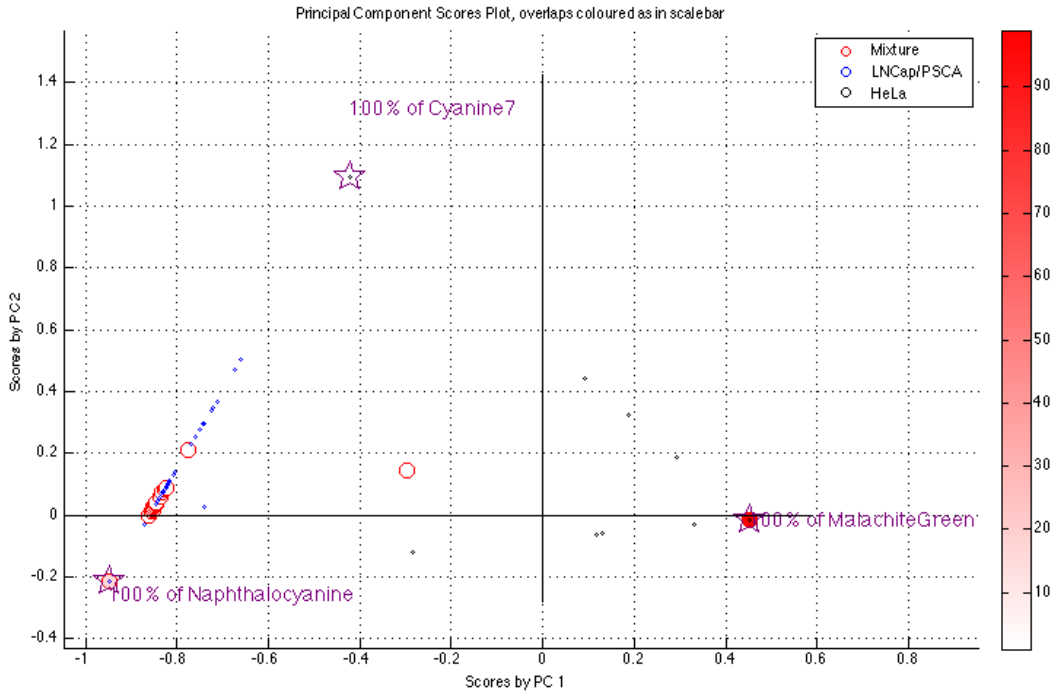

Figure 4.27: Score plots for the sample of HeLa, LNCap/PSCA and the mixed samples. In a) "LNCap/PSCA" cells cluster close to the NPCy(SH)$_2$ flag (100% Naphthalocyanine) are highllighted. In b) "HeLa" are highlighted (100% MalachiteGreen). In c) the mixed cells sample is highlighted and divide into some clustering around "LNCap/PSCA" and some around "HeLa".

Cultural Heritage applications

Proteic matter characterization in artefacts

In the field of cultural heritage, the characterization of the organic matter in artwork samples still remains a challenge due the physical and chemical changes with ageing of these materials.

Nevertheless, due to the uniqueness and rarity of such a samples, the maximum information has to be obtained from the smaller amount of matter. This reflects into the preferential choice for non destructive analysis, and also toward the techniques providing information with the lowest number of measurements.

In the following a comprehensive analytical approach is presented, based on the advantages provided by immunological protocols and SERS spectroscopy.[49]

Traditional Raman spectroscopy is usually applied to the characterization of paint layers, and it provides chemical identification of Raman active compounds present in the artwork. However, the difficulty to identify proteins like ovalbumin, suggested to use immunological protocols based on SERS nanostructures.

The composition and synthesis of SERS-tag are similar to those used for the identification of tumour associated antigens,[74] and are sketched in Figure 4.28.

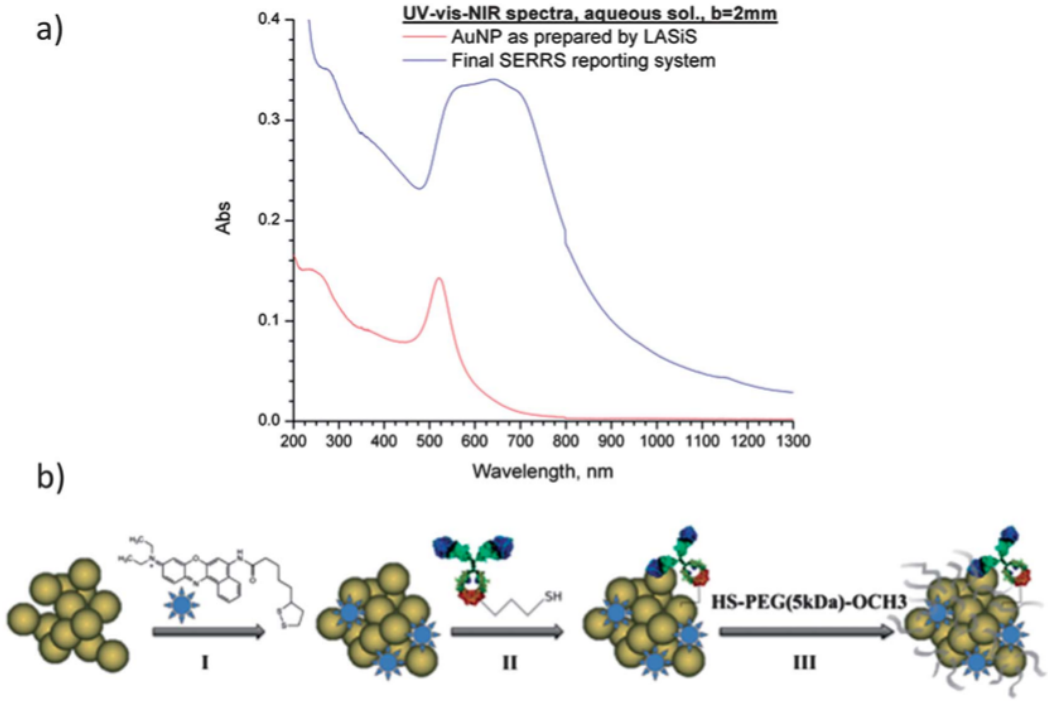

Figure 4.28: a) Absorption spectra of AuNP before and after the aggregation and the functionalization with LipNB, antibody and PEG; b) a sketch representing the synthetic steps involved for the SERS-tag production: the aggregation of AuNP comes first, than the conjugation with the LipNB (I), with thiolated antibody (II) and with a long chain polyethylene glycol (III). From Ref. 49.

We applied these nanostructures to a paint stratigraphic sample, obtained by a micrometric piece of the artefact. The micro-sample was embedded in polyester resin and cut to obtain a stratigraphy. Fine abrasive papers was used to polish the surface.

The stratigraphy was made by two layers, different in composition and physicochemical characteristics.
Despite the synthesis of nanostructures are similar to the previously reported[74], we functionalized AuNP with a secondary anti-rabbit IgG antibody.[49] The immunologic protocol adopted consists on a non-competitive sandwich immunoassay. A primary anti-chicken egg albumin antibody was first added on the stratigraphy. The constant fraction of such antibodies are than recognized by our SERS-tags, due to the presence of secondary antibodies. In this way the SERS signals, related to the nanostructure, are enhanced because of the probability that multiple SERS-tags can recognize the same primary antibody.
We tested our protocols with a standard sample presenting two layers with different proteins and pigments (sample 2L1, Figure 4.29). The sample was mapped acquiring 572 spectra in a 52x11 μm^2 area.
Intensities at selected frequencies were used to reconstruct chemical false coloured maps.

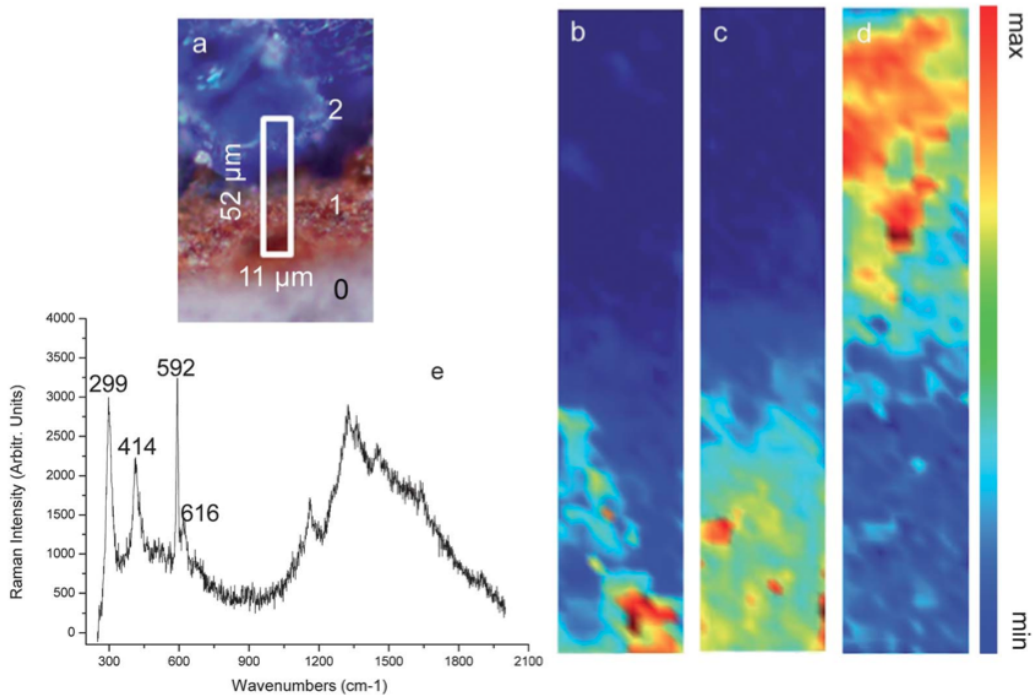

Figure 4.29: a) A image of 2L1 stratigraphic sample; the white box represent the mapped area. b), c), d) the false coloured chemical maps at the frequency of 592, 299 and 400 cm^{-1}, representing respectively ovalbumin (AuNP-LipNB SERS-tag), red ochre (Fe_2O_3) and azurite ($Cu_3(CO_3)_2(OH)_2$). e) a representative spectra by the layer 1 in a). From Ref. 49.

Finally, the proposed method was tested on a historical sample, collected from a Renaissance painting.
The mapped area was 19x3 μm^2 with a total of 57 acquired spectra. The unambiguous localization of our SERS-tag was found on the varnish layer (upper white area in Figure 4.30a), due to the presence of the characteristic band at 592 cm^{-1}.
It was also possible to localize the presence of azurite, with the Cu-O stretching at 400 cm^{-1}, and lead white, with the symmetric CO_3^{2-} stretching at 1051 cm^{-1}, into the pigment layer.

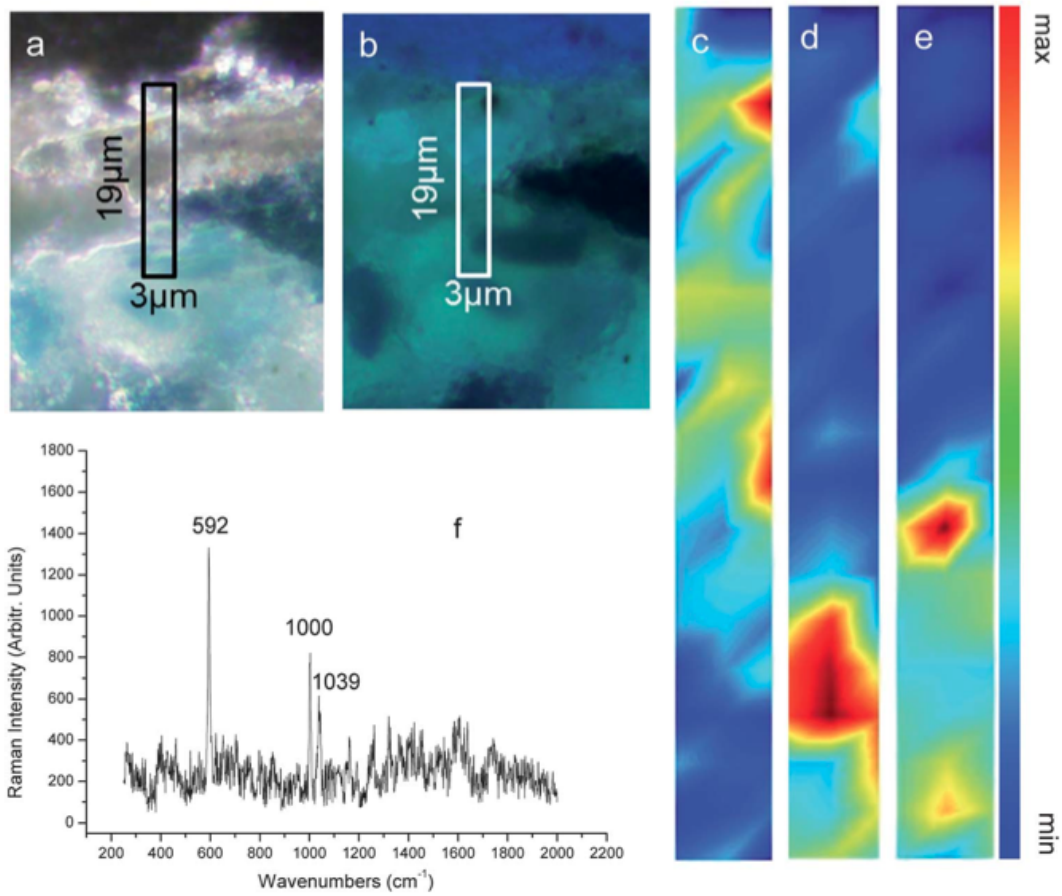

Figure 4.30: a) A image of a Renaissance stratigraphic paint sample, the white box represents the mapped area. b) the same image of a) under UV-light. c), d), e) the false coloured chemical maps at the frequency of 592, 400 and 1051 cm^{-1}, representing respectively ovalbumin (AuNP-LipNB SERS-tag), azurite ($Cu_3(CO_3)_2(OH)_2$) and lead white ($(PbCO_3)_2 \cdot Pb(OH)_2$). e) a representative spectra from the varnish layer. From Ref. 49.

AuNPs for Surface Enhanced IR Absorption

Identification of dyes in natural fibres is an interesting argument in Cultural Heritage because of the importance of characterizing artefacts with historical value. The identification of the dyes with Raman or SERS spectra can be a choice. However, when a molecule is adsorbed on rough metal surfaces, also its infrared absorptions appears more intense than it can be expected. This effect was named Surface Enhanced Infrared Absorption (SEIRA), to recall the analogy with SERS (Surface Enhanced Raman Scattering).[87]

The enhancement factor of SEIRA is some order of magnitude lower than that of SERS.[15, 87] Nevertheless, we investigated this effect using the laser ablated gold nanoparticle in infrared reflection absorption spectroscopy (RAS) for the measurements of the synthetic dye acid orange 7 (AO7) in whole wood.[87]

To record a reference RAS-SEIRA spectra of AO7, we pre-mixed the colloidal solution of AuNPs with AO7, and then we dried a drop over of the solution on a glass slide.

This method was found effective in measuring SEIRA spectra of a $5 \cdot 10^{-5}$ M solution of AO7. Figure 4.31 shows the registered spectra.

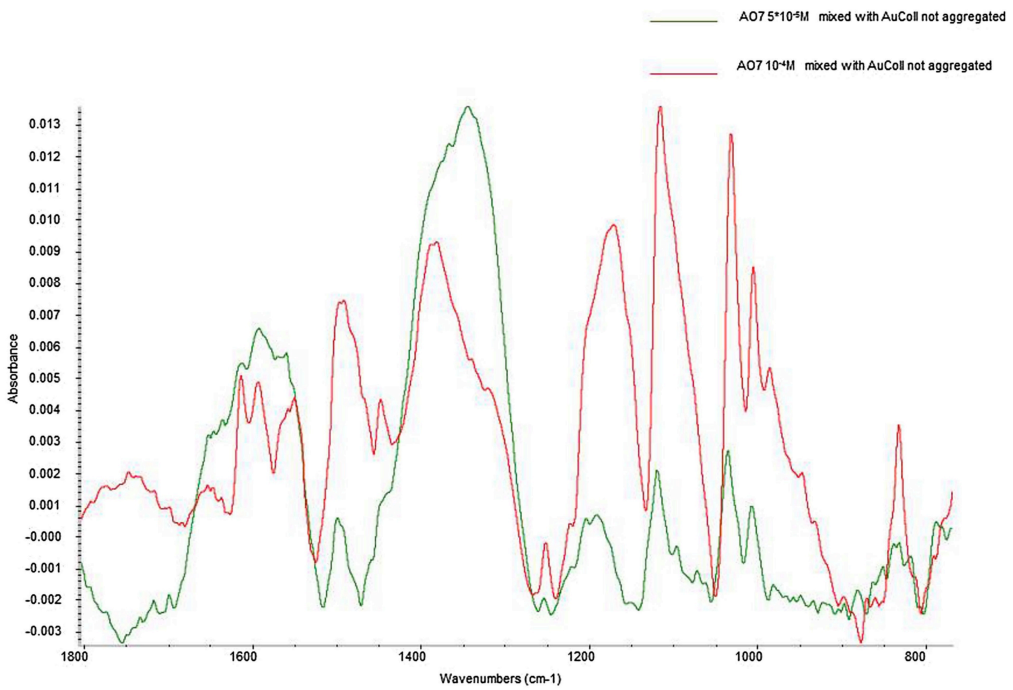

Figure 4.31: RAS SEIRA spectra of AO7 mixed with AuNPs at 10^{-4}M and $5 \cdot 10^{-5}$ M concentration of the dye. From Ref. 87.

The same measurement approach was used to evaluate the AO7 content into a wool fibre. Few mm of a single fibre was used, with a weight of less than 0.01 mg.
The optimized micro extraction method consisted in washing the wool fibre with a small amount of methanol for 60 minutes, than the solvent was evaporated and the dye dissolved into 10 μL of water.
The recorded RAS-SEIRA spectra are reported in Figure 4.32 and were characterized by weak signal intensities, which, however, made possible to identify the dye.

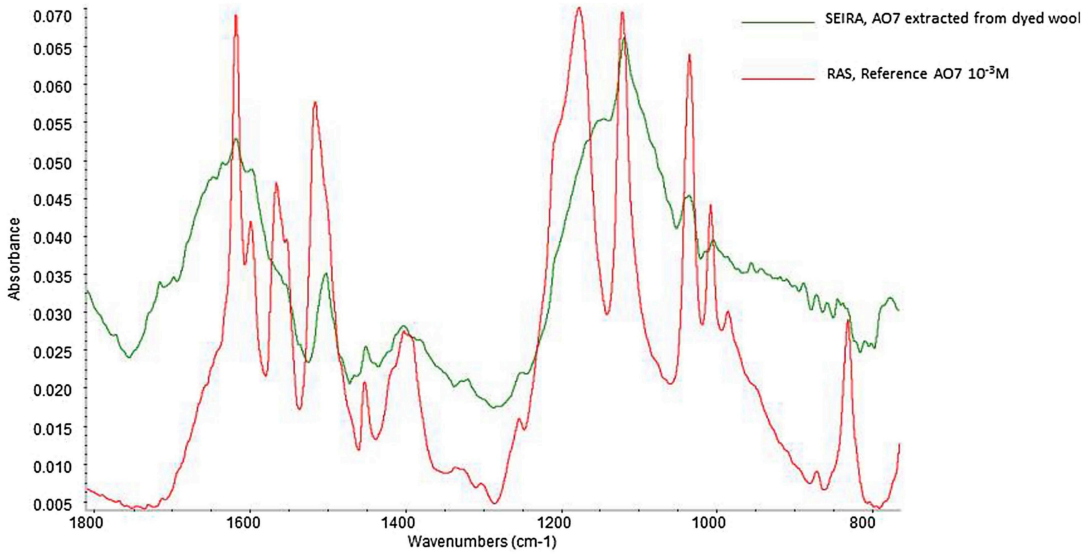

Figure 4.32: RAS SEIRA spectra of AO7 extracted from a dyed wool and mixed with AuNPs (green) and the relative reference spectra (red). From Ref 87.

5. Advanced Diagnostic Tools, part 2

In the field of diagnosis and prognosis of cancer, total-body screening and localization of tumour have crucial importance.
In ideal application perspectives, adequate contrast agents (CAs) should be applied to localize not only the tumour but also the tumour margins during surgical removal.
Both these challenges are extremely difficult to achieve within a single mono-modal contrast agent, that is usually optimized only for a single imaging technique.
Nevertheless, nanotechnology offers the opportunity to merge multiple functionalities into the same nanoobject at nanometric scale.
The so called multimodal contrast agents (MCAs) consist in a single material planned for providing signals for more than one imaging technique. In comparison to multiple administration of mono-modal CAs, MCAs provide contrasts coming from exactly the same points for each technique, while reducing the total amount of submitted agent and therefore, preventing high dose related side effects.
In the following, a proposal for new, advanced, multimodal contrast agents are reported. In particular, two imaging technique like magnetic resonance imaging (MRI) and surface enhanced Raman spectroscopy (SERS), will be considered. Both techniques operate with safe radiations, namely magnetic fields and near infrared visible light. MRI has high tissue penetration, whereas SERS provides spatial resolution down to microns. These properties make MRI and SERS complementary imaging techniques.

AuFe nanoalloy nanoparticles for MRI-CT-Raman imaging

For magnetic resonance imaging (MRI) contrast agents (CAs), a useful parameter for the comparison of effective image contrast is the molar relaxivity (r) related to T_1 (r_1) or T_2 (r_2):

$$\frac{1}{T_{i,observed}} = \frac{1}{T_{i,tissue}} + r_i \cdot [C.A.]$$

… Equation 5.1, from Ref. 25.

Where i = 1 or 2 and *[C.A.]* is the concentration of the relative contrast agent. $T_{i,tissue}$ is the intrinsic relaxation time of the surrounding environment in the absence of contrast agents.
Iron oxide nanoparticles is extensively used as CAs because of the large number of paramagnetic centres present in these nanoparticles, which provide a great magnetic susceptibility which is useful for obtaining a large r_2.[19] Their presence in multimodal CAs (MCAs) derives from the possibility of their coupling to other nanometric structures, with complementary properties.[19, 88-90]
The synthesis of nanostructures for multiple imaging detection, obtained by adding new functions in a layer-by-layer approach, has the disadvantage of a multiple production steps.
The synthetic drawbacks can be reduced in case of MCAs made by a single phase, as in the case of alloy nanoparticles, which show all the planned properties.

We studied multimodal contrast agents based on Au-Fe alloy nanoparticles (AuFeNPs) [91] which can be used for magnetic resonance imaging (MRI), computed tomography (CT) and surface enhanced Raman scattering (SERS).
Laser ablation synthesis in solution was used for the preparation of such MCAs, since it works far from thermodynamic equilibrium, where Au-Fe nanoalloy formation is favoured. By contrast, using wet chemistry *bottom-up* approaches, this kind of nanoparticles are not trivial to obtain.
The optimal composition of AuFeNPs alloy was evaluated by considering the physical properties involved in good contrasts for MRI, CT and SERS.
In Figure 5.1 every contributions to the determination of the best alloy composition are shown.

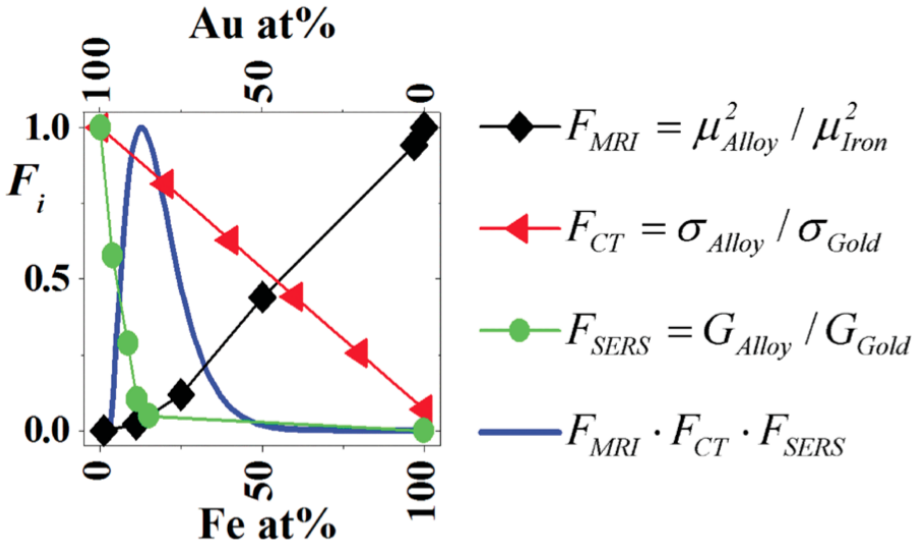

Figure 5.1: The physical parameters involved on each imaging technique were evaluated to determine the best alloy composition. These are the magnetic momentum μ for MRI, the linear attenuation coefficient σ for CT and the enhancement factor at 633 nm excitation G_{SERS} for SERS. Each of these were rationalized with respect to the relative reference. The blue curve determines the most efficient composition to reach for optimal MCAs. From Ref. 91.

Increasing Iron to Gold ratio favours the presence of a net magnetic moment (μ) which grows at Fe atomic fraction higher than 5%.
CT is based on absorption of X-rays, with energy in the 30-120 keV range.
Heavier elements show higher X-ray absorption cross sections, therefore, Au has a X-ray linear attenuation coefficient about 50 times larger than Fe.[91]
SERS effect, due to electromagnetic enhancement, comes from plasmonic substrates and also in this case, higher a gold fraction is preferred.[15, 18, 91] By DDA (discrete dipole approximation) calculations, SERS enhancement factor (G_{SERS}) at the hot spots between two equal spheres can be calculated and one finds that it decays approximately 20 times for a Fe atomic fraction going from 0 to 15%.
Taking into account all these composition dependent properties, the expected best performer nanoalloy composition was found to be at iron atomic content of about 10%.
$Au_{89}Fe_{11}$NPs were synthetized by LASiS in ethanol, of a bulk material with composition $Au_{73}Fe_{27}$.[91] The nanoparticles were proved to be crystalline with Fe atoms homogeneously dispersed into the *fcc* lattice characteristic of AuNP.[91]

The nanoparticles were than conjugated with bis-thiolated SERS dyes (di-thiolated Texas Red, $TR(SH)_2$, and di-thiolated naphthalocyanine, $NPCy(SH)_2$) and a long chain of mercapto-polyethylene-glycol (PEG_{5000}-SH).
The bis-thiolated dyes favoured the formation of nanoparticle dimers and, as a consequence, the *hot spot* feature for greater SERS enhancements. In such a situation, the dye will stay at the nanoparticles junctions, the best position to fully benefit by the surface enhancement.
By numerical calculations based on the DDA approach, we found that *hot spots* in such a representative MCA reach G_{SERS} values as high as 10^{6}.[91]
Magnetic relaxivity measurements were performed at 200 MHz. AuFeNPs give a relaxivity of 60 $mM^{-1} \cdot s^{-1}$ that is an interesting result if compared to the value obtain for the mono-modal commercial agent, Endorem™ (FeO_xNPs), that is about 100 $mM^{-1} \cdot s^{-1}$.
In X-ray absorption measurements, we found 225 HU (Hounsfield Units) for MCAs concentration of 5.5 mg/mL, that is close to the value obtained with pure gold nanoparticles dispersion at the same concentration.
In Figure 5.2 are shown the magnetic resonance and CT results of AuFeNPs nanoalloy compared with reference samples. For MRI, the reference is Endorem™ and for CT a pure AuNP colloidal solution.

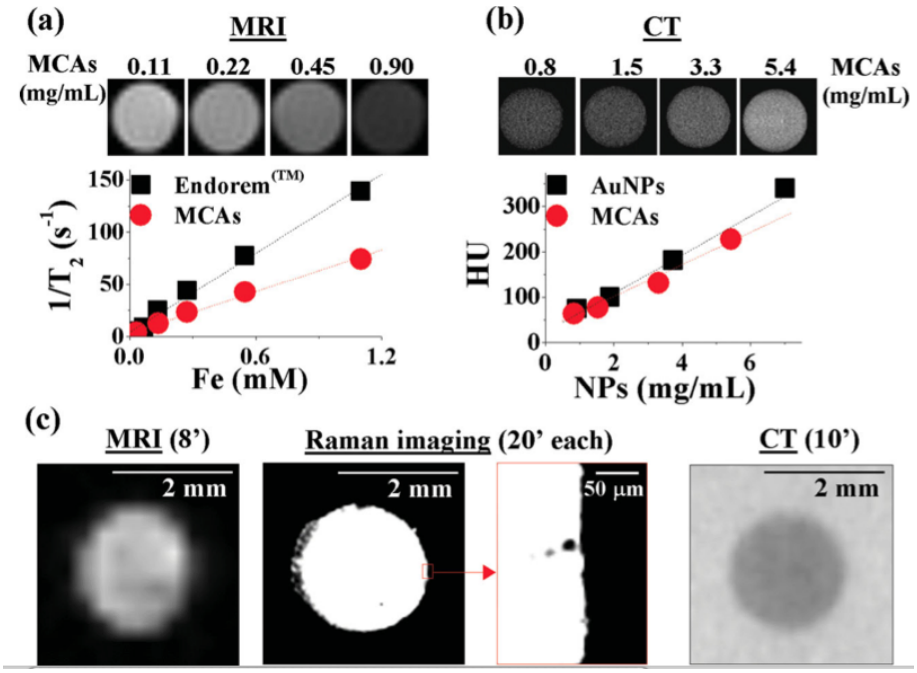

Figure 5.2: The experimental responses for MRI (a) and CT (b) were reported as a function of Iron and nanoparticles concentration with respect to the relative reference sample. In (c) the good spatial resolution of SERS, better than 10 µm, appears clearly with respect to MRI and CT. From Ref. 91.

In Figure 5.2c are also shown the differences in spatial resolution.
The results show that such nanoparticles overcome the drawbacks of each single imaging technique. In fact, MRI and CT have higher tissue penetrations, but they lack in high spatial resolutions (0.15 x 0.15 mm^2 for MRI). In contrast, SERS signal comes from the irradiated area and, therefore, they can be recorded with a spatial resolution determined by the optical objective. The typically found resolution is of the order of some microns or of hundreds of nanometres. The synthesized multimodal contrast

agents show all the pros useful for the considered techniques, and therefore they show high tissue penetration and high spatial resolution.
AuFeNPs were tested with in *in vivo* experiments using Balb/c mice with established sub cute 4T1 tumours. The MCAs were injected intravenously into the tails and MR images were obtained over a period of 24 hours before the animals were sacrificed.
In Figure 5.3 are reported the relaxation time T_2 weighted with the same T_2 measured before the MCAs injection, and the SERS signal intensities obtained with the main organs and tumour in *ex vivo* measurements.

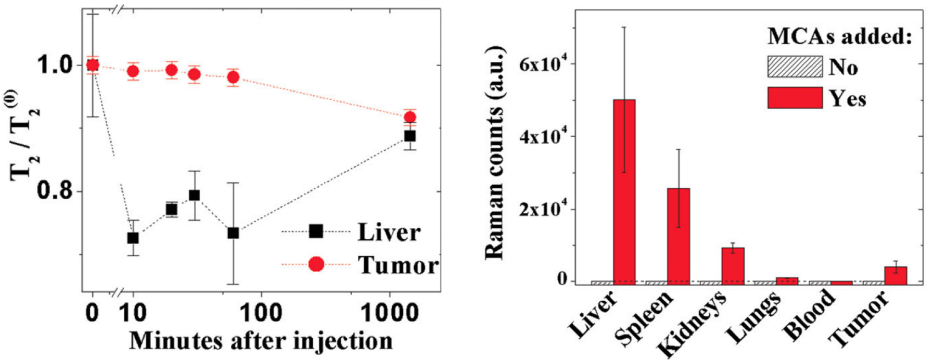

Figure 5.3: Normalized magnetic resonance relaxation time T_2 measured at different times after injection of the MCAs (left) and the ex vivo bio-accumulation of such MCAs measured as Raman signal intensities at 633 nm excitation for TR-$(SH)_2$ functionalized AuFeNPs (right). From Ref. 91.

Data show a fast presence of MCAs into the liver, since its T_2 falls down in just 10 minutes. However, at a time between 2 and 15 hours, the T_2 value of tumour decrease by 10% from the original value. These timescales are compatible with the expected time for the effective accumulation in liver, due to the opsonization, and in tumour, due to the enhanced permeability and retention (EPR) effect.[90]
The biodistribution of MCAs was investigated by Raman spectroscopy *ex vivo* on lysates of explanted organs.
The intensity of Raman signals due to MCAs indicates a prevailing accumulation in liver, spleen, kidneys and tumor, while no signals are detected in lungs and blood.
All these data prove the effective useful application of such a multimodal contrast agents in *in vivo* diagnosis and prognosis of tumour.

SuperDOTA(Gd) functionalized Gold Nanoparticles for multimodal imaging

Magnetic resonance contrast agents with heavy metal cations, such as Gadolinium, provide positive contrasts in T_1 weighted MRI imaging.
However, Gd^{3+} is a toxic lantanide ion, with a size approximating calcium(II), but with a higher charge, which interferes with Ca(II)-required signalling.[21]
Free Gadolinium is also known to bind serum proteins and accumulates within bone, where it becomes tightly and irreversibly associated.[21]
For this reason much attention is dedicated to stable coordination of Gd^{3+}. Currently, all approved gadolinium(III) based MRI contrast agents are nine-coordinate complexes in which ligands occupy eight binding sites at the metal centre and the ninth coordination site is occupied by a solvent water molecule.[21]

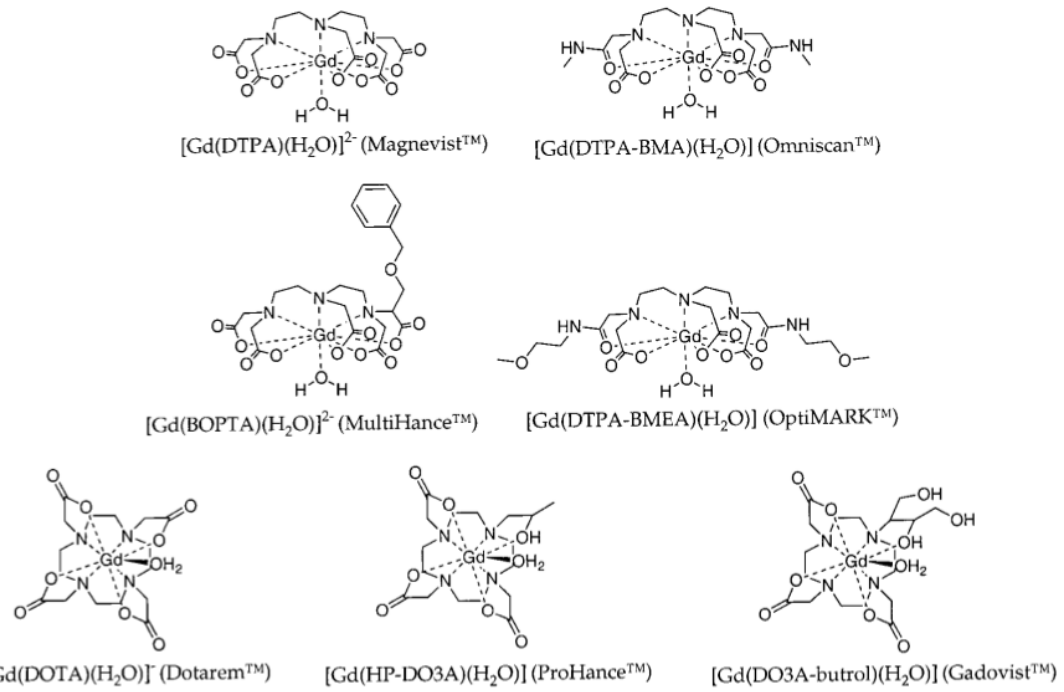

Figure 5.4: Gadolinium chelated compounds approved as MRI contrast agent from 1999. From Ref. 21

With respect to T_2 MRI contrast agents, that are usually based on iron or iron oxides nanoparticles, gadolinium complexes are characterized by low sensitivity, due to their low magnetic relaxivity.[19]
In Table 5.1 are reported some relaxivity values for common gadolinium complexes.

Table 5.1: Relaxivity values for various gadolinium complexes. From Ref. 21.

compound	r_1 ($mM^{-1}s^{-1}$)	r_2 ($mM^{-1}s^{-1}$)	^{1}H freq (MHz)	temp (°C)	pH[a]
		DTPA Derivatives			
DTPA	4.3		20	25	7.4
DTPA	3.8		20	25	
BOPTA	5.2		20	25	7.4
EOB	5.3		20	37	
MP-2269	6.2		20	40	
B-21326/7	6.78	7.77	20	39	7.0
MS-325	6.6		20	37	7.4
DTPA-L1	3.7		20		
BOPTA	4.39	5.56	20	39	7.4
		DOTA Derivatives			
DOTA	4.2		20	25	7.4
DOTA	3.56	4.75	20	39	7.3
DOTA	4.8		20	40	
DOTA	3.5		20	25	

Strategies for enhancing such sensitivity for Gadolinium containing contrast agents are focused on the increasing the number of coordinated water molecules, although a consistent increase of the probability of cations release also occurs.[21]
A second promising approach to the problem follows the synthesis of new classes of contrast agents, based on nanoparticles, where several, up to thousands, Gadolinium cations can be present on a single nanosystem.

Planning the synthesis of new SuperDOTA polymer

Within the second approach, namely the increase of number density of Gd^{3+} for a multimodal T_1-MRI and SERS contrast agent, a new polymer able to coordinate up to three Gd^{3+} ions per single chain, using chelating groups like DOTA was planned and synthetized. This polymer can be also linked to AuNP with a thiol function.
The polymer is called *SuperDOTA*, due to its enhanced cation loading capability.
DOTA residues are bound to the polymer backbone, which, however, was planned to link also other imaging agents, or even drugs, using the same chemistry which is based on the *click chemistry*. The same DOTA can be used, however, for obtaining other complexes useful, for example, for radioimaging.[20]
Sharpless at al. defined *click chemistry* the reactions that can be modular, wide in scope, with very high yields, which produces only inoffensive byproducts (removable preferentially by non chromatographic methods) and that can be also stereospecific.[92]
The most popular *click chemistry* reaction was developed by Huisgen and is the the [3+2] cycloaddition between an azide and an acyclic alkyne.[68, 92, 93] In its primary synthetic route, this reaction required high temperature to overcome the activation barrier needed for deforming the alkyne's bond angle and forming the triazole.[68, 92, 93]
The independent observation by Meldal and Sharpless that Cu(I) ions strongly catalysed the Huisgen reaction, results in a real breakthrough in triazole chemistry.[68, 93]

Despite Cu(I) makes the reaction possible in water at room temperature, the metal cytotoxicity limits its use in living systems or in biological sensitive environments.[93]
Furthermore, considering the presence of DOTA in *SuperDOTA*, Cu cations are competitive coordinating ions with respect to Gd^{3+}.
A solution of this problem came from Bertozzi at al. that investigated the unusual reactivity between cyclooctyne and phenylazide.[94]
The bond angles of the sp-hybridized carbons in cyclooctynes is ~160°, which is distorted toward the transition state of the cycloaddition reaction, resulting in a dramatic rate acceleration, without any Cu(I) ion.[93] The reaction between a strained alkyne and an azide is actually known as *Cu-free click chemistry*.

For the coupling reaction between DOTA fragments and the polymer backbone, we chose dibenzocyclooctine (DBCO) as functional moiety for *Cu-free click chemistry*. The most peculiar feature of *SuperDOTA* molecule are resumed in Figure 5.5.

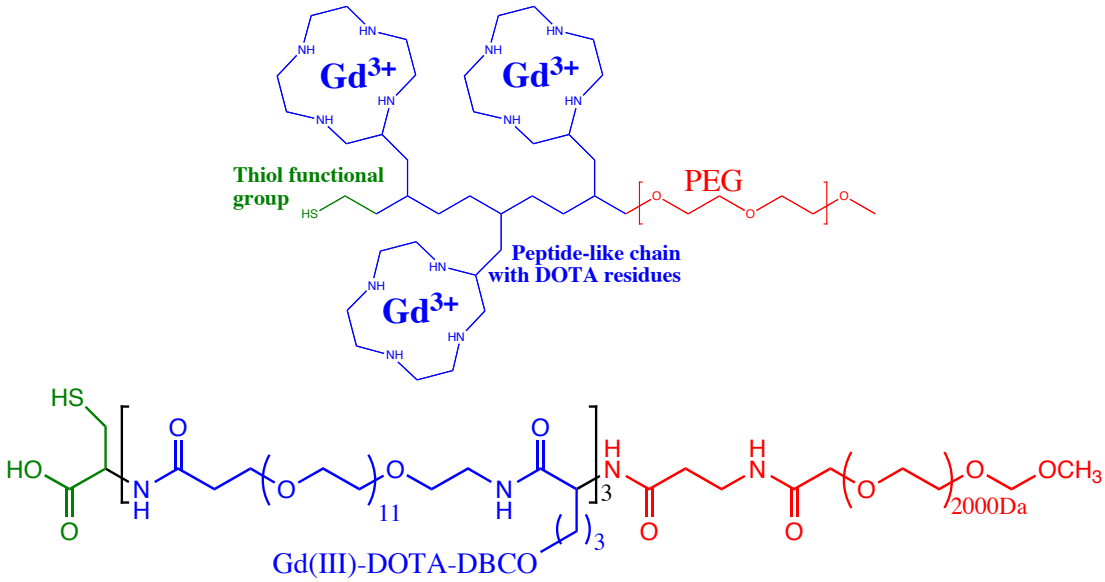

Figure 5.5: A sketch (up) and the molecular structure (down) of the SuperDOTA-Gd(III) polymer. The three fundamental moieties are indicated with different colours.

The sulfhydryl group is present for the link to AuNP. The long polyethylene glycol chain (PEG) provides immunological stealth properties. It was reported that a nanosystem has to circulate, *in vivo,* at least for 6 hours, to have a consistent probability to accumulate to the tumour site due to the enhanced retention and permeability (EPR) effect.[90]

In fact, over 30 different serum proteins are reported to bound to AuNP,[90, 95] and the surface opsonization can effectively promotes their elimination from the circulating system between seconds to minutes.[90]

To overcome this effect, the surface coverage of AuNP by over 1 kDa PEG was found effective in improving stealth properties.[90, 95] The presence of PEG reduces the serum protein adhesion to the nanoparticle surface.[90, 95] In this way nor the macrophages nor the immune system recognise the presence of the so called *complement components* and biological cascade will not be activated.

SuperDOTA, excluding the DOTA-DBCO couplings, was synthetized by solid phase peptide-like synthesis.

The procedure consists of seven couplings and the name of the intermediate products recalls the number of the coupling in the sequence. Therefore, the intermediate *4c* derives from four coupling reactions.

Solid phase synthesis of "7c" polymer

The synthesis of the polymer *7c* was carried out in solid phase according to the schematic procedure show in Figure 5.6.

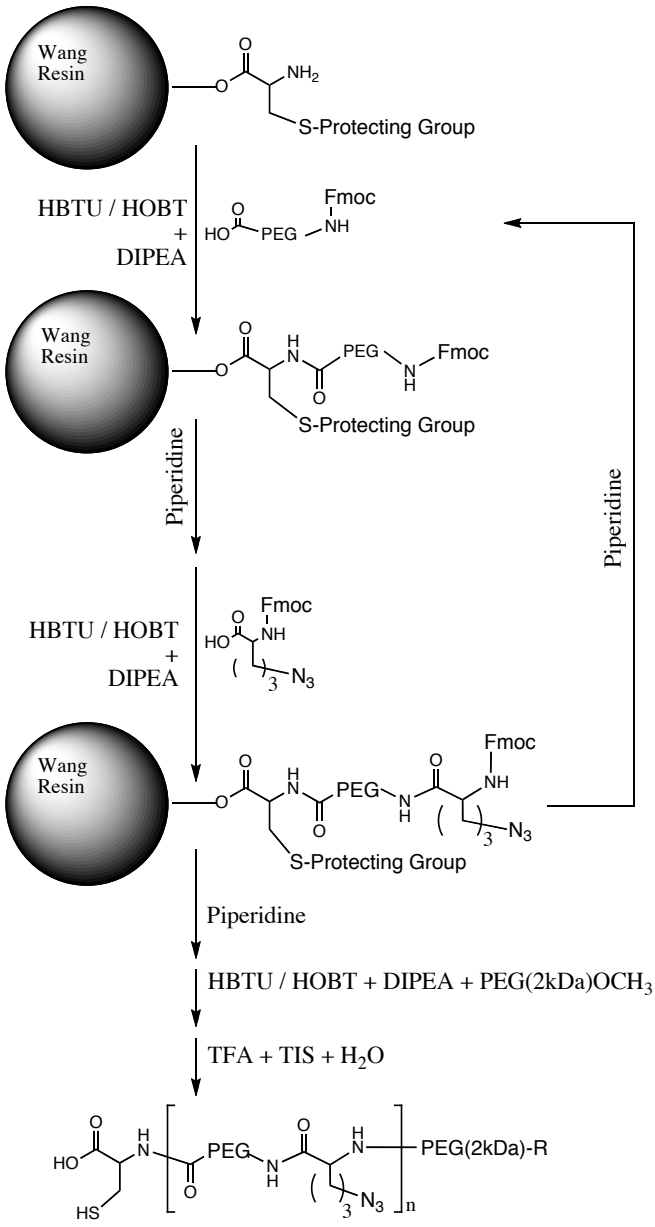

Figure 5.6: Schematic representation of the solid phase synthesis procedure for the 7c polymer.

In 1963, Merrifield et al. developed the first protocol for the solid phase peptide synthesis.[96] This approach had an impressive impact on the production of peptides and, at present, is an ubiquitous technique for this type of synthesis.

The solid phase synthesis consists in coupling a selected sequence of monomers starting with the first one that is linked to an insoluble resin. All the buildings blocks are added and linked one-by-one. Every new coupling is carried out in a consistent excess of reagents to obtain products in quantitative yield.

Since the sequence grows linked to an insoluble substrate, every step is easily purified, and the final product is cleaved from the resin.

The most important implication is that the process is easily automated.

In the synthesis of *7c*, the backbone of *SuperDOTA*, we used a 4-hydroxybenzylic alchol modified chloromethyl polystyrene resin (known as Wang resin), preloaded with cysteine, acting as first building block.
We proceed from C-terminal toward N-terminal using the Fmoc (Fluorenylmethyloxycarbonyl) protecting group for amines, and Trityl (Triphenylmethyl) for thiols.
The azide groups, due to the high selectivity of the *click chemistry*, don't need any protection during the synthesis.[92]
The other building blocks consist in a α-carbossyl-ω-amino-PEG_{12} and in an (S)-5-Azido-2-aminopentanoic acid. These two were alternated along the polymer chain.
The last step involves the coupling of a carbossyl-PEG(2kDa)-OCH_3.
In the final product every building block is present three times, the chain starts with a cysteine and ends with a long polyethylene glycol chain.
The solid phase synthesis was an efficient technique for the production of *7c*. The mass spectroscopy and HPLC analysis of the *4c* and *6c* intermediates (see Appendix A9) confirm the quantitative yield for the coupling reactions.
In Figure 5.7-8-9 are reported the MALDI-TOF mass spectra for the *6c* intermediate, carbossyl-PEG(2kDa)-OCH_3 and for the product *7c*.

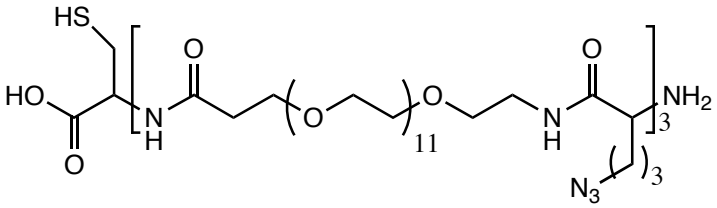

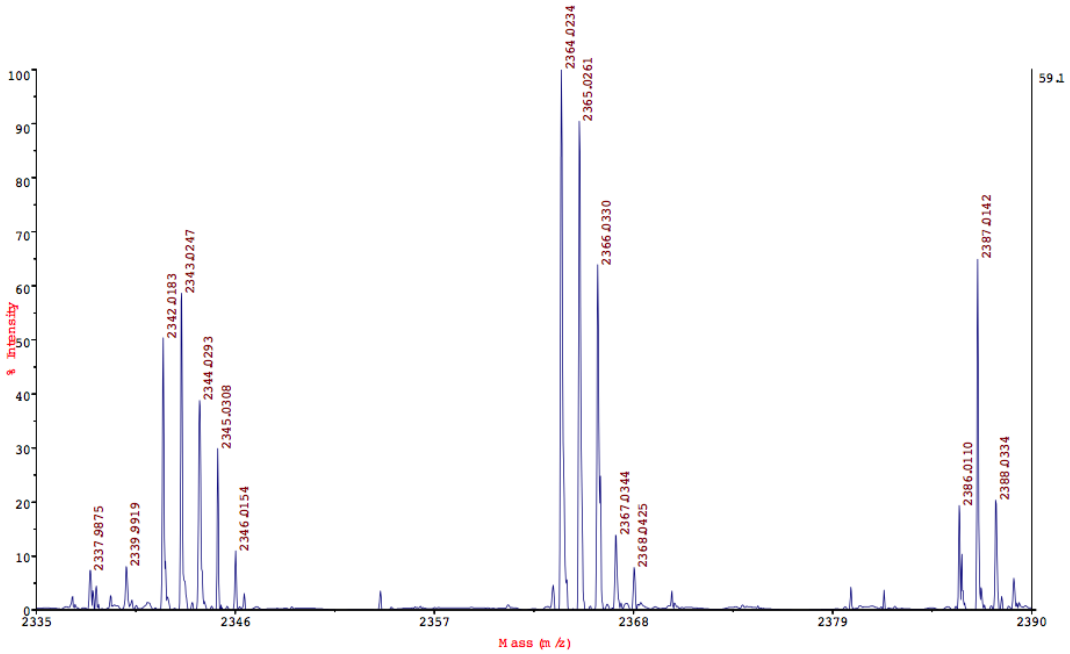

Figure 5.7: Molecular structure (up) and MALDI-TOF mass spectra (down) of the product 6c, DHAP-TFA used as matrix. Theorical mass 2340.7Da, experimental 2342.0 m/z ($[M+H]^+$); 2364.0 m/z ($[M+Na]^+$).

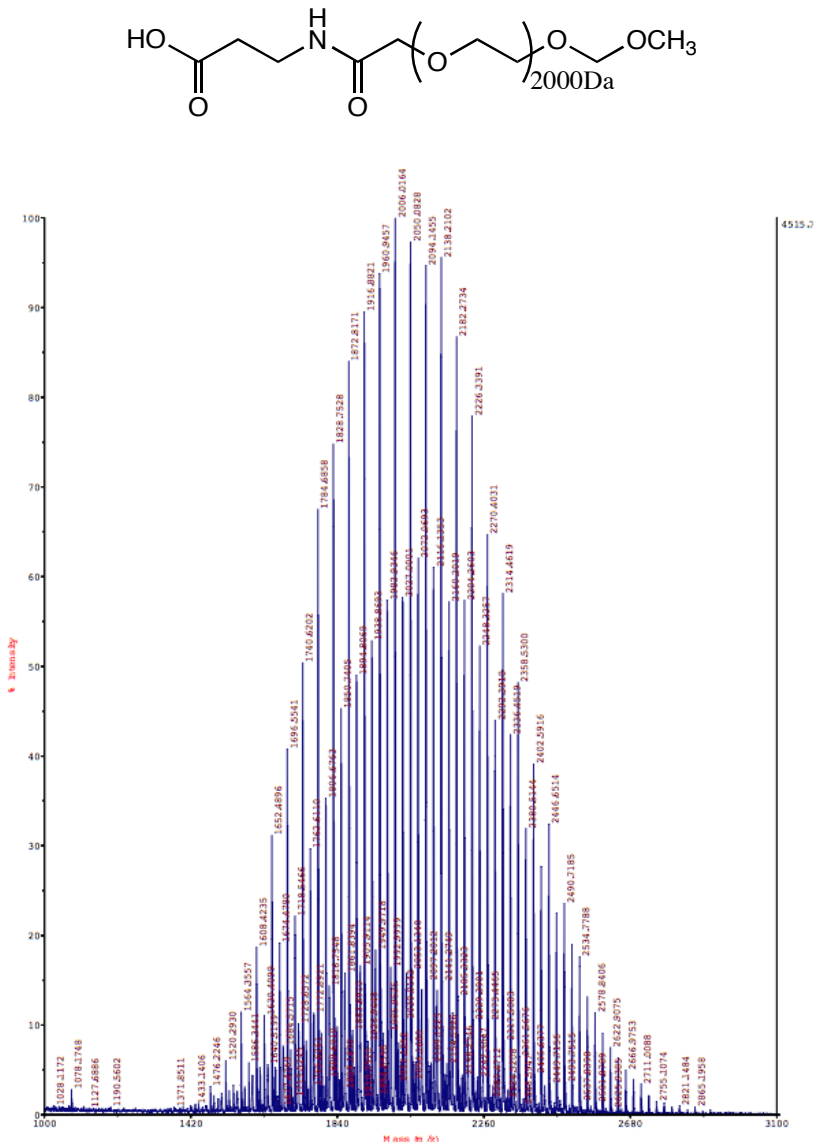

Figure 5.8: Molecular structure (up) and MALDI-TOF mass spectra (down) of the carbossyl-PEG(2kDa)-OCH_3, DHAP-TFA is used as matrix. Distribution peak centred at about 2050 m/z. The distribution of mass peaks is typical for heavy chain polymers. Every signal has a difference of 44 m/z in respect to the next or the previous one, that is the weight of the OCH_2CH_2 monomer unit in PEG.

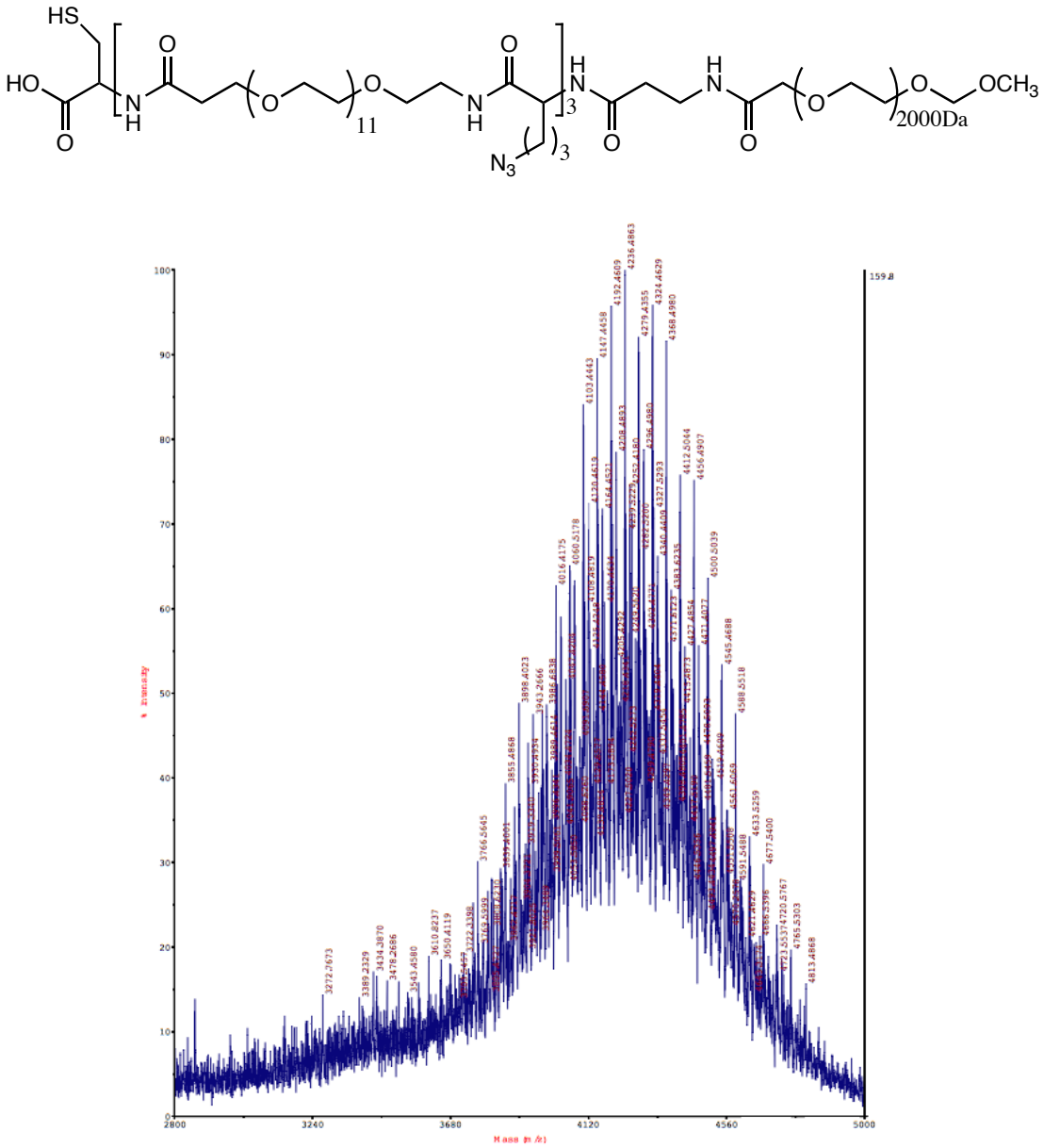

Figure 5.9: Molecular structure (up) and MALDI-TOF mass spectra (down) of the product 7c, DHAP-TFA used as matrix. Theoretical mass distribution centered at 4390 Da (2340 Da for 6c and 2050 Da for final PEG). Experimental mass distribution centered at about 4350 m/z.

The mass spectra distribution for carbossyl-PEG(2kDa)-OCH_3 shifts by more than two thousands mass units after the reaction with the intermediate product *6c*. This result is compatible with the effective production of the final product *7c*. The MALDI-TOF mass spectrum of *7c* does not show peaks related neither to *6c* nor to carbossyl-PEG(2kDa)-OCH_3, in the zone of 2340-2365 *m/z* and 1500-3000 *m/z* respectively (data not shown). Therefore the distribution found at about 4350 *m/z* can be well attributed to the coupling product *7c*.
As a final proof, the reaction product was characterized with a series of mono- and bi-dimensional nuclear magnetic resonance (NMR) experiments.
In Figure 5.10 the hydrogen atoms of the molecular structure *7c* were indicated with numbers according to the attributions reported in Table 5.2.

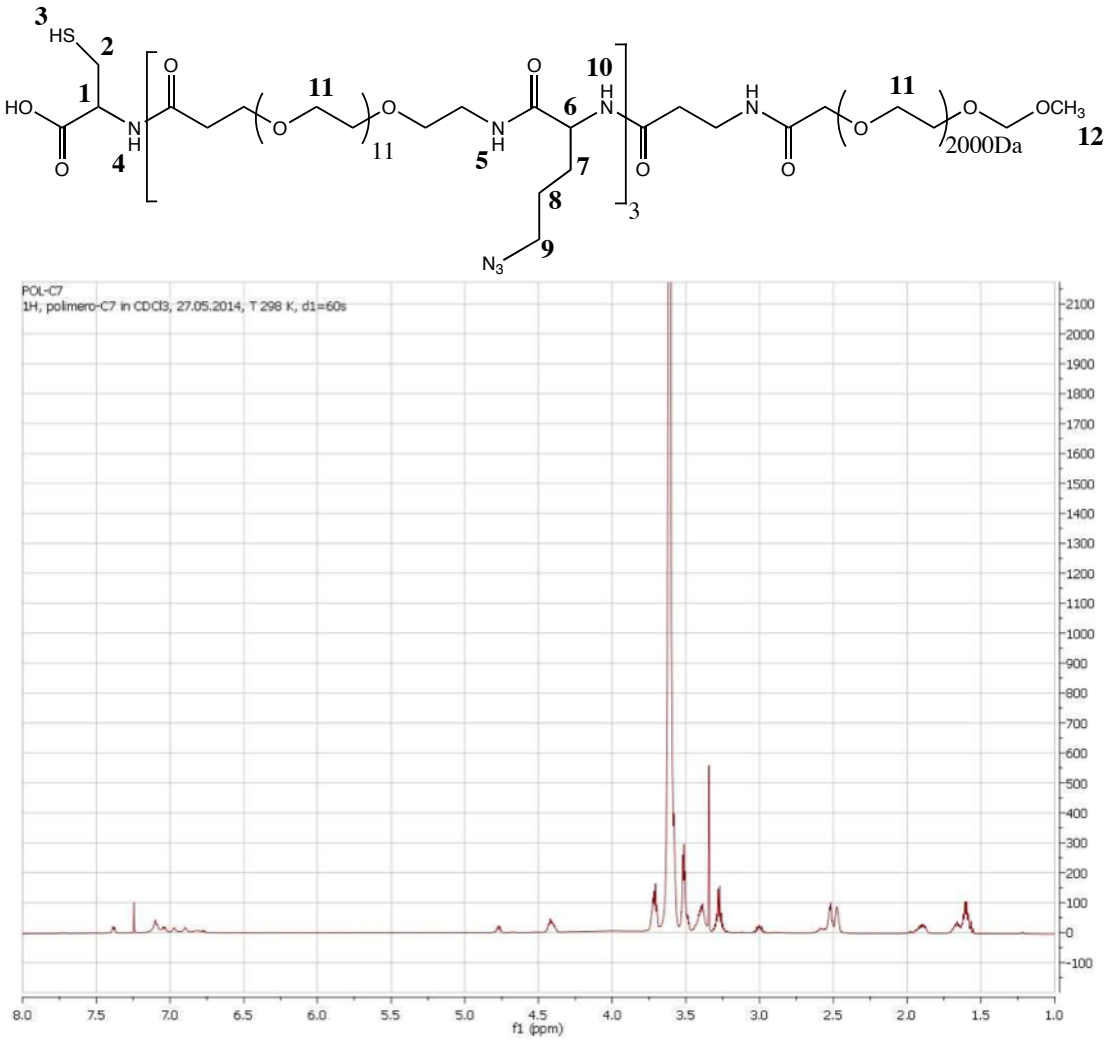

Figure 5.10: The molecular structure of 7c (up) with the hydrogen atoms enumerated as in the NMR attribution analysis and the ^{1}H-NMR spectrum of 7c (down).

Table 5.2: The NMR attribution for the hydrogens and the carbon atoms according to the numbers reported in Figure 5.10.

Atom Index	^{1}H-NMR chemical shift (ppm)	^{13}C-NMR chemical shift (ppm)	^{1}H-NMR theorical area	^{1}H-NMR experimental area
1	4.74	53.81	1	0.8
2	2.97	26.49	2	1.3
3	1.54	-	1	0.3
4	7.38	-	1	0.8
5	7.10	-	-	-
6	4.39	52.47	3	2.9
7	1.87 1.63	29.60	12	10.2
8	1.58	25.00		
9	3.25	50.98	6	6.1
10	7.04	-	-	-
11	3.58	70.51	304	306.5
12	3.31	58.97	3	3.0 (assigned value)

First, attributions come from the ^{1}H-NMR spectra. Polymer amidic protons (**4**, **5**, **10**) fall between 6.70 and 7.40 ppm. The hydrogen number **4** develops a doublet centred at 7.38 ppm. For **5** and **10**, the signals overlaps, but thanks to COSY and TOCSY bidimensional plots (see Figure 5.11) a reasonable attribution became possible at 7.10 and 7.04 ppm respectively.
The methoxy group protons (number **12**) shows a singlet at 3.31ppm, as expected by looking at the molecular structure.
The most intense signal at 3.58 ppm comes form the ethylene-glycol groups (**11**), since their protons are the most abundant in the molecule.
Protons **1** and **6**, being very close to carbonyl and amide electron withdrawing groups, have resonances at 4.30 and 4.80 ppm.
Starting by this observation and thanks to COSY and TOCSY spectra, all other protons' assignments were done.
In particular, carbon at number **6** is a chiral centre. This fact makes pro-chiral points the other carbons **7**, **8** and **9**. Therefore, the hydrogen atoms bound to such a carbons are not magnetically equivalent and differences should be observed in their chemical shifts. However, the distance of the pro-chiral carbon from the chiral one reduces the inhomogeneity. Therefore, only for the protons **7** we observe two distinct signals at 1.63 and 1.87 ppm, while for **8** and **9** only a single peak at 1.58 and 3.25 ppm .
The peak areas were integrated and normalized to that of the methoxy group signal, which was assigned a value of 3.
Since this functional group is only present in *7c* and not in *6c*, the close proximity of the theoretical areas with the experimental ones gives the final confirmation of the presence and purity of the molecule *7c*.
From the ^{1}H^{13}C-HMBC and ^{1}H^{13}C-HMQC bidimensional spectra also carbon chemical shifts were evaluated.

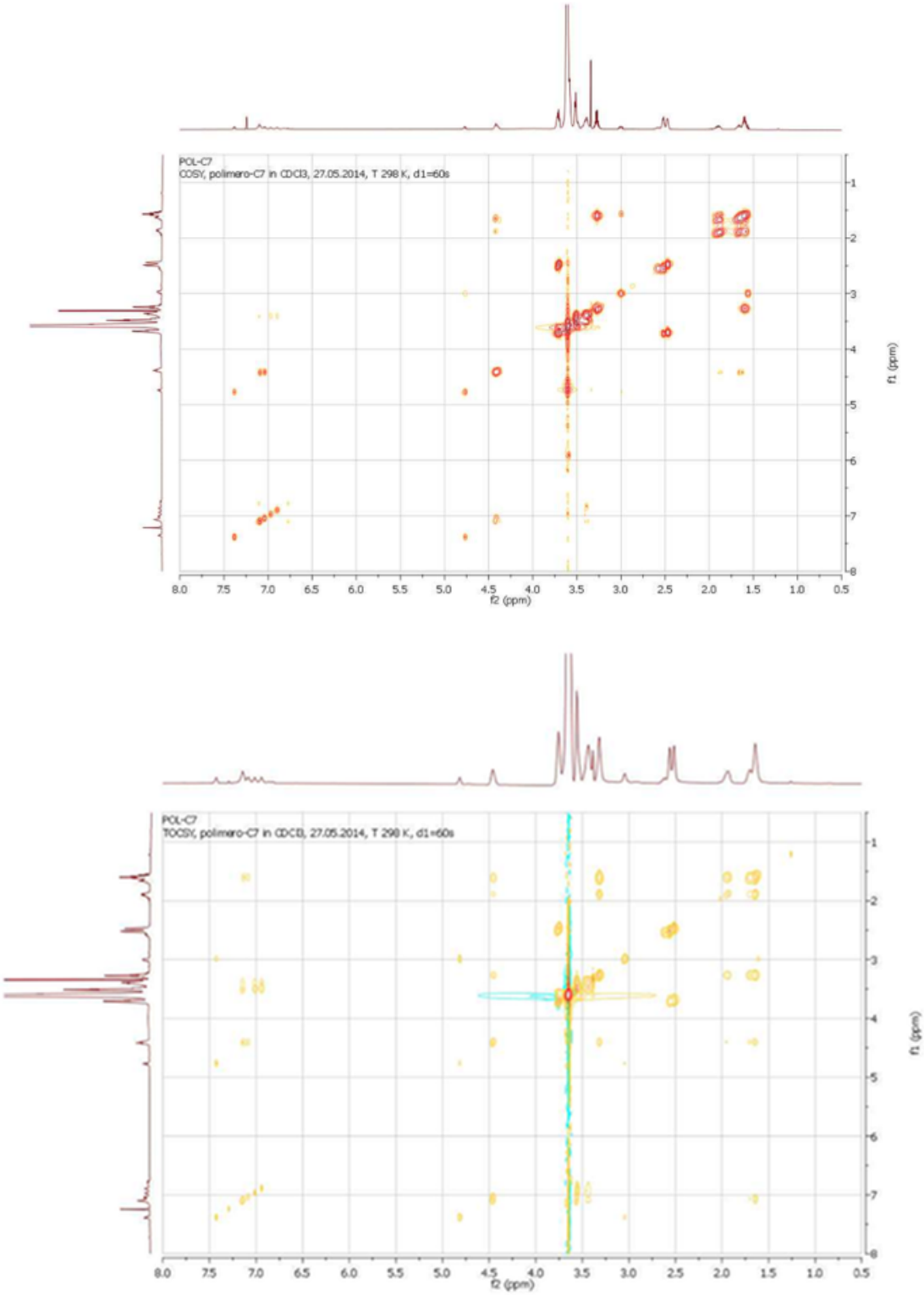

Figure 5.11: Continue…

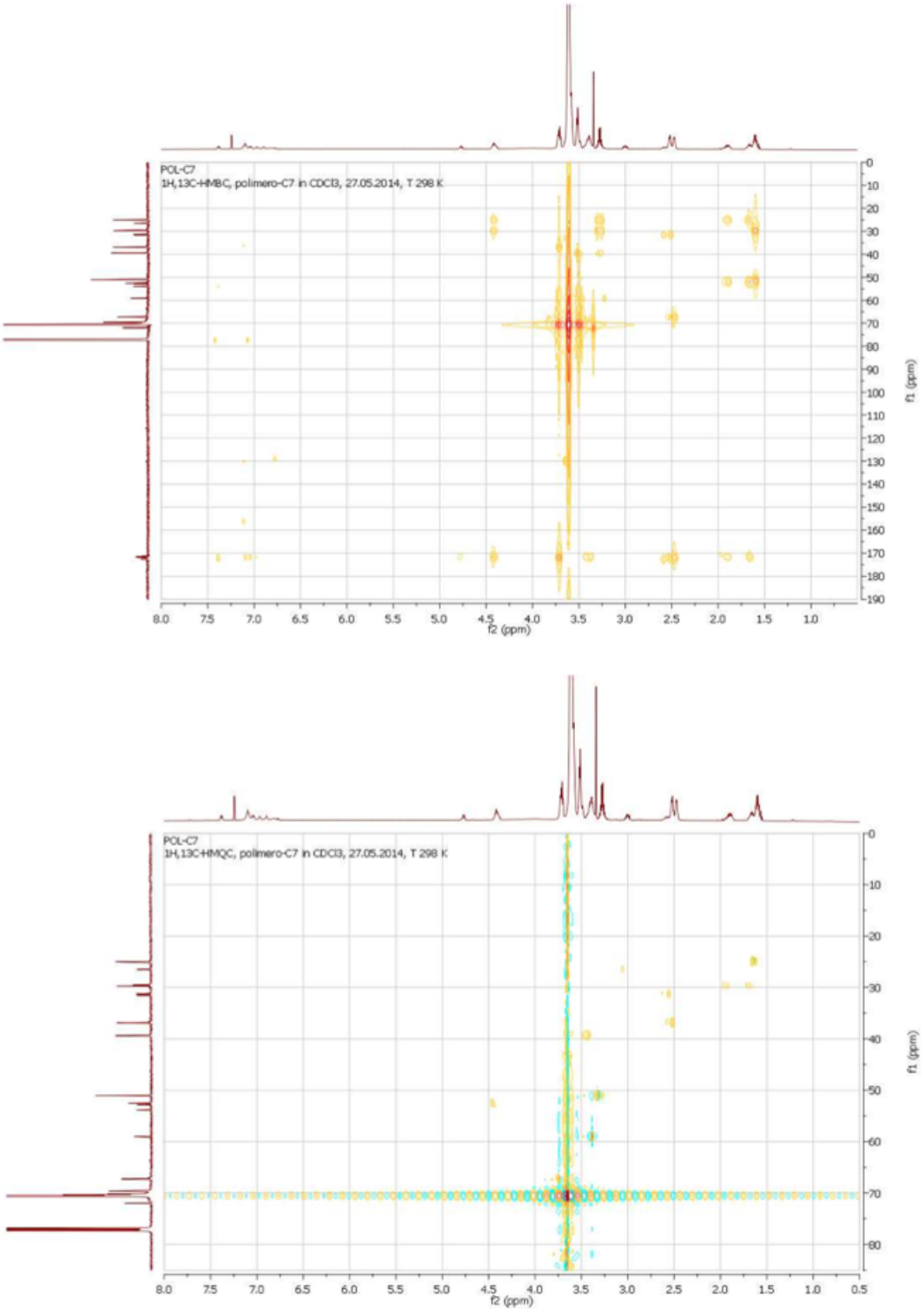

Figure 5.11: The bi-dimensional NMR specra of 7c in $CDCl_3$ at ambient temperature.

The final steps on the synthesis of "SuperDOTA-Gd(III)"

As just discussed before, we chose the Huisgen reaction to link DOTA residues to *7c*. Dibenzocyclooctyne was used for the strained alkyne moiety that we linked to a DOTA derivative with an amide bond. The reaction scheme is reported in Figure 5.12.

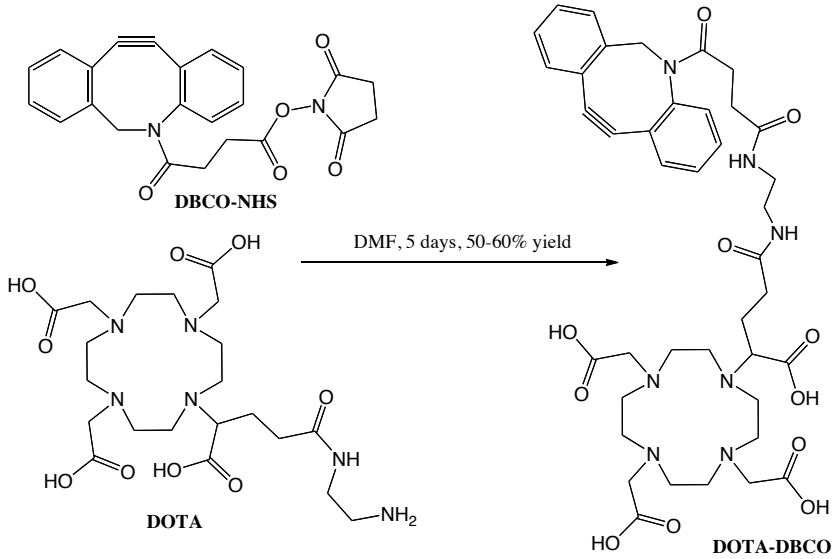

Figure 5.12: The reaction scheme between DOTA and dibenzocyclooctyne-NHS.

The different physicochemical properties of the two reagents allowed to obtain a 50-60% reaction yield. In fact, DBCO-NHS is slightly polar while DOTA is water soluble.

The final product DOTA-DBCO still remains soluble in water due to the polar properties of DOTA. This was also verified by the fact that when Gadolinium cations were added and the complex formed, a precipitation occurred. The solid obtained was no more soluble in a wide variety of solvents and its MALDI-TOF mass spectrometry revealed that the Gd complex was present.

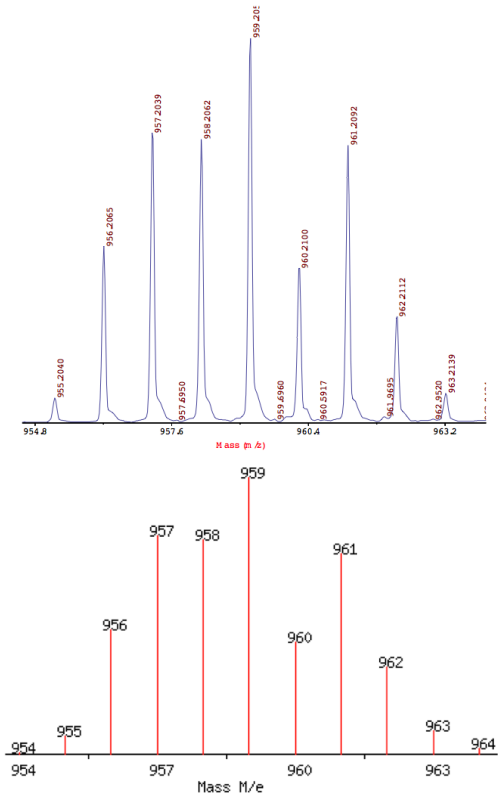

Figure 5.13: MALDI-TOF mass spectra of Gd-DOTA-DBCO insoluble crystals (up), DHAP-TFA was used as matrix. Theoretical mass 959.1 Da; experimental 959.2 m/z ($[M]^-$). The mass spectra was obtained in negative ionization modality, since the total net charge of Gd-DOTA-DBCO is -1. The isotopic distribution follows the simulation provided for the same molecule (down), as a confirmation of its identity.

The ability of DOTA-DBCO to coordinate Gd^{3+} ions was quantitatively evaluated adding a known excess of $GdCl_3$. The unreacted Gd^{3+} was retro-titrated with EDTA and Xylenol Orange as indicator.[97] Our results give a complexation yield of 98.6% over the total DOTA content. This evidence shows two crucial synthetic results: the coordination chemistry of DOTA still remains quantitative after the reaction and the synthesis was contaminant-free, maintaining the macrocycles empty.
Due to the extremely low solubility of Gd-DOTA-DBCO, the *Cu-free click chemistry* between *7c* and DOTA-DBCO was carried out first. The Gadolinium complexation becomes, therefore, the last step, as shown in Figure 5.14.

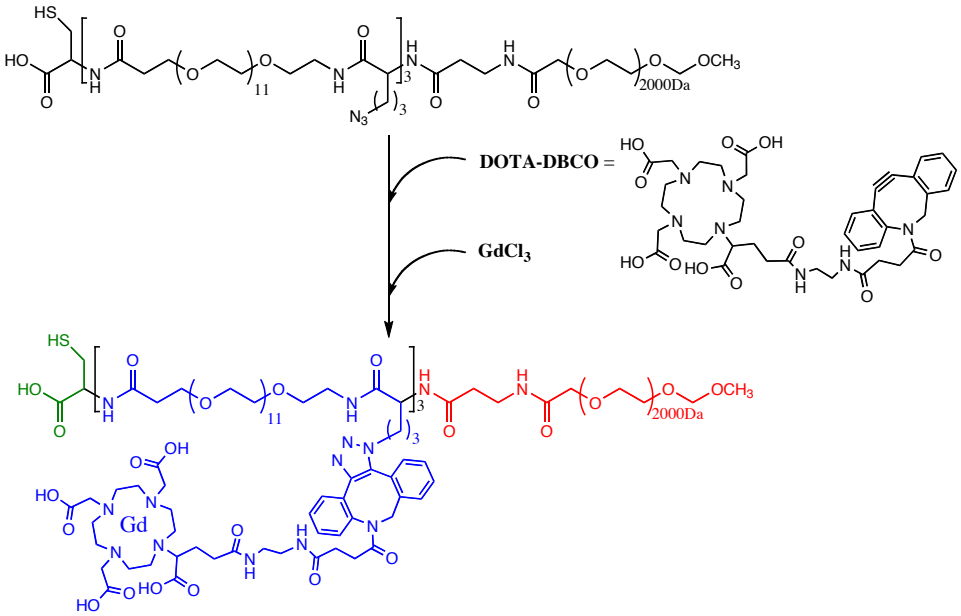

Figure 5.14: A schematic representation of the two final steps for the production of SuperDOTA-Gd. The Gd-DOTA-DBCO is extremely insoluble, so the click chemistry was operated before the complexation.

The Huisgen cycloaddiction was performed simply mixing *7c* and DOTA-DBCO in aqueous solution at room temperature for one day.
Despite the *click* reaction gives quantitative yields, as proved by a test reaction between *6c* and DBCO (data not shown), the complete characterization of the final *SuperDOTA* presented some not trivial complications.
The reaction mixture was first purified by centrifugation, utilizing filtering membranes with 2000 Da molecular cut-off.
The product stopped on the membrane was re-dissolved and analysed by reverse phase HPLC. Despite the chromatogram showed a single, quite broad, signal (see Figure 5.15), the reference chromatogram of *7c* was not available because its polarity made its elution too fast.

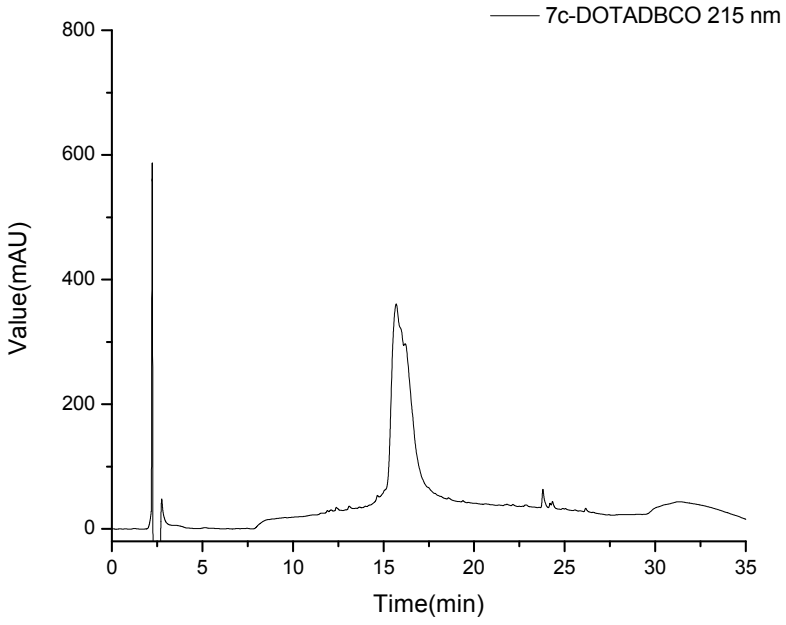

Figure 5.15: HPLC chromatogram of the purified reaction between 7c and DOTA-DBCO. The only, intense, signal is attributed to the SuperDOTA product.

In contrast, the MALDI-TOF mass spectra of *7c*, just reported in Figure 5.9, shows clear signals, while the purified reaction product results only in the slightly broad band reported in Figure 5.16.

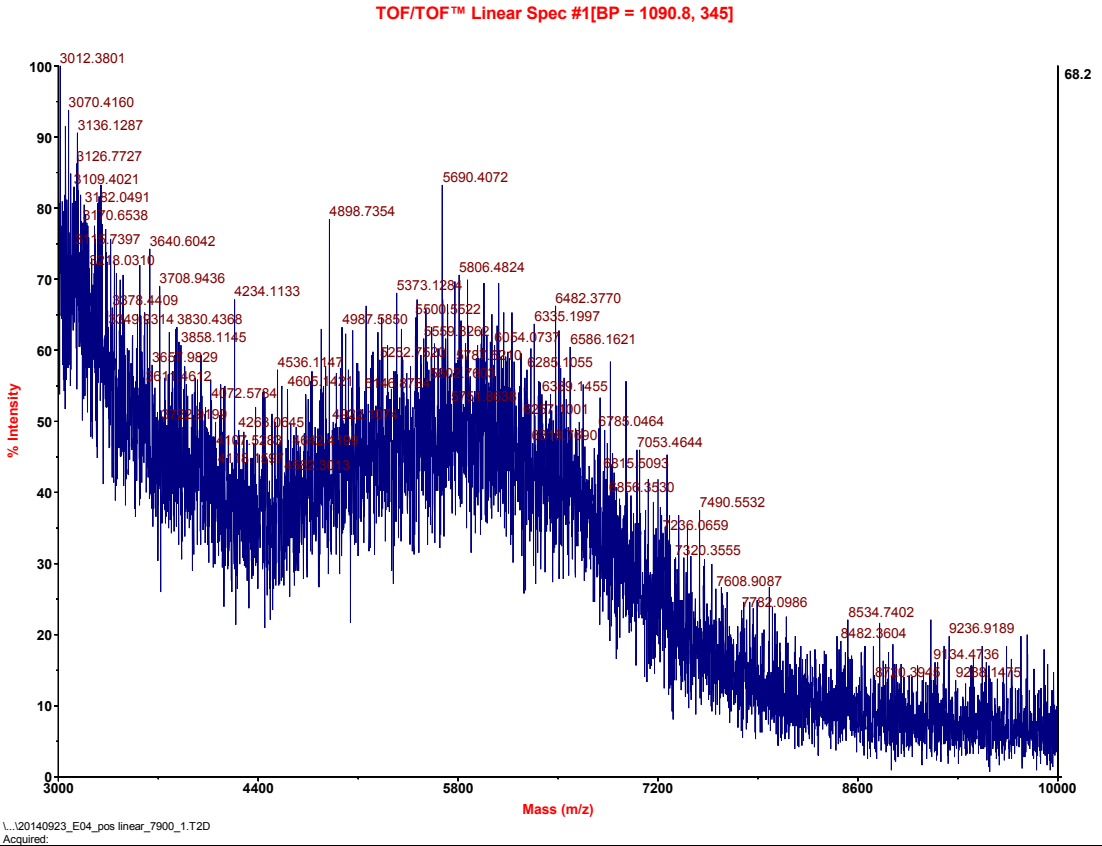

Species	***Molecular Weight, g/mol***
7c	4350 (distribution centre)
DOTA-DBCO	805
7c + DOTA-DBCO	5155
7c + 2 DOTA-DBCO	5960
7c + 3 DOTA-DBCO	6765

Figure 5.16: MALDI-TOF spectra of the purified reaction between 7c and DOTA-DBCO (up), DHAP-TFA was used as matrix. The table (down) reported the predicted mass peaks for 7c, DBCO and for different grades of coupling yields between these two.

The predicted mass centre distributions, reported in the table associated to Figure 5.16, compared to the experimental mass spectra, seems to suggest that the number of DOTA-DBCO linked to the *7c* chain could be less than three. The reason for such a result was not further investigated.
After the coordination with Gadolinium ions, provided by an excess of $GdCl_3$, the titration of thiol content gave us a *SuperDOTA-Gd* concentration value, since only one SH is present for each polymer chain.
This quantitative titration was made using the 4,4'-dithiodipyridine, that develops high absorptions at 324 nm in presence of mercaptan groups.[98-100]
The concentration of *SuperDOTA-Gd* obtained in water was found to be 35 μM.

The magnetic resonance T_1 decay was than measured diluting the same solution and was than compared to an aqueous solution of $GdCl_3$.
The results, in term of $1/T_1$, reported in Table 5.3 show a relaxivity calculated value of 14.1 $mM^{-1} \cdot s^{-1}$ per $GdCl_3$ and 25.9 $mM^{-1} \cdot s^{-1}$ per *SuperDOTA-Gd*.

Table 5.3: Magnetic resonance relaxation times measured for aqueous solutions. The relaxivity values were calculated according to the Equation 5.1. Experimental magnetic field of 4.7T (200MHz).

$1/T_1$ (ms^{-1})	Concentration (μM)	Relaxivity ($mM^{-1} \cdot s^{-1}$)
$GdCl_3$		
0.00746	500	14.1
0.00372	250	
0.00103	50	
$7.358 \cdot 10^{-4}$	25	
$5.227 \cdot 10^{-4}$	10	
SuperDOTA-Gd		
$8.613 \cdot 10^{-4}$	17.5	25.9
Water		
$4.087 \cdot 10^{-4}$	-	-

The relaxivity calculated for *SuperDOTA-Gd* was higher than that for a solution of free Gadolinium proving the characteristic of effective imaging contrast of the new polymer.
Plotting the inverse of the relaxation time versus the gadolinium concentration, as in Figure 5.17, an estimation of the gadolinium content in *SuperDOTA-Gd* is possible.
The comparison between the total polymer and the interpolated Gadolinium concentration gives an estimation of about 2 Gadolinium ions per polymer chain. The same result was previously found with MALDI-TOF mass spectrometry analysis.

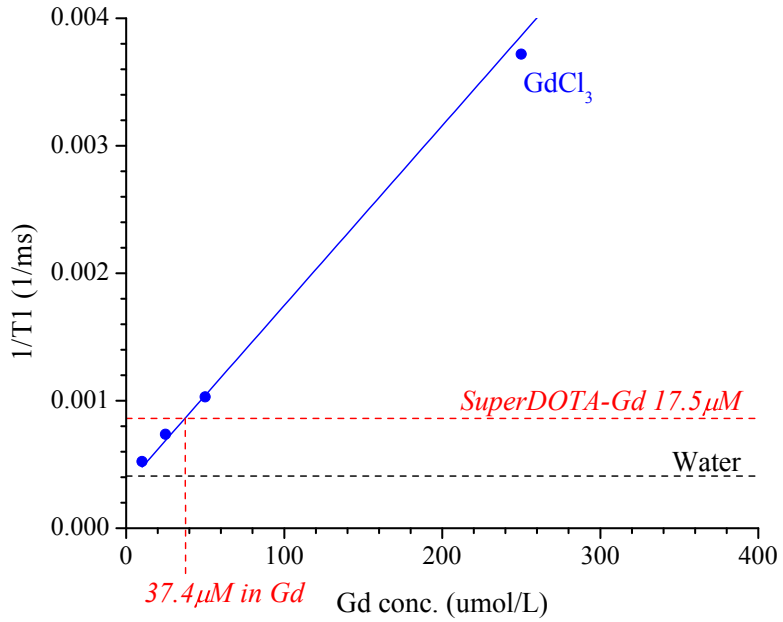

Figure 5.17: The inverse of the relaxation time T_1 versus the concentration of Gd^{3+} for a solution of $GdCl_3$, SuperDOTA-Gd and for pure water as reference.

Functionalization of gold nanoparticles and multimodal imaging characterization

The same solutions of *SuperDOTA-Gd* used for the characterizations were than used for the synthesis of SERS-MRI multimodal contrast agents.
Gold nanoparticles (AuNPs) obtained by laser ablation were first functionalized with lipoic Nile Blue (LipNB), namely one of the optimized SERS reporters. LipNB is able to develops high SERS signals both excited at 633 and at 785nm, as just reported in previous chapters.
The presence of the dye molecules causes a little degree of aggregation, probably due to the reduction of free charges at the surface of nanoparticles.
After a purification steps, performed by centrifugation, an excess of *SuperDOTA-Gd* is added and the functionalization reaction was carried out for one day, to guarantee the maximum coverage of the AuNPs surface.
The reaction mixture was centrifuged to purify the nanoparticles, that were re-dispersed in pure water.
In Fig. 18 are reported the UV-vis and SERS spectra. The Uv-vis spectrum shows that the effective aggregation of the nanoparticles is not very high, whereas the Raman signals of LipNB, shows a very good SERS activity .

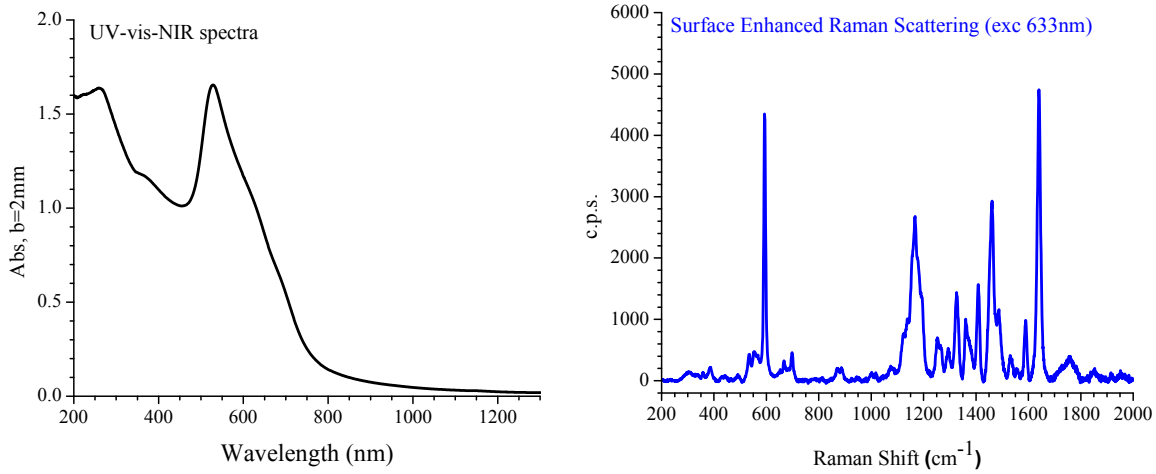

Figure 5.18: UV-vis-NIR absorption spectra (left) and the SERS spectra (right) of AuNP-LipNB-SuperDOTA complex in aqueous solution, Exciting line at 633 nm and 7 mW laser power, with a 5x objective focused at the centre of the cuvette were used.

The concentration of nanoparticles were evaluated by a fitting algorithm[6] of their absorption spectra. The AuNPs concentration of the final colloidal solution was calculated to be about 10.4 nM.
In Table 5.4 are reported the magnetic relaxation times and the relaxivity values for the synthesized SERS-MRI multimodal contrast agent.

Table 5.4: Magnetic resonance relaxation times measured for aqueous solutions. The relaxivity values were calculated according to the Equation 5.1. Experimental magnetic field of 4.7 T (200 MHz).

$1/T_1$ (ms^{-1})	Concentration (nM)	Relaxivity ($mM^{-1} \cdot s^{-1}$)
AuNP-LipNB-SuperDOTA-Gd complex		
$4.435 \cdot 10^{-4}$	10.4	3340
Water		
$4.087 \cdot 10^{-4}$	-	-

The relaxivity value of 3340 $mM^{-1} \cdot s^{-1}$, well reflects the high number of Gadolinium ions present on a single nanoparticle.
It is an impressive value if compared to the relaxation properties of $GdCl_3$ and to these reported in Table 5.1 obtained at 20 MHz field, also considering the approximations done for the nanoparticles concentration calculation.
The estimation of the number of Gd ions per AuNP can be done in the same way just used for *SuperDOTA*. However, in this case, the long magnetic relaxation time shown for the 10.4 nM nanoparticle solution does not allow a direct interpolation with the reference $GdCl_3$ solution, as seen in Figure 5.19.

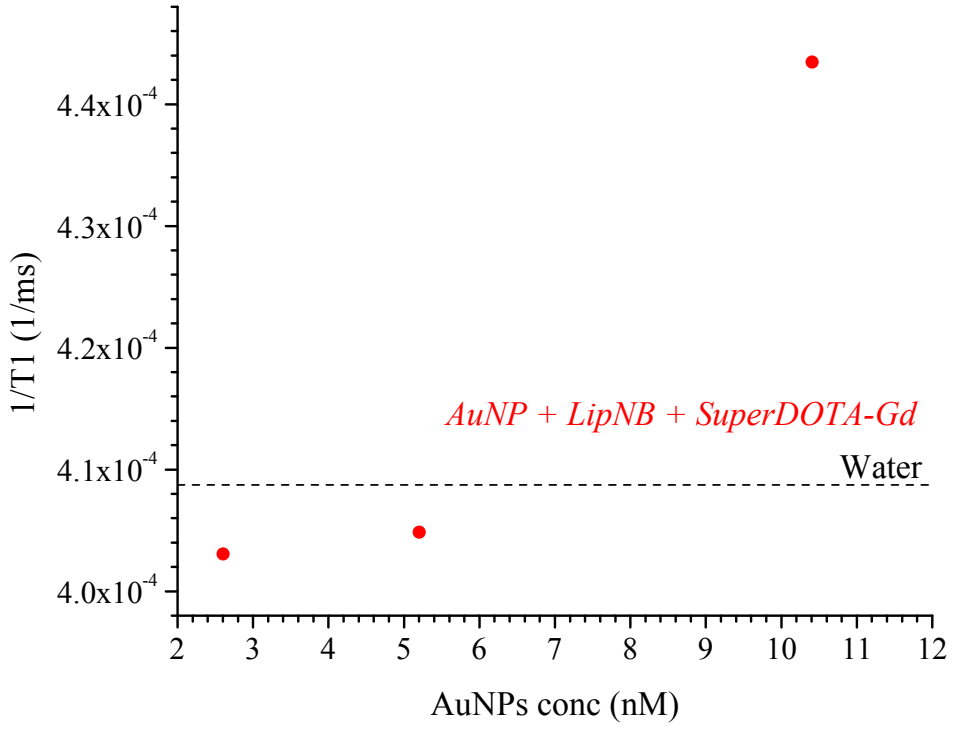

Figure 5.19: The inverse of the relaxation time T_1 for AuNP-LipNB-SuperDOTA-Gd goes rapidly to values comparable to pure water. The direct graphical evaluation of the Gadolinium content with the reference solution of $GdCl_3$ is no more possible.

However, according to the Equation 5.1 and the relaxivity value for $GdCl_3$ reported in Table 5.3, a Gd content of about 2.5 μM was found for the 10.4 nM AuNPs colloidal solution. This corresponds to an average content of about 240 Gd ions per AuNP, or an average value of 120 *SuperDOTA* molecules per AuNP.
Despite the concentration of *SuperDOTA* chains are not very high, they are clearly sufficient for a good magnetic contrast and further experiments will show the degree of applicability of such SERS-MRI multimodal as contrast agents *in vivo*.

6. Summary and Conclusions

The ability of modern science in exploiting the properties and dynamics of nanometre systems, opened the way to the development of a completely new class of materials. Between bulk materials and molecules, nanometre systems show properties with strong dependence on dimensions, still maintaining, in some cases, some order characteristic of a solid.

Among nanostructures, metallic nanoparticles are interesting for their plasmonic properties and as new tools for spectroscopy. Free electrons of a metallic nanoparticles can be excited by an electromagnetic field and the resonance condition is called Localized Surface Plasmon Resonance (LSPR). Molecular species in close proximity to the surface of nanoparticles can feel the incident electromagnetic field enhanced by the LSPR. New spectroscopic techniques grew up exploiting this phenomenon, like Surface Enhanced Raman Spectroscopy (SERS)[14, 15] and Surface Enhanced InfraRed Absorption (SEIRA).[87]

Usually, molecules show low Raman cross sections, but near to a plasmonic surface they can show increased scattering efficiency, by $10^7 – 10^9$ times,[14, 15] making SERS an attractive new spectroscopic tool.

In the present work, nanoparticles have been obtained with the Laser Ablation Synthesis in Solution (LASiS), a recent top-down technique for the production of nanomaterials, directly as colloidal solution without the need of any stabilizing molecule.[26] A typical procedure consists in irradiating a pure metal target immersed in water or in an organic solvent. The irradiation is carried out with a nanosecond pulsed Nd:YAG Laser at the fundamental wavelength. Especially in case of noble metal nanoparticles in water, the synthesis allows to obtain indefinitely stable colloidal nanoparticles with bare surfaces.[27]

AuNP from LASiS for Mass Spectrometry

In recent years, much attention of oncologic clinical practice was focused on the personalization of therapies. At present, the best analytical performances for therapeutic drug monitoring and for a wide range of anticancer drugs are provided by chromatographic techniques, coupled with mass spectrometry.[36]

Matrix Assisted Laser Desorption Ionization (MALDI) is a *soft-ionization* technique for mass spectrometry, frequently used in combination with a *time-of-flight* detection technique.[101] Interesting studies in literature report the utility of MALDI for proteins and peptides characterization,[5, 101, 102] also coupled with mapping and imaging of tissues.[101, 102] The drawback of the technique is that the low mass region cannot be used because the organic matrix signals dominate.

A systematic study on Laser Desorption Ionization (LDI) using gold nanoparticles as matrix is presented in the present thesis work.[28] Five low mass molecules were considered: arginine (174 g/mol), fructose (180 g/mol), atrazine (216 g/mol), anthracene (178 g/mol) and paclitaxel (854 g/mol). Compared to both commercially available nanoparticles and DHAP (a widely used organic matrix), the LASiS produced AuNP with negligible background in the entire mass range. The influence of surface coverage versus particles dimension was also investigated. Although the large excess of surfactant present in commercial nanoparticles was removed by dialysis before the measurement, a consistent amount of these stabilizing molecules remained on the AuNP. This fact was clearly observed in the background associated with that

kind of particles. Two types, LASiS and commercial AuNP, were used, with average size of 10 and 20 nm. In terms of signal-to-noise ratio, a stronger dependence on surface purity instead of dimensions was found.[28] The results show that LASiS AuNP assisted LDI overcome the main limitation of this mass spectrometry technique, making it useful in the low mass region (<500 Da).[28]

SERS for cancer drug detection

There are excellent examples in the field of sensor devices based on plasmonic noble metal nanoparticles, which use the optical properties of the LSPR or related effects like SERS.[5] SERS is attractive because it allows to use fingerprint information (from the vibrational spectra) with intensities comparable to fluorescence.[14, 15] This characteristic makes it an excellent qualitative technique, although for quantitative analysis some care must be used, like fluorescence.[13] The strongest field enhancement in a SERS substrate comes from only few *hot-spots* where the excited plasmons have positive interferences, like in junctions between particles or in tips.[15] Moreover, the complete coverage of the nanoparticles causes saturation effects.[13] In order to study limitations of SERS, the same amount of anticancer drugs (Sunitinib, Paclitaxel, Irinotecan and its active metabolite SN38) was spotted over different plasmonic substrates.[12] . We also used a commercial SERS substrate (Klarite, Renishaw®) where drugs were spotted over fixed area by using a home-made viton mask. The measurements were obtained with different laser excitations: 488, 633 and 785 nm. Results show that LASiS AgNPs give the highest signals. This was expected since silver nanoparticles have very good SERS performances[13-15] and the nanoparticles produced by laser ablation have a clean surface which favours hot-spots.[28] However, Klarite was found to be a good SERS substrate for quantitative evaluation at 633 nm, because of the higher reproducibility of the SERS signals. The SERS signals intensity for the four drugs were found to be highly correlated to the distance of their maximum absorption wavelength to the laser excitation. Sunitinib showed the lowest limit of detection, being the wavelength of its absorption maximum near to the laser excitation at 633 nm. Paclitaxel was found the worst SERS performer at 633 nm over Klarite, since its maximum absorption is present near UV. It was also found that Sunitinib spectra show a linear intensity variation between 125 and 2657 pmol per millimetre square of SERS active area, and a detection limit (DL) between 26 and 37 pmol/mm^2. Irinotecan has the same linear correlation between 191 and 3886 pmol/mm^2, with a DL in the 58-68 pmol/mm^2 range. SN-38 has linear intensity variation between 153 and 1580 pmol/mm^2 and a DL of 29-72 pmol/mm^2.[12]

Since the SN-38 is an active metabolite of Irinotecan, and can be present together in real samples, a procedure based on multivariate analysis was developed to distinguish between solutions of the pure substances and mixtures.

The results showed that quantitative detection of anticancer drugs by SERS could be a realistic tool for clinical practice with sample volumes of few millilitres.

One of the main problem of these analyses is the low SERS cross sections of some analytes which is an intrinsic limit for the technique.

Reactive-SERS

To overcome the problem of molecules with poor SERS performance, a reagent for specific molecular functional groups, showing, after reaction, different SERS signatures was found. Therefore, new SERS signatures increase in intensity with the analyte concentration. Such a protocol was called *Reactive-SERS*. The reagent is an aromatic azide functionalized with a thiol. In a polar aprotic solvent, the reaction

between the aromatic azide and a primary, or secondary, amine takes place by irradiating with a common UV lamp for 10 minutes.[103] In a second step the adduct is linked to the surface of gold nanoparticles with the thiol group. The SERS spectra of the solution, or of some dried drops on a glass slide, were obtained, with a time exposure of few tens of seconds. The reaction and SERS quantitative measurements were verified by mass spectrometry with, as a model analyte, diethylamine (DEA). We found that the variations of the intensity of the SERS spectra changed linearly with DEA concentration up to 8.65 mM.

Tumour Cell antigens identification with SERS

Since Raman spectroscopy provides sharp and characterizing vibrational signature of molecules, it is suitable for *multiplexing analysis*, that is the simultaneous detection of different analytes with a single measurement. In recent literature, some examples of the potentials of SERS for multiplexing can be found.[5, 13, 16, 104] In the present thesis work the mutlplexing analysis of prostatic cancer cells, using SERS nanotags functionalized with selected dyes and antibodies is demonstrated with a very important result for the good targeting specificity of the two prostatic cancer antigens PSMA and PSCA.[74] In a typical synthesis of the nanostructures, the first step is the aggregation of gold nanoparticles, obtained by a controlled centrifugation. These nanosystems still remain soluble and provide very efficient *hot spot* structures. Than the nanostructures are functionalized with a thiolated dye and an antibody for a specific targeting.

The selection of dyes to associate to antibodies is a crucial step. A library of five dyes was selected with the following properties: 1. absorption spectrum in resonance with the excitation laser lines, 2. presence of a thiol for their strong linking to the nanoparticles surface and 3. characteristic SERS spectrum which allows their easy identification. In the first study, as recalled above, we used two nanosystems, the first associating TexasRed and anti-PSMA antibody, and the second Malachite Green and anti-PSCA antibody.[74] After incubation of the nanosystems with tumour cells, we were able to recognize their antigen expression by the SERS signature recorded for every cell. At present, due to the extended dye library, is possible to perform multiplexing analysis in complex mixtures of cell cultures, using up to five different types of antibody-associated nanoparticles.

SERS and Cultural Heritage

The characterization of proteins content in samples, especially in cultural heritage is an open analytical issue, often faced by immunological protocols.[105-108] Eggs, animal glue or other natural proteins were frequently used in ancient paints as binders for pigments or dyes.[105, 106] In a stratigraphic sample of a tiny amount of such a paints, these organic moieties can be recognized by the antibody functionalized SERS tags. In addition, other interesting compounds, present in the paints, like for example inorganic crystals acting as pigments or simple degradation or aging products, can be recognized at the same time in the Raman spectrum. By mapping the stratigraphic sample, previously treated with SERS tag, a complete characterization of the inorganic and protein matter can be obtained. The methodology was applied for obtaining the presence of ovalbumin in a Renaissance artefact and, at the same time, for identifying the presence of inorganic materials, like azurite, and lead white.[49]

Processing and PCA of experimental SERS spectra

The post processing and analysis of the recorded experimental spectra, for applications both in nanomedicine and in cultural heritage, is a challenge issue. At least hundreds of spectra had to be taken simultaneously into account and every interesting species had to be recognised by its signature. Every frequency in hundreds of vibrational spectra acts as a variable. Therefore, multivariate analysis becomes very useful to rationalize Raman mapping images.[109]

For processing the experimental SERS spectra, several graphical interfaces based on MatLab® codes have been developed. For nanomedicine application, an interactive algorithm was also defined for the localization of cells on the samples. This allowed the automated recording of the spectra of hundreds or thousands of cells. Then, together with routines to manipulate the spectra, the codes for a complete analysis of the signals also with a PCA approach, have been developed.

Engineered nanostructures were also used for mapping tumours in live organisms.

Multifunctional nanostructures

Magnetic Resonance Imaging (MRI) is a powerful technique for *in vivo* imaging, utilizing non-ionizing radiation.[19] The image contrast is obtained with differences in protons relaxation times, so the efficiency of MRI is strongly related to proton density, but also to the presence of contrast agents (CAs).[19] MRI is a good technique for the total body screening because the radiations used are safe. However, MRI lacks in spatial resolution and it is not suitable for intrasurgical imaging.[19,22,91]

Nanotechnology offers the possibility to manage different functionalities into a single nanostructure.

The ablation process used to synthesize nanoparticles works far from equilibrium, making possible to produce iron-gold alloy nanoparticles.[91] The plasmonic and magnetic properties are still present in these nanomaterials. Nanoparticles were functionalized with two thiolated dyes, TexasRed (TRSH) for 633 nm and Naphthalocyanine (NPCySH) for 785 nm wavelength, and used as Multimodal Contrast Agents (MCAs).[91] The magnetic relaxivity shown by the alloy nanoparticles was 60 $mM^{-1} \bullet s^{-1}$ which compares well with commercial contrast agents. These MCAs were injected into a Balb/c mice with a tumour and the accumulation of the nanostructures was evidenced by the enhanced T_2 relaxation time at the tumour site. The SERS spectra provided by TRSH, present on the AuFeNPs surface, was found *ex-vivo* in the liver, spleen, kidneys and tumour, while no signal was found in blood and lungs.

Nanoparticles as T_1 magnetic multifunctional contrast agents

Despite magnetic contrast agents based on the relaxation time T_2 are attractive, they provide negative imaging contrast.[19, 91] More interesting are usually considered CAs which operate on the longitudinal T_1 relaxation time which are positive contrast agents.

Lanthanides, especially gadolinium ions, are used as positive magnetic CAs, since they influence the relaxation time T_1.[19, 22, 23] To improve the imaging properties of gold nanoparticles, a new chelating polymer, called *SuperDOTA* was planned and synthesized. This new macromolecule is able to load up to three Gd^{3+} ions per single chain and have a thiol group that guarantees a stable bonding to the AuNP surface.

SuperDOTA was synthetized in solid phase using a cysteine pre-loaded Wang resin. It consists of a backbone made of three parts. The fist is a cysteine, for the binding to the gold surface. The second is a sequence, repeated three times, of 5-Azido-2-(amino)pentanoic acid and H_2N-PEG_{11}-COOH, where the azido functional groups is used for further functionalization via click chemistry. The third is a H_2N-PEG_{2000}-OCH_3 for *in vivo* stealth purposes. The Huisgen azide-alkyne cycloaddition was used to bind DOTA-dibenzocyclooctyne residues to the polymer, before the loading with Gd^{3+}. Gold nanoparticles were functionalized first with lipoic-acid-NileBlue, a SERS reporter, and then with the *SuperDOTA*-Gd. MRI measurements on these nanostructures show a magnetic relaxivity for AuNP-*SuperDOTA*-Gd of 3340 $mM^{-1} \bullet s^{-1}$ which is an interesting result also for *in vivo* applications.
Future perspectives will consider the functionalization with targeting moieties, which will give further perspectives to these nanoystems.

Conclusion

In conclusion, plasmonic nanostructures based on gold nanoparticles were used with interesting results for qualitative and quantitative analysis in biomedical and cultural heritage applications.
The laser ablation synthesis in solution allowed the production of gold nanoparticles which are particularly useful for these types of applications since their naked surface enhances SERS signals and allows their easy functionalization.
SERS signals was optimized with derivative of dyes which allowed the registration of SERRS signals. These signals show cross section of the order of those of fluorescent molecules, but can be used for multiplexing experiments which are not simple or possible with fluorescent compounds.
Engineering nanostructures opens many possible applications and some of them have been explored like for example targeting of antigens on tumour cells or the synthesis of multifunctional nanostructures combining particularly SERS and MRI, which are complementary techniques also for in vivo applications.
The results presented in this thesis work show the high potentiality of nanotechnology in solving challenging tasks and open the ways to other new applications.

7. My Publications (2012 – 2014)

11 L. Litti, *Studio di NanoMedicina a base di Particelle di Oro Funzionalizzate,* Edizioni Accademiche Italiane, 2014, ISBN: 978-3-639-46961-5.

12 L. Litti, V. Amendola, G. Toffoli and M. Meneghetti, Detection of low-quantity chemotherapy drugs by surface enhanced Raman scattering (SERS), *In preparation*.

28 V. Amendola, L. Litti and M. Meneghetti, *Anal. Chem.,* 2013, **85**, 11747-11754.

49 G. Sciutto, L. Litti, C. Lofrumento, S. Prati, M. Ricci, M. Gobbo, A. Roda, E. Castellucci, M. Meneghetti and R. Mazzeo, *Analyst,* 2013, **138**, 4532-4541.

74 M. Meneghetti, A. Scarsi, L. Litti, G. Marcolongo, V. Amendola, M. Gobbo, M. Di Chio, A. Boscaini, G. Fracasso and M. Colombatti, *Small,* 2012, **8**, 3733-3738.

87 I. Bonacini, S. Prati, M. Quaranta, G. Sciutto, A. Ricci, L. Litti, M. Meneghetti and R. Mazzeo, *Heritage Science,* 2014, **Accepted**.

91 V. Amendola, S. Scaramuzza, L. Litti, M. Meneghetti, G. Zuccolotto, A. Rosato, E. Nicolato, P. Marzola, G. Fracasso and C. Anselmi, *Small,* 2014, **10**, 2476-2486.

8. References

1 M. Daniel and D. Astruc, *Chem. Rev.,* 2004, **104**, 293-346.

2 C. L. Cleveland, U. Landman, T. G. Schaaff, M. N. Shafigullin, P. W. Stephens and R. L. Whetten, *Phys. Rev. Lett.,* 1997, **79**, 1873.

3 V. Petkov, Y. Peng, G. Williams, B. Huang, D. Tomalia and Y. Ren, *Physical Review B,* 2005, **72**, 195402.

4 K. M. Mayer and J. H. Hafner, *Chem. Rev.,* 2011, **111**, 3828-3857.

5 J. N. Anker, W. P. Hall, O. Lyandres, N. C. Shah, J. Zhao and R. P. Van Duyne, *Nature materials,* 2008, **7**, 442-453.

6 V. Amendola and M. Meneghetti, *The Journal of Physical Chemistry C,* 2009, **113**, 4277-4285.

7 H. Häkkinen, *Nature chemistry,* 2012, **4**, 443-455.

8 P. D. Jadzinsky, G. Calero, C. J. Ackerson, D. A. Bushnell and R. D. Kornberg, *Science,* 2007, **318**, 430-433 (DOI:318/5849/430 [pii]).

9 A. Cossaro, R. Mazzarello, R. Rousseau, L. Casalis, A. Verdini, A. Kohlmeyer, L. Floreano, S. Scandolo, A. Morgante, M. L. Klein and G. Scoles, *Science,* 2008, **321**, 943-946 (DOI:10.1126/science.1158532 [doi]).

10 E. V. Efremov, F. Ariese and C. Gooijer, *Anal. Chim. Acta,* 2008, **606**, 119-134.

11 L. Litti, *Studio di NanoMedicina a base di Particelle di Oro Funzionalizzate,* Edizioni Accademiche Italiane, 2014, ISBN: 978-3-639-46961-5.

12 L. Litti, V. Amendola, G. Toffoli and M. Meneghetti, Detection of low-quantity chemotherapy drugs by surface enhanced Raman scattering (SERS), *In preparation*.

13 G. McNay, D. Eustace, W. E. Smith, K. Faulds and D. Graham, *Appl. Spectrosc.,* 2011, **65**, 825-837.

14 C. L. Haynes, A. D. McFarland and R. P. V. Duyne, *Anal. Chem.,* 2005, **77**, 338 A-346 A.

15 M. Moskovits, *Physical Chemistry Chemical Physics,* 2013, **15**, 5301-5311.

16 Y. Wang, B. Yan and L. Chen, *Chem. Rev.,* 2012, **113**, 1391-1428.

17 S. Nie and S. R. Emory, *Science,* 1997, **275**, 1102-1106.

18 V. Amendola and M. Meneghetti, *Advanced Functional Materials,* 2012, **22**, 353-360.

19 L. Frullano and T. J. Meade, *JBIC Journal of Biological Inorganic Chemistry,* 2007, **12**, 939-949.

20 S. S. Kelkar and T. M. Reineke, *Bioconjug. Chem.,* 2011, **22**, 1879-1903.

21 P. Caravan, J. J. Ellison, T. J. McMurry and R. B. Lauffer, *Chem. Rev.,* 1999, **99**, 2293-2352.

22 M. F. Kircher, A. de la Zerda, J. V. Jokerst, C. L. Zavaleta, P. J. Kempen, E. Mittra, K. Pitter, R. Huang, C. Campos and F. Habte, *Nat. Med.,* 2012, **18**, 829-834.

23 Y. Song, X. Xu, K. W. MacRenaris, X. Zhang, C. A. Mirkin and T. J. Meade, *Angewandte Chemie International Edition,* 2009, **48**, 9143-9147.

24 P. Atkins and J. De Paula, *Atkins' physical chemistry*, Oxford University Press, 2014.

25 J. T. Bushberg and J. M. Boone, *The essential physics of medical imaging*, Lippincott Williams & Wilkins, 2011.

26 V. Amendola and M. Meneghetti, *Physical chemistry chemical physics,* 2009, **11**, 3805-3821.

27 V. Amendola and M. Meneghetti, *Physical Chemistry Chemical Physics,* 2013, **15**, 3027-3046.

28 V. Amendola, L. Litti and M. Meneghetti, *Anal. Chem.,* 2013, **85**, 11747-11754.

29 V. Amendola, G. A. Rizzi, S. Polizzi and M. Meneghetti, *The Journal of Physical Chemistry B,* 2005, **109**, 23125-23128.

30 E. Blanco, A. Hsiao, A. P. Mann, M. G. Landry, F. Meric-Bernstam and M. Ferrari, *Cancer science,* 2011, **102**, 1247-1252.

31 Y. Wang, P. Brown and Y. Xia, *Nature Materials,* 2011, **10**.

32 Z. Cheng, A. Al Zaki, J. Z. Hui, V. R. Muzykantov and A. Tsourkas, *Science,* 2012, **338**, 903-910.

33 A. Schroeder, D. A. Heller, M. M. Winslow, J. E. Dahlman, G. W. Pratt, R. Langer, T. Jacks and D. G. Anderson, *Nature Reviews Cancer,* 2011, **12**, 39-50.

34 G. Von Maltzahn, J. Park, K. Y. Lin, N. Singh, C. Schwöppe, R. Mesters, W. E. Berdel, E. Ruoslahti, M. J. Sailor and S. N. Bhatia, *Nature materials,* 2011, **10**, 545-552.

35 E. J. Sirot, van der Velden, Jan Willem, K. Rentsch, C. B. Eap and P. Baumann, *Drug Safety,* 2006, **29**, 735-768.

36 S. Nussbaumer, P. Bonnabry, J. Veuthey and S. Fleury-Souverain, *Talanta,* 2011, **85**, 2265-2289.

37 H. Chong, Y. Koo, B. Collins, F. Gomez and Y. Yun, *J Nanomed Biotherapeut Discov,* 2013, **3**, e122.

38 S. A. Soper, K. Brown, A. Ellington, B. Frazier, G. Garcia-Manero, V. Gau, S. I. Gutman, D. F. Hayes, B. Korte and J. L. Landers, *Biosensors and Bioelectronics,* 2006, **21**, 1932-1942.

39 R. D. Espy, N. E. Manicke, Z. Ouyang and R. G. Cooks, *Analyst,* 2012, **137**, 2344-2349.

40 S. Farquharson, C. Shende, F. E. Inscore, P. Maksymiuk and A. Gift, *J. Raman Spectrosc.,* 2005, **36**, 208-212.

41 J. Song, Z. Chen, J. Jin, Y. Chen and R. Yu, *Chemometrics Intellig. Lab. Syst.,* 2014, **135**, 31-36.

42 I. Hidi, A. Mühlig, M. Jahn, F. Liebold, D. Cialla, K. Weber and J. Popp, *Analytical Methods,* 2014, **6**, 3943-3947.

43 J. D. Wulfkuhle, L. A. Liotta and E. F. Petricoin, *Nature reviews cancer,* 2003, **3**, 267-275.

44 E. P. Diamandis, *J. Natl. Cancer Inst.,* 2004, **96**, 353-356.

45 E. A. Punnoose, S. K. Atwal, J. M. Spoerke, H. Savage, A. Pandita, R. Yeh, A. Pirzkall, B. M. Fine, L. C. Amler and D. S. Chen, *PloS one,* 2010, **5**, e12517.

46 V. Backman, M. Wallace, L. Perelman, J. Arendt, R. Gurjar, M. Müller, Q. Zhang, G. Zonios, E. Kline and T. McGillican, *Nature,* 2000, **406**, 35-36.

47 X. Wang, X. Qian, J. J. Beitler, Z. G. Chen, F. R. Khuri, M. M. Lewis, H. J. Shin, S. Nie and D. M. Shin, *Cancer Res.,* 2011, **71**, 1526-1532 (DOI:10.1158/0008-5472.CAN-10-3069 [doi]).

48 H. G. Edwards and T. Munshi, *Analytical and bioanalytical chemistry,* 2005, **382**, 1398-1406.

49 G. Sciutto, L. Litti, C. Lofrumento, S. Prati, M. Ricci, M. Gobbo, A. Roda, E. Castellucci, M. Meneghetti and R. Mazzeo, *Analyst,* 2013, **138**, 4532-4541.

50 J. L. Norris and R. M. Caprioli, *Chem. Rev.,* 2013, **113**, 2309-2342.

51 C. Chiang, W. Chen and H. Chang, *Chem. Soc. Rev.,* 2011, **40**, 1269-1281.

52 R. Pilolli, F. Palmisano and N. Cioffi, *Analytical and bioanalytical chemistry,* 2012, **402**, 601-623.

53 J. A. McLean, K. A. Stumpo and D. H. Russell, *J. Am. Chem. Soc.,* 2005, **127**, 5304-5305.

54 F. Bonaccorso, M. Zerbetto, A. C. Ferrari and V. Amendola, *The Journal of Physical Chemistry C,* 2013, **117**, 13217-13229.

55 C. Yuen, W. Zheng and Z. Huang, *Biosensors and Bioelectronics,* 2010, **26**, 580-584.

56 B. Blanchet, C. Saboureau, A. S. Benichou, B. Billemont, F. Taieb, S. Ropert, A. Dauphin, F. Goldwasser and M. Tod, *Clinica Chimica Acta,* 2009, **404**, 134-139.

57 P. Minkin, M. Zhao, Z. Chen, J. Ouwerkerk, H. Gelderblom and S. D. Baker, *Journal of Chromatography B,* 2008, **874**, 84-88.

58 S. M. Guichard, C. L. Morton, E. J. Krull, C. F. Stewart, M. K. Danks and P. M. Potter, *Clin. Cancer Res.,* 1998, **4**, 3089-3094.

59 G. Masi, A. Falcone, A. Di Paolo, G. Allegrini, R. Danesi, C. Barbara, S. Cupini and M. Del Tacca, *Clin. Cancer Res.,* 2004, **10**, 1657-1663.

60 D. E. Ettlinger, M. Mitterhauser, W. Wadsak, E. Ostermann, A. Farkouh, J. Schueller and M. Czejka, *Anticancer Res.,* 2006, **26**, 1337-1341.

61 A. Loren, C. Eliasson, M. Josefson, K. Murty, M. Käll, J. Abrahamsson and K. Abrahamsson, *J. Raman Spectrosc.,* 2001, **32**, 971-974.

62 C. Eliasson, A. Lorén, K. Murty, M. Josefson, M. Käll, J. Abrahamsson and K. Abrahamsson, *Spectrochimica Acta Part A: Molecular and Biomolecular Spectroscopy,* 2001, **57**, 1907-1915.

63 I. Chourpa, A. Beljebbar, G. D. Sockalingum, J. Riou and M. Manfait, *Biochimica et Biophysica Acta (BBA)-General Subjects,* 1997, **1334**, 349-360.

64 G. T. Hermanson, *Bioconjugate techniques*, Academic press, 2013.

65 S. Athanasas-Platsis, M. J. Somodevilla-Torres, H. Morton and A. C. Cavanagh, *Immunol. Cell Biol.,* 2004, **82**, 361-369.

66 A. Yakovlev, *Neurochemical Journal,* 2009, **3**, 139-144.

67 N. Gritsan and M. Platz, *Chem. Rev.,* 2006, **106**, 3844-3867.

68 S. Bräse, C. Gil, K. Knepper and V. Zimmermann, *Angewandte Chemie International Edition,* 2005, **44**, 5188-5240.

69 L. Karyakina and A. Oleinik, *High Energy Chemistry,* 2007, **41**, 109-113.

70 N. Gritsan and M. Platz, *Photochemistry of azides: the azide/nitrene interface*, John Wiley & Sons, Ltd.: West Sussex, UK, 2010.

71 U. Geiger, Y. Haas and D. Grinstein, *J. Photochem. Photobiol. A.,* 2014, **277**, 53-61.

72 J. A. Burns, J. C. Butler, J. Moran and G. M. Whitesides, *J. Org. Chem.,* 1991, **56**, 2648-2650.

73 Z. A. Nima, M. Mahmood, Y. Xu, T. Mustafa, F. Watanabe, D. A. Nedosekin, M. A. Juratli, T. Fahmi, E. I. Galanzha and J. P. Nolan, *Scientific reports,* 2014, **4**.

74 M. Meneghetti, A. Scarsi, L. Litti, G. Marcolongo, V. Amendola, M. Gobbo, M. Di Chio, A. Boscaini, G. Fracasso and M. Colombatti, *Small,* 2012, **8**, 3733-3738.

75 C. W. Lin, J. R. Shulok, S. D. Kirley, L. Cincotta and J. W. Foley, *Cancer Res.,* 1991, **51**, 2710-2719.

76 F. Ni, H. Feng, L. Gorton and T. M. Cotton, *Langmuir,* 1990, **6**, 66-73.

77 N. Ho, R. Weissleder and C. Tung, *Tetrahedron,* 2006, **62**, 578-585.

78 J. Jose, Y. Ueno and K. Burgess, *Chemistry-A European Journal,* 2009, **15**, 418-423.

79 K. K. Maiti, U. Dinish, A. Samanta, M. Vendrell, K. Soh, S. Park, M. Olivo and Y. Chang, *Nano Today,* 2012, **7**, 85-93.

80 A. Samanta, K. K. Maiti, K. Soh, X. Liao, M. Vendrell, U. Dinish, S. Yun, R. Bhuvaneswari, H. Kim and S. Rautela, *Angewandte Chemie International Edition,* 2011, **50**, 6089-6092.

81 K. KumaráMaiti, *Chemical Communications,* 2011, **47**, 3514-3516.

82 S. A. Hilderbrand, K. A. Kelly, R. Weissleder and C. Tung, *Bioconjug. Chem.,* 2005, **16**, 1275-1281.

83 A. K. Singh, M. A. Hahn, L. G. Gutwein, M. C. Rule, J. A. Knapik, B. M. Moudgil, S. R. Grobmyer and S. C. Brown, *Int. J. Nanomedicine,* 2012, **7**, 2739-2750 (DOI:10.2147/IJN.S28357 [doi]).

84 T. Rawling and A. McDonagh, *Coord. Chem. Rev.,* 2007, **251**, 1128-1157.

85 Z. Li and M. Lieberman, *Inorg. Chem.,* 2001, **40**, 932-939.

86 U. Dinish, G. Balasundaram, Y. Chang and M. Olivo, *Scientific reports,* 2014, **4**.

87 I. Bonacini, S. Prati, M. Quaranta, G. Sciutto, A. Ricci, L. Litti, M. Meneghetti and R. Mazzeo, *Heritage Science,* 2014, **Accepted**.

88 F. Bertorelle, M. Ceccarello, M. Pinto, G. Fracasso, D. Badocco, V. Amendola, P. Pastore, M. Colombatti and M. Meneghetti, *The Journal of Physical Chemistry C,* 2014, **118**, 14534-14541

89 A. Parma, I. Freris, P. Riello, D. Cristofori, C. de Julián Fernández, V. Amendola, M. Meneghetti and A. Benedetti, *Journal of Materials Chemistry,* 2012, **22**, 19276-19288.

90 S. Salmaso and P. Caliceti, *Journal of drug delivery,* 2013, **2013**.

91 V. Amendola, S. Scaramuzza, L. Litti, M. Meneghetti, G. Zuccolotto, A. Rosato, E. Nicolato, P. Marzola, G. Fracasso and C. Anselmi, *Small,* 2014, **10**, 2476-2486.

92 H. C. Kolb, M. Finn and K. B. Sharpless, *Angewandte Chemie International Edition,* 2001, **40**, 2004-2021.

93 J. C. Jewett and C. R. Bertozzi, *Chem. Soc. Rev.,* 2010, **39**, 1272-1279.

94 N. J. Agard, J. A. Prescher and C. R. Bertozzi, *J. Am. Chem. Soc.,* 2004, **126**, 15046-15047.

95 C. D. Walkey, J. B. Olsen, H. Guo, A. Emili and W. C. Chan, *J. Am. Chem. Soc.,* 2012, **134**, 2139-2147.

96 B. Merrifield, *Meth. Enzymol.,* 1997, **289**, 3-13.

97 A. Barge, G. Cravotto, E. Gianolio and F. Fedeli, *Contrast media & molecular imaging,* 2006, **1**, 184-188.

98 I. O. C. Egwim and H. J. Gruber, *Anal. Biochem.,* 2001, **288**, 188-194 (DOI:http://dx.doi.org/10.1006/abio.2000.4891).

99 D. R. Grassetti and J. F. Murray Jr., *Arch. Biochem. Biophys.,* 1967, **119**, 41-49 (DOI:http://dx.doi.org/10.1016/0003-9861(67)90426-2).

100 C. K. Riener, G. Kada and H. J. Gruber, *Analytical and bioanalytical chemistry,* 2002, **373**, 266-276.

101 R. Kaufmann, *J. Biotechnol.,* 1995, **41**, 155-175.

102 R. M. Caprioli, T. B. Farmer and J. Gile, *Anal. Chem.,* 1997, **69**, 4751-4760.

103 M. S. Panov, V. D. Voskresenska, M. N. Ryazantsev, A. N. Tarnovsky and R. M. Wilson, *J. Am. Chem. Soc.,* 2013, **135**, 19167-19179.

104 Y. C. Cao, R. Jin and C. A. Mirkin, *Science,* 2002, **297**, 1536-1540 (DOI:10.1126/science.297.5586.1536 [doi]).

105 L. Cartechini, M. Vagnini, M. Palmieri, L. Pitzurra, T. Mello, J. Mazurek and G. Chiari, *Acc. Chem. Res.,* 2010, **43**, 867-876.

106 A. Heginbotham, V. Millay and M. Quick, *Journal of the American Institute for Conservation,* 2006, **45**, 89-105.

107 B. Ramírez-Barat and S. de la Viña, *Studies in conservation,* 2001, **46**, 282-288.

108 G. Sciutto, L. S. Dolci, A. Buragina, S. Prati, M. Guardigli, R. Mazzeo and A. Roda, *Analytical and bioanalytical chemistry,* 2011, **399**, 2889-2897.

109 L. Zhang, M. J. Henson and S. S. Sekulic, *Anal. Chim. Acta,* 2005, **545**, 262-278.

Appendixes, experimental details

A1. Instrumentation

- *Laser for LASiS*
  Nd:YAG laser (Quantel YG-981E-10), 9ns pulse duration, 10Hz repetition rate.

- *micro-Raman*
  InVia micro-Raman (Renishaw), equipped with motorized stage, 5, 20 and 50x Leica objectives, 488nm Ar-Kr Laser, 633nm He-Ne Laser, 785nm diode Laser, CCD detector.

- *UV-vis-NIR spectrometer*
  Varian UV-vis-NIR Cary 5 Spectrometer

- *MALDI-TOF*
  AB SCIEX 4800 MALDI TOF/TOF Analyzer (AB SIEX Pte Ltd), equipped with a 355nm (3-7ns) pulses of a Nd:YAG laser at a repetition rate of 200Hz

- *ESI-TOF*
  Applied Biosystem 5220
  Mariner ESI-TOF, Perspective Biosystem

- *NMR spectrometer*
  Bruker Avance DMX 600, operating at 600 MHz

- *MRI spectrometer*
  Biospec tomograph (Bruker, Karlsruhe, Germany) with a working field of 4.7T

- *High Performance Liquid Chromatography*
  Dionex P680 equipped with Dionex ASI-100 auto-sampler and Dionex UVD170U detector.
  Vydac C18 218TP104 reverse phase column (250 x 4.6 mm, 5µm particles)
  Elution profile: 10 to 90% of eluent B in 30 minutes. Where eluent A is H_2O + 0.1% TFA, eluent B is 10% H_2O in CH_3CN + 0.1% TFA.

A2. Laser Ablation Synthesis in Solution

AuNP are synthesized by LASiS (laser ablation synthesis in solution) using 9 ns pulses at 1064 nm of a Nd:YAG laser.
The laser beam is focused with a lens (10 cm focal length) on a Au target at the bottom of a cell (3x3x4 cm) filled with 15 ml of 10^{-5} M NaCl bidistilled water solution. Fluences of 10 J•cm^{-2} are used for obtaining nanoparticles with average diameters of 20 nm.
The nanoparticle concentration was estimated by fitting their localised surface plasmon resonance absorption, according to the Mie-Gans model and the SPRFit algorithm.[6]
An example of AuNPs colloidal solution is reported in Figure A.1.

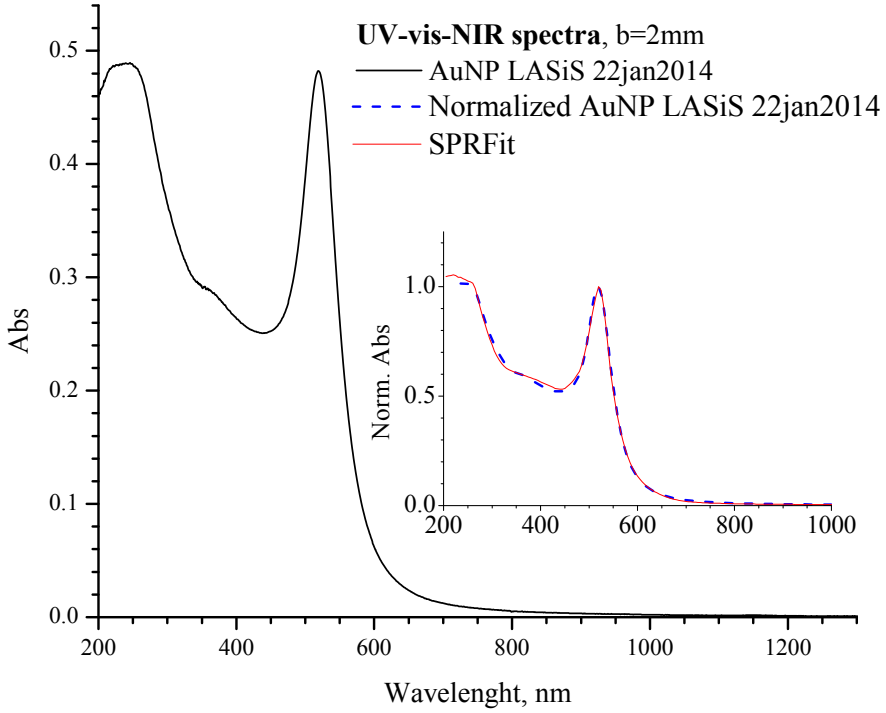

R (nm)	Spheres %	1-RSS	MaxSPA (m^2)	ε (cm^{-1}M^{-1})	Abs$_{b=2mm}$ (520nm)	AuNP conc. (mol/L)
9.7	96	4.15E-04	3.14E-16	8.23E+08	0.4818	2.93E-09

Figure A.1: The UV-vis-NIR absorption behaviour of a AuNP nanoparticle solution (up). The results obtained by the SPRFit algorithm, "R" is the average radius of nanoparticles, "Spheres" explain the percentage between spherical and spheroidal shaped nanoparticles, "1-RSS" is the residual sum of squares between the calculated and experimental spectra, "MaxSPA" is the AuNPs solution calculated extinction cross section and "ε" is the molar extinction coefficient, "Abs$_{b=2mm}$" is the maximum absorption location, "AuNP conc" is the estimated molar concentration of AuNPs.

A3. Gold nanoparticles for LDI (Laser Desorption Ionization) experiments

Experimental procedure reported from Ref. 28.

The following matrixes were used for MALDI-TOF mass spectrometry:

- DHAP (2',6'-dihydroxyacetophenone, Sigma Aldrich, CAS: 490-78-8) at 40g/L solution in CH_3CN, with also 0.1% of TFA (trifluoracetic acid)
- AuNP by LASiS, 10.6nm±22% (LASiS-AuNPs-I)
- AuNP by LASiS, 18.6nm±35% (LASiS-AuNPs-II)
- AuNP by Sigma Aldrich (G1527), 10.2nm±12% (citrate-AuNPs I)
- AuNP by BBI International (EM.GC20), 19.6nm±8% (citrate-AuNPs II)

To obtain the AuNP size reported above, pristine AuNPs were selected by centrifugal cycles. [54]

Briefly, an Eppendrof centrifuge model 5430 equipped with a fixed angle rotor model FA-45-24-11-HS was used. The smallest LASiS-AuNPs (LASiS-AuNPs-I) were obtained by collecting the surnatant after centrifugation at 800 rcf for 60 minutes. The largest LASiS-AuNPs (LASiS-AuNPs-II) were obtained in two centrifugation steps: pristine LASiS-AuNPs were centrifuged for 1 hour at 100 rcf and the sediment discarded, then the remaining solution was centrifuged again for 1 hour at 500 rcf and the sediment collected to give LASiS-AuNPs-II.

All nanoparticles were concentrated by dialysis concentration membranes with a cut off of 2000 Da (Sartorius Vivaspin) up to the same Au atoms concentration of about 0.013M (2.6 mg/ml). The concentration was evaluated by optical absorption spectroscopy according to the protocol described in literature. [6]

L-Arginine (200 mg/L in water), D(-)fructose (200 mg/L in water), atrazine (50 mg/L in methanol:water 1:1), anthracene (350 mg/L in methanol:water 2:1), and paclitaxel (115 mg/L in methanol:water 1:1) from Sigma-Aldrich were used.

Each spot on the stainless steel plate for the analysis consisted of 0.5µl of matrix solution and 0.5µl of analyte solution. For each analyte, we used two deposition methods: pre-mixing of the two solutions or sequential addition of the analyte solution on the dried drop of previously deposed AuNPs solution, and keeping the best result in terms of signal intensity for comparison with the other matrixes. Similarly, we considered the best result among LASiS-AuNPs I and II and we compared it with the best one among citrate-AuNPs I and II and with the organic matrix. This is because we did not observe big differences between samples I and II, while several differences exist between LASiS and citrate AuNPs matrixes.

For the LDI measurements, we used 70% of maximum laser power, corresponding to <10 µJ/pulse, for all measurements. Each spectra was averaged over 400 laser shots and analyzed with the software provided by the instrument. Each measurement was carried out for a minimum of three times. Each of the six sets of measurements (i.e. one for the bare matrixes and five for the analytes) was collected within the same measurement session, in order to minimize the possible effects due to fluctuations in spectrometer settings (i.e. laser power) from one session to another or over different days.

A4. Quantitative SERS measurements

Experimental procedure reported from Ref 12.

Sunitinib malate, paclitaxel, irinotecan hydrochloride, SN-38, doxorubicin hydrochloride were purchased from Sigma-Aldrich. All drugs were dissolved in methanol (HPLC grade, from Sigma Aldrich).

The following types of SERS-active plasmonic substrates were tested: gold nanoparticles in aqueous solution (AuNPs, average size of 30±13nm, 1.0mM in Au atoms) obtained by laser ablation synthesis in solution (LASiS), silver (Ag) NPs in aqueous solution (30±11nm, 1.0mM in Ag atoms) obtained by LASiS, commercial AuNPs in aqueous solution (BBI, 60±6nm, 1.0mM in Au atoms), commercial AgNPs in aqueous solution (Aldrich, 60±6nm, 1.0mM in Ag atoms) and commercial films of gold islands sputtered over silicon pyramids (Klarite, from Renishaw Diagnostics). For comparison, also crystalline silicon was used as a substrate.

In case of plasmonic substrates of NPs, samples were obtained by mixing 6 μL of colloid at the concentration indicated above with 6 μL of drug solution at variable concentrations, and depositing the mixture in cylindrical wells (2 mm in diameter for 4 mm height) obtained in a bulk aluminium plate. Then the liquid was evaporated prior to measurements.

In case of Klarite substrates, a viton mask with a cylindrical hole (1.5 mm in diameter for 3 mm height) was placed on the active area of the substrate and filled with 6 μL of drug solution. After evaporation of the liquid, the mask was removed and the Klarite substrate used for Raman measurements. The mask was reversibly sealed on the substrate by applying a slight mechanical pressure on the viton mask.

All the substrates were used only one time, i.e. they were not washed and recycled for another sample.

Raman spectra were recorded using a 20X objective (NA 0.40, 56% coverage). The software Renishaw WiRE 4.1 was used for data acquisition. We used the 488 nm line of a Ar^+/Kr^+ laser, the 633 nm line of a He-Ne laser and the 785 nm line of a diode laser all three at the power of 1.3 mW.

In our experimental set up, the noise level decreases with the 0.5^{th} power of the acquisition time. A crystalline silicon reference was used before and after each measurement for power calibration to account for daily laser intensity fluctuations (less than 5%).

Raman measurements were performed by homogeneously mapping the deposition area (1.8 mm^2 for Klarite and 3.1 mm^2 for NPs substrates) with 133 equally spaced collection points. The accumulation time for each spectrum was varied between 15 and 120 seconds (i.e. from ~30' to ~4h for each sample), depending on the signal to noise ratio. Baseline subtraction to the datasets of Raman spectra was performed with the Renishaw WiRE 4.1 software.

Principal component analysis (PCA) was performed with a built in routine (princomp) running under MatLab R2012a. The PCA dataset consisted of ~1900 spectra acquired by mapping the 4x4 mm^2 surface of a Klarite substrate with a resolution of less than 100 μm between each acquisition. The PCA dataset was normalized on the 1385 cm^{-1} band and spectra below 100 c.p.s. eliminated.

A5. Notes on Multivariate data analysis and Principal Component Analysis

Spectroscopic imaging analysis needs to register huge multidimensional datasets.
Even in bi-dimensional mapping, imaging techniques produces the so called data "hyper cubes", in which in addiction to the spatial *x* and *y* coordinate, also exist spectral and intensity dimensions.[109]
Usually, these four dimensional dataset are reduced to three dimensions, by expressing the intensities at single spectral coordinate, ea. the intensities at a single frequency for each *xy* point.
Nevertheless, such a univariate data analysis provide only limited information toward the complete composition of sample.
Taking into account the entire spectral range, instead of only a selected frequency, needs the use of a multivariate analysis.
Zhang et al. reported the multivariate analysis of a pharmaceutical model tablet made of four different chemical substances.[109] The authors analysed chemical micro-Raman imaging using different multivariate models and approaches. They also compared the final results in terms of quality and robustness of provided information.
The models used in the study were:[109]

- *principal component analysis (PCA)*: it is a statistical procedure to transform possible correlated variable (ea. spectral features) into a set of new orthogonal ones, called principal components. It has the advantage to reduce the number of variable giving the maximum information on the system.
- *cluster analysis*: it is a pattern recognition technique, which group objects as a function of similar characteristics. To do this, a feature extraction method is usually first applied to the original dataset, sometimes PCA.
- *direct classical least squares (DCLS)*: this approach can be applied only if reference spectra are available, because it is based on linear combination of such references.
- *multivariate curve resolution (MCR)*: it refers to a broad range of self-modelling mixture analysis method. Often additional constrains are applied to avoid the so called rotational ambiguity, namely the possibility to represent the data by multiple possible solutions.

PCA was extensively applied, because it doesn't need any preliminary information about the sample and is operator independent.
In a typical PCA, the four-dimensional dataset is expressed as a list of pixels, each one having its own spectral feature. In this way the dataset can be described with a matrix $\boldsymbol{D}$ made by M rows (number of spectra) and N columns (spectral frequencies). Each cell of the matrix $\boldsymbol{D}$ is an intensity value.
PCA decomposes $\boldsymbol{D}$ in such a way that $\boldsymbol{D} = \boldsymbol{T}\boldsymbol{P}^T + \boldsymbol{E}$, where $\boldsymbol{T}$ is the $M \times Q$ score matrix, $\boldsymbol{P}$ is the $N \times Q$ loading matrix, $\boldsymbol{E}$ is the $M \times N$ model residual matrix and Q is the number of principal components (PCs).[109] The principal components are obtained with the highest possible variance in such a way that, usually, the firsts few PCs represent over the 95% of the total variance.
The $\boldsymbol{P}$ loading matrix expresses the correlation between original variables (frequencies) and the principal components. So a PC loading usually appears with a spectral-like feature.

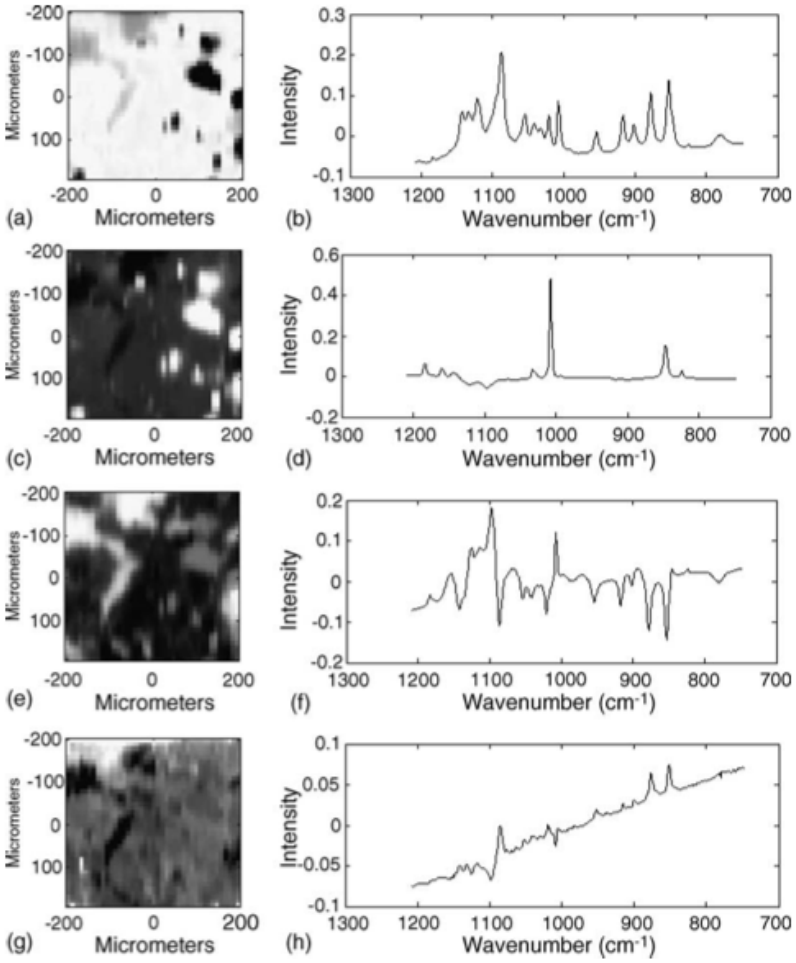

Figure A.2: PCA score images and loadings obtained by mapping a pharmaceutical tablet with Raman spectroscopy: PC1 (a - b), PC2 (c - d), PC3 (e - f), PC4 (g - h). The pixels in the score image with the higher score values are represented brighter. From Ref. 109.

At the same time the ***T*** score matrix are related to the level of representation of every point of analysis along every principal component. So a false colour map is usually employed to enhance which image pixel expresses similar behaviour along a PC. For example, as shown in Figure A.2 from the study of Zhang et al., the largest amount of mapped surface are well represented by the first PC (Figure A.2a-b), while only other little areas are represented by PC 2 and 3 (Figure A.2c-d and e-f).
If reference pure substances are available, quantitative evaluation of the correlation between each PC and real chemical species are possible by the correlation coefficients. For the spectra reported by Zhang et al., one can see in Table A.1 that PC1 results to be correlated largely to lactose and avicel, while PC2 almost exclusively to sodium benzoate and PC3 again to avicel. This explains why the same area appears the brightest in Figure A.2a and the darkest in Figure A.2e.

Table A.1: Correlation coefficient between PC loadings and pure reference spectra. From Ref. 109.

	Avicel	Lactose	Sodium benzoate	Magnesium stearate
PC 1	0.666	0.912	0.169	0.163
PC 2	−0.338	−0.105	0.973	−0.164
PC 3	0.647	−0.282	0.149	0.212
PC 4	−0.098	−0.132	−0.032	−0.104
PC 5	−0.070	−0.221	0.012	0.089
PC 6	0.011	−0.062	0.000	−0.210
PC 7	0.047	0.015	0.012	−0.826
Avicel	1	0.491	−0.117	0.277
Lactose		1	0.012	0.115
Sodium benzoate			1	−0.106
Magnesium stearate				1

Despite PCA often needs a certain level of interpretation, the huge quantity of information provided in such an automated and user independent procedure, makes it a potent multivariate analysis technique for chemometric imaging.

A6. Reactive SERS

List of stock solutions used for the reactions:

- Bis[2-(4-azidosalicylamido)ethyl] disulphide ($ASAES_2$, Sigma Aldrich, CAS: 199804-21-2) 3.15mM in CH_3CN
- Diethylamine (DEA, Sigma Aldrich, CAS: 109-89-7) 17.3mM in CH_3CN
- Tris(2-carboxyethyl)phosphine hydrochloride (TCEP, Sigma Aldrich, CAS: 51805-45-9) 130mM in H_2O
- Gold nanoparticles (AuNP) obtaind by LASiS in 10^{-5}M NaCl aqueous solution, average diameter 20nm, about 3nM in AuNP.

Reduction of $ASAES_2$ with TCEP

The following reaction scheme (Figure A.4) were used to verify the ability of TCEP to selective reduce the di-sulphur group instead of the azide group.

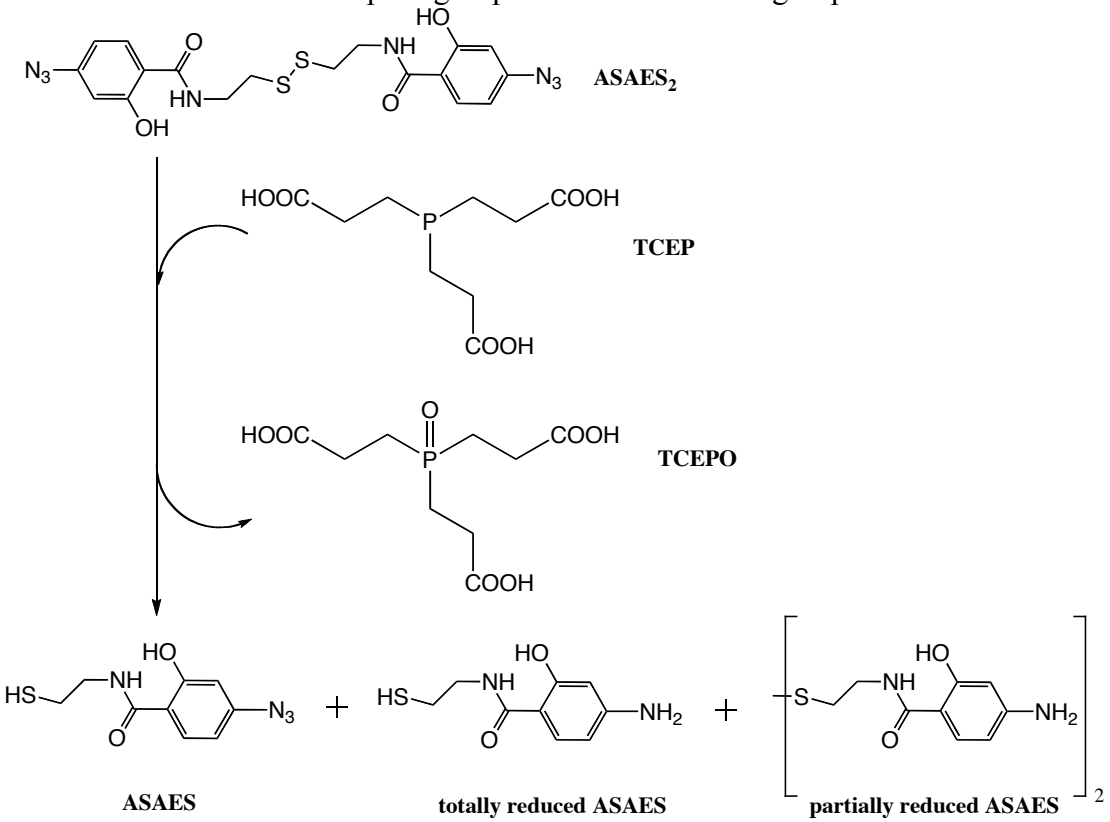

Reaction ID	TCEP 130mM (μL)	$ASAES_2$ 3.15mM (μL)	Molar ratio TCEP / $ASAES_2$
1:20	0.5	410	0.05
1:1	10	410	1
10:1	100	410	10

Figure A.3: Reaction scheme for the reduction of $ASAES_2$ with TCEP and the amount of reactants used.

The relative amounts of $ASAES_2$ and TCEP were mixed together under mechanical stirring for 1 hour at room temperature. Then the reaction mixture was directly analysed by MALDI-TOF mass spectrometry using DHAP-TFA as matrix in positive ionization modality, as reported in Figure 3.25.

Quantification of diethylamine with ReactiveSERS

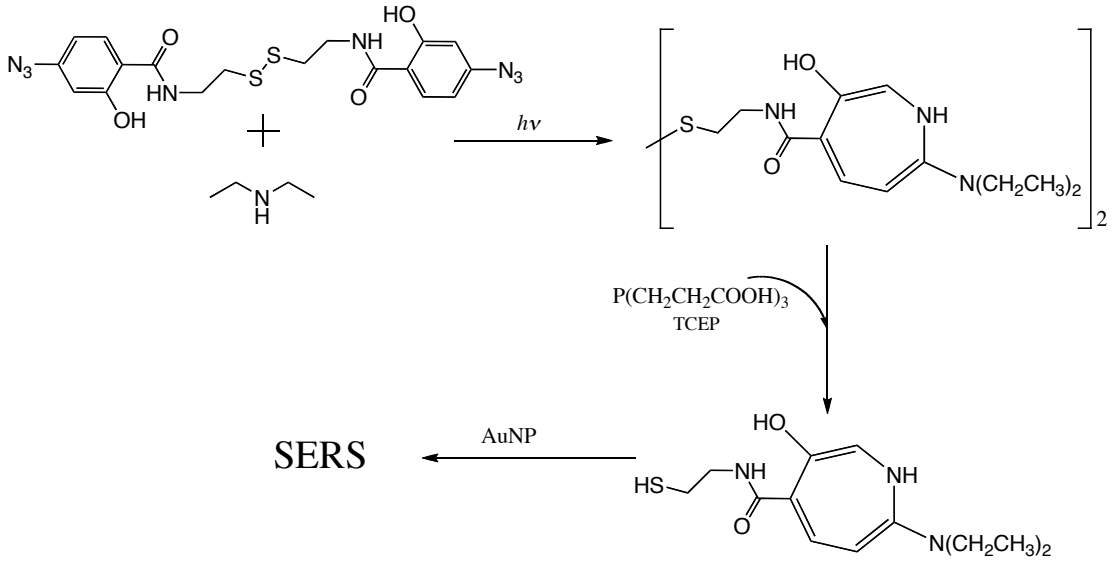

Reaction ID	$ASAES_2$ 3.15mM		DEA 17.3mM		CH_3CN	TCEP 130mM		Molar ratio DEA / $ASAES_2$
	Volume (μL)	Mass (μmol)	Volume (μL)	Mass (μmol)	Volume (μL)	Volume (μL)	Mass (μmol)	
A	500	1.57	0	0	200	15	1.95	0
B	500	1.57	50	0.86	150	15	1.95	0.55
C	500	1.57	100	1.73	100	15	1.95	1.10

Figure A.4: Reactions scheme for the ReactiveSERS protocol adopted as preliminary proof of principle, and a table with the amounts of reactant used.

Each reaction follows the same procedure. The relative amount of $ASAES_2$ and DEA are mixed into a quartz cuvette with 2mm of optical path. It is then irradiated with a common laboratory UV-lamp for 10 minutes.
Before the addition of TCEP, a little aliquot of the reaction mixture is removed and analysed by MALDI-TOF mass spectrometry, as reported in Figure 3.22.
Then the TCEP is added and the reaction proceeds under mechanical stirring for 1 hour.
The amount of 100 μL of reaction mixture is removed and mixed with 1 mL of AuNPs (about 3nM, $3 \cdot 10^{-12}$ mol). The reaction proceeds for 3 hours immersed into a sonication bath.
The particles are then centrifuged at 30,000 RCF for 10 minutes, the supernatant is removed and the particles dispersed in pure water. The same purification procedure is repeated for three times.
For Raman measurements, 20 μL of colloidal solution are dried on a glass slide and analysed with the 20x objective, 633 nm excitation wavelength at 0.3 mM of power for 10 seconds.
Each sample is analysed on 16 different areas, then all acquisitions are baseline subtracted and averaged into the spectra reported in Figure 3.26.

A7. Synthesis of functionalized Raman Active Dyes

Nile Blue

The functionalization reaction uses the amidic bond formation between the aromatic amine of Nile Blue A (NB, Sigma Aldrich, CAS: 53340-16-2) and the lipoic acid (Ac. Lip., CAS: 1200-22-2). The reaction was obtained in dimethylformamide (DMF) in presence of the base 2,4,6-trimethylpyridine (Collidine, Sigma Aldrich, CAS: 108-75-8) and 7-Aza-1H-benzotriazole-1-yl)-1,1,3,3-tetramethyluronium hexafluoro-phosphate (HATU, Sigma Aldrich, CAS: 148893-10-1).

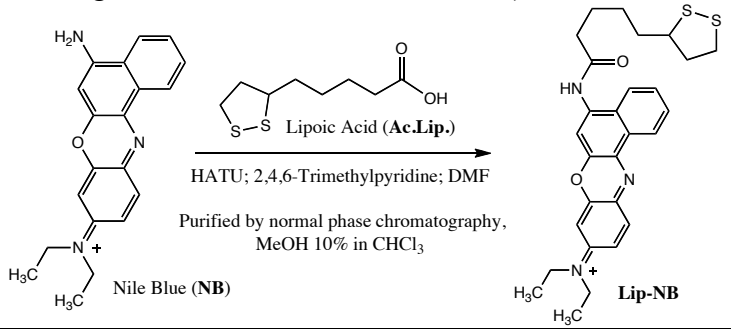

	Density [g/cm^3]	Volume [ml]	MW [g/mol]	Weight [mg]	Weight [µmol]	Equivalents
NB	-	-	417,85	20,75	49,7	1
Ac.Lip.	-	-	206,33	20,33	98,5	2
Collidine	0,92	0,065	121,18	59,8	493,5	9,9
HATU	-	-	380,23	38,34	100,8	2
DMF	0,94	1,5	-	-	-	-

Figure A.5: The reaction scheme for the Nile Blue functionalization (up) and the reagents used (down).

The reaction was followed by normal phase TLC using the eluent composed by $CHCl_3$ (87%): MeOH (13%). NB and LipNB show a blue colour whereas HATU and Collidine can be revealed under UV lamp. Lipoic acid was developed by the Kaiser test.

After about 6 hours the solvent was evaporated and the residue dissolved into the minimum amount of CH_3CN with 5% of MeOH. The mixture was then purified by normal phase chromatography using CH_3CN with 10% MeOH as eluent.

The final product was characterized by ESI-TOF mass spectrometry with positive ionization modality (theorical mass $[M]^+$ = 506.1930 Da, experimental mass $[M^+]$ = 506.1899 m/z).

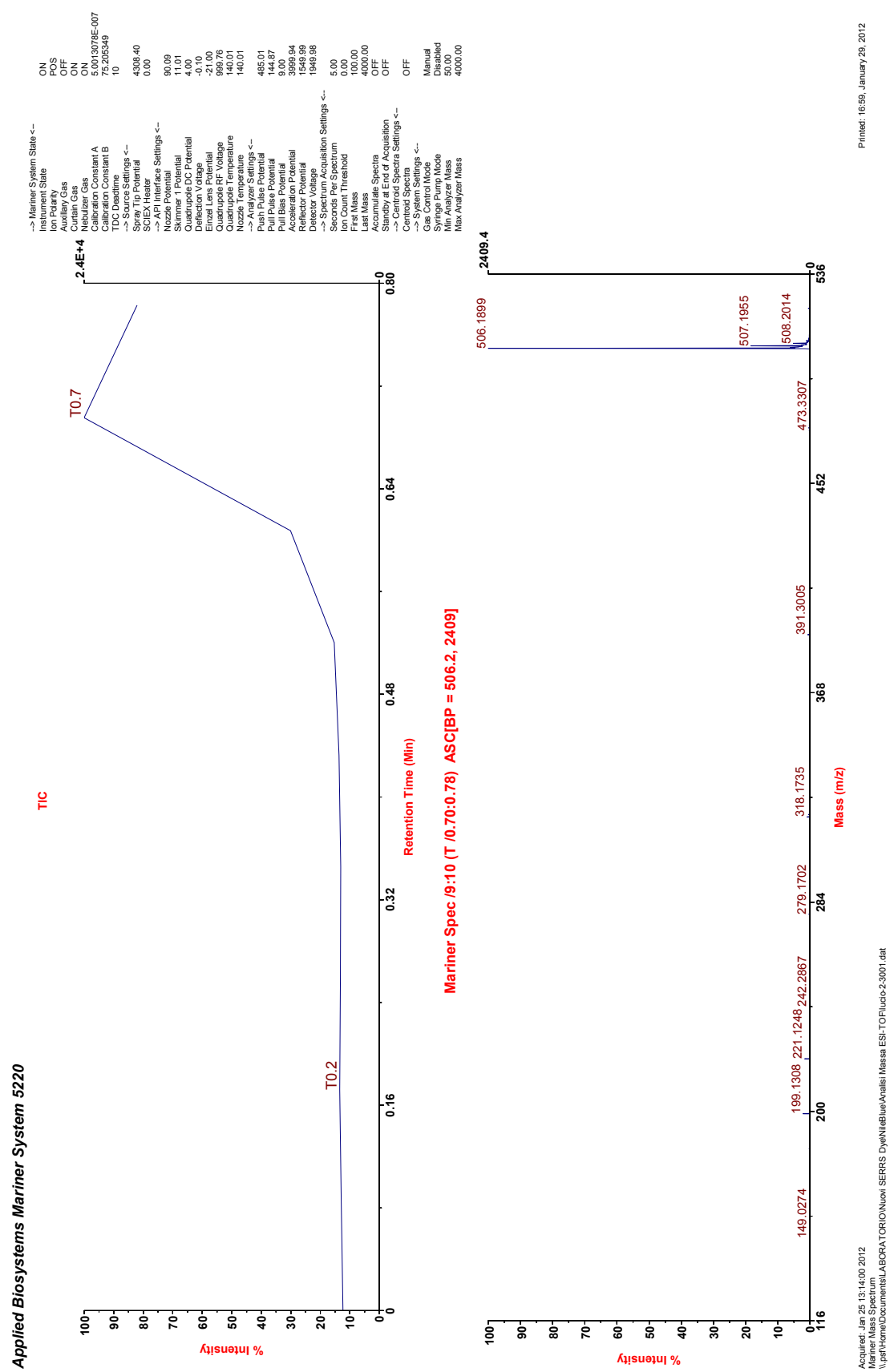

Figure A.6: ESI-TOF mass spectra of the final product LipNB obtained in positive modality.

Cy7SH

The commercial available IR783 dye (Sigma Aldrich, CAS: 115970-66-6) is well soluble in water, methanol and dimethylformamide, but slightly in dichloromethane (DCM). Nevertheless, its solubility in DCM is sufficient for the following reaction and DCM allows further liquid/liquid extraction with water.

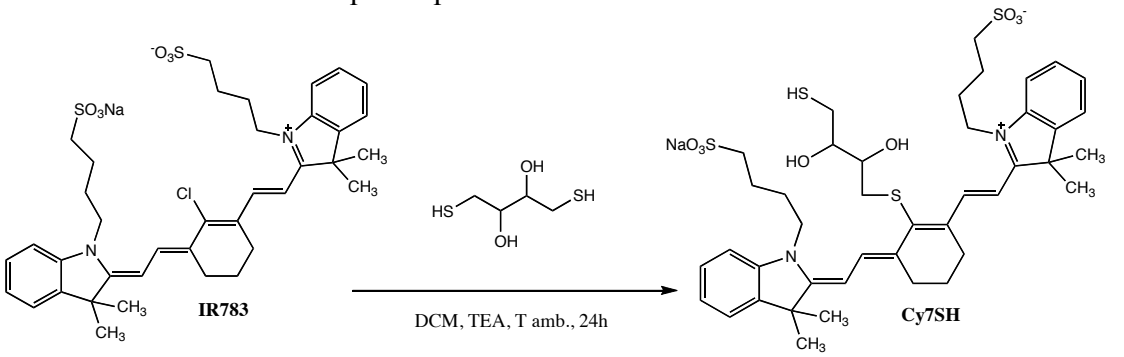

	MW, g/mol	Weight, mg	Weight, moli	Volum, uL	Density, g/mL	Conc, mol/L	Equivalents
IR783	749.35	12.3	1.64E-05	-	-	5.47E-03	1.00
DTT	154.25	2.7	1.75E-05	-	-	5.83E-03	1.07
DCM	-	-	-	3000	1.33	-	-
TEA	101.19	7.3	7.18E-05	10	0.727	2.39E-02	4.38

Figure A.7: The reaction scheme for the IR783 functionalization (up) and the reagents used (down).

IR783 are solubilized in DCM under magnetic stirring, then dithiothreitol (DTT, Sigma Aldrich, CAS: 3483-12-3) and triethylamine (TEA, Sigma Aldrich, CAS: 121-44-8) are added. The reaction proceeds for one day and is purified by liquid/liquid extraction using NaCl saturated aqueous solution. The aqueous phase is removed and, after two days, abundant precipitation occured.
A little fraction of the dark green solid is solubilized with methanol and characterized with MALDI-TOF mass spectrometry, showing the desired Cy7SH product (theoric mass $[M+H]^+$ = 867Da; experimental $[M+H]^+$ = 866.9m/z).
On the same MALDI-TOF analysis, a consistent signal from the reactant IR783 is present at 784.9m/z ($[IR783+H]^+$).
Analytical high pressure liquid chromatography, using a reverse phase C18 column, showed a reaction yield of about 50%.

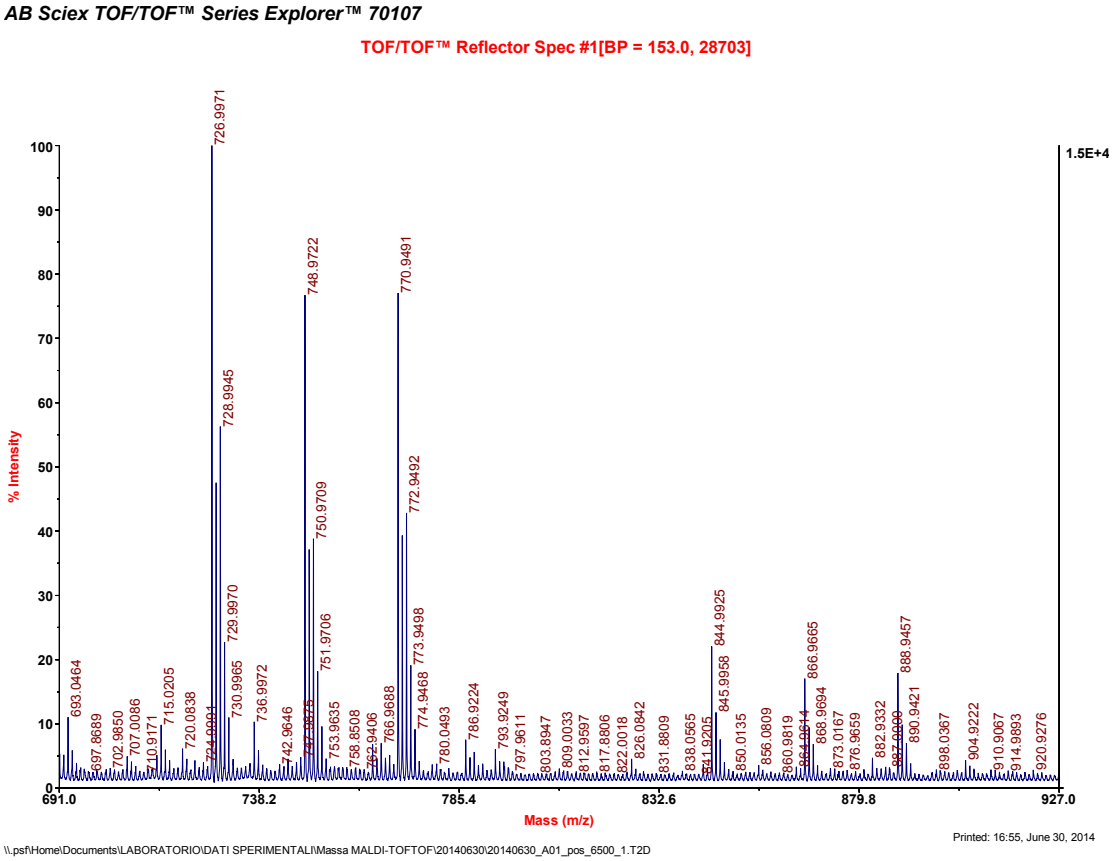

Figure A.8: MALDI-TOF mass spectra of the final product Cy7SH obtained in positive modality. DHAP-TFA was used as matrix.

NPCy(SH)$_2$

For the synthesis of mercaptoethanol substituted Silicon 2,3-naphthalocyanine dichloride (Sigma, CAS: 92396-91-3) 49.5mg of $NPCyCl_2$ were dissolved in 3mL of mercaptoethanol (Sigma) and a drop of triethilamine (TEA).

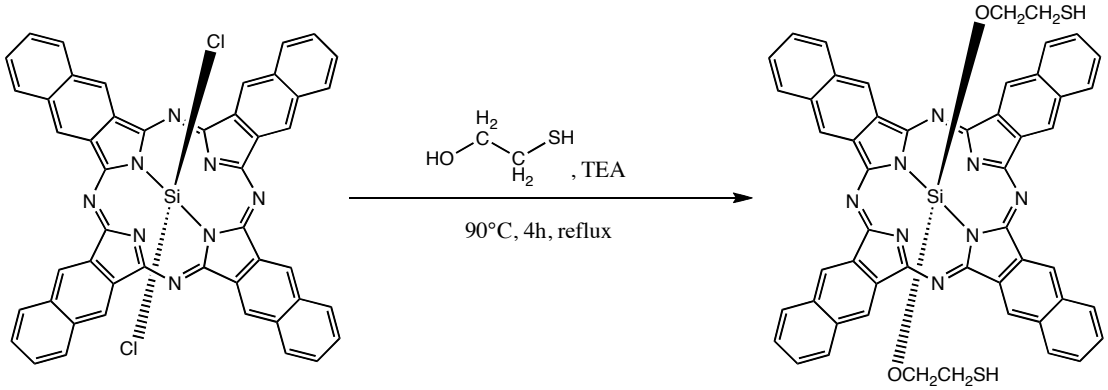

$NPCyCl_2$ **$NPCy(SH)_2$**

Figure A.9: The reaction scheme used for the synthesis of NPCy(SH)$_2$

The solution was stirred at 90°C under reflux for 4 hours and then the solvent was evaporated. The product was purified by a liquid-liquid extraction using dichloromethane and sodium chloride saturated aqueous solution. The final organic fraction was dried with $MgSO_4$ and the solvent evaporated. The product $NPCy(SH)_2$ was dissolved in methanol and characterized by UV-vis-NIR absorption (most intense band at 780 nm) and MALDI-TOF/TOF mass spectrometry with positive ionization mode and 2,4-dihydroxyacetophenone as matrix (theoretical 895,2015 m/z; experimental 894,9735 m/z).

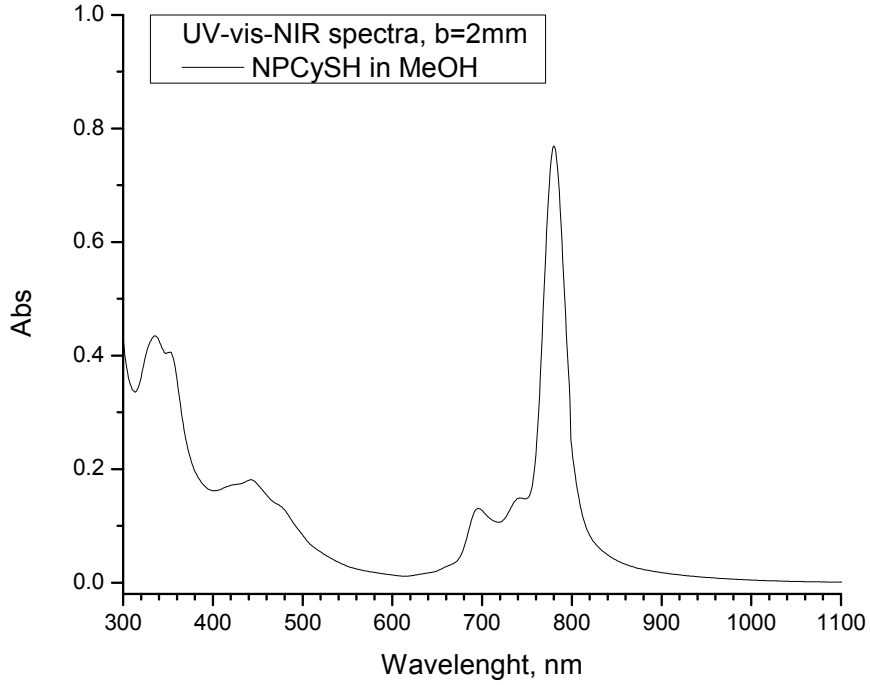

Figure A.10: UV-vis-NIR absorption spectra of NPCy(SH)$_2$ showing the characteristic band at 780 nm.

AB Sciex TOF/TOF™ Series Explorer™ 70107

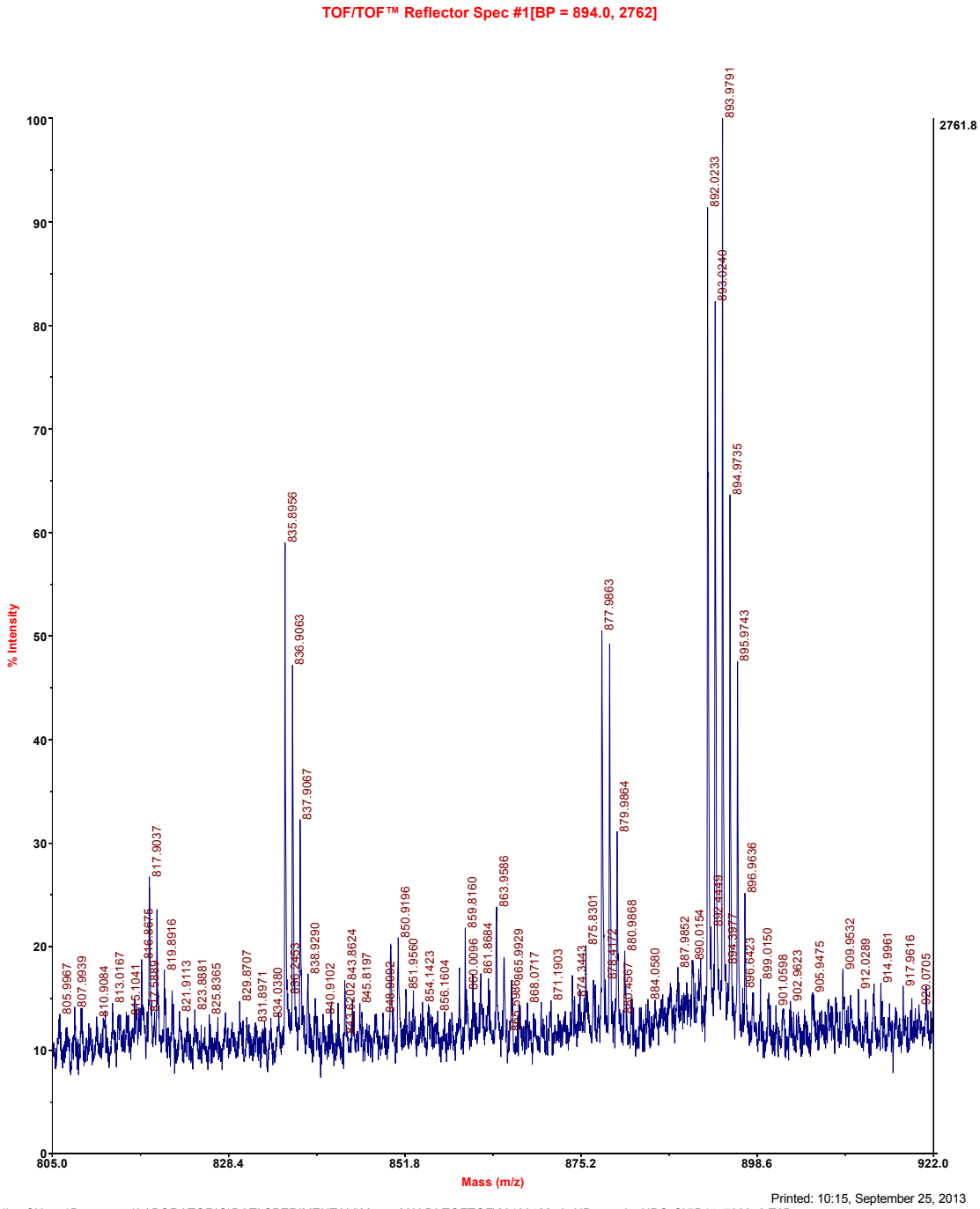

Figure A.11: MALDI-TOF mass spectra of the final product NPCy(SH)$_2$ obtained in positive modality. DHAP-TFA was used as matrix.

A8. Typical Synthesis of SERRS tags

In the following, a typical procedure used to synthesize SERS and SERRS tags is presented.[49, 74]

The entire protocol can be sketched as in Figure A.12.

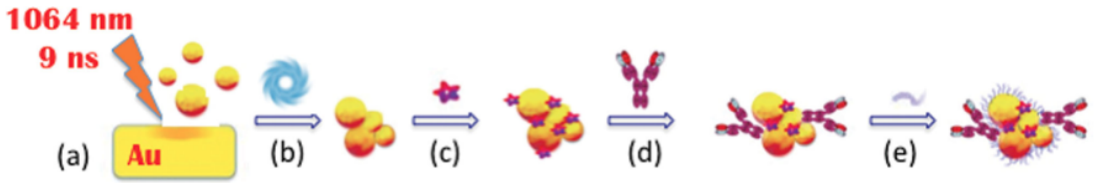

Figure A.12: A sketch representing the general steps involved in SERS and SERRS tag synthesis. a) AuNPs are synthesized by LASiS; b) centrifugation procedures allow to controlled aggregation of AuNPs; c) one of the Raman reporters is bound to nanoparticles; d) a previously thiolated antibody is added; e) long chains of mercapto-polyethylen glycol guarantee the complete surface coverage. From Ref. 74.

Antibody functionalization

Antibodies (Ab) are functionalized with a thiol group using 2-iminothiolane (2-IT). 150 µl of 1M solution of $NaHCO_3$ are mixed with a solution of 2-IT•HCl (0.5 g/L) and 0.7 mg of Ab. The reaction proceeds for two hours at room temperature and then overnight at 4 °C. The antibody is purified by centrifugal ultrafiltration (5000 Da, Vivaspin 500 Sartorius) and washed for three times with a PBS solution.

The degree of functionalization was obtained with the Ellman test, giving the average value of 1 new thiol group per Ab.

AuNPs aggregation and functionalization

4 ml of colloidal solution of gold nanoparticles obtained by LASiS (3 nM in water) are centrifuged at 30,000 RCF for 10 minutes and the aggregated nanoparticles are dispersed in bidistilled water by mild sonication.

About 100 µL of Raman reporter solution (always 50 µM) are stirred with the colloidal solution of the aggregated AuNP for 1 hour and are purified by centrifugation at 30,000 g . These nanoparticles are mixed with the solution of the thiol functionalized antibody. The reaction continues for 6 hours at room temperature and then overnight at 4° C.

The prepared nanostructures are purified by centrifugation at 30,000 g and then mixed with 100 µL of a solution of mercapto-Polyethylen glycol (5,000 Da, Rapp Polymere) (0.5 g/L). The reaction proceeds for 3 hours at room temperature. Purification of the nanostructures is obtained by centrifugation at 30,000 g. The precipitated nanoparticles are finally dissolved with a PBS solution and mixed with 5mg of BSA (bovine serum albumin) per mL of SERS tag.

UV-vis-NIR absorption and Raman spectroscopy are used to characterize the final product and the intermediate steps.

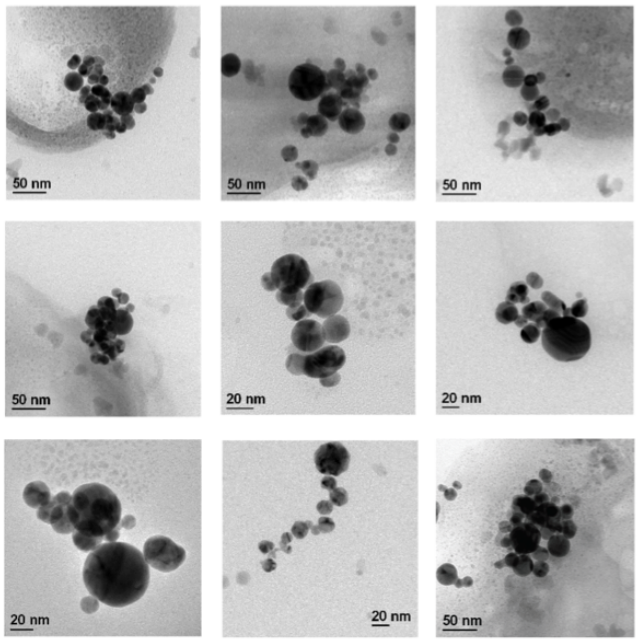

Figure A.13: TEM images of aggregated Au nanoparticles included in PVA to avoid their clustering after the solvent evaporation on TEM grids. From Ref. 74.

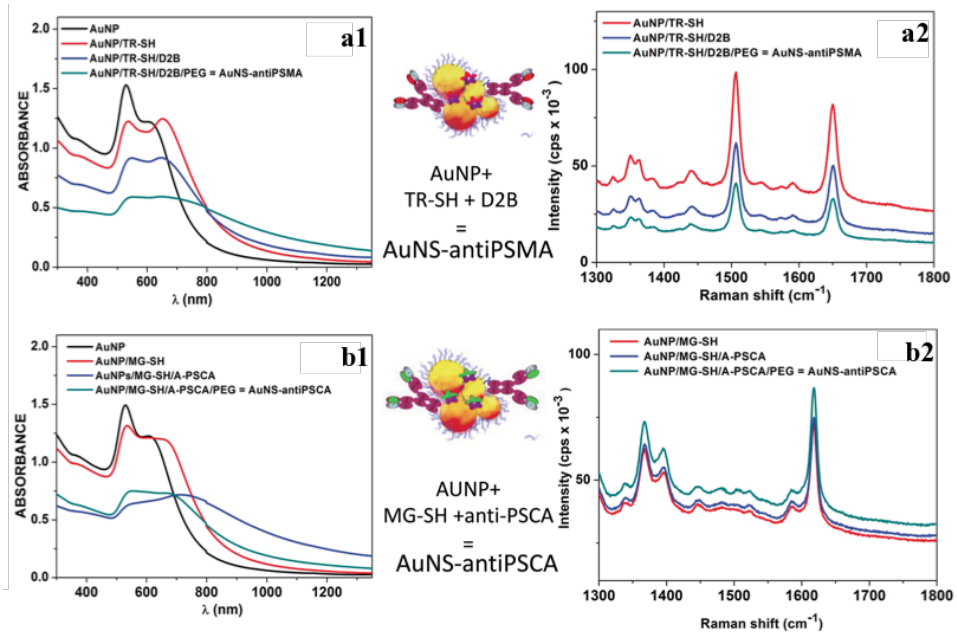

Figure A.14: UV-vis-NIR spectra (a1 and b1), and the relative SERS spectra (a2 and b2), of two representative SERRS tags during the main synthetic steps. The nanoparticles absorption shows broader bands after the antibody is added, but the SERS signals still remain intense and characterizing. From Ref. 74.

A9. SuperDOTA

A list of the reagents used for the solid phase and solution synthesis of the *SuperDOTA* and *SuperDOTA-Gd(III)* polymer:

- Fmoc-Cys(Trt)-Wang resin LL (100-200 mesh), Cys content of 0.30mmol/g, (***Wang resin***) Merk Millipore
- Fmoc-NH-PEG_{12}-COOH, (***PEG_{12}***) Iris Biotech, CAS: 867062-95-1
- (S)-5-Azido-2-(Fmoc-amino)pentanoic acid, (***AAN_3***) Sigma Aldrich, CAS: 1097192-04-5
- CH_3O-PEG-NHCO-C_2H_4-COOH, (***$mPEG_{2000}$***) Rapp Polymer, MW≈2,000 Da
- Dibenzocyclooctyne-N-hydroxysuccinimidyl ester, (***DBCO-NHS***) Sigma Aldrich
- NH_2-DOTA-GA, (***DOTA***) CheMatech, CAS: 306776-79-4
- $GdCl_3$•$6H_2O$, (***$GdCl_3$***) Sigma Aldrich, CAS: 1350-84-5

Synthesis of 7c and characterization

100mg of Wang resin and 2mL of dimethylformamide (DMF) are mixed together for 1 hour to make the resin swelling.

The entire polymer chain is obtained by the repetition of seven analogue coupling reactions. In the first six, PEG_{12} and AAN_3 are added alternatively, while the 7th coupling is obtained with $mPEG_{2000}$, as in Figure 5.6.

Each step occurs with the same following procedure.

The resins is treated for 5 minutes with a solution of 20% of piperidine in DMF, then the solvent is filtered and another aliquot of the same solution is added for 20 minutes. The solvent is removed again and the solid washed six times with 2mL of pure DMF. Then 80 μmol of reactant (PEG_{12}, AAN_3 or $mPEG_{2000}$) is added with HBTU/HOBT solution (*2 - (1H - Benzotriazole - 1 - yl) - 1,1,3,3 - tetramethyluronium hexafluorophosphate* and *1 – Hydroxybenzotriazole*, 150μL, 0.5M), DIPEA (N,N-*diisopropylethylamine*, 150μL, 1M) and DMF (700μL).

The reaction proceeds under mechanical stirring for 90 minutes, then the solvent is filtered and the resin washed six times with 2mL of pure DMF.

During the synthesis, little amounts of 4c and 6c intermediate (means after 4 and 6 coupling reactions) are extracted and analysed.

This procedure is repeated until the 7th coupling and then the polymer is removed from the resin. Two treatments with piperidine 20% in DMF are performed. Then the resin is washed with DCM (dichloromethane) and dried for about 10 minutes. A solution of 95% TFA (trifluoroacetic acid), 2.5% TIS (triisopropylsilane) and 2.5% H_2O is added and the reaction proceeds for 90 minutes.

The solution is separated by the solid and evaporated under nitrogen gas flow.

The residue is purified by crystallization in cold ethylic ether for three times.

The final light yellow solid and the intermediate products 4c and 6c are characterized by mass spectrometry and HPLC (only 4c and 6c).

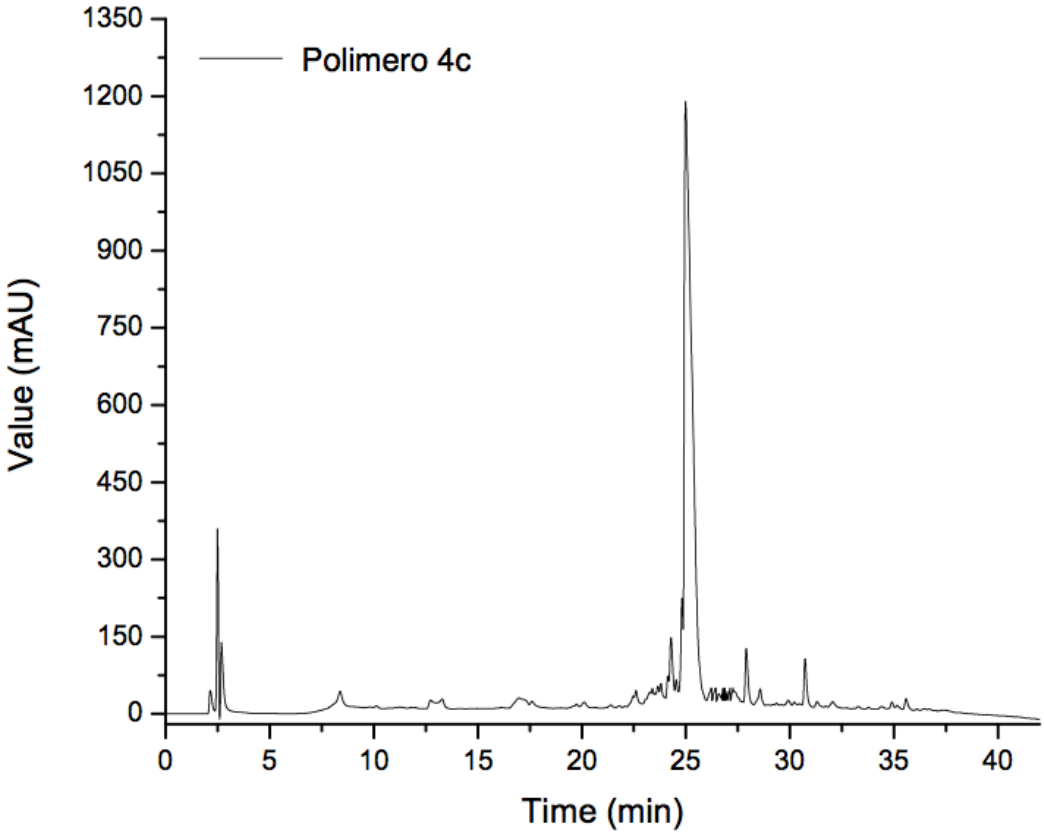

Figure A.15: Reverse phase HPLC of 4c intermediate solutions.

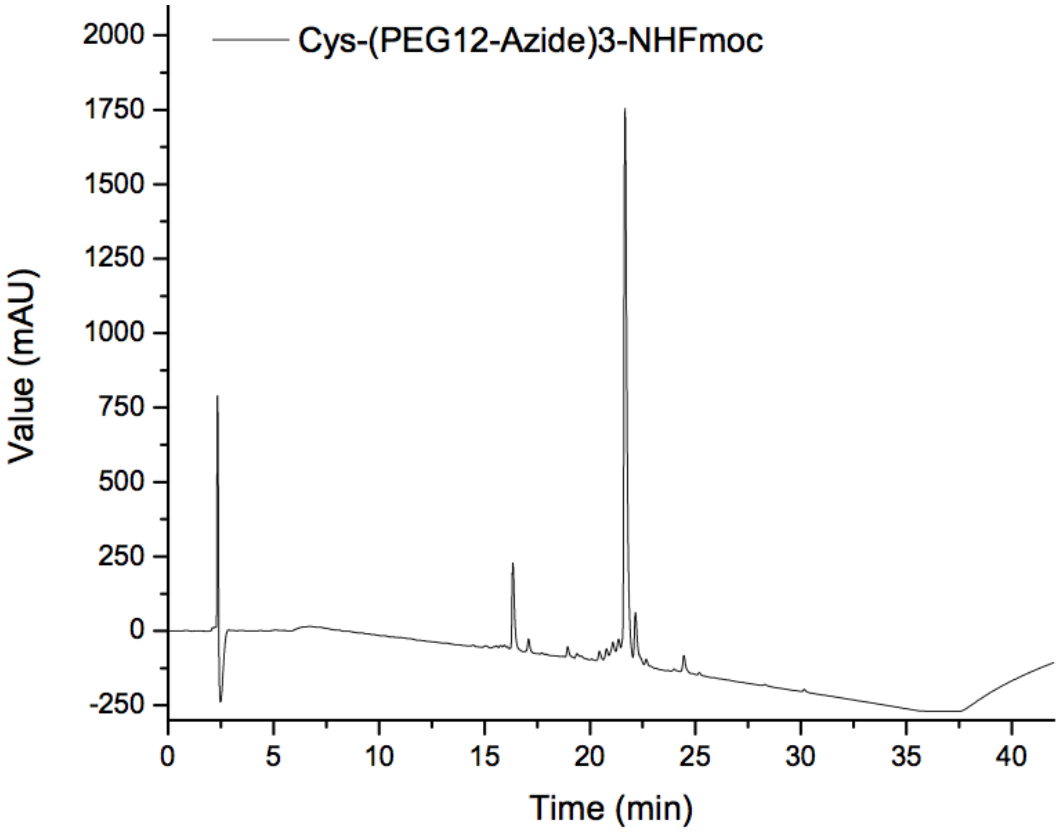

Figure A.16: Reverse phase HPLC of 6c intermediate solution.

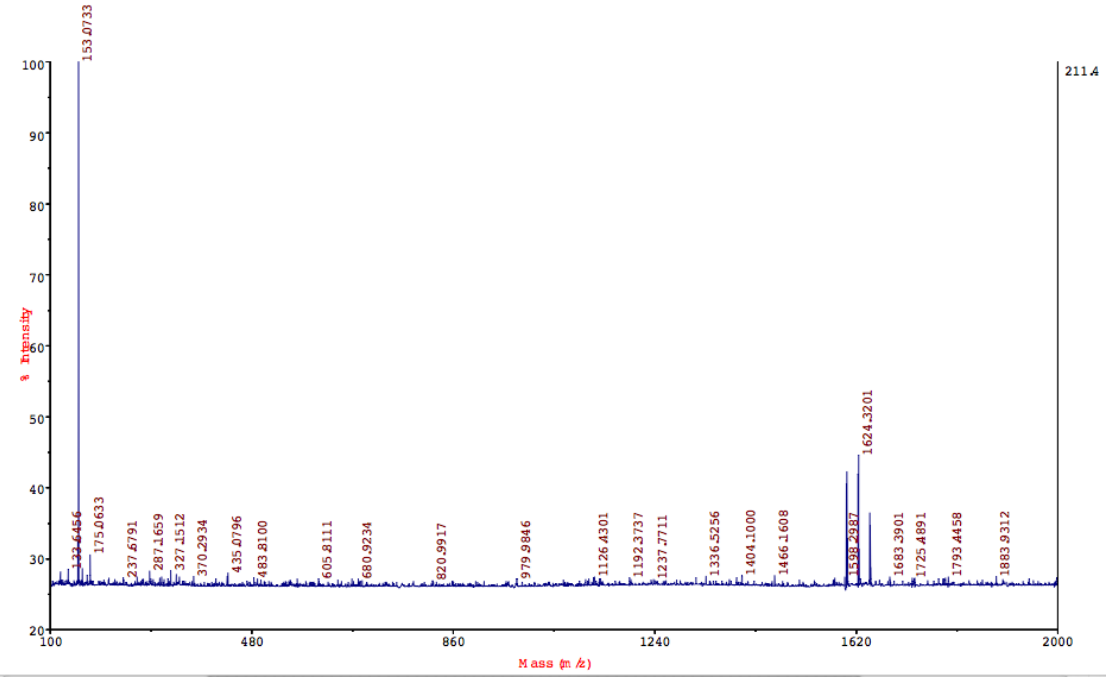

Figure A.17: MALDI-TOF mass spectra of intermediate 4c with positive ionization modality. DHAP-TFA was used as matrix. Theoretical MW = 1600.75 Da; experimental $[M+H]^+$ = 1601.34 m/z

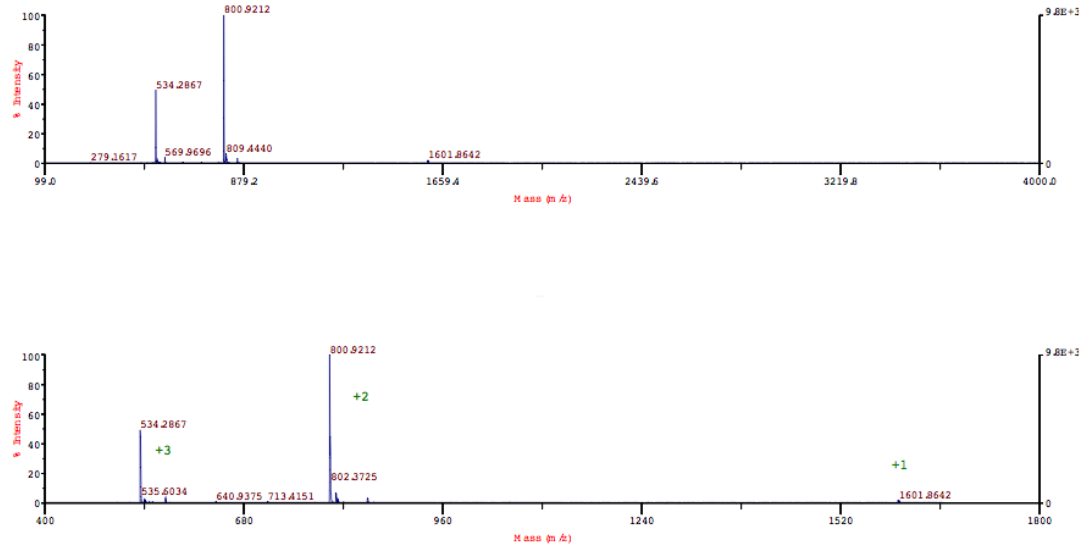

Figure A.18: ESI-TOF mass spectra of intermediate 4c with positive ionization modality. Theoretical MW = 1600.75 Da; experimental $[M+H]^+$ = 1601.86 m/z

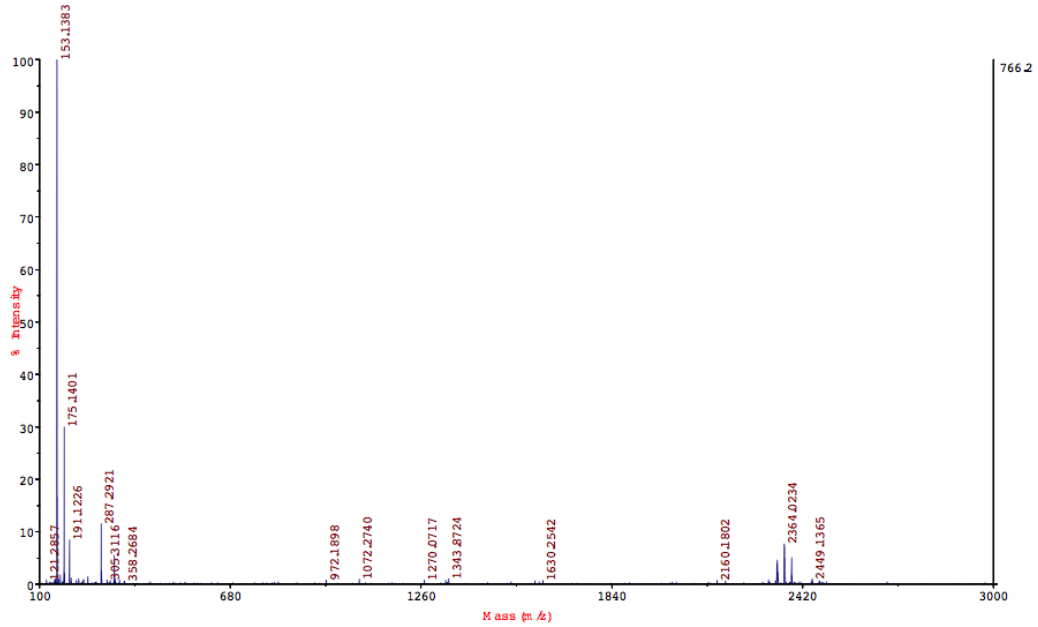

Figure A.19: MALDI-TOF mass spectra of intermediate 6c with positive ionization modality. DHAP-TFA was used as matrix. Theoretical MW = 2340.73 Da; experimental $[M+H]^+$ = 2342.01 m/z

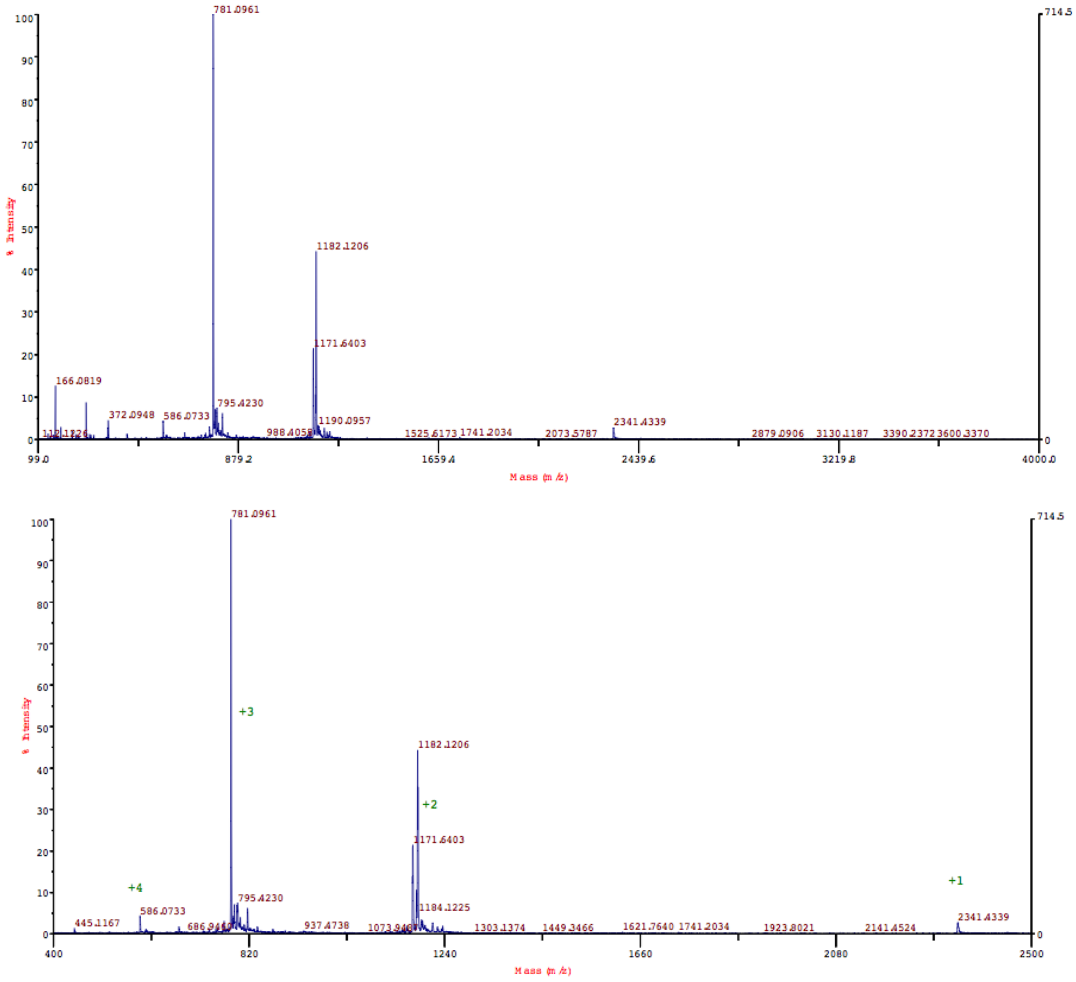

Figure A.20: ESI-TOF mass spectra of intermediate 6c with positive ionization modality. Theoretical MW = 2340.73 Da; experimental $[M+H]^+$ = 2341.43 m/z

Synthesis of SuperDOTA-Gd(III)

50.1 mg of DOTA (96.6 µmol) and 32.8 mg of DBCO-NHS (81.5 µmol) are mixed with 8mL of anhydrous DMF and 75 µL of DIPEA (diisopropylethylamine, 438 µmol), as in Figure 5.12.
The reaction proceeds for 5 days and then the solvent is evaporated and the residue re-dissolved in methanol.
The desired product was separated by water/ethyl acetate liquid phase extraction, washing the organic fraction four times. Nitrogen gas is then gurgled into the final aqueous solution to complete remove the ethyl acetate.
By ESI-TOF mass spectrometry and HPLC analysis, DOTA and DOTA-DBCO are found in the aqueous fraction (Figures A.21 and A.23), while DBCO-OH, DBCO-OCH_3 and DBCO-NHS in the organic fraction (Figure A.22 and A.23).

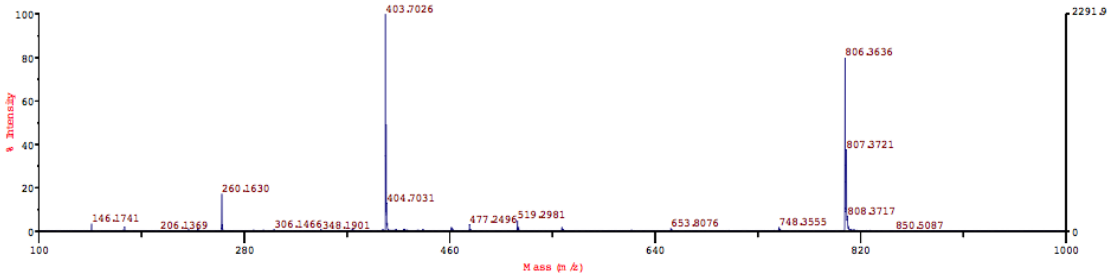

Figure A.21: ESI-TOF mass spectra of extracted aqueous fraction with positive ionization modality. Experimental $[DOTA\text{-}DBCO+H]^+$ = 806.36 m/z; $[DOTA+H]^+$ = 519.30 m/z

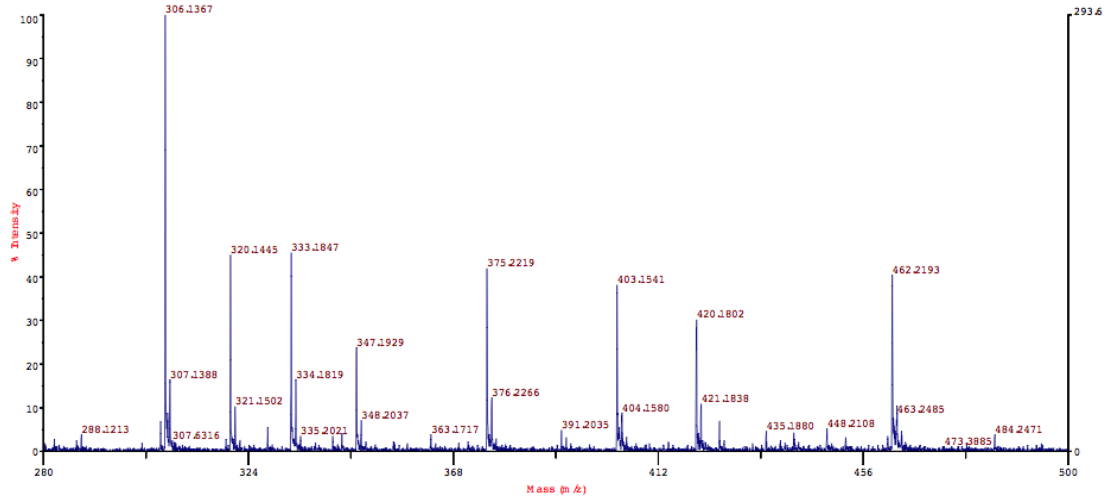

Figure A.22: ESI-TOF mass spectra of extracted organic fraction with positive ionization modality. Experimental $[DBCO\text{-}NHS+H]^+$ = 403.15 m/z; $[DBCO\text{-}OH+H]^+$ = 306.14 m/z; $[DBCO\text{-}OCH_3+H]^+$ = 320.14 m/z

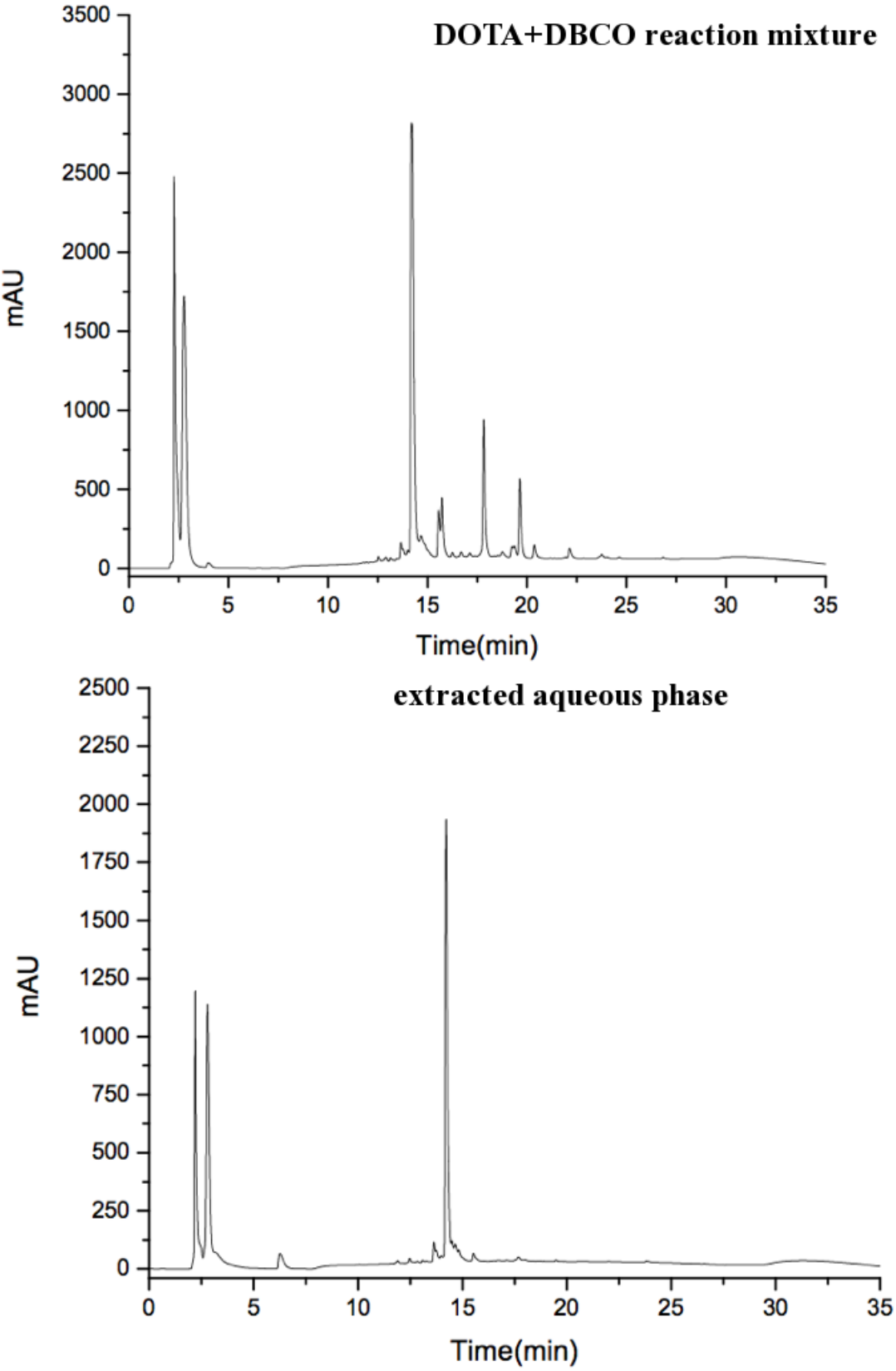

Figure A.23: Continue…

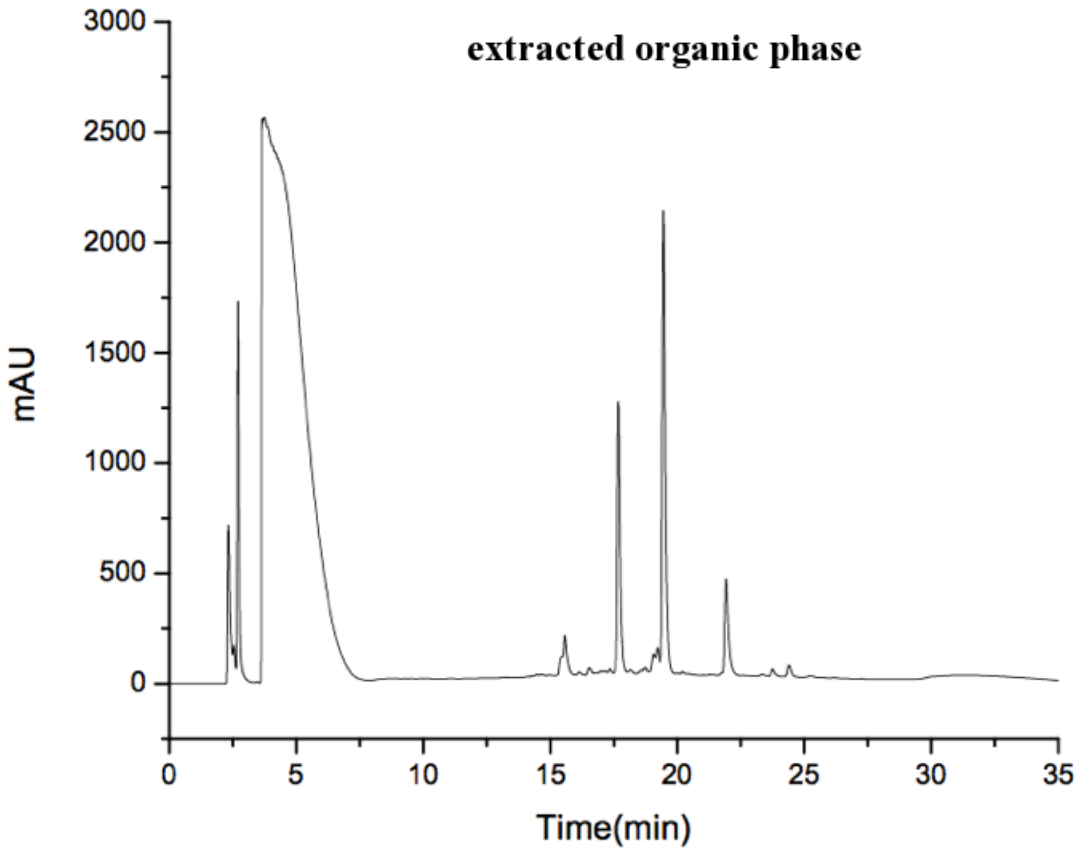

Figure A.23: Reverse phase HPLC of the DOTA-DBCO reaction mixture (top), the extracted aqueous solution (middle) and the extracted organic solution (down). The signal at about 14 minutes correspond to DOTA-DBCO.

Considering an approximate reaction yield of 50% between the total DOTA and the DOTA-DBCO, we estimated a DOTA-DBCO concentration in the aqueous phase of 2.4 mM.
2mL of such a solution (about 4.9 µmol of DOTA-DBCO) are mixed with 5.2 mg of 7c polymer (about 1.2 µmol). The reaction proceeds under mechanical stirring for one day. The reaction product (*SuperDOTA*) is purified by filtration on 2,000 Da cut-off membrane (Vivaspin, Sartorius) and re-dispersed in water. The product is characterized by HPLC and MALDI-TOF mass spectrometry (see Figure 5.15 and 5.16).
The *SuperDOTA* concentration is calculated by quantitative evaluation of free thiol content, following the Ellman and DTDP test procedures reported in literature.[100] We found 39 µM of thiols.
Then, 90 µL of *SuperDOTA* solution were mixed with a 10 fold excess of $GdCl_3$ (215 µL, 164 µM) in pure water, for one day under stirring. The gadolinium excess were then removed by osmosis using a 2,000 Da cut-off membrane (Vivaspin, Sartorius) for one day.
Then, the solution are recovered and directly used for the conjugation to AuNPs and magnetic resonance characterization (see Figure 5.17).

Synthesis of AuNP functionalized with SuperDOTA-Gd(III)

Gold nanoparticles are synthetized by LASiS in NaCl 10^{-5} M and characterized by UV-vis-NIR absorption using the Mie-Gans model as reported in literature.[6]

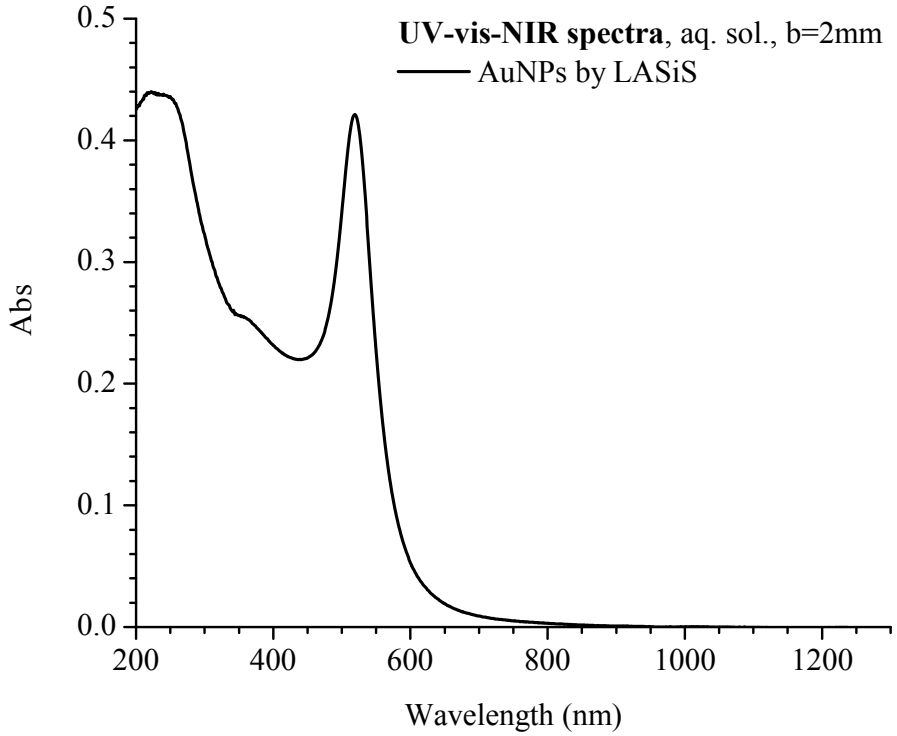

R (nm)	Spheres %	1-RSS	MaxSPA (m^2)	ε ($cm^{-1}M^{-1}$)	$Abs_{b=2mm}$ (519nm)	C (mol/L)
9.6	97%	4.13E-04	3.03E-16	7.94E+08	0.4213	2.65E-09

Figure A.24: UV-vis-NIR spectra of AuNPs synthetized by LASiS and the relative properties calculated.

3 mL of such AuNPs solution are mixed with 30 µL of LipNB 50 µM for 2 hours under sonication.

The colloidal solution is then centrifuged for 30 seconds at 30,000 RCF. The supernatant was eliminated and the particle dispersed in pure water by sonication. The solution was centrifuged again for 30 seconds at 30,000 RCF, the supernatant eliminated and the particles re-dispersed with 250 µL of the *SuperDOTA-Gd(III)* solution.

The reaction proceeded for one day and then the colloidal solution was purified by centrifugation (5 minutes at 30,000 RCF) for three times.

The final pellet is dispersed in 500 µL of pure water and characterized by UV-vis-NIR, Raman and magnetic resonance spectroscopy (see Figures 5.18 and 5.19).